Organization and fluctuations in living systems

Gabriel Morgado

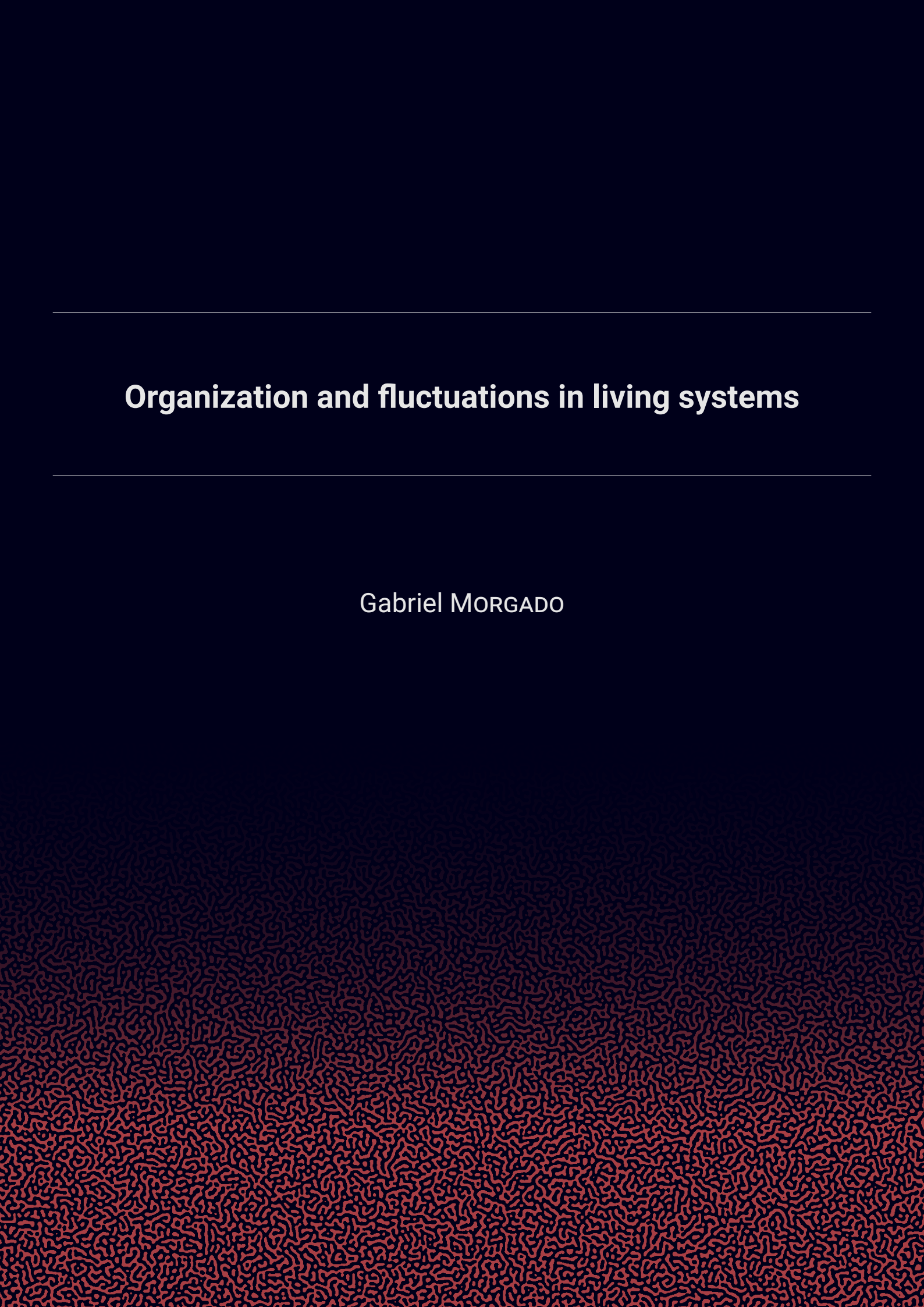

IChF
Institute of Physical Chemistry PAS

SORBONNE UNIVERSITÉ

Thesis submitted for the degree
of
Doctor of Philosophy

prepared within the

International PhD Studies

of the

Institute of Physical Chemistry of the Polish Academy of Sciences in Warsaw

presented by

Gabriel Rochinha Morgado

Organization and fluctuations in living systems

supervised by

dr. hab. Bogdan Nowakowski
&
Dr. Annie Lemarchand, HdR

Institute of Physical Chemistry of the Polish Academy of Sciences
ul. Kasprzaka 44/52, 01-224 Warszawa

Warsaw, February 2021

Acknowledgements

The totality is not, as it were, a mere heap, but the whole is something besides the parts.

Aristotle

First of all, I would like to thank the members of the NaMeS project for giving me the opportunity to carry out my research work in an institution of excellence. I will always remember my time at IChF.

I would like to thank my two supervisors, starting with my thesis supervisor Bogdan Nowakowski. I would like to express my sincere thanks to him for sharing his extensive knowledge in kinetic theory and for always helping me in any way he could.

Also, I express my deep gratitude to Annie, with whom I have been working for the past 5 years. She introduced me to the world of research and has been able to get the best out of me. I would especially like to thank her for the hard work she has done during all these years and for having gone far beyond her obligations.

I thank all the professors from Department VIII for facilitating my integration, especially Professor Gorecki for his always pertinent remarks, Professor Gozdz for helping me with Mathematica, Professor Ciach for organizing nice group lunches. I would like to thank Konrad and Slavko, who have greatly contributed to my integration into the group.

I sincerely thank Professor Kolos for his valuable help, as well as the administrative staff of the institute, in particular Patrycja Niton and Monika Kuczynska.

I would like to thank the other doctoral students, especially Richard for his unwavering good mood and for the good times in Warsaw. I thank the PhD students with whom I enjoyed sharing my office, Carolina for her kindness, Horacio for his precious help and discussions and Ashmita for her help.

I also thank Airit for the trips with the whole group and for the heated debates on American wrestling. I also thank all the other NaMeS PhD students (Jeel, Ying, Wassie, Ayesha, Viknasvarri, Alcina, Dusan, Nabila, Kumar, Faria, Yu-Kai, Yu-Ting, Mahsa, Rashmi, and Natalia). I would also like to thank Janek for helping me on my first day and throughout the time we spent at the institute, as well as Tomek for his interesting questions during my presentations.

I would also like to thank all my friends who accompanied me during my studies at the university. Many thanks to my undergraduate friends (Antoine for his unfailing friendship, Nico, Yassine, Quentin, Denis, Alban, Sylvie, Mija, Naoual, Matthieu and you too Martin); my friends in Roma (Michele and Rafaelle); my mates from M1 (Maxime

aka Nice Body, Yanis, David, Flo, Lucie, Léon, Luis) and all the members of Cucu (J-B, Géraud, again you Martin, Mathis, Tamara, Yassine, Soso, Thomas, Charlotte, Loutre, Kortchak, the ghost and all the others); my mates from M2 (Leo, Jules, stop following me Martin, Mathilde, Marion, Erwan, Subas). Many thanks to Jean-Mi, for all these enriching political discussions and these chess games soon to be avenged. Thank you to Youssef and Agnès from LPTMC for amazing shared moments.

Lastly, I thank my old friends from high school (Noaman, Rayane), my sister Silvia, my brother Jorge and his brother Theo, my parents, who gave me the freedom to realize what I wanted. Finally, I thank Vale for her unfailing love, support, and patience, and who, without this thesis, I would never have met.

Acknowledgements to funders

This research is part of a project that has received funding from the European Union's Horizon 2020 research and innovation programme under the Marie Skłodowska-Curie grant agreement No. 711859. Scientific work funded from the financial resources for science in the years 2017-2022 awarded by the Polish Ministry of Science and Higher Education for the implementation of an international co-financed project.

Abstract

The formation of structures in living organisms is addressed within the framework of far-from-equilibrium chemical systems using methods of statistical physics, such as kinetic theory and stochastic methods, at an intermediate, mesocopic scale. Three directions are explored. For the purpose of investigating the stochastic elimination of a fast variable, a fast species is eliminated from a nonlinear chemical mechanism. The fluctuations of the slow species using Langevin equations and a master equation are not correctly predicted by the reduced mechanism. The coupling between the fluctuations and the nonlinearities of deterministic dynamics makes the use of the quasi-steady-state approximation delicate when the studied system requires a good control such as in fluorescence correlation spectroscopy (FCS). A submicrometric Turing pattern is simulated in a concentrated system in order to refute certain objections to Turing's model regarding the preservation of proportions in embryos. Assuming an appropriate role of the solvent in the chemical mechanism is sufficient to control the wavelength of the structure by monitoring the concentration of the solution. The results can be exploited to design materials with controlled submicrometric properties in chemical engineering. Following a biomimetic approach, experimental conditions leading to the termination of the Turing structure associated with a decrease of the wavelength are proposed. The sensitivity of the Fisher-Kolmogorov, Petrovsky, Piskunov wave front to small perturbations is used to characterize the effects of the deviation from the dilution limit on diffusion. As a result, the shift of the concentration profiles of two species associated with different diffusion coefficients is a well-adapted criterion to detect perturbations induced by high concentrations. Contrary to the results of a deterministic description, the front speed deduced from the master equation in the dilute case sensitively depends on the diffusion coefficient of the consumed species. In the case of a concentrated solution, the properties of the wave front obtained in the dilute case remain valid but are mitigated by cross-diffusion terms which reduce the impact of different diffusion coefficients.

Streszczenie

Tworzenie struktur w organizmach żywych rozważane jest w ramach odległych od równowagi układów chemicznych przy użyciu metod fizyki statystycznej, takich jak teoria kinetyczna i metody stochastyczne, w pośredniej, mezoskopowej skali. Badane są trzy kierunki. W celu zbadania eliminacji szybkiej zmiennej stochastycznej, wprowadzono szybko reagujący związek do nieliniowego mechanizmu chemicznego. Fluktuacje związku o powolnej dynamice uzyskane za pomocą równań Langevina i równania master nie są prawidłowo przewidywane w mechanizmie zredukowanym. Sprzężenie fluktuacji z nieliniowością dynamiki deterministycznej sprawia, że stosowanie przyblizenia quasi-stacjonarnego jest delikatne, gdy badany układ wymaga dobrej kontroli, np. w spektroskopii korelacji fluorescencyjnej (FCS). Submikrometryczna struktura Turinga jest symulowana w układzie stężonym w celu odrzucenia pewnych zastrzeżeń do modelu Turinga dotyczących zachowania proporcji w zarodkach. Przyjęcie odpowiedniej roli rozpuszczalnika w mechanizmie chemicznym jest wystarczające do kontroli długości fali struktury poprzez monitorowanie stężenia roztworu. Wyniki mogą być wykorzystane do projektowania materiałów o kontrolowanych właściwościach submikrometrycznych w inżynierii chemicznej. Zgodnie z podejściem biomimetycznym, proponowane są warunki doświadczalne prowadzące do zakończenia struktury Turinga związane ze zmniejszeniem długości fali. Wrażliwość frontu fali Fishera-Kolmogorowa, Petrovskiego, Piskunova na małe perturbacje jest wykorzystywana do scharakteryzowania wpływu odchylenia od granicy rozcieńczenia na dyfuzję. W rezultacie, rozsunięcie profili stężeń dwóch składników związanych z różnymi współczynnikami dyfuzji jest kryterium dobrze dostosowanym do wykrywania perturbacji wywołanych przez wysokie stężenia. W przeciwieństwie do wyników opisu deterministycznego, prędkość frontu wyprowadzona z równania master w przypadku rozcieńczonym zależy od współczynnika dyfuzji gatunku konsumowanego. W przypadku roztworu stężonego, właściwości frontu fali uzyskane dla przypadku rozcieńczonego pozostają ważne, ale są łagodzone przez efekty dyfuzji krzyżowej, które zmniejszają wpływ odmiennych współczynników dyfuzji.

Contents

Preamble

Living organisms are fascinating examples of reaction-diffusion systems evolving into self-organized structures through sustained exchanges with the environment. Periodic time oscillations of concentrations, chaotic behaviors, and complex spatial structures are observed in chemical systems maintained far from equilibrium [1, 2, 3, 4].

The formation of Turing patterns and the propagation of a wave front are recognized as playing an essential role in the structuring of living organisms [2]. In 1952, Turing proved that reaction-diffusion processes in initially homogeneous far-from-equilibrium systems may lead to the formation of periodic spatial patterns observed in biology [5]. Zebra stripes and leopard spots are classical illustrations of the contribution of far-from-equilibrium reaction-diffusion systems to the modeling of morphogenesis. Turing's model is now used as a chemical basis for embryo development, e.g. in limb formation and teeth development [6, 7]. Even earlier, in 1937, Fisher built a model describing the propagation of a favored trait in a population. Simultaneously, Kolmogorov, Petrosky, and Piskunov studied the traveling solution of the same equation, further referred to as the FKPP wave front. The information conveyed by a signaling wave front during segmentation is at the base of different models of development [8, 9, 10, 11, 12].

Although associated with chemical mechanisms involving elementary steps between molecules, Turing patterns and FKPP wave fronts were first studied within the framework of a macroscopic approach based on partial differential equations. However, the description of phenomena arising during the early development, when the embryo is composed of a small number of cells, may require approaches at smaller scales. The interplay between fluctuations and nonlinear dynamics is known to induce non intuitive, model-specific behaviors [1, 13, 14]. The description of reaction-diffusion systems at the mesoscopic scale requires stochastic methods introducing random variables but still ignoring the detail of molecular dynamics [15, 16]. The crudest stochastic method used to describe reaction-diffusion systems consists in adding a Langevin force to the deterministic equations and assuming that the probability distribution of the concentrations is Gaussian [13, 14]. The correct description at the mesoscopic scale leads to a master equation relying on the well-founded hypothesis that reactions and diffusion are Markov processes. Reac-

tions are seen as birth and death processes, whereas diffusion is interpreted as jumps between adjacent spatial boxes [1]. Numerical simulations become necessary to describe dynamics at the molecular scale. When the details of electronic reorganization within a molecule can be ignored, classical mechanics is sufficient to describe particle dynamics. Simulations of molecular dynamics involve the computationally expensive deterministic processing of particle displacements and collisions, which could compromise reaching the space and time scales necessary for the emergence of structures in growing systems. In these conditions, it is appealing to consider the smart method intuited and developed by Graeme Bird and known as the direct simulation Monte Carlo (DSMC) [17, 18, 19]. DSMC has been designed to simulate the dynamics of dilute gases and is particularly adapted to space applications [20, 21, 22]. The collisions are efficiently treated through a random procedure known as Monte Carlo. It has been proven [23] that DSMC simulates the Boltzmann equations governing the evolution of the distribution functions for position and velocity of the particles [24]. In addition to following the laws of kinetic theory, DSMC provides stochastic trajectories and correctly simulates the fluctuations in agreement with the master equation [25]. Hence, the direct simulation Monte Carlo method offers an efficient alternative to molecular dynamics and gives access to space and time scales compatible with the simulation of emerging micrometric structures.

In this work, I developed stochastic approaches to far-from-equilibrium structures and focused on Turing patterns and Fisher-Kolmogorov, Petrovsky, and Piskunov wave fronts, both for their relevance in biology and the richness of their behavior from a fundamental point of view. Within this framework, several usual approximations have been revisited. The question of the elimination of a variable, encountered in the study of Turing patterns, incited me to investigate the validity of the widely used steady-state approximation in systems with large fluctuations. I was also led to consider the deviation from the high-dilution limit as a possible way to tune the features of a pattern. Beyond the application to the adaptability of a structure, dealing with concentrated systems prompted me to deepen my knowledge of the cross-diffusion phenomenon and the associated form of Fick's law deduced from irreversible thermodynamics in the linear domain [26]. In parallel, extending both the master equation and the direct simulation Monte Carlo method to concentrated solutions was an attractive challenge.

The manuscript is organized as follows. In the Chapter I, I recall the analytical and numerical methods that I used and adapted to concentrated systems.

The validity of the steady-state approximation in a small chemical system is questioned in Chapter II. In order to investigate to which extent the description of the fluctuations remains correct after elimination of a fast variable, I compared the correlations of concentration fluctuations for two different chemical mechanisms leading to the same reduced

mechanism in which a reactive intermediate species has been omitted. I first drew an analogy between the steady-state approximation and the Born-Oppenheimer approximation and expressed the conditions of validity of the steady-state approximation applied at the macroscopic scale. Then, I developed two stochastic approaches. Using an analytical Langevin approach and simulations of the master equation, I showed that the correlations of concentration fluctuations of the slow species are different depending on whether a fast intermediate species is considered or not in the reaction scheme. In biology, Fluorescence Correlation Spectroscopy (FCS) is widely used to study the dynamics of labeled species, for example to evaluate rate constants when the reaction scheme is supposed to be known [27, 28]. The interpretation of the results requires the comparison of the experimental data with analytical expressions of the correlations. My results point out that, even if it enables the analytical computation of the correlations, a tractable reduced reaction scheme could be misleading. The results have been published in G. Morgado, B. Nowakowski, and A. Lemarchand, Elimination of fast variables in stochastic nonlinear kinetics, Phys. Chem. Chem. Phys. **22**, 20801 (2020) [29].

Chapter III is devoted to Turing patterns. After recalling the basics of Turing structures, I place the subject in the context of morphogenesis. Turing's model relies on a remarkably small number of processes involving two initially homogeneously distributed chemical substances that interact to produce stable patterns. The model involves two chemical species, an activator and an inhibitor. The minimal reaction-diffusion scheme for the emergence of Turing patterns requires the autocatalytic production of the activator and the faster diffusion of the inhibitor [30]: The structure develops through local self-enhancement in conjunction with long-range lateral inhibition [31]. The wavelength of the periodic spatial structure is determined by the reaction rate constants and the diffusion coefficients of the chemical species. Contrary to Taylor vorticies in hydrodynamics, the striking property of Turing patterns is that the wavelength of the structure does not depend on the boundary conditions. The robustness of Turing patterns is a strong feature, but also an argument against them in morphogenesis. Indeed, Turing patterns lack scaling properties: they do not account for size adaptation of the wavelength to the global size of the system. Yet, models of somitogenesis should reflect that the size of the vertebrae is proportional to the size of the embryo [32, 33, 34, 35]. I addressed two points related to the growth of a Turing pattern in a growing system, the question of the scaling properties of a periodic spatial structure and the question of the termination of the structure.

Recently, the Polish-French group proposed to solve the problem of scaling of a Turing pattern at the macroscopic scale by considering the possible perturbations induced by high concentrations of reactants [36]. In these conditions, the variation of the concentration

of the solvent cannot be neglected. The model that the group developed includes the participation of the solvent into the reaction scheme. This third substance introduces an additional variable concentration that can be harnessed to control the behavior of the system. Changing the dilution of the medium makes it possible to tune the wavelength of the emerging Turing pattern. During this PhD, I performed a deeper analysis of the three-variable model at the microscopic scale and examined if the deviation from the high-dilution limit also induces a control of the pattern in small systems. A proof of concept based on simulations of particle dynamics was necessary. To this goal, I considered the direct simulation Monte Carlo (DSMC) method and adapted it to concentrated solutions. The simulations show that doubling the concentration of the solute leads to decreasing the wavelength of the structure by a factor of 2. The results can be considered as a possible interpretation for proportion preservation of embryos in morphogenesis. They can also be used to design materials with controlled submicrometric properties in chemical engineering. The results have been published in G. Morgado, B. Nowakowski, and A. Lemarchand, Scaling of submicrometric Turing patterns in concentrated growing systems, Phys. Rev. E **98**, 032213 (2018) [37] and were presented at the 31st International Symposium on Rarefied Gas Dynamics in Glasgow, in 2018 [38].

The question of the termination of a spatial structure is compelling in morphogenesis: The spine of the vertebrates ends with smaller vertebrae and the fingers with smaller phalanges. Within the framework of Turing patterns, this phenomenon implies both a decrease of the amplitude of the spatial oscillations and a decrease of the wavelength. Deciphering the mechanisms actually controlling the termination of the spine in an embryo is far beyond the scope of this work. The aim was to propose a possible mechanism, inspired by biological structures and compatible with the implementation in a chemical engineering context. The boundary conditions chosen by the group in 2016 [36] to model the growth of the spine behind a freely propagating wave front are well adapted to the design of an artificial spatial structure. I performed a systematic analysis of the effect of all rate constants and diffusion coefficients on the stability and the wavelength of the structure. Interestingly, a monotonous variation of almost any of the dynamical parameters leads to the simultaneous loss of stability of the structure and the decrease of the wavelength. Only the variation of the diffusion coefficient of the activator causes anticorrelated results. Locally varying a rate constant or the diffusion coefficient of the inhibitor in a given chemical system is not straightforward from an experimental point of view. For an easy implementation in chemical engineering, I suggest to impose an appropriate spatial profile for the concentration of the reservoir of inhibitor, resulting in the expected variation of the effective rate constant controlling the injection of the inhibitor in the system and leading to the desired termination of the structure. The results have been published in G. Morgado, L. Signon, B. Nowakowski, and A. Lemarchand, Termination

mechanism of Turing patterns in growing systems, Acta Phys. Pol. B, 50, 1369 (2019) [39].

The results obtained for the model of Turing patterns with a reactive solvent have opened new directions of research. The deviation from the high-dilution limit has an impact on both reaction and diffusion. In the case of Turing patterns, the perturbation of diffusion induced by high concentrations has a negligible effect on the wavelength of the structure. In order to investigate the possible consequences of the perturbation of diffusion in a concentrated reaction-diffusion system, I considered the case of pulled wave fronts, known to be sensitive to even small perturbations [40]. The results dealing with wave fronts are given in Chapter IV. For species with identical diffusion coefficients, the group already showed that an FKPP front is sensitive to the discrete nature of particles [41] and to reaction-induced deviations from partial equilibrium [42]. I proposed an FKPP-based model involving two species A and B engaged in the reaction $A + B \longrightarrow 2\,A$ with different diffusion coeffcients. In a concentrated system, the resulting wave front turns out to be a sensor revealing perturbations of diffusion at the macroscopic scale. Specifically, I showed that the difference of concentrations between the two species A and B at the inflection point of the A profile is a good indicator for diffusion perturbation in concentrated systems. The results have been published in G. Morgado, B. Nowakowski, and A. Lemarchand, Fisher-Kolmogorov-Petrovsky-Piskunov wave front as a sensor of perturbed diffusion in concentrated systems, Phys. Rev. E **99**, 022205 (2019) [43].

Deviations from the high-dilution limit are more prone to happen in small systems, typically in a living cell, where the amplitude of concentration fluctuations are significant. I therefore performed a stochastic analysis of fluctuation effects on an FKPP front with perturbed diffusion in a mesoscopic system. Unexpected results on a more than eighty-year-old problem have been obtained: In a dilute system of small size, the wave front propagates more slowly than expected if species B diffuses faster than species A. In a concentrated system, the results are mitigated by cross-diffusion which reduces the effect of different diffusion coefficients. The results have been published in G. Morgado, B. Nowakowski, and A. Lemarchand, Stochastic approach to Fisher and Kolmogorov, Petrovskii, and Piskunov wave fronts for species with different diffusivities in dilute and concentrated solutions, Physica A **558**, 124954 (2020) [44].

Chapter V contains conclusions.

Chapter I

Methods

This chapter presents different theroretical tools of macroscopic and stochastic descriptions of dynamical systems in chemistry that will be used in later chapters. Mathematical notations are also introduced.

I.1 Chemical kinetics

All considered systems involve reactive species and possibly non reactive species such as the solvent. The steps of a reaction scheme are supposed to be elementary reactions for which the standard laws of kinetics apply. The left-hand side of elementary steps involve one or more molecules. When only one molecule is involved in the left-hand side, the step leads to a *first-order* reaction rate. At the microscopic scale, it usually corresponds to an internal molecular reorganization. When two molecules are involved in the left-hand side, the step leads to a *second-order* reaction rate. At particle scale, it occurs through reactive collisions between two molecules.

It is very unlikely that a collision of more than two molecules occurs. Therefore, we consider that reactions of order higher than two result from the reduction of a set of elementary steps of first and second orders. The assumptions making this reduction possible will be discussed in Sec. II. Each chemical species is assumed to be subject to diffusive transport.

For some systems, we introduce *reservoirs*. A *reservoir* maintains the concentration of a chemical substance constant by instantaneously removing or adding molecules when needed. A *reservoir* is denoted by the letter R in a reaction scheme, and its constant concentration denoted by c_R.

I.1.1 Rate equations

We consider a reaction scheme involving m different steps with n different species $\mathrm{X_i}$. Each step j is associated with a rate constant k_j such that

$$\sum_{i=1}^{n} \alpha_{i,j} \mathrm{X_i} \xrightarrow{k_j} \sum_{i=1}^{n} \beta_{i,j} \mathrm{X_i} \tag{I.1}$$

where $\alpha_{i,j}$ and $\beta_{i,j}$ are possibly vanishing stoichiometric coefficients.

The rate equations for the concentrations c_i of species X_i associated with this reaction scheme are

$$\mathrm{d}_t c_i = \sum_{j=1}^{m} k_j \left[\beta_{i,j} - \alpha_{i,j}\right] \prod_{i'=1}^{n} c_{i'}^{\alpha_{i',j}} \tag{I.2}$$

where the symbol d_t denotes the derivative with respect to time $\dfrac{\mathrm{d}}{\mathrm{d}t}$.

The system state at a given time t is then defined by the vector of concentrations $\mathbf{c} = (c_1(t), c_2(t), ..., c_n(t))$

If the chemical species $\mathrm{X_i}$ is involved in a second or higher-order reaction, the system given in Eq. (I.2) is nonlinear and, in most cases, has no analytical solution.

I.1.2 Reaction-diffusion equation and Fick's law

In addition to the reaction, we introduce diffusive transport. Diffusion tends to homogenize concentrations in an inhomogeneous medium. According to Fick's law, the diffusive flux $\mathbf{j_i}$ of a given chemical species $\mathrm{X_i}$ is proportional to the concentration gradient

$$\mathbf{j}_i = -D_i \nabla c_i \tag{I.3}$$

where D_i is the diffusion coefficient of species $\mathrm{X_i}$. In a reaction-diffusion system, the local variation of concentration c_i of species $\mathrm{X_i}$ is expressed as the sum of a reactive term and a diffusive term, where the latter is given by the divergence of the flux

$$\partial_t c_i = \sum_{j=1}^{m} k_j \left[\beta_{i,j} - \alpha_{i,j}\right] \prod_{i'=1}^{n} c_{i'}^{\alpha_{i',j}} - \nabla \cdot \mathbf{j}_i \tag{I.4}$$

where the symbol ∂_t denotes the partial derivative with respect to time $\dfrac{\partial}{\partial t}$.

In concentrated mixtures involving more than two species, cross-diffusion effects may appear and are discussed in Sec. I.3

Equation (I.4) is valid in a macroscopic approach, in which local fluctuations have been neglected.

I.1.3 Linear stability analysis

In the general case of a homogeneous chemical system, dynamics is governed by a nonlinear system of differential equations for the concentration vector $\mathbf{c} = (c_1, ..., c_n)$

$$\mathrm{d}_t \mathbf{c} = f(\mathbf{c}) \tag{I.5}$$

where f is a vector function characterizing the reaction rates.

The local dynamics around a steady state $\mathbf{c^0} = (c_1^0, ..., c_n^0)$ obeying

$$\mathrm{d}_t c_i^0 = 0, \, \forall i \tag{I.6}$$

can be studied by the linearized dynamics around this state. In order to perform a linear stability analysis, we introduce the small deviation $\delta c_i = c_i - c_i^0$ to the steady state which obeys

$$\mathrm{d}_t \delta\mathbf{c} = \mathbf{M^0} \delta\mathbf{c} \tag{I.7}$$

where $\delta\mathbf{c} = (\delta\mathbf{c_1}, ..., \delta\mathbf{c_n})$ and

$$\mathbf{M^0} = \left(\frac{\partial f(\mathbf{c})}{\partial \mathbf{c}} \right)_{\mathbf{c}=\mathbf{c^0}} \tag{I.8}$$

is the Jacobian matrix for $\mathbf{c} = \mathbf{c}^0$, called the *stability matrix*. Some laws of conservation can be observed and reduce the number of independent variables. We consider that the n variables are all independent. The deviation $\delta\mathbf{c}$ is related to the vector $\gamma = (\gamma_1, ..., \gamma_n)$ in the eigenbasis of $\mathbf{M^0}$ by

$$\delta\mathbf{c} = \mathbf{P}\gamma \tag{I.9}$$

where $\mathbf{P}$ is the change-of-basis matrix. The linear differential equations given in Eq. (I.7) lead to uncoupled equations in the eigenbasis of $\mathbf{M^0}$

$$\mathrm{d}_t \gamma_i = \mu_i \gamma_i \tag{I.10}$$

where μ_i are the eigenvalues of $\mathbf{M^0}$. Equation (I.10) is straightforwardly solved, leading

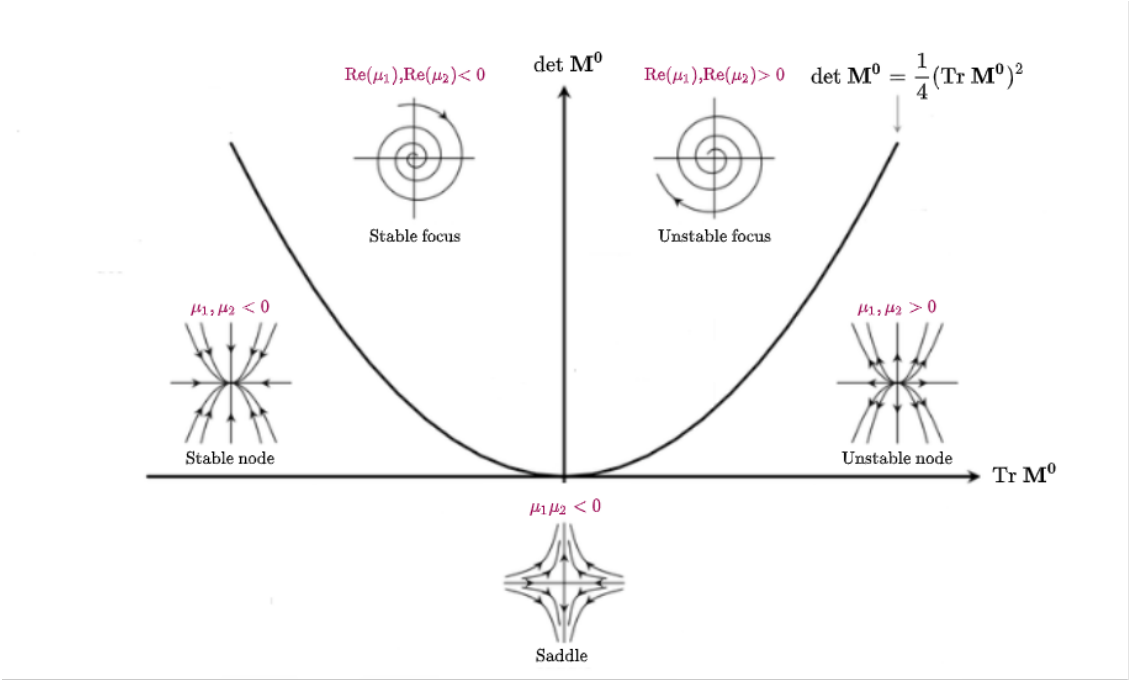

Fig. I.1 *The five typical phase portraits for an $n = 2$ system. [2]*

to

$$\gamma_i = \gamma_i^{\mathrm{ini}} e^{\mu_i t} \tag{I.11}$$

where γ_i^{ini} is the initial value of γ_i.

From Eq. (I.11), it appears that the linear stability of the system is governed by the eigenvalues μ_i. If the real parts of all eigenvalues are negative, then the system eventually converges towards the steady state $\mathbf{c^0}$. The time $\tau_i = 1/|\mathrm{Re}(\mu_i)|$ corresponds to the typical relaxation time in the direction associated with γ_i, as long as the deviation $\delta\mathbf{c}$ is in the linear domain around the steady state $\mathbf{c^0}$.

In Fig. I.1, different phase portraits are presented for an $n = 2$ system. Five typical phase portraits exist: the *stable node* corresponds to two real negative eigenvalues, $\mu_1 < 0$ and $\mu_2 < 0$, the *stable focus* corresponds to two complex-conjugate eigenvalues whose real parts are negative, $\mathrm{Re}(\mu_1) < 0$ and $\mathrm{Re}(\mu_2) < 0$, the *unstable node* corresponds to two real positive eigenvalues, $\mu_1 > 0$ and $\mu_2 > 0$, the *unstable focus* corresponds to two complex-conjugate eigenvalues whose real parts are positive, $\mathrm{Re}(\mu_1) > 0$ and $\mathrm{Re}(\mu_2) > 0$, and the *saddle* corresponds to two real eigenvalues with different signs, $\det \mathbf{M^0} = \mu_1\mu_2 < 0$.

Finally, substituting Eq. (I.11) for γ_i into Eq. (I.9), we obtain

$$\delta c_i = \sum_j P_{ij} \gamma_j^{\text{ini}} e^{\mu_j t} \tag{I.12}$$

Linear analysis describes local evolution around a steady state within the framework of a macroscopic, deterministic approach. In small systems, close to situations where the dynamics is sensitive to small perturbations, such as bifurcations, a deterministic analysis may be insufficient. A stochastic approach, including the description of the fluctuations at the mesoscopic scale, is then required.
I have used linear stability analyses extended to inhomogeneous systems to study the termination of a Turing structure [39] presented in Sec. III.2.

I.2 Stochastic chemical kinetics

Although chemical dynamics is driven by discrete elementary processes, it is usually sufficient to consider deterministic equations to describe the macroscopic evolution of a chemical system. However, fluctuations may not be negligible in small systems and a stochastic approach may be required [1, 16, 45]. In this section, we introduce two different stochastic descriptions of a chemical system, the chemical Langevin equations [13, 14] and the master equation [1].

I.2.1 Chemical Langevin equations

In this subsection, we introduce a probabilistic approach to a reactive system [46]. We consider the vector of concentrations $\mathbf{c}$ as a vector of random variables. Intuitively, the propensity or transition rate $p_j(\mathbf{c})$ that the j-th step of the reaction occurs in the next time interval $[t, t+dt]$ depends on the order of the step. The probability for a first-order step to occur is proportional to the number of molecules N_i in the system, since each molecule is susceptible to be re-organized

$$\begin{aligned} p_j^I(\mathbf{c})dt = &\text{Probability that a molecule re-organizes itself} \\ &\times \text{Number of molecules } N_i \end{aligned} \tag{I.13}$$

The probability for a second-order step to occur depends on the product of two probabilities

$$\begin{aligned} p_j^{II}(\mathbf{c})dt = &\text{Probability that two given molecules collide} \\ &\times \text{Probability that two colliding molecules react} \\ &\times \text{Number of possible pairs of molecules} \end{aligned} \tag{I.14}$$

According to kinetic theory, the first probability is proportional to the average relative speed and collision cross-section of the two molecules and inversely proportional to the system size Ω. The second probability expresses that reaction occurs if the collision energy exceeds a certain threshold known as activation energy. The product of these two probabilities gives the so-called rate constant introduced in Sec. I.1, except that specific care is needed in order to convert a probability derived from a discrete number of molecules into a proportionality factor that deals with continuous concentrations. Specifically, the conversion introduces as much Ω factors as the order of the reaction.

If concentrations c_i are locally homogeneous, $p_j(\mathbf{c})$ is typically similar to the reactive term in Eq. (I.2) for all reaction orders

$$p_j(\mathbf{c}) \simeq \Omega k_j \prod_{i=1}^{n} c_i^{\alpha_{i,j}} \tag{I.15}$$

During a finite but small time interval $[t, t+\tau]$, the number of reactions $r_j(\mathbf{c}, \tau)$ of step j is a random variable whose mean $\langle r_j \rangle_{t,\tau}$ is deduced from Eq. (I.14)

$$\langle r_j \rangle_{t,\tau} = p_j(\mathbf{c})\tau \tag{I.16}$$

where the concentration $\mathbf{c}$ is evaluated at time t. For the reaction scheme given in Eq. (I.1), the concentration c_i at time $t+\tau$ is given by

$$c_i(t+\tau) = c_i(t) + \frac{1}{\Omega} \sum_{j=1}^{m} (\beta_{i,j} - \alpha_{i,j})\, r_j(\mathbf{c}, \tau) \tag{I.17}$$

Some conditions must be fulfilled for Eqs. (I.16) and (I.17) to hold. On the one hand, τ must be sufficiently small for the variations of concentration between two consecutive time steps to be small. It implies that the propensity given in Eq. (I.14) is constant over the time interval $[t, t+\tau]$. This condition is satisfied if the number of each type of molecules in the system is much larger than 1. On the other hand, τ must be sufficiently large for $r_j(\mathbf{c}, \tau)$ to be substantial, i.e. for the mean number of reactions $\langle r_j \rangle_{t,\tau}$ to be much larger than one. It is not unusual to find systems with sufficiently large numbers of molecules that respect both conditions. Typically, mesoscopic systems are of adequate size for these

two conditions to be satisfied.

It can be argued that each random variable $r_j(\mathbf{c},\tau)$ follows an independent *Poisson* distribution of mean μ. However, the construction of a standard Langevin equation introduces independent first and second cumulants of the probability distribution of $\mathbf{c}$. Using the condition that the system contains a large amount of molecules, each *Poisson* random variable $r_j(\mathbf{c},\tau)$ can be approximated by a normal random variable $\mathcal{N}(\mu,\sigma^2)$ of same mean μ and variance σ^2. The linear combination theorem for normal distributions

$$\mathcal{N}(\mu,\sigma^2) = \mu + \sigma\mathcal{N}(0,1) \tag{I.18}$$

and Eq. (I.16) allow us to write Eq. (I.17) into the form

$$c_i(t+\tau) = c_i(t) + \frac{1}{\Omega}\sum_{j=1}^{m}(\beta_{i,j}-\alpha_{i,j})\left[p_j(\mathbf{c})\tau + (p_j(\mathbf{c})\tau)^{1/2}\mathcal{N}(0,1)\right] \tag{I.19}$$

Considering the time τ as an infinitesimal time interval $\mathrm{d}t$ that respects the conditions mentioned above and using Eq. (I.15), we write Eq. (I.19) as a *chemical Langevin equation*

$$\frac{\mathrm{d}c_i}{\mathrm{d}t} = \sum_{j=1}^{m} k_j(\beta_{i,j}-\alpha_{i,j})\prod_{i'=1}^{n} c_{i'}^{\alpha_{i',j}} + \sum_{j=1}^{m}(\beta_{i,j}-\alpha_{i,j})\left[k_j\prod_{i'=1}^{n} c_{i'}^{\alpha_{i',j}}\right]^{1/2}\xi_j(t) \tag{I.20}$$

with independent Gaussian white noises $\xi_j(t)$

$$\begin{aligned}\langle\xi_j(t)\rangle &= 0\\ \langle\xi_j(t)\xi_{j'}(t')\rangle &= \delta_{j,j'}\delta(t-t')\end{aligned} \tag{I.21}$$

In Eq. (I.20), the first term is the deterministic rate equation given in Eq. (I.2) and the second term is a noise term denoted by η_i. The noise η_i is written as the sum of the noises $\eta_{i,j}$ associated with the reaction steps j involving the chemical species $\mathrm{X_i}$

$$\eta_i(t) = \sum_{j=1}^{m}\eta_{i,j}(t) = \sum_{j=1}^{m}(\beta_{i,j}-\alpha_{i,j})\left[k_j\prod_{i'=1}^{n} c_{i'}^{\alpha_{i',j}}\right]^{1/2}\xi_j(t) \tag{I.22}$$

The variances and covariances of the noises $\langle\eta_i(t)\eta_j(t')\rangle$ are given by

$$\langle\eta_i(t)\eta_j(t')\rangle = \left[\sum_{j'=1}^{m} k_{j'}(\beta_{i,j'}-\alpha_{i,j'})(\beta_{j,j'}-\alpha_{j,j'})\prod_{i'=1}^{n} c_{i'}^{\alpha_{i',j'}}\right]\delta(t-t') \tag{I.23}$$

I have used the Langevin approach in the study of the stochastic elimination of fast variables [29] presented in Sec. II.

I.2.2 Master equation

a) Reactive-only system

Although a Langevin approach is a good start, it requires some assumptions on the size of the system and the nature of the fluctuations. The master equation offers a better description of a system at a mesoscopic scale [1, 14, 47]. We consider that the system has a given probability $P(\{\Phi\}, t)$ to be in a given state

$$\{\Phi\} = \{N_1, N_2, ..., N_n\} \tag{I.24}$$

at time t. The system state is described by the discrete numbers N_i of molecules of each chemical species X_i. During a finite time interval $[t, t+\tau]$, the probability of finding the system in a given state $\{\Phi\}$ evolves according to all possible reactions. The reactions are assumed to be Markov processes. Consequently, the probability $P(\{\Phi\}, t+\tau)$ for the system to be in state $\{\Phi\}$ at time $t+\tau$ only depends on system state at time t and the transition rates or propensities between all states at time t and the state $\{\Phi\}$ at time $t+\tau$

$$\begin{aligned} P(\{\Phi\}, t+\tau) =& P(\{\Phi\}, t) \times \text{Probability to remain in the state } \{\Phi\} \\ &+ \sum_{\{\Phi'\}} [P(\{\Phi'\}, t) \times \text{Probability to jump from state } \{\Phi'\} \text{ to state } \{\Phi\}] \end{aligned} \tag{I.25}$$

The probability of leaving a given state is the sum of the probabilities to go from that state to any other one. The probability to remain in a given state is simply (1− Probability of leaving that state). If we note $T(\{\Phi\} \to \{\Phi'\})$ the transition rate from state $\{\Phi\}$ to state $\{\Phi'\}$, Eq. (I.25) can be written as

$$P(\{\Phi\}, t+\tau) - P(\{\Phi\}, t) = \sum_{\{\Phi'\}} [P(\{\Phi'\}, t) \times T(\{\Phi'\} \to \{\Phi\}) - P(\{\Phi\}, t) \times T(\{\Phi\} \to \{\Phi'\})] \tag{I.26}$$

Intuitively, the probability of leaving the current state $\{\Phi\}$ is the probability that one reaction occurs in the time interval $[t, t+\tau]$, as in Eq. (I.14). Therefore, we use the same assumption as in Eq. (I.15) but with discrete numbers of molecules

$$\sum_{\{\Phi'\}} T(\{\Phi\} \to \{\Phi'\}) = \sum_{j=1}^{m} p_j \tau = \sum_{j=1}^{m} k_j \prod_{i'=1}^{n} A_{\alpha_{i',j}}^{N_{i'}} \tau \tag{I.27}$$

where we made explicit the number of possible pairs of molecules

$$A_{\alpha_{i',j}}^{N_{i'}} = \frac{N_{i'}!}{(N_{i'} - \alpha_{i',j})!} \tag{I.28}$$

Finally, assuming that the time τ is sufficiently small to be considered as an infinitesimal time interval $\mathrm{d}t$ and using Eqs. (I.26) and (I.27), we write the *master equation* for a homogeneous reactive system

$$\partial_t P(\{\Phi\},t) = \sum_{j=1}^{m} k_j \left[\prod_{i'=1}^{n} A_{\alpha_{i',j}}^{N_{i'}-(\alpha_{i',j}-\beta_{i',j})} P(\{\Phi'_j\},t) - \prod_{i'=1}^{n} A_{\alpha_{i',j}}^{N_{i'}} P(\{\Phi\},t) \right] \tag{I.29}$$

where the state $\{\Phi'_j\}$ is the state that evolves into the state $\{\Phi\}$ after one elementary reaction j.

b) With diffusion

In order to take diffusion into account in a master equation, we introduce at least one space dimension and the transition rates describing the diffusive processes. For any reaction-diffusion system, the master equation can be divided into two terms

$$\partial_t P(\{\Phi\},t) = \partial_t P(\{\Phi\},t)|_{\text{reaction}} + \partial_t P(\{\Phi\},t)|_{\text{diffusion}} \tag{I.30}$$

where the first term accounts for the reactive processes described in Eq. (I.29) and the second term accounts for the diffusive processes. For the sake of simplicity, we assume that there are N molecules of only one chemical species X. The system is a one-dimensional array of length L, divided into ℓ boxes of length $\Delta x = \dfrac{L}{\ell}$

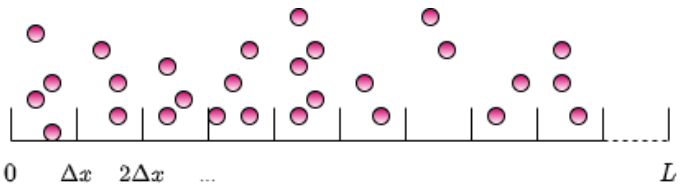

where each box is considered homogeneous. We use periodic boundary conditions. The number of molecules in each box i is denoted by $N(i,t)$. The state of the system is given by

$$\{\Phi\} = \{N(1,t), N(2,t), ..., N(i,t), ..., N(\ell,t)\} \tag{I.31}$$

Similarly to Eq. (I.26), the probability to leave the state $\{\Phi\}$ during a time interval $[t, t+\tau]$ is equal to the probability that a single molecule of the system jumps from its current box to a neighboring one [1, 14]. Assuming that boxes are independent, the probability to leave the state $\{\Phi\}$ can be written as the sum of all probabilities in each box for one

molecule to jump

$$\text{Prob. to leave state } \{\Phi\} = \sum_{\{\Phi'\}} T(\{\Phi\} \to \{\Phi'\}) \tag{I.32}$$

$$= \sum_{i=1}^{\ell} \text{Prob. that one molecule leaves box } i \tag{I.33}$$

The probability to remain in the state $\{\Phi\}$ is then simply (1-Probability to leave state $\{\Phi\}$). Hence, we only need to determine the probability that a molecule leaves a box i. This probability is given by the propensity d_i that one molecule leaves the box i

$$d_i dt = (\text{Probability that the molecule jumps to the left} \tag{I.34}$$

$$+\text{Probability that the molecule jumps to the right}) \tag{I.35}$$

$$\times \text{Number of molecules in the box } i \tag{I.36}$$

According to kinetic theory, the probability for a molecule to go left or right is proportional to the square root of temperature [14]. The Einstein relation gives the relation between the macroscopic diffusion coefficient of Eq. (I.3) and temperature. Typically, in large systems, the diffusive flux between two cells is related to the propensity d_i. We have

$$d_i \simeq \frac{2D}{\Delta x^2} N(i,t) \tag{I.37}$$

where D is the diffusion coefficient of the chemical species X. Using this approximation, we write the diffusion term of Eq. (I.30) for a single species in the form

$$\partial_t P(\{\Phi\},t)|_{\text{diffusion}} = \frac{D}{\Delta x^2} \sum_{i=1}^{\ell} (N_i + 1) \left[P(\{N(i-1,t)-1, N(i,t)+1\} + P(\{N(i,t)+1, N(i+1,t)-1\}\right.$$

$$- 2N_i P(\{\Phi\},t) \tag{I.38}$$

where only the number of molecules differing from $N(i,t)$ in cell i are made explicit.

I have used a master equation approach in the study of the stochastic elimination of a fast variable [29] presented in Sec. II and in the analysis of fluctuation effects of an FKPP wave front [44] presented in Sec. IV.2.2.

I.3 Concentrated solution

Usually, in solutions, solvent particles are nonreactive and in large excess compared to reactants. Hereafter, a solution is said highly diluted when the local solvent concentration is arguably constant. Considering the high-dilution limit ensures that the diffusion

coefficient of all reactants and the concentration of the solvent are constant. Hence, in the case of a reactive solvent, its concentration can be included into the rate constants of the corresponding reactions. However, small systems may be crowded, which invalidates the approximation of a large amount of solvent. The study of the effects of a deviation from the high-dilution limit in small systems is therefore necessary.

I.3.1 High-dilution limit

We present the effect of the deviation from the high-dilution limit on the reaction-diffusion dynamics using a simple example. We consider the Verhulst model [48]

$$\mathrm{A} + \mathrm{S} \xrightarrow{k} 2\,\mathrm{S} \tag{I.39}$$

where A is a reactive species and S a reactive solvent. In the absence of hypothesis on the relative orders of magnitude of the concentrations c_A and c_S of species A and S, the rate equation for A is

$$\mathrm{d}_t c_A = -k c_A c_S \tag{I.40}$$

The total concentration c^{tot} of chemical species

$$c^{\mathrm{tot}} = c_A + c_S \tag{I.41}$$

is constant according to Eq. (I.39). Therefore, we can eliminate Eq. (I.40)'s dependency on c_S

$$\mathrm{d}_t c_A = -k c^{\mathrm{tot}} c_A \left(1 - \frac{c_A}{c^{\mathrm{tot}}}\right) \tag{I.42}$$

and recognize the logistic function. The solution of Eq. (I.42) is

$$c_A(t) = \frac{c^{\mathrm{tot}} c_A^{\mathrm{ini}} e^{-k c^{\mathrm{tot}} t}}{c^{\mathrm{tot}} + c_A^{\mathrm{ini}} (e^{-k c^{\mathrm{tot}} t} - 1)} \tag{I.43}$$

where c_A^{ini} is the initial value of c_A.
However, if the reaction scheme involves more steps and is more complex, the associated rate equations may not be solvable. In this case, it is possible to assume that the concentration of solvent c_S is much larger than the concentration of reactants. Consequently, c_S is considered constant and the reaction step becomes a lower-order reaction

$$\mathrm{A} \xrightarrow{k_S} 2\,\mathrm{S} \tag{I.44}$$

where the modified rate constant k_S is given by

$$k_S = kc_S \tag{I.45}$$

This approximation is what we call the *high-dilution limit*. Our aim is to characterize the deviation from the high-dilution limit. Thus, we define the parameter

$$\delta = \frac{\sum\limits_{i \neq S} c_i^0}{c^{\text{tot}}} = 1 - \frac{c_S^0}{c^{\text{tot}}} \tag{I.46}$$

that represents the ratio of the sum of the concentrations c_i^0 of all non-solvent reactants evaluated at a steady state and the total concentration. When δ tends to 0, the solvent is in large excess with respect to the other species and the high-dilution approximation is valid. On the contrary, when δ increases, the deviation from the high-dilution limit increases, and the previous assumption fails. This parameter is defined at a homogeneous stationary state such that it remains constant even if the system exhibits spatial structures such as Turing patterns. If the system exhibits multiple stationary states, the parameter is defined according to the stable homogeneous stationary state of interest.

I.3.2 Modified Fick's law in a concentrated solution

According to Fick's law applied to a dilute system, the diffusive flux of one species is proportional to the gradient of its concentration. The associated diffusion coefficient is derived from kinetic theory according to the characteristics of the species. In a concentrated solution, the concentration of one species has an impact on the diffusion of another species and cross-diffusion terms must be considered. We consider a concentrated solution of species A and B. The solvent S is still considered in excess but not in great excess, so that we are confronted with a ternary mixture of A, B, and S particles [36].

In a highly diluted solution, the center of mass of the solvent and the center of mass of the system are typically the same. However, we expect that, in a concentrated system, the two centers of mass are different. The idea is to exploit the frame of the solvent in which Fick's law takes a simpler form [26, 36]. The flux of species X=A,B in the frame of the solvent is

$$\mathbf{j}_X^S = c_X(\mathbf{u}_X - \mathbf{u}_S) \tag{I.47}$$

where $\mathbf{u}_X$ is the velocity of the center of mass of species X in the frame of the system.

By definition, the flux of the solvent vanishes in the frame of the solvent

$$\mathbf{j}_S^S = 0 \tag{I.48}$$

The fluxes in the frame of the solvent can be expressed in terms of the fluxes in the frame of the system using Eq. (I.47)

$$\mathbf{j}_X^S = c_X(\mathbf{u}_X - \mathbf{u} + \mathbf{u} - \mathbf{u}_S) \tag{I.49}$$

$$= \mathbf{j}_X - \frac{c_X}{c_S}\mathbf{j}_S \tag{I.50}$$

which gives, using the law of conservation $c^{\text{tot}} = c_A + c_B + c_S$ and Eq. (I.48)

$$\mathbf{j}_A = \left(1 - \frac{c_A}{c^{\text{tot}}}\right)\mathbf{j}_A^S - \frac{c_A}{c^{\text{tot}}}\mathbf{j}_B^S \tag{I.51}$$

$$\mathbf{j}_B = -\frac{c_B}{c^{\text{tot}}}\mathbf{j}_A^S + \left(1 - \frac{c_B}{c^{\text{tot}}}\right)\mathbf{j}_B^S \tag{I.52}$$

Next step consists in using Fick's law relating the fluxes in the frame of the solvent and the concentration gradients. Within the framework of linear irreversible thermodynamics, the entropy production per unit mass due to isothermal diffusion is given by

$$\sigma = \frac{1}{T}\sum_{X=A,B,S} \mathbf{j}_X \cdot (-\nabla_T \mu_X) \tag{I.53}$$

where T is the temperature, ∇_T the spatial gradient at constant temperature, and μ_X the chemical potential of species X. Assuming that the deviation from the high-dilution limit remains sufficiently small, the chemical potential for a given species is the same as in an ideal solution

$$\mu_X = \mu_X^0 + k_B T \log \frac{c_X}{c^{\text{tot}}} \tag{I.54}$$

where μ_i^0 is the standard chemical potential of species X and k_B is the Boltzmann constant. At constant pressure and temperature, the Gibbs-Duhem equation states that

$$\sum_{X=A,B,S} c_X \cdot (-\nabla_T \mu_X) = 0 \tag{I.55}$$

Using Eqs. (I.48) and (I.55), we write Eq. (I.53) in the form

$$\sigma = \frac{1}{T} \sum_{X=A,B,S} c_X(\mathbf{u}_X - \mathbf{u}_S + \mathbf{u}_S - \mathbf{u}) \cdot (-\nabla_T \mu_X) \tag{I.56}$$

$$= \frac{1}{T} \sum_{X=A,B} \mathbf{j}_X^S \cdot (-\nabla_T \mu_X) \tag{I.57}$$

By introducing phenomenological coefficients Ω_{XY} to write linear relationships between fluxes and forces

$$\mathbf{j}_X^S = \sum_{Y=A,B} \Omega_{XY}(-\nabla_T \mu_Y) \tag{I.58}$$

and using Eq. (I.54), we obtain the Fick's law in the frame of the solvent

$$\mathbf{j}_X^S = \sum_{Y=A,B} D_{XY}^S(-\nabla c_Y) \tag{I.59}$$

where D_{XY}^S are diffusion coefficients. However, even in a concentrated solution the notion of solvent keeps some relevance. Although the variation of the concentration of the solvent cannot be ignored, the concentrations of A and B are significantly smaller than the concentration of the solvent S. In these conditions, the vast majority of the binary collisions involve at least one S solvent particle. Hence, diffusion of species X=A,B is mainly imposed by the collisions between X and the solvent S while the impact of the collisions between A and B is negligible. We therefore admit that D_{XY}^S is negligible for X≠Y and we denote D_{XX}^S by D_X^S, for X=A,B. Consequently, Eq. (I.59) becomes

$$\mathbf{j}_X^S = D_X^S(-\nabla c_X) \text{ with X=A,B} \tag{I.60}$$

so that the flux of X in the frame of the solvent only depends on the concentration of X. Finally, the modified Fick's law in the frame of the system that accounts for the deviation from the high-dilution limit in a ternary mixture is given by

$$\mathbf{j}_A = -\left(1 - \frac{c_A}{c^{\text{tot}}}\right) D_A^S \nabla c_A + \frac{c_A}{c^{\text{tot}}} D_B^S \nabla c_B \tag{I.61}$$

$$\mathbf{j}_B = \frac{c_B}{c^{\text{tot}}} D_A^S \nabla c_A - \left(1 - \frac{c_B}{c^{\text{tot}}}\right) D_B^S \nabla c_B \tag{I.62}$$

$$\tag{I.63}$$

which can also be written under the matrix form

$$\begin{pmatrix} \mathbf{j}_A \\ \mathbf{j}_B \end{pmatrix} = \begin{pmatrix} \left(1 - \dfrac{c_A}{c^{\text{tot}}}\right) & -\dfrac{c_A}{c^{\text{tot}}} \\ -\dfrac{c_B}{c^{\text{tot}}} & \left(1 - \dfrac{c_B}{c^{\text{tot}}}\right) \end{pmatrix} \begin{pmatrix} -D_A^S \nabla c_A \\ -D_B^S \nabla c_B \end{pmatrix} \tag{I.64}$$

I have used the modified Fick's law to study the effect of the deviation from the high-dilution limit in Sec. IV.2.

I.4 Numerical methods

I.4.1 Gillespie algorithm

In the general case, the master equation presented in Eq. (I.29) is not solvable. Nevertheless, it is possible to generate a stochastic trajectory using the Gillespie algorithm [49]. Gillespie uses a kinetic Monte Carlo procedure to directly simulate the reaction and diffusion processes and solve the master equation. The general formulation of the algorithm contains several steps, which are presented hereafter.

a) Reactive-only system

We consider the reaction scheme presented in Eq. (I.1) and the associated master equation given in Eq. (I.29). Each reaction step j has a certain probability to occur within a random time interval $[t, t+\tau]$. During this time interval, the propensity p_j that the next elementary reaction is a reaction j is given by Eq. (I.14), with the same assumptions as for Eq. (I.27)

$$p_j = k_j \prod_{i'=1}^{n} A_{\alpha_{i',j}}^{N_{i'}} \tag{I.65}$$

Thus, the propensity p_0 that any reaction occurs is the sum of all propensities p_j of the m steps

$$p_0 = \sum_{j=1}^{m} p_j \tag{I.66}$$

If the time interval $[t, t+\tau]$ is split into infinitesimal intervals dt

then the probability $P_{\oslash}(\tau)$ that no reaction occurs in the time interval $[t, t+\tau]$ is equal

to

$$P_{\oslash}(\tau) = \lim_{dt\to 0}(1 - p_0 dt)^{\frac{\tau}{dt}} = e^{-p_0\tau} \tag{I.67}$$

Therefore, the probability P_0 that *at least* one reaction occurs is

$$P_0 = 1 - e^{-p_0\tau} \tag{I.68}$$

implying that the probability distribution of random reaction time τ is

$$p(\tau) = \partial_\tau P_0 = p_0 e^{-p_0\tau} \tag{I.69}$$

The random reaction time τ is exponentially distributed with mean

$$\langle\tau\rangle = \frac{1}{p_0} \tag{I.70}$$

The first step of the simulation is the initialization of all numbers of molecules, rate constants of the reaction, and the random number generators. Then, in the second step, we generate a random time interval according to Eq. (I.69) and select a random elementary reaction proportionally to its propensity using Eq. (I.66). In the third step, we update the number of molecules according to the reaction that occurred and increase the time step by the randomly generated reaction time. Finally, we go back to the second step where we generate a new random reaction time and a new elementary reaction. Eventually, the simulation stops when the number of reactants has reached zero or the simulation time has run out.

b) With diffusion

When diffusion processes are involved, the Gillespie algorithm can be easily adapted. We now consider the system described by Eq. (I.30). During a random time interval $[t, t+\tau]$, the propensity d_i^{X} that a molecule X leaves the box i is given by Eq. (I.37)

$$d_i^{\mathrm{X}} = d_i^{\mathrm{X}}|_{\mathrm{left}} + d_i^{\mathrm{X}}|_{\mathrm{right}} \simeq \frac{2D_X}{\Delta x^2} N_X(i,t) \tag{I.71}$$

where $d_i^{\mathrm{X}}|_{\mathrm{left}}$ and $d_i^{\mathrm{X}}|_{\mathrm{right}}$ denote the propensity that a molecule X in the box i jumps to the left or to the right, respectively. *A priori*, these two propensities are equal. The propensity d_0 that any molecule leaves its box is

$$d_0 = \sum_X \sum_{i=1}^{\ell} d_i^{\mathrm{X}} \tag{I.72}$$

which can be added to the propensity given by Eq. (I.66). Then, we adapt the second step of the algorithm such that a random elementary process (reaction or diffusion) is selected proportionaly to its propensity.

I have used Gillespie algorithm in the study of the elimination of a fast variable [29] presented in Sec. II and the study of an FKPP wave front in a concentrated system [44] presented in Sec. IV.2.2.

I.4.2 Direct Simulation Monte Carlo method

a) Concept

The Direct Simulation Monte Carlo method (DSMC), developed by Graeme Bird in the 60's, is a numerical method used to compute molecular gas flows in aerodynamics [17, 18, 50]. It has been successfully extended to include reactive mechanisms and can be used to simulate highly diluted solutions. The method relies on a kinetic Monte Carlo algorithm which generates stochastic trajectories of particles and amounts to a direct simulation of the Boltzmann equations including fluctuations. Particles are hard spheres of mass m and radius r with continuous positions and velocities. Initial positions of the particles, compatible with the macroscopic initial conditions for the concentrations, are randomly chosen. The initial velocities are sampled according to a Maxwellian distribution with $k_BT = 1$. During a time step, positions are updated according to the velocities. The main feature of DSMC is to treat collisions statistically. The space is discretized into cells of length Δx, where particles are susceptible to collide only with particles inside the same cell. According to the collision integral of the Boltzmann equation, the probability of collision of two particles is proportional to their relative velocity [24]. The "No Time Counter" (NTC) algorithm [17, 18] derives an integer upper bound to the maximum number of collisions to be performed during the time step. An acceptance-rejection method is then used to test whether a collision between two randomly chosen particles in a box is accepted or not. The collisions are considered elastic from the mechanical point of view and the final relative velocity of the colliding pair is determined according to isotropic scattering.
During a collision, a chemical reaction may happen. The reaction occurs with a probability proportional to the corresponding rate constant determined by a steric factor ρ_{AB} and an activation energy E_A. According to kinetic theory, in a binary mixture of A and B species, the collision frequency is given by

$$Z_{\mathrm{AB}} = c_{\mathrm{A}} c_{\mathrm{B}} \sigma_{\mathrm{AB}} \sqrt{\frac{8 k_B T}{\pi \mu_{\mathrm{AB}}}} \tag{I.73}$$

where σ_{AB} is the cross-section of the collision and $\mu_{\mathrm{AB}} = \dfrac{m_A m_B}{m_A + m_B}$ is the reduced mass of the reactants. Only the fraction of encounters that has a relative kinetic energy greater than the activation energy E_A of the reaction reacts. Therefore, the rate of the reaction is

$$v_{\mathrm{AB}} = Z_{\mathrm{AB}} \rho_{\mathrm{AB}} \exp\left(-\frac{E_A}{RT}\right) \tag{I.74}$$

If we compare this result to Eq. (I.2), where the rate of a binary reaction is $v_{\mathrm{AB}} = k_j c_A c_B$, the expression of the rate constant as a result of kinetic theory is

$$k_{\mathrm{AB}} = \rho_{\mathrm{AB}} \sigma_{\mathrm{AB}} \sqrt{\frac{8 k_B T}{\pi \mu_{\mathrm{AB}}}} \exp\left(-\frac{E_A}{RT}\right) \tag{I.75}$$

In the simulations that we performed, it is assumed that the activation energy of all reactions is equal to 0 and that no reaction is endothermic or exothermic. Therefore, the temperature is constant and homogeneous in all simulations. The cross-section of the collisions between two molecules A and B is given by

$$\sigma_{\mathrm{AB}} = \pi (r_{\mathrm{A}} + r_{\mathrm{B}})^2 \tag{I.76}$$

for all collisions considered. The procedure used to obtain desired diffusion coefficients is also derived from kinetic theory. In a binary mixture, the diffusion coefficients of both A and B particles are equal and given by

$$D_{\mathrm{A}} = D_{\mathrm{B}} = D_{\mathrm{AB}} \simeq \frac{3}{8(c_{\mathrm{A}} + c_{\mathrm{B}})(r_{\mathrm{A}} + r_{\mathrm{B}})^2} \sqrt{\frac{k_B T}{\pi \mu_{\mathrm{AB}}}} \tag{I.77}$$

In this expression, the diffusion coefficient depends on the local concentration $c_{\mathrm{A}} + c_{\mathrm{B}}$. However, diffusion coefficients are assumed to be constant in space and time in Eq. (I.4). This hypothesis requires that no particle is created *ex nihilo* or destroyed, and that exchanges with the exterior (such as *reservoirs*) do not radically change the local concentration. Therefore, we make sure that the concentration $c_{\mathrm{A}} + c_{\mathrm{B}}$ is arguably constant in the simulation. Another condition for collisions to be correctly simulated is that the cell length Δx is smaller than the mean free path of colliding particles

$$\ell = \frac{1}{\sqrt{2} c^{\mathrm{tot}} \pi (r_A + r_B)^2} \tag{I.78}$$

In highly diluted solutions, the excess of solvent makes this condition hard to fulfill while keeping reasonable computation times. The condition can be relaxed if the mean gradients of concentration between two neighboring cells are typically smaller that the amplitude

of the concentration fluctuations.
I have used the DSMC method to simulate species with different diffusion coefficients and Turing structures in a concentrated system [37]. The results are presented in Sec. III.3.

b) Third-order reaction

In the article [37] presented in Chapter III, we consider a ternary mixture of A, B, and S species where one step of the reactive mechanism is a third-order reaction. The difficulty was to adapt the DSMC algorithm to correctly simulate a third-order reaction. The issue has been solved as follows by M. Mareschal *et al.* [51] and already used by the group [52]. The reaction

$$2\,\mathrm{A} + \mathrm{B} \xrightarrow{k} 3\,\mathrm{A} \tag{I.79}$$

is split into two second-order reactions

$$\mathrm{A} + \mathrm{B} \xrightarrow{k_1=k} \mathrm{AB} \tag{I.80}$$

$$\mathrm{AB} + \mathrm{A} \xrightarrow{k_2\to\infty} 3\,\mathrm{A} \tag{I.81}$$

where the first reaction occurs with the same rate constant k as the third-order reaction and the second reaction is supposed instantaneous. The simulations reproduce the third-order reaction given in Eq. (I.79) as follows. When a binary collision between a particle A and a particle B is accepted in a given spatial box, a complex AB is supposed to be formed. A third particle is randomly chosen in the same spatial box. If it is an A particle, the AB complex is immediately transformed into two A particles. Hence, according to Eq. (I.75) and the probability $\frac{c_A}{c^{tot}}$ of picking a particle A, the rate constant k obeys

$$k = \frac{4(r_\mathrm{A} + r_\mathrm{B})^2}{c^\mathrm{tot}}\sqrt{\pi k_B T} \propto \frac{1}{c^\mathrm{tot}} \tag{I.82}$$

with $\mu_{AB} = E_A = \rho_{AB} = 1$. Due to the proportionality to $1/c^\mathrm{tot}$, the rate constant k depends on the deviation δ from the high-dilution limit from Eq. (I.46).

c) Diffusion in a ternary mixture

Observing a Turing structure requires the simulation of sufficiently different diffusion coefficients for the activator and the inhibitor. As already mentioned, the diffusion coefficients of the two components are identical in a binary mixture. The solvent, introduced to study concentrated solutions, advantageously plays the role of the third kind of particles with respect to diffusion. The problem of tuning the diffusion coefficients in the simulation of a ternary mixture has already been addressed by the group [53] and I recall the main lines

of the method. Qualitatively, faster diffusion of the inhibitor is obtained by considering particles of the same mass but different diameters. In a ternary mixture of A, B, and S [54], the fluxes of matter $\mathbf{j}_A$, $\mathbf{j}_B$, and $\mathbf{j}_S$ are expressed as

$$\mathbf{j}_X = D'_{XY}\partial_x c_Y + D'_{XZ}\partial_x c_Z \tag{I.83}$$

for $X, Y, Z = A, B, R$, where the three-component diffusion coefficients D'_{AB}, D'_{AS}, and D'_{BS} are derived from the two-component diffusion coefficients D_{AB}, D_{AS}, and D_{BS} from Eq. (I.77)

$$D'_{XY} = D_{XY}\left[1 + \frac{c_Z(D_{XZ} - D_{XY})}{c_X D_{YZ} + c_Y D_{XZ} + c_Z D_{XY}}\right] \tag{I.84}$$

The presence of the concentrations in the expression of the diffusion coefficients may imply non desired space-dependent diffusivities. However, considering

$$c_S D'_{AB} \gg c_A D'_{BS} + c_B D'_{AS} \tag{I.85}$$

$$c_S \gg c_A \tag{I.86}$$

$$c_S \gg c_B \tag{I.87}$$

and using Eq. (I.84) leads to

$$D'_{AB} \simeq D'_{AS} \simeq D_{AS} \tag{I.88}$$

$$D'_{BA} \simeq D'_{BS} \simeq D_{BS} \tag{I.89}$$

which, combined with Eq. (I.83) for $c^{\text{tot}} = c_A + c_B + c_S$ constant, gives

$$\mathbf{j}_A = -D_{AS}\partial_x c_A \tag{I.90}$$

$$\mathbf{j}_B = -D_{BS}\partial_x c_B \tag{I.91}$$

Thus, when the solvent is sufficiently in excess, the diffusion coefficients of A and B species are the same as in a binary mixture of A and S particles and B and S particles, respectively. Intuitively, in a system with S particles in excess, the proportion of collisions involving no S particles is negligible. Hence, we assume that the diffusive mechanism of A and B particles is dominated by their interaction with the S particles. For the sake of simplicity, we write

$$D_A \simeq D_{AS} \tag{I.92}$$

$$D_B \simeq D_{BS} \tag{I.93}$$

In Eq. (I.77), the diffusion coefficient depends on the local concentration of the two species involved in the diffusive process. In Chapter. III, we study Turing structures with spatial oscillations of the concentrations, which undermines the hypothesis of constant diffusion coefficients. In order to derive appropriate diameters for the different types of particles [53], we consider spatial averages of the concentrations. Then, writing $d = \frac{D_B}{D_A}$ and $m_A = m_B$, and using Eq. (I.77), we get

$$r_B = \frac{r_A + (1 - \sqrt{d'})r_S}{\sqrt{d'}} \tag{I.94}$$

where $d' = \frac{d(c_S + c_A)}{c_R + c_B} \simeq d$. As r_B must be positive, we obtain the condition

$$r_A > (\sqrt{d'} - 1)r_S \tag{I.95}$$

If this last condition is satisfied with a small margin, then

$$r_B \ll r_A \tag{I.96}$$

and $D_B \gg D_A$ as desired.
Finally, introducing Eq. (I.95) into Eq. (I.85), we obtain the condition on the concentration of solvent S for the proper simulation of the diffusion coefficients

$$c_S \gg \sqrt{(dc_A + c_B)(c_A + c_B)} \left(1 - \frac{1}{\sqrt{d'}}\right) \tag{I.97}$$

Chapter II

Stochastic approach to the steady-state approximation

The usual adiabatic elimination often encountered in chemistry is the steady-state approximation, consisting in eliminating a fast concentration. In a complex mechanism, identifying a fast concentration is not straightforward [55, 56, 57, 58, 59, 60]. A linear analysis may be locally performed and requires linearizing the rate equations, computing the eigenvalues, and using the change-of-basis matrix to relate the concentrations and the eigenmodes. The relationships between the eigenvalues and the rate constants may not be trivial and the knowledge of the rate constants is not always sufficient to identify a fast variable at first glance.

II.1 Context

We give an example of steady-state approximation in a simple case involving two elementary steps with rate constants of different orders of magnitude, sufficient to generate a fast concentration. The example also illustrates how third-order steps may be obtained by reduction of a mechanism containing second-order steps.

We consider a reaction scheme involving two elementary steps and four species A, B, C, and D

$$\begin{aligned} \mathrm{A} + \mathrm{B} &\xrightarrow{\varepsilon k} \mathrm{C} \\ \mathrm{A} + \mathrm{C} &\xrightarrow{k} 2\,\mathrm{D} \end{aligned} \tag{II.1}$$

The first step is supposed to be much slower than the second one, i.e. the parameter ε obeys $\varepsilon \ll 1$. The quantities $c_A + c_C + c_D$ and $c_A - 2c_B - c_C$ are conserved and dynamics involves two independent variables. It is however simpler to keep the three variables c_A,

c_B, and c_C. The rate equations are given by

$$\mathrm{d}_t c_A = -\varepsilon k c_A c_B - k c_A c_C \tag{II.2}$$

$$\mathrm{d}_t c_B = \varepsilon k c_A c_B \tag{II.3}$$

$$\mathrm{d}_t c_C = \varepsilon k c_A c_B - k c_A c_C \tag{II.4}$$

Introducing a new time scale $\tau = \varepsilon t$, expanding the concentrations into power series of ε, and using Eq. (II.4) at zeroth order, we deduce that $c_C^{(0)} = 0$. Consequently, we have

$$\mathrm{d}_\tau c_C^{(0)} = k c_A^{(0)} (c_B^{(0)} - c_C^{(1)}) = 0 \tag{II.5}$$

which implies $c_C^{(1)} = c_B^{(0)}$. Finally, Eqs. (II.2) and (II.3) lead to

$$\mathrm{d}_\tau c_A^{(0)} = -2 k c_A(0) c_B(0) \tag{II.6}$$

$$\mathrm{d}_\tau c_B^{(0)} = -k c_A(0) c_B(0) \tag{II.7}$$

which corresponds to the rate equations associated with a third-order reaction

$$2\,\mathrm{A} + \mathrm{B} \xrightarrow{\varepsilon k} 2\,\mathrm{D} \tag{II.8}$$

The reaction between nitrogen monoxide and chlorine

$$2\,\mathrm{NO} + \mathrm{Cl_2} \longrightarrow 2\,\mathrm{NOCl} \tag{II.9}$$

illustrates the reduced mechanism given in Eq. (II.8). The mechanism proposed in Eq. (II.1) does not rely on any chemical considerations and is only one possible two-step mechanism compatible with the reaction between nitrogen monoxide and chlorine.

II.2 Summary of the results

In the previous example, the dynamics of the system is described at a macroscopic scale. The nonlinearities of the deterministic dynamics and the large fluctuations reached in small systems are known to interact [61, 62, 63] and make the elimination of fast concentrations a nontrivial problem in stochastic systems [58, 64, 65]. In biological experiments, Fluorescence Correlation Spectroscopy (FCS) [66] is widely used to study the dynamics of labeled species, for example, to evaluate rate constants when the reaction scheme is supposed to be known. The interpretation of the results requires the comparison of the experimental data with analytical expressions of the correlations of concentration fluctuations for the reaction scheme of interest. However, reaction schemes in biology often

involve hundreds of steps and the computation of the correlations is not tractable before a reduction of the mechanism. Defining the scope of fast concentration elimination in stochastic nonlinear dynamics is therefore essential to interpret FCS results. Similarly, the reduction of a mechanism may lead to nonpolynomial nonlinearities, as exemplified by the reduced Michaelis–Menten scheme. The conclusions that could be derived from the stochastic analysis of the reduced Michaelis–Menten model may differ from the direct analysis of the complete scheme [67]. In order to analyze the consequences of mechanism reduction, I consider a minimal chemical model involving two species of variable concentrations capable of evolving into a Turing pattern. Then, the two-variable model is assumed to be the reduction of two different three-variable models. The problem is to determine if the correlations of fluctuations in the three-variable models are correctly predicted by the two-variable model, in the limit where the reduction of deterministic dynamics is valid. I developed an analytical approach based on chemical Langevin equations linearized around the steady state of interest as presented in Sec. I.2.1. Following the method applied in references [61, 62, 63] to characterize the asymmetry of time cross-correlations in far-from-equilibrium systems, I determined the expressions of the correlations of concentration fluctuations in the two- and three-variable models. In parallel, I performed simulations of the corresponding master equations (see Sec. I.2.2) using Gillespie algorithm according to the procedure given in Sec. I.4.1. The weaknesses of the Langevin approach in the description of the internal fluctuations in a nonlinear chemical system have been highlighted [68]. The master equation approach has proven that the two-variable model does not correctly predict the fluctuations in the three-variable systems. We concluded that the coupling between the fluctuations and the nonlinearities of deterministic dynamics makes the use of the steady-state approximation delicate when the studied system requires a good control of the fluctuations. The predictions of the correlations based on a reduced mechanism must be considered with special care when preventing hazards in explosive phenomena, modeling pattern formation in biology, or dealing with small systems in which variances of fluctuations are detected as in fluorescence correlation spectroscopy [65, 69].

II.3 Publication

The results are published in the article “Elimination of fast variables in stochastic nonlinear kinetics”, G. Morgado, B. Nowakowski, and A. Lemarchand, *Phys. Chem. Chem. Phys.*, **22**, 20801-20814 (2020) [29].

PCCP

ROYAL SOCIETY OF CHEMISTRY

PAPER

View Article Online
View Journal

Cite this: DOI: 10.1039/d0cp02785e

Elimination of fast variables in stochastic nonlinear kinetics

Gabriel Morgado,[ab] Bogdan Nowakowski[ac] and Annie Lemarchand *[b]

A reduced chemical scheme involving a small number of variables is often sufficient to account for the deterministic evolution of the concentration of the main species contributing to a reaction. However, its predictions are questionable in small systems used, for example in fluorescence correlation spectroscopy (FCS) or in explosive systems involving strong nonlinearities such as autocatalytic steps. We make precise dynamical criteria defining the validity domain of the quasi-steady-state approximation and the elimination of a fast concentration in deterministic dynamics. Designing two different three-variable models converging toward the same two-variable model, we show that the variances and covariance of the fluctuations of the slow variables are not correctly predicted using the two-variable model, even in the limit of a large system size. The more striking weaknesses of the reduced scheme are figured out in mesoscaled systems containing a small number of molecules. The results of two stochastic approaches are compared and the shortcomings of the Langevin equations with respect to the master equation are pointed out. We conclude that the description of the fluctuations and their coupling with nonlinearities of deterministic dynamics escape reduced chemical schemes.

Received 22nd May 2020,
Accepted 31st July 2020

DOI: 10.1039/d0cp02785e

rsc.li/pccp

1 Introduction

The quasi-steady-state approximation is currently used in chemistry to eliminate a fast variable and build tractable reaction mechanisms involving a few species while satisfactorily accounting for the dynamical behavior of the system.[1–4] However, in a small system containing a small number of particles, fluctuations reach large amplitudes.[5] Our goal is to make precise how eliminating a fast variable in a model of growing Turing patterns[6] may affect the prediction on the amplitude of concentration fluctuations. The interplay between nonlinearities of deterministic dynamics and fluctuations makes the elimination of fast variables in stochastic dynamics non trivial.[7–12] The issue is essential to estimate the ability of a reduced chemical scheme to report on experiments in small samples such as fluorescence correlation spectroscopy (FCS) experiments.[13,14] For this purpose we consider a minimal chemical model involving two species of variable concentrations, able to reproduce the propagation of a chemical wave front toward a stable steady state and a spatially-periodic structure of Turing type.[15–18] The minimum model is assumed to result from the reduction of three-variable models. The question is to determine if the amplitude of the fluctuations deduced from a three-variable model is correctly predicted by the two-variable model, in the limit where the reduction of deterministic dynamics is valid and for homogeneous conditions in the vicinity of a steady state.

The paper is organized as follows. In Section 2, we determine the conditions for the parameters on the deterministic dynamics of the two- and three-variable models to be as close as possible. In particular, we look for conditions ensuring that the steady states coincide in order to make the comparison between the models relevant. Section 3 is devoted to the stochastic description of the different models. Langevin equations with internal noise[19] deduced from the chemical master equation are used to derive analytical expressions of the variances and covariances of concentration fluctuations for the two-variable and three-variable models.[20–22] Choosing the nontrivial stable steady state of the two-variable and three-variable models as an initial condition, we simulate the master equation using the kinetic Monte Carlo method introduced by Gillespie[23] and determine the variances and covariance of the fluctuations of the slow variables. The accuracy of the Langevin approach is checked by comparing the results given by the two stochastic approaches. Section 4 is devoted to discussion and conclusion.

2 Deterministic dynamics

2.1 Two-variable model

The following chemical mechanism, inspired by the Schnakenberg model[24] and the Gray–Scott model,[25] has been designed to

[a] Institute of Physical Chemistry, Polish Academy of Sciences, Kasprzaka 44/52, 01-224 Warsaw, Poland
[b] Laboratoire de Physique Théorique de la Matière Condensée, Sorbonne Université, CNRS, 4 Place Jussieu, Case Courrier 121, 75252 Paris CEDEX 05, France. E-mail: annie.lemarchand@sorbonne-universite.fr
[c] SGGW, Warsaw University of Life Sciences, Nowoursynowska 159, 02-776 Warsaw, Poland

account for different self-organization phenomena in open systems[26]

$$X \xrightarrow{k_1} R_1 \tag{1}$$

$$2X + Y \xrightarrow{k_2} 3X \tag{2}$$

$$Y \underset{k_{-3}'}{\overset{k_3}{\rightleftharpoons}} R_2 \tag{3}$$

In particular, we used it to study the impact of fluctuations[15] on growing Turing structures with possible application towards the development of periodic patterns in embryos.[16–18] The concentrations of the species R_1 and R_2 are assumed to be constant through appropriate matter exchanges with reservoirs, also called chemostats by analogy with thermostats capable of fixing temperature through heat exchanges. The model involves two species X and Y of variable concentrations X and Y governed by the following differential equations

$$\frac{\mathrm{d}X}{\mathrm{d}t} = -k_1 X + k_2 X^2 Y \tag{4}$$

$$\frac{\mathrm{d}Y}{\mathrm{d}t} = k_{-3} - k_3 Y - k_2 X^2 Y \tag{5}$$

where the k_i's, for $i = 1, 2, 3, -3$, are rate constants. For the sake of simplicity, we set $k_{-3} = k_{-3}'R_2$.

For parameter values obeying $\Delta < 0$ with $\Delta = {k_{-3}}^2 - 4{k_1}^2 k_3/k_2$, the two-variable model admits a single steady state ($X_2^0 = 0$, $Y_2^0 = k_{-3}/k_3$). If $\Delta \geq 0$, the model has three stationary states (X_2^0,Y_2^0), (X_1^0,Y_1^0), and (X_0^0,Y_0^0) with

$$X_1^0 = \frac{k_{-3} - \sqrt{\Delta}}{2k_1} \tag{6}$$

$$Y_1^0 = \frac{k_{-3} + \sqrt{\Delta}}{2k_3} \tag{7}$$

$$X_0^0 = \frac{k_{-3} + \sqrt{\Delta}}{2k_1} \tag{8}$$

$$Y_0^0 = \frac{k_{-3} - \sqrt{\Delta}}{2k_3} \tag{9}$$

In the domain of existence of the three stationary states, (X_1^0,Y_1^0) is unstable whereas (X_0^0,Y_0^0) and (X_2^0,Y_2^0) are stable. The model has been designed to have a steady state obeying $X_2^0 = 0$, unable to create X species *ex nihilo* and consequently insensitive to internal fluctuations. Hence, in a spatially extended system, it is possible to prepare a region of space in the state (X_2^0,Y_2^0) and study how it is invaded by a propagating chemical wave front. After the passage of the wave front, the system relaxes towards the steady state (X_0^0,Y_0^0) and can be destabilized by inhomogeneous perturbations, being then replaced by a periodic spatial pattern of Turing type.[16–18]

In the following discussion, we focus on a homogeneous system and study the linear dynamics in the vicinity of the steady state (X_0^0,Y_0^0). Introducing the deviations $x = X - X_0^0$ and $y = Y - Y_0^0$ from the steady state, we locally characterize dynamics using the linearized equations

$$\frac{\mathrm{d}\zeta}{\mathrm{d}t} = \mathbf{M}\zeta \tag{10}$$

where $\zeta = \begin{pmatrix} x \\ y \end{pmatrix}$ is the vector representing the deviation from the steady state and $\mathbf{M}$ is the stability matrix, given by

$$\mathbf{M} = \begin{pmatrix} m_{11} = k_1 & m_{12} = k_2(X_0^0)^2 \\ m_{21} = -2k_1 & m_{22} = -k_3 - k_2(X_0^0)^2 \end{pmatrix} \tag{11}$$

The eigenvalues of $\mathbf{M}$ are

$$\lambda_1^0 = \frac{k_1 - k_3 - k_2(X_0^0)^2 + \sqrt{\Delta'}}{2} \tag{12}$$

$$\lambda_2^0 = \frac{k_1 - k_3 - k_2(X_0^0)^2 - \sqrt{\Delta'}}{2} \tag{13}$$

with $\Delta' = (k_2(X_0^0)^2 + k_3 - k_1)^2 - 4k_1(k_2(X_0^0)^2 - k_3)$ and X_0^0 given in eqn (8). The vector $\chi = \begin{pmatrix} x_1 \\ x_2 \end{pmatrix}$ of coordinates in the eigenbasis of $\mathbf{M}$ is related to vector ζ through $\zeta = \mathbf{P}^0\chi$ where the change of the basis matrix is

$$\mathbf{P}^0 = \begin{pmatrix} p_{11}^0 = k_2(X_0^0)^2 & p_{12}^0 = k_2(X_0^0)^2 \\ p_{21}^0 = \lambda_1 - k_1 & p_{22}^0 = \lambda_2 - k_1 \end{pmatrix} \tag{14}$$

The dynamics around the steady state is locally characterized by the two relaxation times $\tau_i^0 = 1/|R(\lambda_i^0)|$, with $i = 1, 2$, where R returns to the real part of the argument.

Two different three-variable models converging to the two-variable model after the elimination of a fast variable Z are introduced in the next subsections.

2.2 Three-variable model *A*

One of the simplest ways to introduce a third variable concentration Z consists in considering an intermediate species Z,[27] reversibly formed through the second reaction with rate constants k_2' and k_{-2}' and irreversibly transformed into $3X$ with rate constant k_2'' according to the three-variable model *A*

$$X \xrightarrow{k_1} R_1 \tag{15}$$

$$2X + Y \underset{k_{-2}'}{\overset{k_2'}{\rightleftharpoons}} Z \tag{16}$$

$$Z \xrightarrow{k_2''} 3X \tag{17}$$

$$Y \underset{k_{-3}'}{\overset{k_3}{\rightleftharpoons}} R_2 \tag{18}$$

The goal of this subsection is to determine the conditions for which the three-variable model reduces to the two-variable model. The rate equations associated with model *A* are

$$\frac{\mathrm{d}X}{\mathrm{d}t} = -k_1 X - 2k_2' X^2 Y + (2k_{-2}' + 3k_2'')Z \tag{19}$$

$$\frac{dY}{dt} = k_{-3} - k_3 Y - k_2' X^2 Y + k_{-2}' Z \quad (20)$$

$$\frac{dZ}{dt} = k_2' X^2 Y - (k_{-2}' + k_2'') Z \quad (21)$$

On the slow manifold[4,28,29] defined by $\frac{dZ}{dt} = 0$, *i.e.*

$$Z = \frac{k_2'}{k_{-2}' + k_2''} X^2 Y \quad (22)$$

dynamics becomes

$$\frac{dX}{dt} = -k_1 X + \frac{k_2' k_2''}{k_{-2}' + k_2''} X^2 Y \quad (23)$$

$$\frac{dY}{dt} = k_{-3} - k_3 Y - \frac{k_2' k_2''}{k_{-2}' + k_2''} X^2 Y \quad (24)$$

which exactly matches the dynamics of the two-variable model given in eqn (4) and (5) provided that:

$$\frac{k_2' k_2''}{k_{-2}' + k_2''} = k_2 \quad (25)$$

In particular, when the above condition is satisfied, the steady state (X_0,Y_0,Z_0) of model *A* obeys

$$X_0 = X_0^0 \quad (26)$$

$$Y_0 = Y_0^0 \quad (27)$$

$$Z_0 = \frac{k_1 X_0^0}{k_2''} \quad (28)$$

where the expressions of the steady concentrations X_0^0 and Y_0^0 for the two-variable model are given in eqn (8) and (9). Provided that eqn (25) is obeyed, the steady concentrations of the three-variable model *A* do not depend on the rate constants k_2' and k_{-2}'. The variation of the steady concentration *versus* the rate constant k_2'' is given in Fig. 1 for the two-variable model and the three-variable model *A*. For the chosen parameter values, the steady concentration Z_0 of the eliminated species is never negligible with respect to X_0^0 and Y_0^0. However this qualitative statement cannot be considered as a criterion to check the validity of the quasi-steady-state approximation, which refers to dynamics and not to steady properties.

The dynamics of the three-variable model depends on the three rate constants k_2', k_{-2}', and k_2'', in addition to the parameters of the two-variable model. We study the behavior of the system in two cuts of the parameter space (k_2',k_{-2}',k_2''). In case a, parameter k_{-2}' is set at $k_{-2}' = 1$ and k_2' varies with k_2'' according to $k_2' = k_2(1 + k_{-2}'/k_2'')$ in order to obey eqn (25). Case b corresponds to $k_2' = 10$ and $k_{-2}' = k_2''(-1 + k_2'/k_2)$, which also obeys eqn (25). We adopt analogous notations as in the two-variable model to characterize the linearized dynamics around the steady state. In particular, the deviations from the steady state are denoted by $x = X - X_0^0$, $y = Y - Y_0^0$, and $z = Z - Z_0$. The matrix form of the linearized equations around the steady state are similar to eqn (10) with $\zeta = \begin{pmatrix} x \\ y \\ z \end{pmatrix}$ and a 3 × 3 matrix

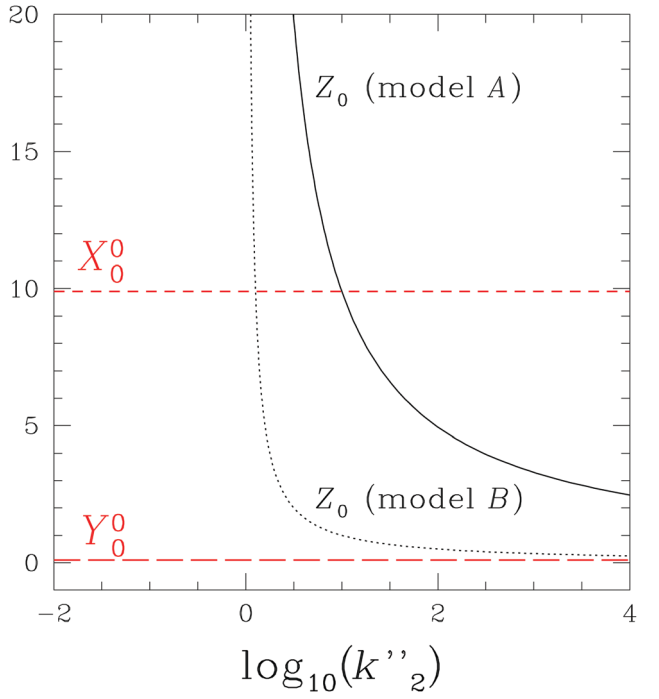

Fig. 1 Steady concentrations of species *X* and *Y* for the two-variable model and the three-variable models *A* and *B* (the red short-dashed line for $X_0 = X_0^0$ and the red long-dashed line for $Y_0 = Y_0^0$) and the steady concentration Z_0 of the three-variable model *A* (black solid line) and the three-variable model *B* (black dotted line) *versus* $\log_{10}(k_2'')$ for $k_1 = k_2 = k_3 = 1$, $k_{-3} = 10$, and $\frac{k_2' k_2''}{k_{-2}' + k_2''} = k_2$.

M associated with eigenvalues λ_i, with $i = 1, 2, 3$. The vectors $\chi = \begin{pmatrix} x_1 \\ x_2 \\ x_3 \end{pmatrix}$ and ζ are related to $\zeta = \mathbf{P}\chi$, where **P** is the 3 × 3 change of the basis matrix. The expressions of the eigenvalues and eigenvectors associated with the three-variable model *A* are given in Appendix A. The variation of the eigenvalues λ_i, for $i = 1, 2, 3$, *versus* k_2'' is given in Fig. 2. The eigenvalues λ_1^0 and λ_1 of the two- and three-variable models are identical in the entire k_2'' range. The time $\tau_i = 1/|R(\lambda_i)|$ associated with variable x_i characterizes the evolution along the corresponding eigendirection.

In the linear domain around the steady state, the elimination of variable *Z* according to the quasi-steady-state approximation can be performed if two conditions are fulfilled. First, the relaxation in one eigendirection must be particularly fast. This condition implies that the real part of the eigenvalue associated with the fast eigendirection, for example λ_3, must be significantly larger in absolute value than the two others:[2–4]

$$|R(\lambda_3)| > \max(|R(\lambda_1)|, |R(\lambda_2)|) \quad (29)$$

Second, coordinate *z* must vary in the same way as x_3 during the time interval $[0,\tau_3]$. This condition can be expressed using the inverse change of basis matrix $\mathbf{P}^{-1}$

$$x_3 = q_{31}x + q_{32}y + q_{33}z \quad (30)$$

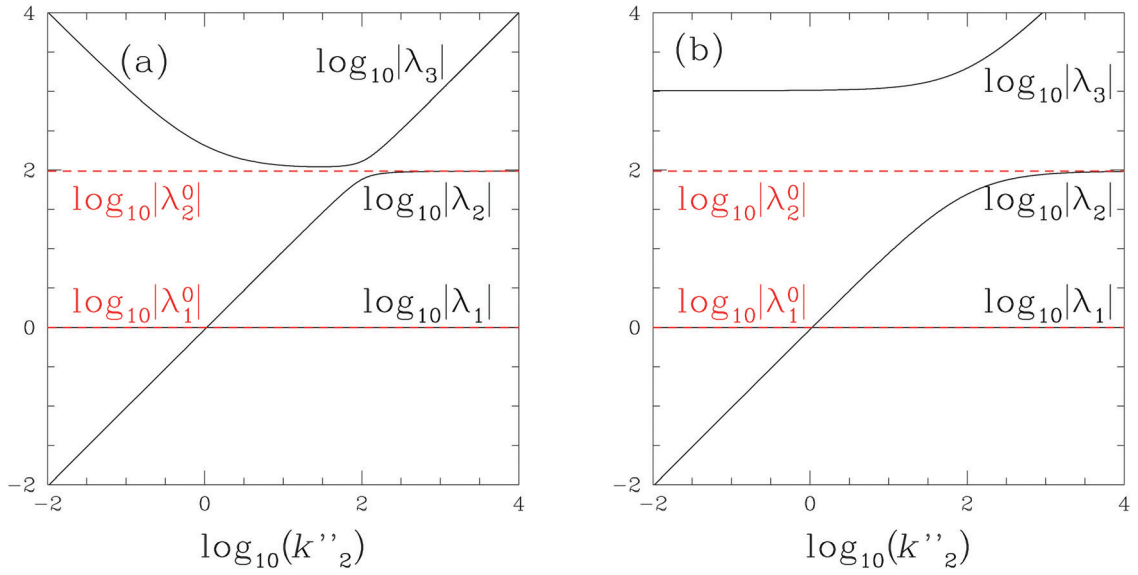

Fig. 2 Logarithm of absolute eigenvalues $\log_{10}|\lambda_i^0|$, i = 1, 2, of the two-variable model (red dashed lines) and $\log_{10}|\lambda_i|$, i = 1, 2, 3, of the three-variable model A (black solid lines) *versus* $\log_{10}(k_2'')$ for $k_1 = k_2 = k_3 = 1$, $k_{-3} = 10$. All eigenvalues are real. (a) Case a: $k_{-2}' = 1$ with $k_2' = k_2(1 + k_{-2}'/k_2'')$. (b) Case b: $k_2' = 10$ with $k_{-2}' = k_2''(-1 + k_2'/k_2)$.

leading to

$$|R(q_{33})| > \max(|R(q_{31})|,|R(q_{32})|) \quad (31)$$

where q_{3i}, for $i = 1, 2, 3$, are the elements of the third line of $\mathbf{P}^{-1}$ and for initial conditions with departures from the steady states x, y, and z of the same order of magnitude. An equivalent condition can be written using the change of basis matrix $\mathbf{P}$, provided that its column vectors, *i.e.* the eigenvectors, are normalized

$$z = p_{31}x_1 + p_{32}x_2 + p_{33}x_3 \quad (32)$$

which reads

$$|R(p_{33})| > \max(|R(p_{31})|,|R(p_{32})|) \quad (33)$$

where p_{3i}, for $i = 1, 2, 3$, are the elements of the third line of $\mathbf{P}$. Hence, the eigendirections associated with the two small absolute real parts of the eigenvalues are close to plan $z = 0$. If the two conditions given in eqn (29) and (31) are fulfilled, the relaxation with the short characteristic time τ_3 along the x_3-axis can be considered to be instantaneous. Further evolution, including Z evolution, occurs with the slower relaxation times on the slow manifold given in eqn (22). The slow manifold is tangent to the slow eigendirections and is close to the $z = 0$ plane in the vicinity of the steady state.

According to Fig. 2 and for the chosen parameter values, the eigenvalues of the three-variable model A are always real, negative, and obey eqn (29) except for k_2'' around 100 in case a. The variable x_3 of model A which evolves with the characteristic time $\tau_3 = 1/|R(\lambda_3)|$ can be considered to be fast with respect to variables x_1 and x_2 nearly in the entire range of k_2'' values. The eigenvalues λ_1 and λ_2 of the three-variable model A coincide with the eigenvalues λ_1^0 and λ_2^0 of the two-variable system in a smaller interval, $k_2'' > 100$.

Using the vocabulary of quantum chemistry, we notice that an avoided crossing between λ_2 and λ_3 is observed in Fig. 2a for $k_2'' \simeq 100$. The parallelism with a known case of failure of the Born–Oppenheimer approximation can be drawn. Both the quasi-steady-state approximation and the Born–Oppenheimer approximation belong to the class of adiabatic approximations.[1] The Born–Oppenheimer approximation consists in ignoring the fast movements of the electrons and only considering the slow components of their displacements in response to the movement of the nuclei. Introducing a perturbation to the Hamiltonian splits the degenerate energy states and leads to an avoided crossing, exactly as shown in Fig. 2a when switching from the two-variable model to the three-variable model. The cut of the parameter space associated with case b does not lead to an avoided crossing for λ_2 and λ_3 as shown in Fig. 2b. It is to be noted that, for $k_2'' = 1$, the crossing of the two eigenvalues λ_1 and λ_2 associated with the slow dynamics is not avoided in model A in both cases a and b.

As shown in Fig. 3, imposing that z evolves like x_3 is more restrictive than eqn (29). The condition for the elements of $\mathbf{P}^{-1}$ given in eqn (31) is obeyed for $k_2'' > 10^{2.48}$ in cases a and b. Eqn (33) based on the elements of $\mathbf{P}$ leads to similar results. The avoided crossing of λ_3 and λ_2 observed in Fig. 2a is associated with a maximum for $|R(q_{32})|$ in Fig. 3a. We note the absence of both phenomena in Fig. 2b and 3b.

We conclude that the two conditions given in eqn (29) and (31) are satisfied in the range $k_2'' > 10^{2.48}$ in which the linear dynamics of the two-variable model and the three-variable model A are close for the two cases a and b. It is worth noting that eqn (29) and (31) are only necessary conditions for the validity of the quasi-steady-state approximation. But they do not warrant that the two-variable model remains valid when non-linearities become important, typically when the system is far from the steady state or close to a bifurcation.

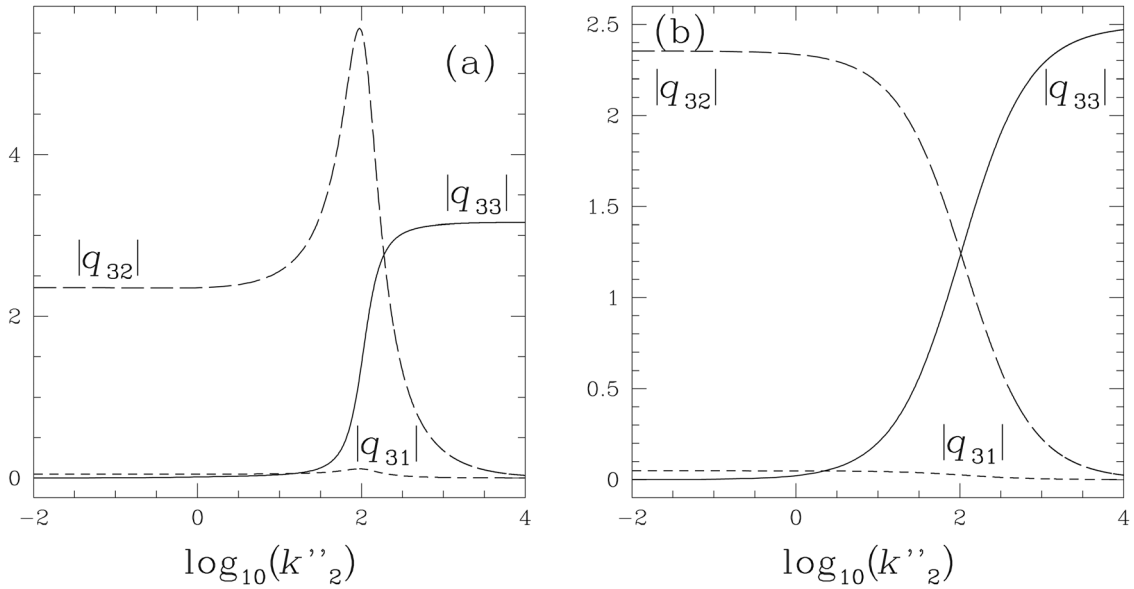

Fig. 3 Three-variable model *A*: absolute elements $|q_{31}|$ (short-dashed line), $|q_{32}|$ (long-dashed lines), and $|q_{33}|$ (solid line) of the inverse change of the basis matrix *versus* rate constant $\log_{10}(k_2'')$ for the parameter values given in the caption of Fig. 2. (a) Case a and (b) case b.

2.3 Three-variable model *B*

The second reaction of the two-variable model can also be decomposed into two reactions involving an intermediate species Z according to

$$X \xrightarrow{k_1} R_1 \tag{34}$$

$$X + Y \underset{k_{-2}'}{\overset{k_2'}{\rightleftharpoons}} Z \tag{35}$$

$$X + Z \xrightarrow{k_2'} 3X \tag{36}$$

$$Y \underset{k_{-3}'}{\overset{k_3}{\rightleftharpoons}} R_2 \tag{37}$$

leading to the following differential equations:

$$\frac{dX}{dt} = -k_1 X - k_2' XY + k_{-2}' Z + 2k_2'' XZ \tag{38}$$

$$\frac{dY}{dt} = k_{-3} - k_3 Y - k_2' XY + k_{-2}' Z \tag{39}$$

$$\frac{dZ}{dt} = k_2' XY - k_{-2}' Z - k_2'' XZ \tag{40}$$

The slow manifold $\frac{dZ}{dt} = 0$ is now given by $Z = \frac{k_2' XY}{k_{-2}' + k_2'' X}$. The dynamics on the slow manifold obeys

$$\frac{dX}{dt} = -k_1 X + \frac{k_2' k_2''}{k_{-2}' + k_2'' X} X^2 Y \tag{41}$$

$$\frac{dY}{dt} = k_{-3} - k_3 Y - \frac{k_2' k_2''}{k_{-2}' + k_2'' X} X^2 Y \tag{42}$$

which never rigorously converges to the dynamics associated with the two-variable model given in eqn (4) and (5). Applying the quasi-steady-state approximation to model *B* does make it possible to reduce the number of variables. However, due to the nonpolynomial form of eqn (41) and (42), the reduced equations cannot be interpreted as rate laws associated with a chemical mechanism involving elementary steps. In particular, the two-variable model defined by eqn (1)–(3) does not account for the nonlinearities of eqn (41) and (42) of order higher than 3.

Nevertheless, imposing the relation

$$\frac{k_2' k_2''}{k_{-2}' + k_2'' X_0^0} = k_2 \tag{43}$$

ensures that a steady state of model *B* obeys

$$X_0 = X_0^0 \tag{44}$$

$$Y_0 = Y_0^0 \tag{45}$$

$$Z_0 = k_1/k_2'' \tag{46}$$

where (X_0^0, Y_0^0) is the steady state of interest of the two-variable model. The variation in the steady concentration of model *B* *versus* the rate constant k_2'' is given in Fig. 1. As k_2'' increases, the value of Z_0 decreases earlier in the case of model *B* compared to that of model *A*, which cannot be considered at this stage to be indicating a larger domain of validity of the quasi-steady-state approximation applied to model *B*.

As shown in Fig. 4a and b, the variation in the eigenvalues of the three-variable model *B* with k_2'' is very similar to the two cases a and b. As k_2'' decreases, several bifurcations are observed. Three real eigenvalues are observed in the range $k_2'' > 10^{-0.22}$. As for model *A*, the two eigenvalues λ_1 and λ_2 coalesce for $k_2'' > 10^{-0.22}$. Only two real parts of eigenvalues are

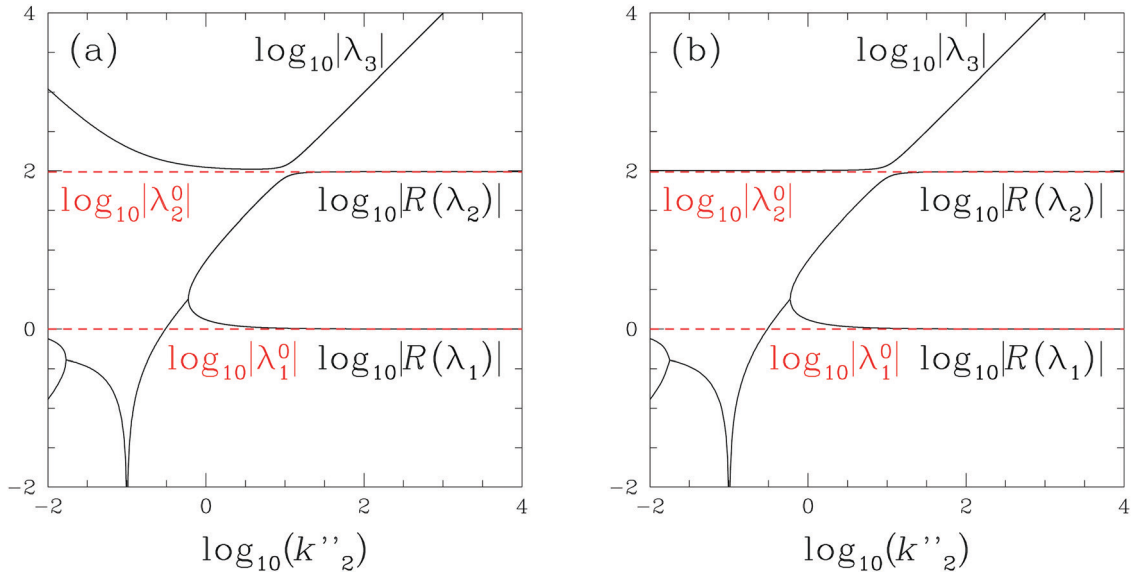

Fig. 4 Same caption as in Fig. 2 for the three-variable model B using the real part $R(\lambda_i)$ (i = 1, 2) of the eigenvalues when they are complex. (a) Case a: $k_{-2}' = 1$ with $k_2' = k_2(X_0^0 + k_{-2}'/k_2'')$. (b) Case b: $k_2' = 10$ with $k_{-2}' = k_2''(-X_0^0 + k_2'/k_2)$.

observed in the range $10^{-1.75} < k_2'' < 10^{-0.22}$ revealing the existence of two complex conjugate eigenvalues λ_1 and λ_2. As k_2'' becomes smaller than 0.1, the real part of λ_1 and λ_2 becomes positive, as evidenced by the divergence of the logarithm of $|R(\lambda_1)| = |R(\lambda_2)|$ observed for $k_2'' = 0.1$. The steady state (X_0^0, Y_0^0, Z_0) is then unstable. Another bifurcation occurs for $k_2'' \simeq 10^{-1.75}$, for which the eigenvalues become real again but remain negative. If one excepts the neighborhood of $k_2'' = 10$ for which the orders of magnitude of λ_2 and λ_3 are comparable, model B obeys the condition given in eqn (29) in the entire range of the explored k_2'' values. The two eigenvalues λ_1^0 and λ_2^0 of the two-variable model coincide with the eigenvalues λ_1 and λ_2 of the three-variable model B if $k_2'' > 10$ in the two cases a and b.

According to Fig. 5, the variation of the elements of the inverse change of the basis matrix *versus* k_2'' is similar for the two cases a and b. The avoided crossing between λ_2 and λ_3 observed in Fig. 4a and b reveals that x_2 and x_3 evolve with analogous characteristic times and eqn (29) is not obeyed for $k_2'' \simeq 10$. This phenomenon is accompanied by a high peak for $|R(q_{32})|$ and a significant departure from the condition given in eqn (31). The condition imposing that variable z behaves like

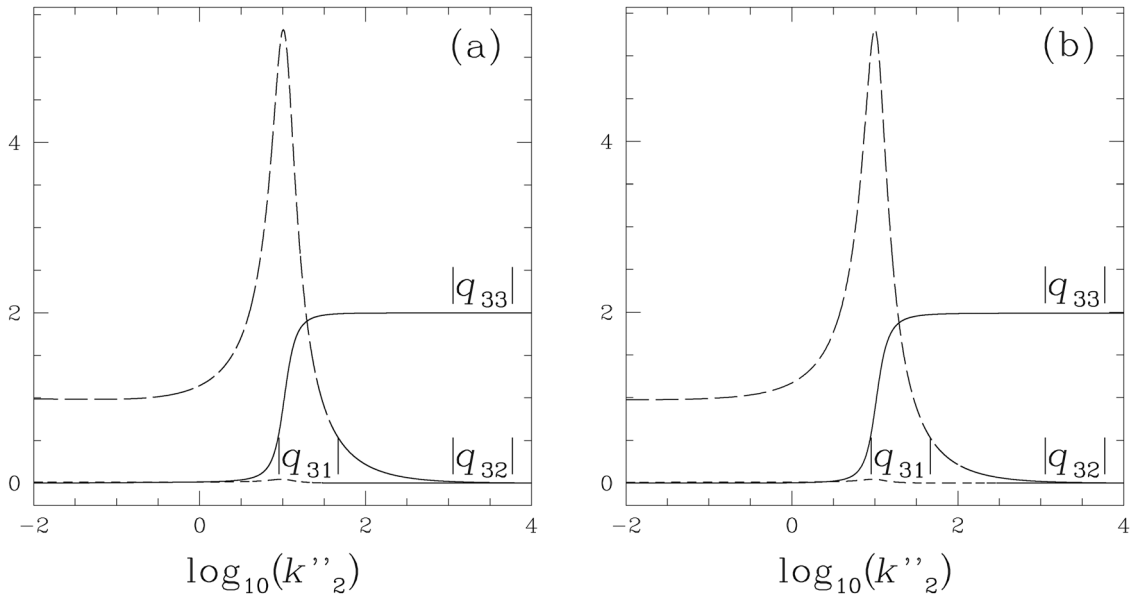

Fig. 5 Same caption as in Fig. 3 for the three-variable model B. (a) Case a: $k_{-2}' = 1$ with $k_2' = k_2(X_0^0 + k_{-2}'/k_2'')$. (b) Case b: $k_2' = 10$ with $k_{-2}' = k_2''(-X_0^0 + k_2'/k_2)$.

the fast variable x_3 is obeyed in the range $k_2'' > 10^{1.48}$. Following the linear analysis, we conclude that the quasi-steady-state approximation is valid in the range $k_2'' > 10^{1.48}$ for the three-variable model *B* in the two cases a and b.

3 Stochastic descriptions

The effect of internal noise in a chemical system can be modeled in an approximate way within the framework of Langevin equations using the expressions of the Langevin forces deduced from the chemical master equation.[23,30] In this section, we consider Langevin equations linearized in the vicinity of the steady state to compute approximate analytical expressions of variances and covariance of fluctuations for the slow concentrations *X* and *Y*. The method is illustrated in the case of the two-variable model. The Langevin equations are integrated in the eigenbasis. The inverse change of basis and the large-time limit is then used to find the steady variances of the concentrations.[20–22] Deriving the corresponding expressions for the three-variable models is more tedious but follows the same intuitive procedure. The results are given in Appendix B. Another method, using an implicit matrix equation for the variances, is proposed by Gardiner[30] and leads to analogous results.

The linearized Langevin equations for the two-variable model are written as

$$\frac{dx}{dt} = m_{11}x + m_{12}y + \frac{1}{\sqrt{\Omega}}\xi_x(t) \tag{47}$$

$$\frac{dy}{dt} = m_{21}x + m_{22}y + \frac{1}{\sqrt{\Omega}}\xi_y(t) \tag{48}$$

where Ω scales as the system size, m_{ij} are the elements of the matrix **M** given in eqn (11) and $\xi_x(t)$ and $\xi_y(t)$ are zero-mean Langevin forces. Due to the linearization of the Langevin equations, we have $\langle X\rangle = X_0^0$ and $\langle Y\rangle = Y_0^0$ and $\langle x\rangle = \langle y\rangle = 0$. The variances and covariance of the Langevin forces evaluated in the steady state are given by

$$\langle \xi_x(t)\xi_x(t')\rangle = F_{xx}\delta(t - t') \tag{49}$$

$$\langle \xi_x(t)\xi_y(t')\rangle = F_{xy}\delta(t - t') \tag{50}$$

$$\langle \xi_y(t)\xi_y(t')\rangle = F_{yy}\delta(t - t') \tag{51}$$

with[19]

$$F_{xx} = k_1X_0^0 + k_2(X_0^0)^2Y_0^0 \tag{52}$$

$$F_{xy} = -k_2(X_0^0)^2Y_0^0 \tag{53}$$

$$F_{yy} = k_2(X_0^0)^2Y_0^0 + k_3Y_0^0 + k_{-3} \tag{54}$$

Using the change of basis matrix $\mathbf{P^0}$ given in eqn (14), we determined the scaled variances and covariance

$$\Omega\langle x^2\rangle = (p_{11}^0)^2F_{11} + 2p_{11}^0p_{12}^0F_{12} + (p_{12}^0)^2F_{22} \tag{55}$$

$$\Omega\langle xy\rangle = p_{11}^0p_{21}^0F_{11} + (p_{11}^0p_{22}^0 + p_{12}^0p_{21}^0)F_{12} + p_{12}^0p_{22}^0F_{22} \tag{56}$$

$$\Omega\langle y^2\rangle = (p_{21}^0)^2F_{11} + 2p_{21}^0p_{22}^0F_{12} + (p_{22}^0)^2F_{22} \tag{57}$$

with

$$F_{ij} = \frac{q_{i1}q_{j1}F_{xx} + (q_{i1}q_{j2} + q_{i2}q_{j1})F_{xy} + q_{i2}q_{j2}F_{yy}}{-\lambda_i - \lambda_j} \tag{58}$$

where $i, j = 1, 2$ and the q_{ij}'s are the elements of the inverse matrix of **P**.

The chemical master equation for the two-variable model is[5,30]

$$\begin{aligned}\frac{\partial P}{\partial t} = {} & k_1[(N_X+1)P(\{N_X+1\}) - N_XP] + \frac{k_2}{\Omega^2}[(N_X-1)(N_X-2)\\ & \times(N_Y+1)P(\{N_X-1, N_Y+1\}) - N_X(N_X-1)N_YP]\\ & + k_3[(N_Y+1)P(\{N_Y+1\}) - N_YP] + k_{-3}\Omega[P(\{N_Y-1\}) - P]\end{aligned} \tag{59}$$

for N_X and N_Y particles of species *X* and *Y* at time *t* in a system of size Ω. Only the dependence of probability *P* on the number of particles *X* and *Y* differing from N_X and N_Y, respectively, is explicitly indicated. The kinetic Monte Carlo algorithm developed by Gillespie[23] is used to directly simulate the reaction processes and numerically solve the master equation for a system prepared in the steady state with $N_X(t = 0) = \Omega X_0^0$ and $N_Y(t = 0) = \Omega Y_0^0$. The scaled variances $\Omega\langle(N_X - \langle N_X\rangle)^2\rangle$ and $\Omega\langle(N_Y - \langle N_Y\rangle)^2\rangle$ and the covariance $\Omega\langle(N_X - \langle N_X\rangle)(N_Y - \langle N_Y\rangle)\rangle$ of the fluctuations are computed using a statistics over 10^4 realizations.

The master equations associated with the three-variable models are given in Appendix C.

Fig. 6a and b display the variation of the scaled variance of the concentration fluctuations of species *X versus* rate constant k_2'' for the three-variable model *A* in cases a and b. The variance is multiplied by Ω, so that the scaled results $\Omega\langle x^2\rangle$ deduced from the Langevin approach (see eqn (73)) are not sensitive to system size and more easily compared to the corresponding result, $\Omega\langle(N_X - \langle N_X\rangle)^2\rangle$, deduced from the master equation. The results of the three-variable model *A* are compared with those of the two-variable model for both stochastic approaches. In the following description, we refer to the Langevin approach applied to the two- and three-variable models as L2 and L3, respectively. The master equation applied to the two- and three-variable models is referred to as M2 and M3. Due to the logarithmic scale adopted to represent the large range covered by the L3 results, the L2 and M2 approaches seem to coincide as shown in Fig. 6a and b. The results of the master equation applied to the two-variable model depend little on system size Ω at the scale of the figure and only the results obtained for $\Omega = 1000$ are shown. Indeed, the parameter values of the two-variable model are chosen far from any situation associated with large fluctuation effects such as bifurcations. In this kind of situation, the results of the linearized Langevin approach are satisfying and the agreement with the results of the master equation is expected even for quite small system sizes.[20–22]

No appreciable deviation is observed between the M3 results obtained for different values of system size Ω in both cases a and b. At figure scale, the M3 results converge to the L2 and M2 result for large k_2'' values ($k_2'' > 10^{2.48}$) and deviate from it as

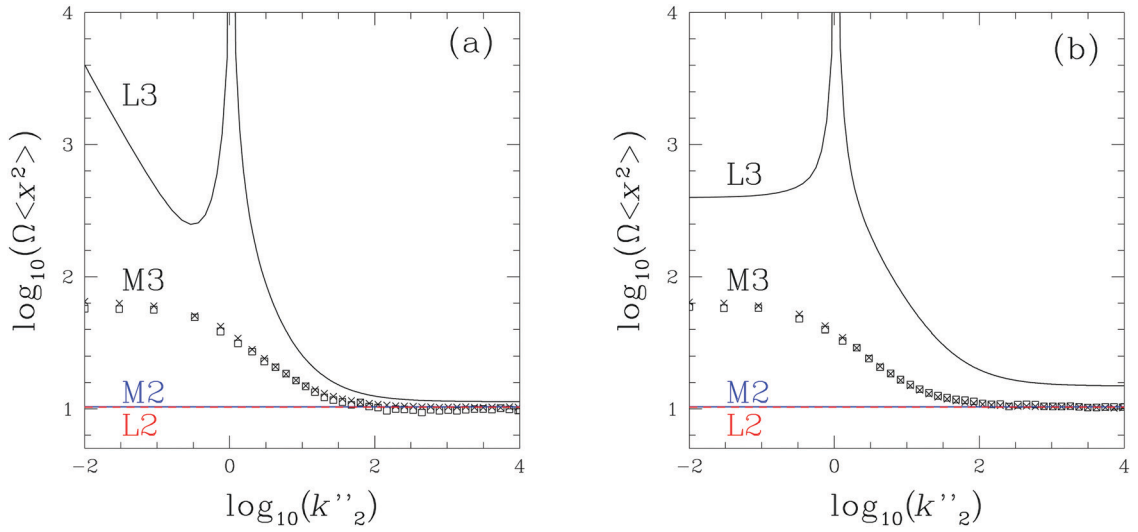

Fig. 6 Three-variable model *A*: logarithm of the scaled variance associated with species *X versus* $\log_{10}(k_2'')$ for the Langevin approach ($\log_{10}(\Omega\langle x^2\rangle)$, black solid line) and the master equation ($\log_{10}(\Omega\langle(N_X - \langle N_X\rangle)^2\rangle)$) for $\Omega = 3$ (□) and $\Omega = 1000$ (×). Two-variable model: the red dashed line gives the results of the Langevin approach and the blue solid line, the results of the master equation for $\Omega = 1000$. The other parameter values are given in the caption of Fig. 2. (a) Case a and (b) case b.

k_2'' decreases. Typically, for $k_2'' \simeq 1$, the scaled variance deduced from M3 is multiplied by a factor of 3 with respect to the M2 results. When compared to M3, the L3 results are found to markedly overestimate the deviation between the results of the three- and two-variable models in the range $k_2'' < 10$. The L3 results display a spurious divergence for $k_2'' = 1$, in relation to the crossing of the two eigenvalues λ_1 and λ_2 observed in Fig. 2. In spite of the logarithmic scale, a discrepancy between the L3 result and the L2, M2, and M3 results can be observed in the limit of the largest investigated k_2'' values, in particular in Fig. 6b. The discrepancy between the L3 and M3 results has two origins. First, the Langevin approach introduces Gaussian noises, which implies the intrinsic truncation of the cumulants of the probability distribution function to the second order. Second, the analytical expressions of the variances are deduced from the linearization of the Langevin equations around the steady state whereas the master equation provides an exact stochastic description at a mesoscopic scale.

The variation in the scaled variance $\Omega\langle y^2\rangle$ or $\Omega\langle(N_Y - \langle N_Y\rangle)^2\rangle$ of the concentration fluctuations of species *Y* with k_2'' is given in Fig. 7. The two stochastic approaches L2 and M2 for the two-variable model agree. The L3 results are entirely different from both the M3 results and the L2 and M2 results, including in the large k_2'' limit. Contrary to the L3 results, the M3 results are

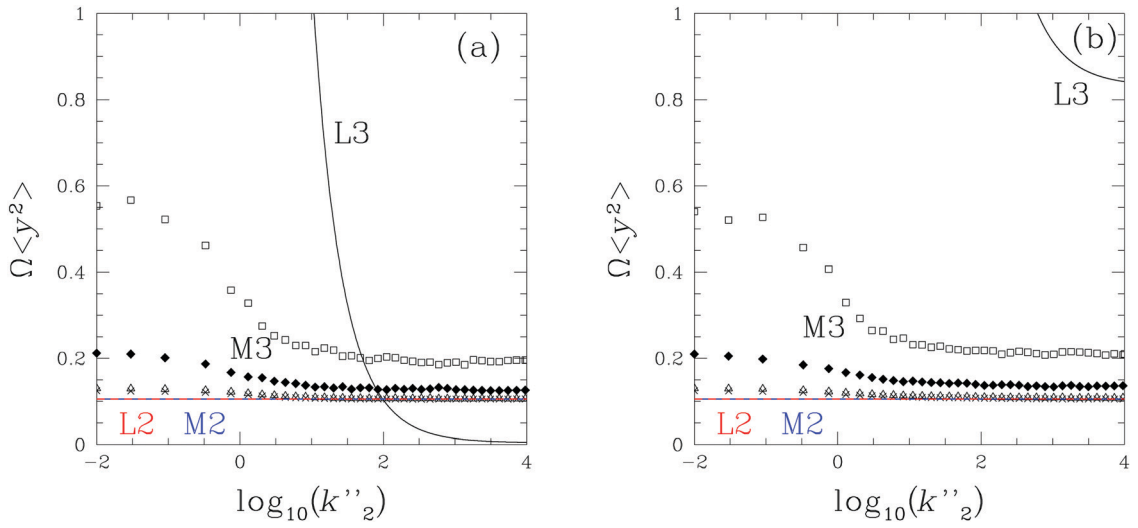

Fig. 7 Three-variable model *A*: scaled variance associated with species *Y versus* $\log_{10}(k_2'')$ for the Langevin approach ($\Omega\langle y^2\rangle$, black solid line) and the master equation ($\Omega\langle(N_Y - \langle N_Y\rangle)^2\rangle$) for $\Omega = 3$ (□), $\Omega = 10$ (♦), $\Omega = 100$ (△), and $\Omega = 1000$ (×). Two-variable model: the red dashed line gives the results of the Langevin approach and the blue solid line, the results of the master equation for $\Omega = 1000$. The other parameter values are given in the caption of Fig. 2. (a) Case a and (b) case b.

similar in cases a and b. The L3 results significantly deviate from the M3 predictions for $k_2'' < 10^{1.48}$. The M3 results converge towards the L2 and M2 results in the limit of large k_2'', ($k_2'' > 100$), and large system size, ($\Omega \geq 100$). Interestingly, the M3 results obtained for sufficiently small system sizes ($\Omega < 100$) never coincide with the L2 and M2 results: Even in the parameter domain $k_2'' > 10^{1.48}$, where the quasi-steady-state approximation is valid from the deterministic point of view, the behavior of the variance of species Y in the three-variable model significantly differs from the behavior obtained in the two-variable model.

The effect is more marked in the case of species Y than in the case of species X, due to the smaller value of the steady concentration Y_0^0: with concentration being a positive variable, the fluctuations around the mean value become asymmetrical when they reach the order of Y_0^0, *i.e.* for a sufficiently small system size Ω. As shown in Fig. 8, this phenomenon leads to the increase of the scaled variance $\Omega\langle(N_Y - \langle N_Y\rangle)^2\rangle$ as Ω decreases. In addition, the mean value $\langle N_Y\rangle$ is shifted from the deterministic steady state Y_0^0.

The scaled covariance $\Omega\langle xy\rangle$ or $\Omega\langle(N_X - \langle N_X\rangle)(N_Y - \langle N_Y\rangle)\rangle$ associated with species X and Y is shown in Fig. 9. In case a, the results of the two stochastic approaches for the three-variable model converge toward the results obtained for the two-variable model in the limit of large k_2''. However, as k_2'' becomes smaller than 1000, the L3 results increase and even become positive whereas the M3 results decrease and begin to appreciably depart from the M2 results only as k_2'' becomes smaller than 10. In case b, the L3 results are always far from the L2 results. As shown in Fig. 2, the convergence of the eigenvalue λ_2 of the three-variable model A toward the corresponding eigenvalue λ_2^0 of the two-variable model as k_2'' increases is slower in case b than in case a. Similarly, the increase of the absolute element $|q_{33}|$ as k_2'' increases is slower in case b than in case a, as observed in Fig. 3. This could explain that for large values of k_2'', the Langevin approach L3 is more different from L2 in case b than in case a shown in Fig. 6, 7 and 9. The master equation approach is less sensitive to this feature. Only a small increase of the M3 results with respect to the M2 results is detectable in Fig. 9b in the limit of large k_2'' for a small system size $\Omega = 3$, whereas the corresponding L3 results are much larger than the L2 results. These observations suggest that the nonlinearities ignored in the linearized Langevin approach mitigate the effect of the discrepancies between the eigenvalues of the two- and three-variable models. The sign of the covariance can be easily deduced for the two-variable model, in which the second reaction given in eqn (2) forms species X and consumes species Y: The covariance is negative. The situation is different for the three-variable model A, in which both species X and Y are consumed (formed, resp.) by the forward (backward, resp.) reaction given in eqn (16) whereas only X is formed by the third reaction given in eqn (17). According to Fig. 9, the master equation approach M3 captures the sign of the covariance even for small values of k_2'' for which the elimination of Z is not valid whereas L3 fails.

Fig. 10–12 give the variances and covariance for the fluctuations of the slow variables X and Y for the three-variable model B. Due to the similarity of the behaviors observed in cases a and b, only case a is represented. The results of the stochastic approaches are not given in the parameter domain $k_2'' < 0.1$ in which the steady state is unstable, as shown in Fig. 4a.

According to Fig. 10, the scaled variance $\Omega\langle x^2\rangle$ deduced from L2 is slightly smaller than the result deduced from M2. The small gap between L2 and M2 results could not be seen in Fig. 6 due to the adopted logarithmic scale. The L3 results of the Langevin approach applied to the three-variable model completely differ from the L2 predictions in the entire range of k_2'': the L3 limit at large k_2'' underestimates the L2 value by a factor

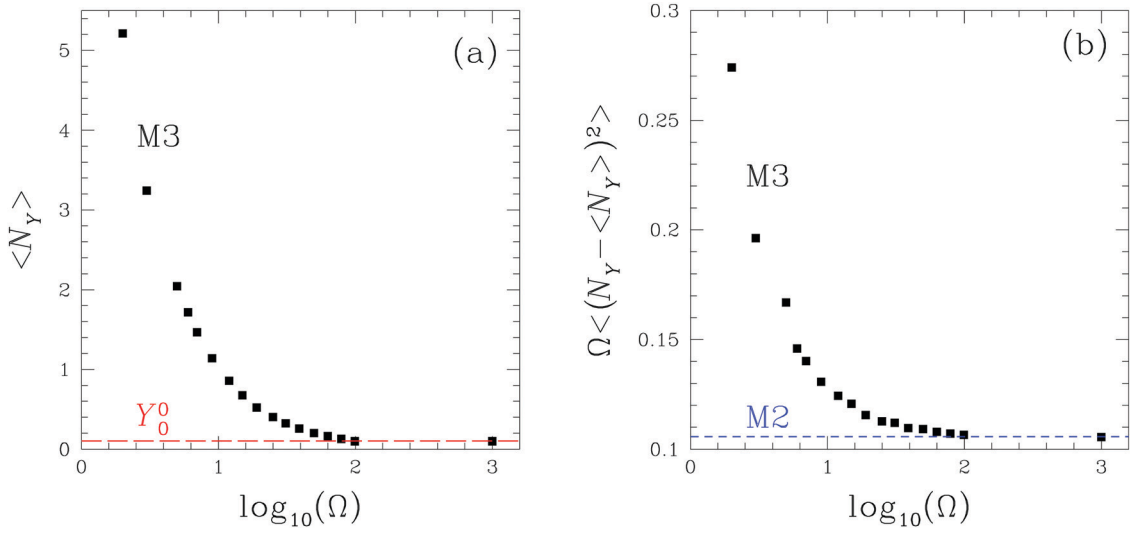

Fig. 8 Three-variable model A in case a for $k_2'' = 10^4$: (a) mean value $\langle N_Y\rangle$ deduced from the master equation (■) and deterministic prediction Y_0^0 (red long-dashed line) *versus* $\log_{10}(\Omega)$. (b) Scaled variance $\Omega\langle(N_Y - \langle N_Y\rangle)^2\rangle$ deduced from the master equation for the three-variable model A (■) and the two-variable model (blue short-dashed line) *versus* $\log_{10}(\Omega)$. The other parameter values are given in the caption of Fig. 2a.

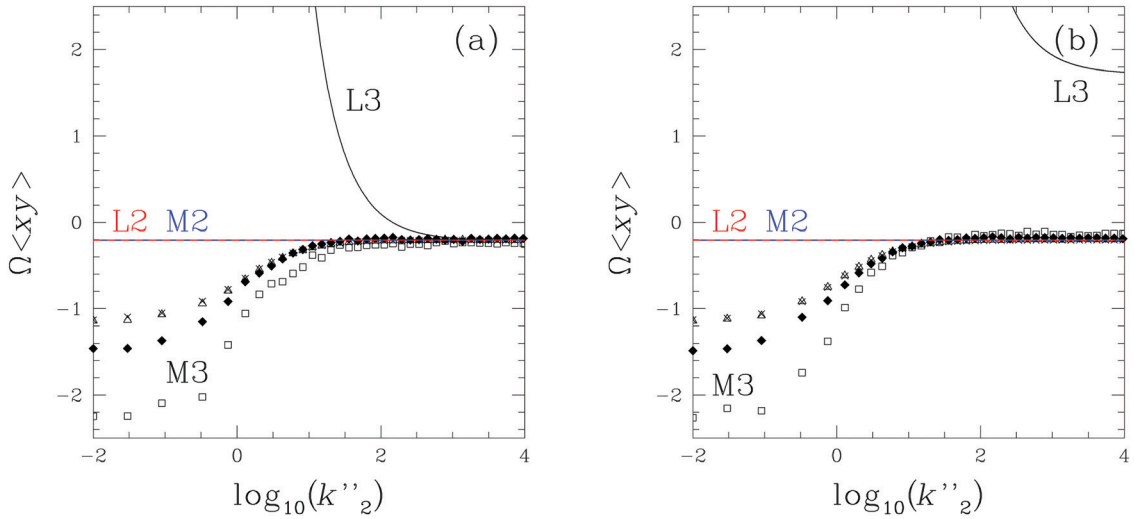

Fig. 9 Three-variable model *A*: same caption as in Fig. 7 for the scaled covariance $\Omega\langle xy\rangle$ (Langevin approach) or $\Omega\langle(N_X - \langle N_X\rangle)(N_Y - \langle N_Y\rangle)\rangle$ (master equation). (a) Case a and (b) case b.

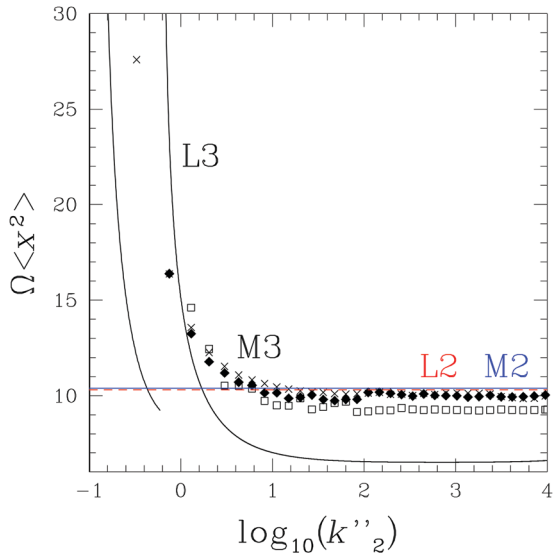

Fig. 10 Three-variable model *B* in case a: scaled variance associated with species *X* *versus* $\log_{10}(k_2'')$ for the Langevin approach ($\Omega\langle x^2\rangle$, black solid line) and the master equation ($\Omega\langle(N_X - \langle N_X\rangle)^2\rangle$) for $\Omega = 3$ (□), $\Omega = 10$ (♦), and $\Omega = 1000$ (×). Two-variable model: the red dashed line gives the results of the Langevin approach and the blue solid line, the results of the master equation for $\Omega = 1000$. Case a: $k_{-2}' = 1$ with $k_2' = k_2(X_0^0 + k_{-2}'/k_2'')$. The other parameter values are given in the caption of Fig. 2.

of 1.6 and the spurious divergence observed for $k_2'' = 0.6$ due to the coalescence of the eigenvalues λ_1 and λ_2 (see Fig. 4) induces a rapid increase of $\Omega\langle x^2\rangle$ in the range $10^{-0.22} < k_2'' < 100$. The M3 results for the scaled variance $\Omega\langle(N_X - \langle N_X\rangle)^2\rangle$ do not converge toward the M2 results even in the limit of large k_2'' and Ω. The fact that, for the same parameter values, Z_0 is smaller in the case of model *B* than model *A* (see Fig. 1) is not sufficient to ensure the matching between the stochastic predictions of the two-variable model and the three-variable model *B*. Indeed, the nonlinearities observed in the rate laws (see eqn (41) and (42)) after applying the quasi-steady-state approximation to model *B* are different from the nonlinearities present in the original two-variable model. The nonconvergence of the M3 results toward the M2 results at large k_2'' and Ω in the case of model *B* illustrates the decisive role played by the nonlinearities of the deterministic dynamics in fluctuation properties.

The sensitivity of the M3 results to system size for species *X* in Fig. 10 is small, compared to the results observed in Fig. 11 for species *Y*. As already mentioned, the sensitivity of $\Omega\langle(N_Y - \langle N_Y\rangle)^2\rangle$ to Ω is related to the small value of Y_0^0 which induces asymmetrical fluctuations around the mean value for sufficiently small system sizes. The results given in Fig. 11 for model *B* are qualitatively the same as those given in Fig. 7 for model *A*.

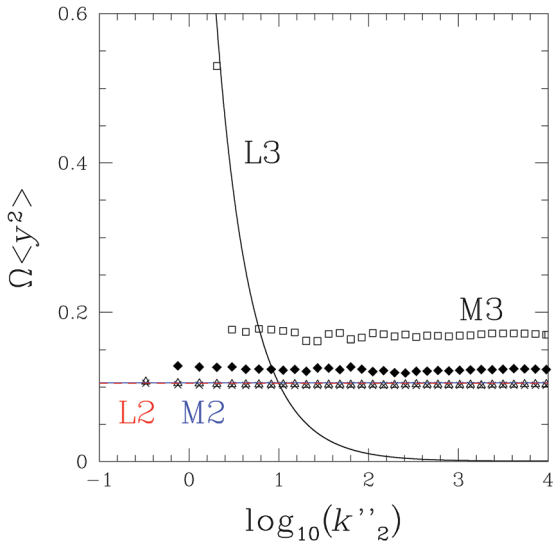

Fig. 11 Three-variable model *B*: same caption as in Fig. 10 for the scaled variance $\Omega\langle y^2\rangle$ (Langevin approach) or $\Omega\langle(N_Y - \langle N_Y\rangle)^2\rangle$ (master equation) associated with species *Y*.

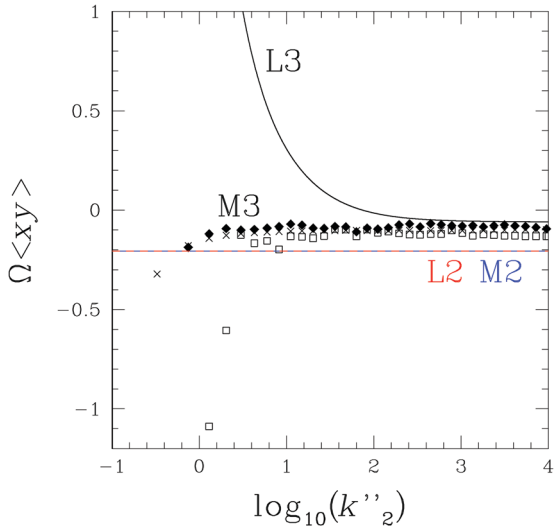

Fig. 12 Three-variable model *B*: same caption as in Fig. 10 for the scaled covariance $\Omega\langle xy\rangle$ (Langevin approach) or $\Omega\langle(N_X - \langle N_X\rangle)(N_Y - \langle N_Y\rangle)\rangle$ (master equation).

The results obtained for the covariance in the case of model *B* are given in Fig. 12. Contrary to model *A* (see Fig. 9) for which the results of the master equation converge toward the L2 and M2 limit at large k_2'', the M3 results obtained for model *B* remain larger than the L2 and M2 limit, even for a large system size $\Omega = 1000$. The covariance deduced from the M3 approach decreases as k_2'' approaches the critical value $k_2'' = 0.1$ below which the steady state becomes unstable.

Although the three-variable models *A* and *B* converge to the same deterministic two-variable model, at least for the steady properties and linear dynamics, the variances and covariance of the slow variables in models *A* and *B* have different behaviors. Hence, the proper description of the fluctuations in models *A* and *B* by the two-variable model deduced from the steady-state-approximation is not ensured in systems of small size. Sizes of the order of $\Omega = 1000$ have to be reached for the results of the master equation applied to the three-variable models to converge toward the results of the two-variable model.

4 Discussion and conclusion

In this paper, we introduce a fast species in a chemical mechanism and show that it perturbs the fluctuations of the slow species even in the domain of validity of the quasi-steady-state approximation, in which the deterministic dynamics is correctly predicted by the reduced mechanism in the linear domain.

The study provides an opportunity to revisit the quasi-steady-state approximation. By completely neglecting fast relaxation and restricting the dynamics to the slow manifold, the approximation can be considered as a zeroth-order perturbation method, which masks the small parameter and makes the definition of the validity domain less obvious.

The existence of a fast variable is sufficient to reduce dynamics but, in the general case, the slow variables are non trivial functions of the entire set of the initial variables, *e.g.* a linear combination of all concentrations in the framework of a linear analysis. The quasi-steady-state approximation eliminates a chemical species and consequently requires that the fast variable is close to an actual concentration. In the linear domain, characteristic relaxation times are assigned to the evolution along eigendirections and the notion of fast or slow variables to coordinates in the eigenbasis. We express the conditions of validity of the approximation using the eigenvalues and appropriate elements of the change of the basis matrix. The parallelism with the Born–Oppenheimer approximation in quantum chemistry is drawn, in particular in the case of avoided crossing between two eigenvalues.

The approximation is applied to two three-variable models *A* and *B* and the possible reduction to the same two-variable model is discussed. Conditions for the parameters of the three-variable models are made explicit for the two- and three-variable models to have the same steady state of interest. Model *B* offers a simple example showing that small concentrations for a slowly formed and rapidly consumed species cannot be considered as a valid condition of elimination. The intuitive belief used to eliminate a very reactive intermediate through a mechanism coincides with the dynamical criteria made precise in Section 2 in the case of intrinsically linear dynamics but does not coincide in general. In the case of model *A*, the steady value $Z_0 \simeq 2.5$ of the eliminated variable *Z* that is reached for $k_2'' = 10^4$ is already reached for $k_2'' = 10^{0.3}$ in the case of model *B*. According to the master equation and for a given value of Z_0, the deviations of the variances and covariance in the three-variable models to the corresponding quantities in the two-variable model are smaller for model *A* than model *B*. More precisely, for a large system size, $\Omega = 1000$, the M3 value of the variance $\Omega\langle(N_X - \langle N_X\rangle)^2\rangle$ in model *A* for $k_2'' = 10^4$ underestimates the M2 value by less than 1% whereas the corresponding result associated with the same Z_0 value in model *B*, *i.e.* for $k_2'' = 10^{0.3}$, overestimates the M2 value by 18%. Similarly, the M3 result for the covariance $\Omega\langle(N_X - \langle N_X\rangle)(N_Y - \langle N_Y\rangle)\rangle$ in model *A* for $k_2'' = 10^4$ overestimates the M2 value by only 0.6% whereas the corresponding result in the case of model *B* for $k_2'' = 10^{0.3}$ overestimates the M2 value by 38%. The larger discrepancies between M3 and M2 results in the case of model *B* for the same value of Z_0 are related to the specific nonlinearities introduced in the macroscopic rate equations when eliminating the fast variable *Z*. These nonpolynomial nonlinearities differ from the nonlinearities of the two-variable model and the interplay between the nonlinearities of the deterministic dynamics and the fluctuations is known to be complex and model specific.[20–22] The two-variable mechanism does not correctly account for the nonlinearities of the reduced dynamics of the three-variable model *B* and can only claim to model the linearized properties of the three-variable model around the steady state. The reduction of a mechanism often leads to such nonpolynomial nonlinearities, as for example in the case of the reduced Michaelis–Menten scheme.[31] Our results show that the conclusions that could be deduced from a stochastic analysis relying on the reduced Michaelis–Menten model may differ from the direct analysis of the complete scheme.

In the parameter range in which the reduction of the deterministic dynamics is valid in the linear domain and for both three-variable models A and B, the variances and covariance of the fluctuations of the slow concentrations do not always coincide with the corresponding quantities obtained for the two-variable model. The deficiencies of the linearized Langevin approach in capturing the properties of the internal fluctuations in a nonlinear chemical system and the necessary resort to the master equation are pointed out. Even the sign of the covariance of the fluctuations is not always correctly predicted by the Langevin equations. With the small value Y_0^0 of the steady concentration of species Y inducing asymmetrical fluctuations, the variance of the Y-fluctuations deduced from both three-variable models significantly depends on system size and differs from the prediction of the two-variable model for sufficiently small system sizes leading to fluctuation amplitudes larger than Y_0^0. The variance of the fluctuations around the large steady concentration X_0^0 deduced from the three-variable model B is not very sensitive to system size and does not converge toward the prediction of the two-variable model. We already pointed out the differences between the nonlinearities of the reduced dynamics obtained for model B and those of the two-variable model of reference. The coupling between the fluctuations and the nonlinearities of deterministic dynamics makes the use of the quasi-steady-state approximation delicate when the studied system requires a good control. The predictions of a reduced mechanism must be considered with special care when modeling pattern formation in biology, preventing hazards in explosive phenomena, or when dealing with small systems in which variances of fluctuations are detected as in fluorescence correlation spectroscopy (FCS).

Conflicts of interest

There are no conflicts to declare.

A Eigenvalues and eigenbasis of the three-variable models

The eigenvalues of the three-variable models are solutions to a cubic polynomial, determined through Cardano's method. In the case of the three-variable model A, the stability matrix $\mathbf{M}$ is

$$\mathbf{M} = \begin{pmatrix} m_{11} = -k_2' Y_0^0 - k_1 + 2k_2'' Z_0 & m_{12} = -k_2' X_0^0 & m_{13} = k_{-2}' + 2k_2'' X_0^0 \\ m_{21} = -k_2' Y_0^0 & m_{22} = -(k_2' X_0^0 + k_3) & m_{23} = k_{-2}' \\ m_{31} = k_2' Y_0^0 - k_2'' Z_0 & m_{32} = k_2' X_0^0 & m_{33} = -(k_{-2}' + k_2'' X_0^0) \end{pmatrix} \quad (61)$$

where the steady concentrations X_0^0 and Y_0^0 are given in eqn (8) and (9) and Z_0 is given in eqn (46).

Following Cardano's method, we set for each three-variable model

$$a = 1, \quad b = -(m_{11} + m_{22} + m_{33}), \quad (62)$$

$$c = -m_{12}m_{21} - m_{13}m_{31} - m_{23}m_{32} + m_{11}m_{22} + m_{11}m_{33} + m_{22}m_{33}, \quad (63)$$

$$d = m_{11}(m_{23}m_{32} - m_{22}m_{33}) + m_{21}(m_{12}m_{33} - m_{13}m_{32}) + m_{31}(m_{13}m_{22} - m_{12}m_{23}) \quad (64)$$

$$e = -\frac{b^2}{3a^2} + \frac{c}{a}, \quad (65)$$

$$f = \frac{b}{27a}\left(2\frac{b^2}{a^2} - 9\frac{c}{a}\right) + \frac{d}{a}, \quad \delta = -(4e^3 + 27f^2) \quad (66)$$

If $\delta \geq 0$, we set

$$u^3 = \frac{-f + i\sqrt{\delta/27}}{2}, \quad v^3 = \frac{-q - i\sqrt{\delta/27}}{2} \quad (67)$$

and if $\delta < 0$, we write

$$u^3 = \frac{-f + \sqrt{-\delta/27}}{2}, \quad v^3 = \frac{-q - \sqrt{-\delta/27}}{2} \quad (68)$$

The eigenvalues of the 3×3 matrix $\mathbf{M}$ are given by

$$\lambda_1 = \ell u + \bar{\ell} v - \frac{b}{3a} \quad (69)$$

$$\lambda_2 = u + v - \frac{b}{3a} \quad (70)$$

$$\lambda_3 = \bar{\ell} u + \ell v - \frac{b}{3a} \quad (71)$$

where $\ell = -1/2 + i\sqrt{3}/2$.

The jth eigenvector, *i.e.*, the jth column $\mathbf{P}_j$ for $j = 1, 2, 3$ of the change of basis matrix $\mathbf{P}$ can also be written in a form valid for

$$\mathbf{M} = \begin{pmatrix} m_{11} = -(4k_2' X_0^0 Y_0^0 + k_1) & m_{12} = -2k_2' (X_0^0)^2 & m_{13} = 2k_{-2}' + 3k_2'' \\ m_{21} = -2k_2' X_0^0 Y_0^0 & m_{22} = -(k_2' (X_0^0)^2 + k_3) & m_{23} = k_{-2}' \\ m_{31} = 2k_2' X_0^0 Y_0^0 & m_{32} = k_2' (X_0^0)^2 & m_{33} = -(k_{-2}' + k_2'') \end{pmatrix} \quad (60)$$

both three-variable models

$$\mathbf{P}_j = \begin{pmatrix} p_{1j} = 1 \\ p_{2j} = \dfrac{\lambda_j - m_{11} - m_{13}p_{31}}{m_{12}} \\ p_{3j} = \dfrac{(\lambda_j - m_{11})(\lambda_j - m_{22}) - m_{12}m_{21}}{m_{13}(\lambda_j - m_{22}) + m_{12}m_{23}} \end{pmatrix} \quad (72)$$

where the eigenvalues λ_j are given in eqn (69)–(71) and the elements m_{ij} are given in eqn (60) for model *A* and eqn (61) for model *B*.

B Variances and covariance of concentration fluctuations in the three-variable models deduced from the Langevin equations

Extending the approach given in Section 3 for a two-variable system to three-variable systems, we obtain the scaled variances and covariance of the deviations x and y to the steady concentrations X_0^0 and Y_0^0

$$\Omega\langle x^2\rangle = (p_{11})^2F_{11} + (p_{12})^2F_{22} + (p_{13})^2F_{33} + 2p_{11}p_{12}F_{12} + 2p_{11}p_{13}F_{13} + 2p_{12}p_{13}F_{23} \quad (73)$$

$$\Omega\langle y^2\rangle = (p_{21})^2F_{11} + (p_{22})^2F_{22} + (p_{23})^2F_{33} + 2p_{21}p_{22}F_{12} + 2p_{21}p_{23}F_{13} + 2p_{22}p_{23}F_{23} \quad (74)$$

$$\Omega\langle xy\rangle = p_{11}(p_{21}F_{11} + p_{22}F_{12} + p_{23}F_{13}) + p_{12}(p_{21}F_{12} + p_{22}F_{22} + p_{23}F_{23}) + p_{13}(p_{21}F_{13} + p_{22}F_{23} + p_{23}F_{33}) \quad (75)$$

with

$$F_{ij} = \frac{q_{i1}(q_{j1}F_{xx} + q_{j2}F_{xy} + q_{j3}F_{xz}) + q_{i2}(q_{j1}F_{xy} + q_{j2}F_{yy} + q_{j3}F_{yz}) + q_{i3}(q_{j1}F_{xz} + q_{j2}F_{yz} + q_{j3}F_{zz})}{-(\lambda_i + \lambda_j)} \quad (76)$$

for $i, j = 1, 2, 3$ and where q_{ij} are the elements of the inverse matrix of the change of basis matrix $\mathbf{P}$ (see eqn (72)) and the variances and covariances of the Langevin forces are

$$F_{xx} = k_1X_0^0 + 4k_2'(X_0^0)^2Y_0^0 + (4k_{-2}' + 9k_2'')Z_0 \quad (77)$$

$$F_{yy} = k_2'(X_0^0)^2Y_0^0 + k_{-2}'Z_0 + k_3Y_0 + k_{-3} \quad (78)$$

$$F_{zz} = k_2'(X_0^0)^2Y_0^0 + (k_{-2}' + k_2'')Z_0 \quad (79)$$

$$F_{xy} = 2k_2'(X_0^0)^2Y_0^0 + 2k_{-2}'Z_0 \quad (80)$$

$$F_{xz} = -2k_2'(X_0^0)^2Y_0^0 - (2k_{-2}' + 3k_2'')Z_0 \quad (81)$$

$$F_{yz} = -k_2'(X_0^0)^2Y_0^0 - k_{-2}'Z_0 \quad (82)$$

in the case of model *A* and

$$F_{xx} = k_1X_0^0 + k_2'X_0^0Y_0^0 + (k_{-2}' + 4k_2''X_0^0)Z_0 \quad (83)$$

$$F_{yy} = k_2'X_0^0Y_0^0 + k_{-2}'Z_0 + k_3Y_0^0 + k_{-3} \quad (84)$$

$$F_{zz} = k_2'X_0^0Y_0^0 + (k_{-2}' + k_2''X_0^0)Z_0 \quad (85)$$

$$F_{xy} = k_2'X_0^0Y_0^0 + k_{-2}'Z_0 \quad (86)$$

$$F_{xz} = -k_2'X_0^0Y_0^0 - (k_{-2}' + 2k_2'')Z_0 \quad (87)$$

$$F_{yz} = -k_2'X_0^0Y_0^0 - k_{-2}'Z_0 \quad (88)$$

in the case of model *B*.

C Master equation of the three-variable models

The master equation associated with the three-variable model *A* is

$$\begin{aligned}\frac{\partial P}{\partial t} &= k_1[(N_X+1)P(N_X+1) - N_XP] \\ &+ \frac{k_2'}{\Omega^2}[(N_X+2)(N_X+1)(N_Y+1)P(N_X+2,N_Y+1,N_Z-1) \\ &- N_X(N_X-1)N_YP] \\ &+ k_{-2}'[(N_Z+1)P(N_X-2,N_Y-1,N_Z+1) - N_ZP] \\ &+ k_2''[(N_Z+1)P(N_X-3,N_Z+1) - N_ZP] \\ &+ k_3[(N_Y+1)P(N_Y+1) - N_YP] + k_{-3}\Omega[P(N_Y-1) - P]\end{aligned} \quad (89)$$

The master equation for model *B* is

$$\begin{aligned}\frac{\partial P}{\partial t} &= k_1[(N_X+1)P(N_X+1) - N_XP] \\ &+ \frac{k_2'}{\Omega}[(N_X+1)(N_Y+1)P(N_X+1,N_Y+1,N_Z-1) - N_XN_YP] \\ &+ k_{-2}'[(N_Z+1)P(N_X-1,N_Y-1,N_Z+1) - N_ZP] \\ &+ \frac{k_2''}{\Omega}[(N_X-2)(N_Z+1)P(N_X-2,N_Z+1) - N_XN_ZP] \\ &+ k_3[(N_Y+1)P(N_Y+1) - N_YP] + k_{-3}\Omega[P(N_Y-1) - P]\end{aligned} \quad (90)$$

Acknowledgements

This publication is a part of the project that has received funding from the European Union's Horizon 2020 (H2020-EU.1.3.4.)

research and innovation program under the Marie Sklodowska-Curie Actions (MSCA-COFUND ID 711859) and from the Ministry of Science and Higher Education, Poland, for the implementation of an international cofinanced project.

References

1 N. G. Van Kampen, *Phys. Rep.*, 1985, **124**, 69–160.
2 L. A. Segel and M. Slemrod, *SIAM Rev.*, 1989, **31**, 446–477.
3 T. Turanyi, A. S. Tomlin and M. J. Pilling, *J. Phys. Chem.*, 1993, **97**, 163–172.
4 A. N. Gorban, *Curr. Opin. Chem. Eng.*, 2018, **21**, 48–59.
5 G. Nicolis and I. Prigogine, *Self-organization in nonequilibrium systems*, Wiley, New York, 1977.
6 A. M. Turing, *Philos. Trans. R. Soc. London, Ser. B*, 1952, **237**, 37–72.
7 M. Frankowicz, M. Moreau, P. P. Szczesny, J. Toth and L. Vicente, *J. Chem. Phys.*, 1993, **97**, 1891–1895.
8 Y. Lan, T. C. Elston and G. A. Papoian, *J. Chem. Phys.*, 2008, **129**, 214115.
9 N. A. Sinitsyn, N. Hengartner and I. Nemenman, *Proc. Natl. Acad. Sci. U. S. A.*, 2009, **106**, 10546–10551.
10 P. Thomas, R. Grima and A. V. Straube, *Phys. Rev. E: Stat., Nonlinear, Soft Matter Phys.*, 2012, **86**, 041110.
11 G. W. A. Constable, A. J. McKane and T. Rogers, *J. Phys. A: Math. Theor.*, 2013, **46**, 295002.
12 G. W. Constable and A. J. McKane, *Phys. Rev. E: Stat., Nonlinear, Soft Matter Phys.*, 2014, **89**, 032141.
13 H. Qian and E. L. Elson, *Proc. Natl. Acad. Sci. U. S. A.*, 2004, **101**, 2828–2833.
14 S. Charier, A. Meglio, D. Alcor, E. Cogné-Laage, J.-F. Allemand, L. Jullien and A. Lemarchand, *J. Am. Chem. Soc.*, 2005, **127**, 15491–15505.
15 A. Lemarchand and B. Nowakowski, *EPL*, 2011, **94**, 48004.
16 P. Dziekan, L. Signon, B. Nowakowski and A. Lemarchand, *J. Chem. Phys.*, 2013, **139**, 114107.
17 L. Signon, B. Nowakowski and A. Lemarchand, *Phys. Rev. E*, 2016, **93**, 042402.
18 G. Morgado, B. Nowakowski and A. Lemarchand, *Phys. Rev. E*, 2018, **98**, 032213.
19 D. T. Gillespie, *J. Chem. Phys.*, 2000, **113**, 297–306.
20 C. Bianca and A. Lemarchand, *J. Chem. Phys.*, 2014, **140**, 224105.
21 C. Bianca and A. Lemarchand, *J. Chem. Phys.*, 2014, **141**, 144102.
22 C. Bianca and A. Lemarchand, *Phys. A*, 2015, **438**, 1–16.
23 D. T. Gillespie, *J. Chem. Phys.*, 1977, **81**, 2340–2361.
24 J. Schnakenberg, *J. Theor. Biol.*, 1979, **81**, 389–400.
25 P. Gray and S. K. Scott, *Chem. Eng. Sci.*, 1984, **39**, 1087–1097.
26 J. D. Murray, *Mathematical Biology, I. An Introduction*, Springer, New York, 2002.
27 G. B. Cook, P. Gray, D. G. Knapp and S. K. Scott, *J. Phys. Chem.*, 1989, **93**, 2749–2755.
28 N. Fenichel, *J. Differ. Equations*, 1979, **31**, 53–98.
29 S. J. Fraser, *J. Chem. Phys.*, 1988, **88**, 4732–4738.
30 C. W. Gardiner, *Handbook of Stochastic Methods for Physics, Chemistry and the Natural Sciences*, Springer, Berlin, 1985.
31 G. E. Briggs and J. B. S. Haldane, *Biochem. J.*, 1925, **19**, 338–339.

Chapter III

Turing patterns

In 1952, Alan Turing presents one of his later most famous works [5]. He proposes a mathematical analysis of reaction-diffusion systems that may exhibit periodic spatial structures from an initially homogeneous state. The discovery of time oscillations in a chemical reaction was made in the 50s by the Russian biochemist B. Belousov, while looking for a non-organic analog to the Krebs cycle [70]. A young chemist, A. Zhabotinsky, became famous in the 60s for the work he devoted to this reaction with the observation of spatial structures and chemical wave fronts [71]. Nowadays, the tradition associates their two names to designate this complex reaction. Experimental evidence of Turing type nonequilibrium chemical patterns has been provided in 1990 by the group of De Kepper [72].

III.1 Emergence of a Turing pattern

Turing patterns (or Turing structures) only appear in out-of-equilibrium systems, therefore relying on the outside environment to maintain the pattern. Initial conditions and parameters such as the kinetic rate constants and the diffusion coefficients of the reactive species are also crucial for the existence and the shape of the pattern. The patterns appear when an inhomogeneous perturbation arises in a homogeneous stationary state. One of the simplest systems that exhibits Turing patterns is the Gray-Scott model [73], which involves two reactive species A and B in a third-order autocatalytic reaction

$$\mathrm{A} \xrightarrow{k_1} \mathrm{R_A} \tag{III.1}$$

$$2\,\mathrm{A} + \mathrm{B} \xrightarrow{k_2} 3\,\mathrm{A} \tag{III.2}$$

$$\mathrm{B} \underset{k_{-3}^*}{\overset{k_3}{\rightleftharpoons}} \mathrm{R_B} \tag{III.3}$$

where R_A and R_B are *reservoirs* of particles A and B, respectively. The associated reaction-diffusion equations are

$$\partial_t c_A = -k_1 c_A + k_2 c_A^2 c_B + D_A \partial_x^2 c_A \tag{III.4}$$

$$\partial_t c_B = -k_2 c_A^2 c_B - k_3 c_B + k_{-3} + D_B \partial_x^2 c_B \tag{III.5}$$

where $k_{-3} = k^*_{-3} c_{R_B}$ with c_{R_B} constant. The system possesses three stationary states. The steady state

$$c_A^0 = 0 \tag{III.6}$$

$$c_B^0 = \frac{k_{-3}}{k_3} \tag{III.7}$$

corresponds to the absence of A particles and is obviously stable according to the chemical scheme given in Eqs. (III.1-III.3). The two other states are derived from Eqs. (III.4) and (III.5)

$$c_A^{\pm} = \frac{k_{-3} \pm \sqrt{k_{-3}^2 - 4\dfrac{k_1^2 k_3}{k_2}}}{2k_1} \tag{III.8}$$

$$c_B^{\pm} = \frac{k_{-3} - k_1 c_A^{\pm}}{k_3} = \frac{k_{-3} \mp \sqrt{k_{-3}^2 - 4\dfrac{k_1^2 k_3}{k_2}}}{2k_3} \tag{III.9}$$

By performing a linear stability analysis, as presented in Sec. I.1.3, we show that the state (c_A^+, c_B^+) is stable towards homogeneous perturbations whereas (c_A^-, c_B^-) is unstable. Knowing that Turing patterns emerge from inhomogeneous perturbations, we consider the evolution of a local inhomogeneous perturbation $\delta\mathbf{c} = (\delta c_A, \delta c_B)$ around the state (c_A^+, c_B^+). According to Eqs.(III.4) and (III.5) and in the framework of a linear approach, the Fourier transform of the perturbation

$$\delta\tilde{\mathbf{c}} = \frac{1}{\sqrt{2\pi}} \int \mathrm{d}x \delta c \cdot e^{-iqx} \tag{III.10}$$

obeys

$$\partial_t \delta\widetilde{c_A} = -k_1 \delta\widetilde{c_A} + k_2 \left(2c_A^+ c_B^+ \delta\widetilde{c_A} + {c_A^+}^2 \delta\widetilde{c_B}\right) - q^2 D_A \delta\widetilde{c_A} \tag{III.11}$$

$$\partial_t \delta\widetilde{c_B} = -k_2 \left(2c_A^+ c_B^+ \delta\widetilde{c_A} + c_A^2 \delta\widetilde{c_B}\right) - k_3 \delta\widetilde{c_B} - q^2 D_B \delta\widetilde{c_B} \tag{III.12}$$

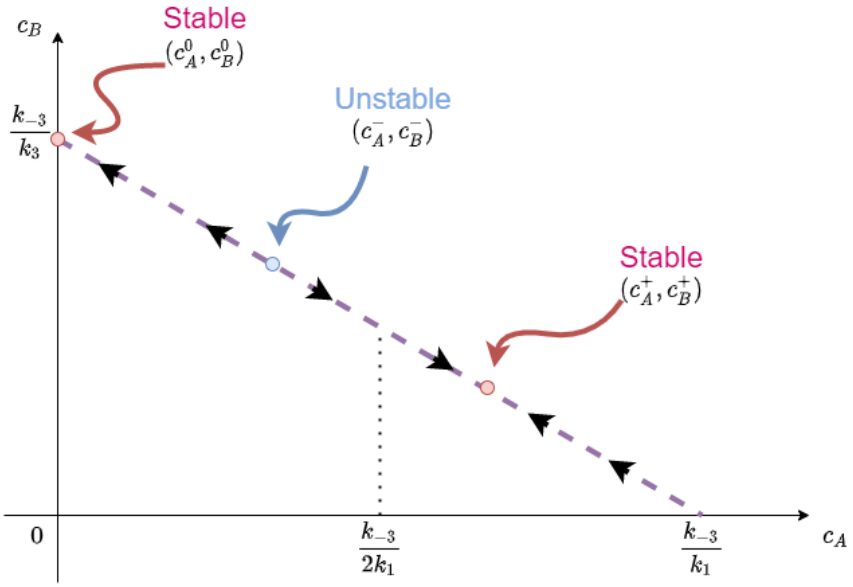

Fig. III.1 *Stationary states of the model given in Eqs. (III.1-III.3)* in the space of concentrations (c_A, c_B)

from which we obtain the stability matrix

$$\mathbf{M} = \begin{pmatrix} m_{11} - q^2 D_A & m_{21} \\ m_{12} & m_{22} - q^2 D_B \end{pmatrix} \tag{III.13}$$

where

$$m_{11} = -k_1 + 2k_2 c_A^+ c_B^+ \tag{III.14}$$
$$m_{21} = k_2 {c_A^+}^2 \tag{III.15}$$
$$m_{12} = -2k_2 c_A^+ c_B^+ \tag{III.16}$$
$$m_{22} = -k_2 {c_A^+}^2 - k_3 \tag{III.17}$$

The two eigenvalues of the stability matrix are

$$\mu_\pm = \frac{1}{2}\left[m_{11} + m_{22} - q^2(D_A + D_B) \pm \sqrt{[(m_{11} - m_{22}) - q^2(D_A - D_B)]^2 + 4m_{21}m_{12}}\right] \tag{III.18}$$

The steady state (c_A^+, c_B^+) is unstable if the real part of one eigenvalue is positive. We look for the Fourier mode $q_{\max}$ that maximizes the largest eigenvalue μ_+

$$q_{\max} = \sqrt{\frac{m_{11} - m_{22}}{D_A - D_B} - \frac{D_A + D_B}{D_A - D_B}\sqrt{\frac{-m_{12}m_{21}}{D_A D_B}}} \tag{III.19}$$

If the value $\mu_+(q_{\max})$ is positive, then the inhomogeneous perturbation grows and a Turing pattern emerges. The pattern consists of sinusoidal oscillations of A and B concentrations with the wavelength

$$\lambda = \frac{2\pi}{q_{\max}} \tag{III.20}$$

Equation (III.19) is valid for any reaction mechanism involving two chemical species susceptible to evolve into a Turing pattern. We can therefore express general conditions for the emergence of Turing patterns. First, we remark that if the two diffusion coefficients are equal, i.e. $D_A = D_B$, then Eq. (III.19) diverges and no Turing pattern can emerge. Second, the wavelength depends only on the rate constants and the diffusion coefficients, and not on the boundary conditions of the system. This makes the Turing pattern independent of the size of the system, at least at the macroscopic scale [74, 75, 76].

III.2 Termination mechanism of Turing patterns

III.2.1 Context

Models of periodic spatial patterns usually involve infinite systems or periodic boundary conditions [77, 78, 79]. However, in morphogenesis, the question of the termination of a structure arises [80, 81]. Specifically, the spine of the vertebrates ends with smaller vertebrae. In the framework of Turing patterns, this phenomenon implies both a decrease of the amplitude of the spatial oscillations and a decrease of the wavelength. Deciphering the mechanisms controlling the termination of the spine in an embryo is far beyond the scope of this work. Our aim is to propose a possible mechanism at the macroscopic scale, inspired by biological structures and compatible within a chemical engineering context. The boundary conditions chosen by the group in 2016 [36] to model the growth of the spine are well adapted to the design of an artificial spatial structure. In the model of reference [36], the Turing pattern develops behind a wave front propagating from left to right. Neumann or second-type boundary conditions are chosen at the left boundary at which the derivative of the concentration with respect to the spatial coordinate x vanishes. The emerging Turing pattern will therefore possess an extremum at the left boundary. A free boundary is imposed at the right, i.e. the system grows freely in this direction, so

that the propagation of the wave front to the right is not perturbed. The right part of the Turing pattern, located behind the front, is free and not affected by the boundaries.

III.2.2 Summary of the results

As explained in Sec. III.1, the stability of the Turing pattern is related to the eigenvalues of the stability matrix around the homogeneous steady state. A real, positive eigenvalue μ_+ corresponds to an unstable homogeneous steady state and a stable Turing structure. As μ_+ tends to 0, the amplitude of the spatial oscillations decreases. Destabilization is reached when $\mu_+ = 0$. Using Eqs. (III.18) and (III.20), I performed a systematic analysis of the effect of all rate constants and diffusion coefficients of the model given in Eqs. (III.4) and (III.5) on the eigenvalue μ_+ and the wavelength of the structure λ. Interestingly, a monotonous variation of almost any of the dynamical parameters leads to the desired behavior. In particular, either the increase or the decrease of a rate constant leads to the simultaneous loss of stability of the structure and the decrease of its wavelength. Only the variation of the diffusion coefficient D_A of the activator causes anti-correlated results, i.e. a decrease of the oscillation amplitude and an increase of the wavelength. For a given chemical system, locally varying a rate constant or the diffusion coefficient D_B of the inhibitor is not straightforward in the framework of chemical engineering. For an easy implementation, I suggest to impose an appropriate spatial profile for the concentration of the reservoir $\mathrm{R_B}$, resulting in the increase of the effective rate constant $k_{-3}R_B$ of the process given in Eq. (III.3) and the desired termination of the structure.

III.2.3 Publication

The results are published in the article "Termination mechanism of Turing patterns in growing systems", G. Morgado, L. Signon, B. Nowakowski, and A. Lemarchand, Acta Phys. Pol. B, **50**, 1369 (2019) [39].

TERMINATION MECHANISMS OF TURING PATTERNS IN GROWING SYSTEMS

Gabriel Morgado[a,b], Laurence Signon[b], Bogdan Nowakowski[c]
Annie Lemarchand[b,†]

[a]Institute of Physical Chemistry, Polish Academy of Sciences
Kasprzaka 44/52, 01-224 Warszawa, Poland
[b]Sorbonne Université, Centre National de la Recherche Scientifique (CNRS)
Laboratoire de Physique Théorique de la Matière Condensée (LPTMC)
4 place Jussieu, Case courrier 121, 75252 Paris Cedex 05, France
[c]Warsaw University of Life Sciences (SGGW), Department of Physics
Nowoursynowska 159, 02-776 Warszawa, Poland

(Received January 28, 2019; accepted April 24, 2019)

The question of the termination of a periodic spatial structure of Turing-type in a growing system is addressed in a chemical engineering perspective and a biomimetic approach. The effects of the dynamical parameters on the stability and the wavelength of the structure are analytically studied and used to propose experimental conditions for which a Turing pattern stops by itself with a decreasing wavelength. The proposed mechanism is successfully checked by the numerical integration of the equations governing the dynamics of the activator and the inhibitor. We conclude that a local increase of the concentration of the reservoir which controls the injection rate of the inhibitor into the system can be used to achieve the appropriate termination of a Turing pattern.

DOI:10.5506/APhysPolB.50.1369

1. Introduction

During embryonic development, segmented structures of the body such as the spine and the digits are formed by the production of repeated elements. Since the seminal work of Turing [1] accounting for the formation of biological pattern in the framework of reaction–diffusion models, experimental evidences of Turing structures have been given in chemistry [2–4] and biology [5, 6]. Recent years have witnessed a growing number of papers where reaction–diffusion principles are proposed to model the formation of biological periodic spatial structures [7–13]. Following Turing, a

† Corresponding author: anle@lptmc.jussieu.fr

two-component chemical system composed of an autocatalytically-produced activator by consumption of an inhibitor that diffuses faster may produce periodic spatial structures such as stripes in one-dimensional (1D) systems and hexagons in 2D. In other words, a Turing pattern emerges by local self-activation and lateral inhibition [14]. The concepts developed to model living systems provide a source of inspiration in chemical engineering [15–22]. However, standard models of Turing patterns generate structures in infinite systems and the question of the termination of a striped structure in a finite system arises in a perspective of biomimetism in material science. Specifically, it is desirable to find experimentally achievable conditions creating a finite-size structure, whose growth stops by itself with decreasing oscillation amplitude and respects the decrease of the wavelength during the termination process. To this aim, we use an as simple as possible reaction–diffusion model [23] admitting a Turing structure developing behind a propagating wave front and examine the effect of all parameters on both the stability and the wavelength of the structure [5, 22]. We already used a stochastic approach to a Turing pattern [23] and showed that, contrary to intuition, the internal fluctuations may have a constructive effect and stabilize the structure outside the domain of stability predicted by a deterministic description. Here, we adopt a macroscopic approach. Our goal is to select suitable conditions from this systematic approach and to propose termination mechanisms compatible with processing in chemical engineering.

The paper is organized as follows. In Section 2, a reaction–diffusion model involving local activation and long-range inhibition is presented. An analytical stability condition and the wavelength expression of the Turing pattern are given. The influence of the parameters of the model on the stability and the wavelength of the pattern is studied in Section 3. The analysis of the results leads to the selection of a user-friendly termination mechanism in the framework of chemical engineering. The analytical predictions regarding stability and wavelength are compared to numerical results for the chosen mechanism. Section 4 contains conclusions. The possibility that the different mechanisms exhibited could be found as termination scenarios in morphogenesis is raised.

2. Model

We consider the following reaction mechanism inspired from the Schnakenberg model [24] and the Gray–Scott model [25]:

$$\mathrm{A} \xrightarrow{k_1} \mathrm{R}_1\,, \tag{1}$$

$$2\mathrm{A} + \mathrm{B} \xrightarrow{k_2} 3\mathrm{A}\,, \tag{2}$$

$$\mathrm{B} \underset{k_{-3}}{\overset{k_3}{\rightleftharpoons}} \mathrm{R}_2\,, \tag{3}$$

where R_1 and R_2 are reservoirs. The concentrations R_1 and R_2 of the reservoirs are assumed to be constant in time. The reaction given in Eq. (2) autocatalytically produces species A and consumes species B. Due to the ability of accelerating its own production, species A is called an activator whereas species B, which is consumed by the same process, is called an inhibitor. The macroscopic dynamics of the system is governed by two partial differential equations [9, 23]

$$\frac{\partial A}{\partial t} = -k_1 A + k_2 A^2 B + D_A \frac{\partial^2 A}{\partial x^2}\,, \tag{4}$$

$$\frac{\partial B}{\partial t} = k_{-3} R_2 - k_3 B - k_2 A^2 B + D_B \frac{\partial^2 B}{\partial x^2} \tag{5}$$

for the concentrations A and B of the activator and the inhibitor supposed to have different diffusion coefficients D_A and D_B. For appropriate rate constant values, such that

$$\Delta = (k_{-3}R_2)^2 - 4k_1^2 k_3/k_2 \geq 0\,, \tag{6}$$

the system admits two steady states ($A_0 = 0, B_0 = k_{-3}R_2/k_3$) and

$$A_\mathrm{T} = \frac{k_{-3}R_2 + \sqrt{\Delta}}{2k_1}\,, \tag{7}$$

$$B_\mathrm{T} = \frac{k_{-3}R_2 - \sqrt{\Delta}}{2k_3} \tag{8}$$

that are stable with respect to homogeneous perturbations. The index T stands for Turing. A linear stability analysis of Eqs. (4) and (5) reveals that the steady state $(A_\mathrm{T}, B_\mathrm{T})$ can be destabilized by inhomogeneous perturbations [3, 5, 9, 23]. The Fourier transforms $A_q(t) = \int_{-\infty}^{\infty} A(x,t)e^{-iqx}\mathrm{d}x$ and $B_q(t) = \int_{-\infty}^{\infty} B(x,t)e^{-iqx}\mathrm{d}x$, where q is the Fourier mode, are introduced. In the Fourier space, the linear stability operator M is given by

$$M = \begin{pmatrix} k_1 - D_A q^2 & k_2 A_\mathrm{T}^2 \\ -2k_1 & -\frac{k_2 k_{-3} R_2}{k_1} A_\mathrm{T} - D_B q^2 \end{pmatrix}. \tag{9}$$

The eigenvalues of the matrix M obey the characteristic equation $\mu^2+\alpha\mu+\beta=0$, with $\alpha = k_1 - \frac{k_2 k_{-3} R_2}{k_1} A_\mathrm{T} - (D_A+D_B)q^2$ and $\beta = 2k_1^2 A_\mathrm{T}/B_\mathrm{T} - (k_1 - D_A q^2)(k_{-3}R_2/B_\mathrm{T} + D_B q^2)$. The Turing structure develops if the largest eigenvalue

$$\mu = \frac{1}{2}\left(k_1 - \frac{k_2 k_{-3} R_2}{k_1} A_\mathrm{T} - (D_A+D_B)q^2 + \sqrt{\left(k_1 + \frac{k_2 k_{-3} R_2}{k_1} A_\mathrm{T} + (D_B - D_A)q^2\right)^2 - 8k_1 k_2 A_\mathrm{T}^2}\right) \tag{10}$$

is real and positive [3, 5]. Indeed, a system of differential equations, linearized around a homogeneous steady state, is easily solved by diagonalizing the linear operator. Then, the solution is a linear combination of eigenmodes which exponentially depend on time according to the corresponding eigenvalues. A term associated with a real, positive eigenvalue grows in time, leading to trajectories in the concentration space that move away from the fixed point [5]. In the studied system, the destabilization of the steady state occurs in favor of a Turing pattern. Equation (10) imposes conditions on the parameter values. In particular, the diffusion coefficient D_B of the inhibitor B must be sufficiently larger than the diffusion coefficient D_A of the activator A: The destabilization of the homogeneous steady state $(A_\mathrm{T}, B_\mathrm{T})$ requires local self-activation, ensured by the autocatalytic production of the activator through the reaction given in Eq. (2), as well as long-range inhibition, due to the larger diffusion coefficient of the inhibitor. The mode q_max, which maximizes the eigenvalue μ, is the most unstable Fourier mode

$$q_\mathrm{max} = \sqrt{\frac{A_\mathrm{T}(D_A+D_B)\sqrt{2k_1 k_2 D_A/D_B} - k_1 - k_2 k_{-3} R_2 A_\mathrm{T}/k_1}{D_B - D_A}}\,. \tag{11}$$

In order to account for the termination of the Turing pattern in a growing system, including the fact that the structure ends with a gradually shorter spatial oscillation, we need to find conditions for which the structure tends to lose its stability while its wavelength decreases. The wavelength of the periodic structure is given by

$$\lambda = \frac{2\pi}{q_\mathrm{max}}\,. \tag{12}$$

The Turing structure becomes unstable as the value of the largest eigenvalue vanishes for the mode q_max associated with the maximum of μ

$$\mu_{\max} = \frac{1}{2}\left(k_1 - \frac{k_2 k_{-3} R_2}{k_1} A_{\mathrm{T}} - (D_A + D_B) q_{\max}^2 + \sqrt{\left(k_1 + \frac{k_2 k_{-3} R_2}{k_1} A_{\mathrm{T}} + (D_B - D_A) q_{\max}^2\right)^2 - 8 k_1 k_2 A_{\mathrm{T}}^2}\right) \quad (13)$$

with $q_{\max}$ given in Eq. (11). Figure 1 illustrates the behavior of $\mu_{\max}$ for parameter values associated with a stable Turing pattern with $\mu_{\max} > 0$. It is also shown that it is sufficient to increase the value of $k_{-3}R_2$ to shift the curve $\mu(q^2)$ down and lose the stability of the Turing pattern.

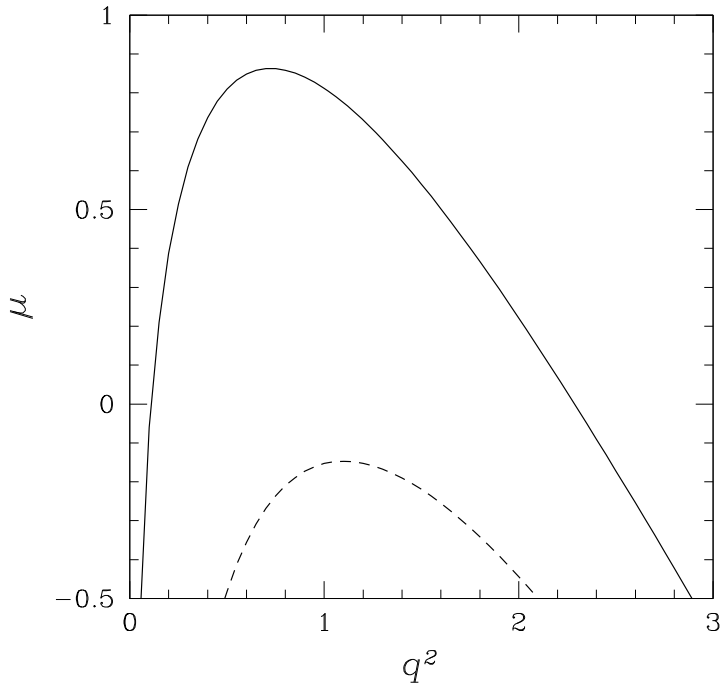

Fig. 1. The largest eigenvalue μ of the linear operator M *versus* square of Fourier mode q^2. Solid line: $k_{-3}R_2 = 8.76$. Dashed line: $k_{-3}R_2 = 10$. Other parameter values: $k_1 = 2.92$, $k_2 = 1$, $k_3 = 2.19$, $D_A = 1$, $D_B = 10$.

In the next section, we investigate the behavior of λ and $\mu_{\max}$ as each parameter controlling dynamics varies. Specifically, we aim at identifying diffusion coefficients or rate constants whose variation leads both to a decrease of the wavelength and a destabilization of the Turing structure, *i.e.* negative values for the maximum of the eigenvalue.

3. Results

The concentration R_2 of the inhibitor reservoir is first assumed to be homogeneous. Figures 2 and 3 show the variations of the wavelength λ and the maximum value $\mu_{\max}$ of the eigenvalue with one of the diffusion

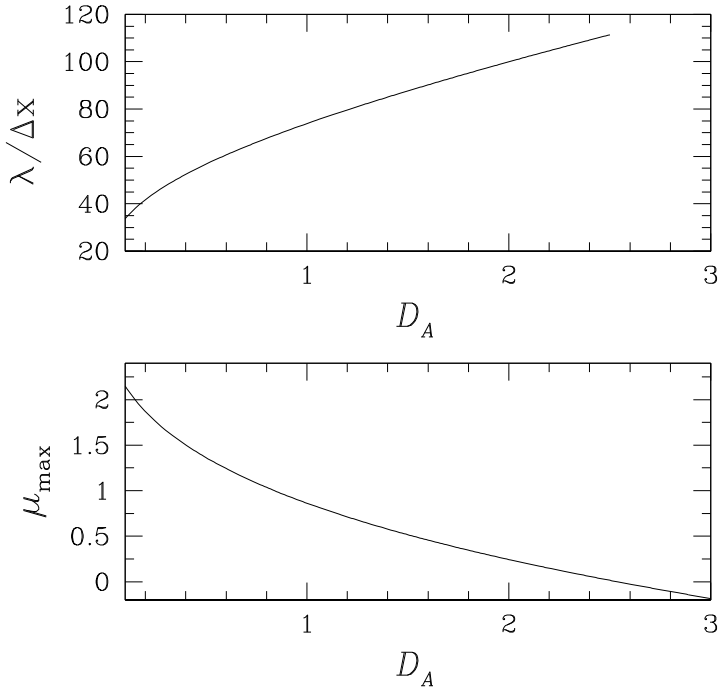

Fig. 2. Top: Scaled wavelength $\lambda/\Delta x$ of the Turing pattern *versus* diffusion coefficient D_A of species A. Bottom: Maximum value $\mu_{\max}$ of the largest eigenvalue of the linear operator M *versus* D_A. Parameter values: $k_1 = 2.92$, $k_2 = 1$, $k_3 = 2.19$, $k_{-3}R_2 = 8.76$, $D_B = 10$, $\Delta x = 0.1$.

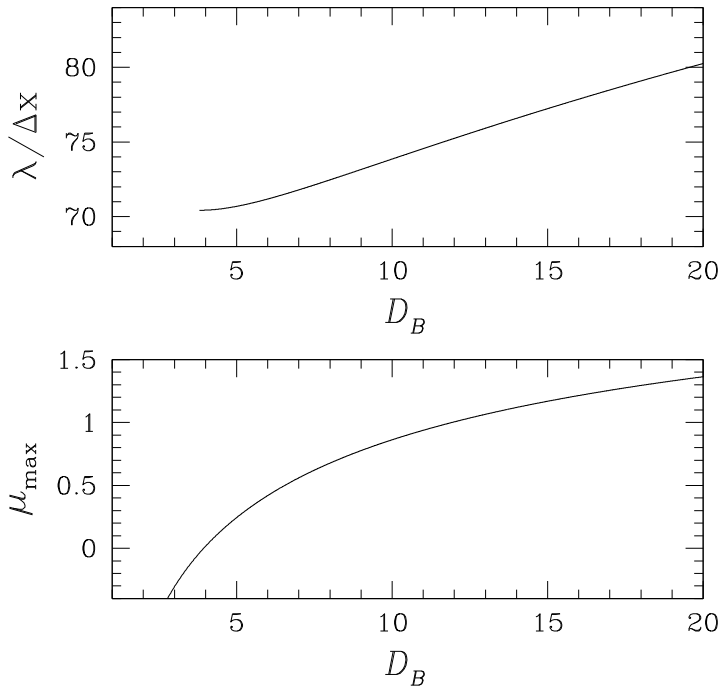

Fig. 3. Top: Scaled wavelength $\lambda/\Delta x$ of the Turing pattern *versus* diffusion coefficient D_B of species B. Bottom: Maximum value $\mu_{\max}$ of the largest eigenvalue of the linear operator M *versus* D_B. Parameter values: $k_1 = 2.92$, $k_2 = 1$, $k_3 = 2.19$, $k_{-3}R_2 = 8.76$, $D_A = 1$, $\Delta x = 0.1$.

coefficients, the other parameters being constant. The results are deduced from Eqs. (11) and (12) for λ and Eq. (13) for $\mu_{\max}$, the expressions of the steady state $(A_{\mathrm{T}}, B_{\mathrm{T}})$ being given in Eqs. (7) and (8). To facilitate the comparison with the numerical integration of Eqs. (4) and (5) that will be performed in the following, the wavelength is given in a number of spatial cells of length $\Delta x = 0.1$. As shown in Fig. 2, the decrease in the maximum value $\mu_{\max}$ of the eigenvalue as the diffusion coefficient D_A of species A increases is accompanied by an increase of the wavelength λ: The loss of stability of the Turing structure occurs with an increase of the spatial period. We conclude that a variation of the diffusion coefficient D_A cannot be argued as a justification of the termination process. The behavior with respect to the diffusion coefficient D_B of species B is different. The simultaneous loss of stability of the structure and the decrease of the wavelength are observed in Fig. 3 as D_B decreases: The diffusion coefficient D_B of species B can be considered as a suitable parameter in the search for a termination model.

Figures 4–7 show the variations of the wavelength λ and the maximum value $\mu_{\max}$ of the eigenvalue with rate constants. The variations of λ are given in a bounded interval of rate constant values, in which the Turing pattern is stable. At one of the endpoints of the interval, the eigenvalue $\mu_{\max}$ vanishes and at the other endpoint, the condition of existence of the steady

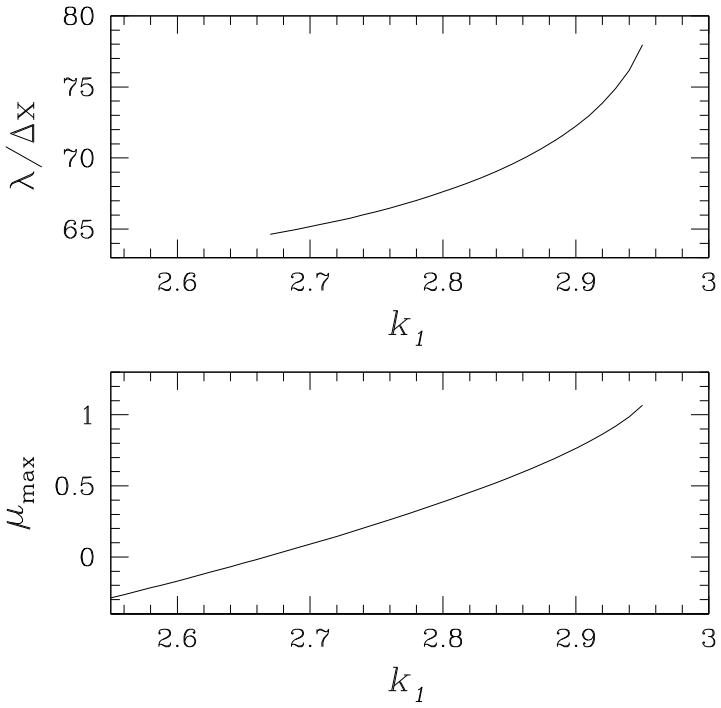

Fig. 4. Top: Scaled wavelength $\lambda/\Delta x$ of the Turing pattern *versus* rate constant k_1 of the chemical reaction given in Eq. (1). Bottom: Maximum value $\mu_{\max}$ of the largest eigenvalue of the linear operator M *versus* k_1. Parameter values: $k_2 = 1$, $k_3 = 2.19$, $k_{-3}R_2 = 8.76$, $D_A = 1$, $D_B = 10$, $\Delta x = 0.1$.

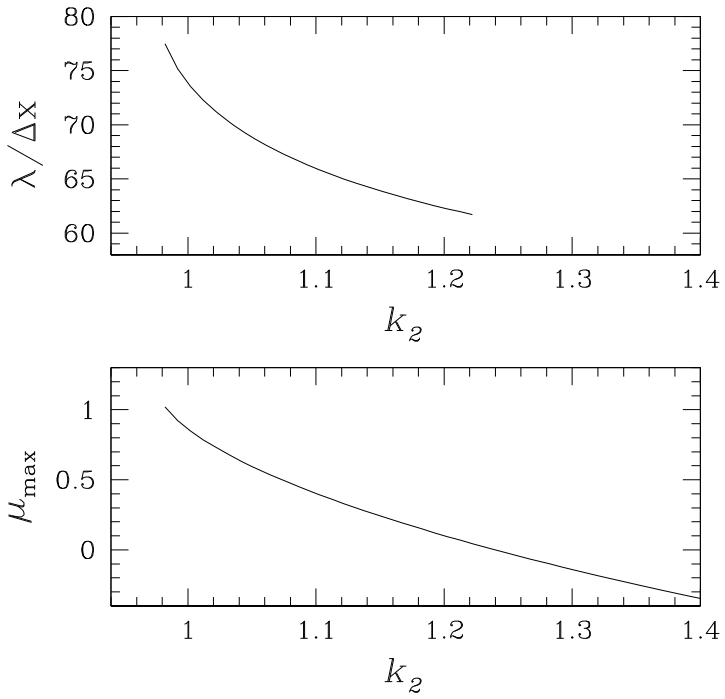

Fig. 5. Top: Scaled wavelength $\lambda/\Delta x$ of the Turing pattern *versus* rate constant k_2 of the chemical reaction given in Eq. (2). Bottom: Maximum value $\mu_{\max}$ of the largest eigenvalue of the linear operator M *versus* k_2. Parameter values: $k_1 = 2.92$, $k_3 = 2.19$, $k_{-3}R_2 = 8.76$, $D_A = 1$, $D_B = 10$, $\Delta x = 0.1$.

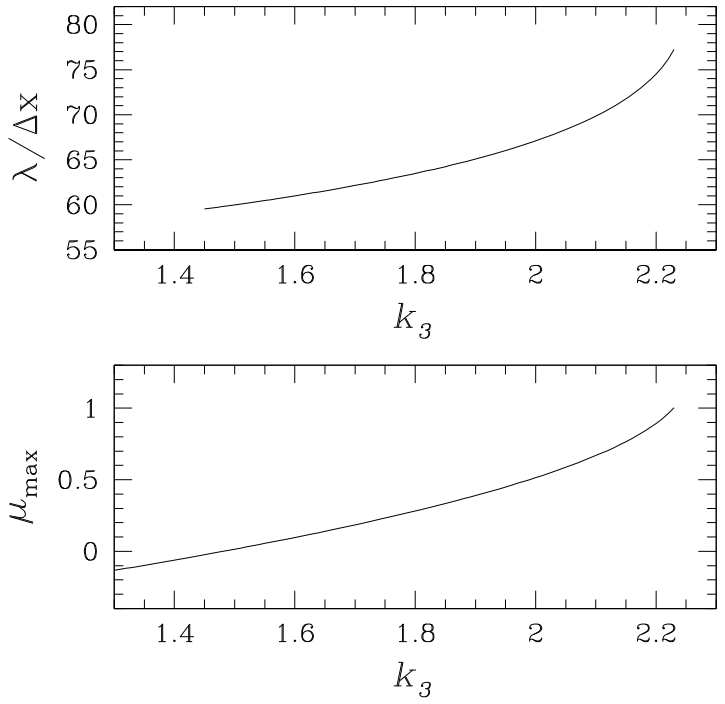

Fig. 6. Top: Scaled wavelength $\lambda/\Delta x$ of the Turing pattern *versus* rate constant k_3 of the forward chemical reaction given in Eq. (3). Bottom: Maximum value $\mu_{\max}$ of the largest eigenvalue of the linear operator M *versus* k_3. Parameter values: $k_1 = 2.92$, $k_2 = 1$, $k_{-3}R_2 = 8.76$, $D_A = 1$, $D_B = 10$, $\Delta x = 0.1$.

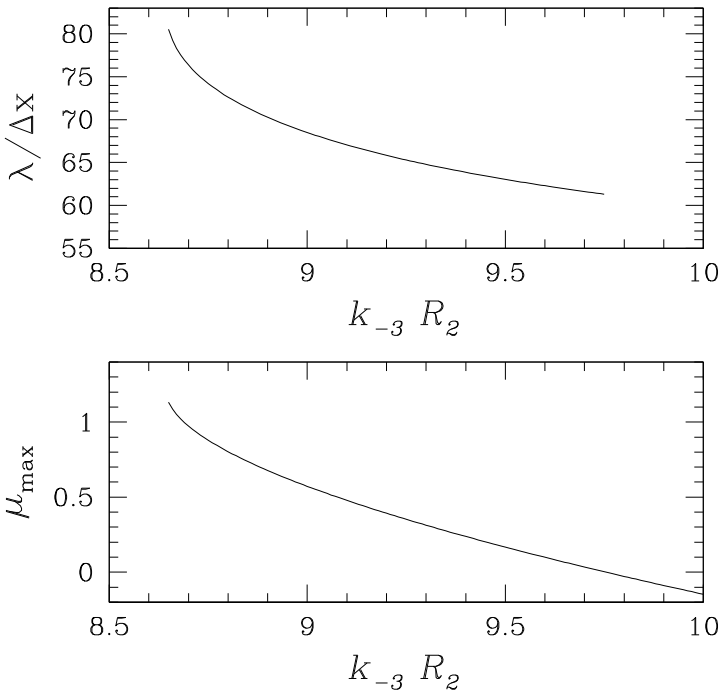

Fig. 7. Top: Scaled wavelength $\lambda/\Delta x$ of the Turing pattern *versus* rate constant $k_{-3}R_2$ of the backward chemical reaction given in Eq. (3). Bottom: Maximum value $\mu_{\max}$ of the largest eigenvalue of the linear operator M *versus* $k_{-3}R_2$. Parameter values: $k_1 = 2.92$, $k_2 = 1$, $k_3 = 2.19$, $D_A = 1$, $D_B = 10$, $\Delta x = 0.1$.

state $(A_{\mathrm{T}}, B_{\mathrm{T}})$ given in Eq. (6) is no longer satisfied. The two desired behaviors, *i.e.* the decrease of both λ and $\mu_{\max}$, are observed as k_1 decreases, k_2 increases, k_3 decreases, and $k_{-3}R_2$ increases. For an assumed homogeneous concentration R_2 of the reservoir, the variations of λ and $\mu_{\max}$ with R_2 are analogous to the variations with $k_{-3}R_2$. According to the chemical reaction given in Eq. (1), decreasing the rate constant k_1 tends to increase the concentration of species A. Following Eq. (2), increasing the rate constant k_2 of the autocatalytic step tends to increase the concentration of species A and decrease the concentration of species B. This last result seems to be inconsistent with the consequences drawn from the decrease in k_3 or the increase in $k_{-3}R_2$, which result in increasing the concentration of species B according to Eq. (3). However, we already stated that increasing B through soliciting the reservoir R_2 results in consuming species B faster by the autocatalytic step given in Eq. (2) [9, 26]. In particular, we observed that introducing a local source of species B leads to the nonintuitive local decrease of B concentration. Hence, all the variations of the rate constants that lead to a loss of stability of the Turing pattern are eventually associated with an increase of A concentration and a decrease of B concentration.

The diffusion coefficients and the rate constants characterize dynamics and are intrinsic to the reaction–diffusion system. Nevertheless, it is always possible to imagine spatial variations of the dynamical parameters. Well-chosen variations of the diffusion coefficient D_B of the inhibitor and each of the four rate constants of the chemical mechanism could be *a priori* used to build a termination model. In the framework of the application to developmental biology, steric hindrance and molecular crowding in the tail of an embryo may be invoked to justify the decrease of the diffusion coefficients. In chemical engineering, a local increase of temperature could be used to induce a local increase of the rate constants. However, a local increase of molecular crowding or temperature is susceptible to simultaneously affect several dynamical parameters [13, 22, 27–32]. Whereas a decrease of D_B is desired to destabilize the Turing pattern, while decreasing its wavelength, a simultaneous decrease of D_A would be detrimental. Similarly, an increase of k_2 and k_{-3} due to temperature increase could be satisfying but the joint decrease of k_1 and k_3 could blur the effect on the Turing structure. The simplest way to imagine the control of a targeted parameter leading to the desired behavior is to impose well-chosen spatial variations of the reservoir concentration R_2. Indeed, the product $k_{-3}R_2$ plays the role of an apparent rate constant for the backward reaction given in Eq. (3) that can be fixed at will in chemical engineering in the case of a single dynamical system with uniquely defined intrinsic parameters.

According to Fig. 7, increasing R_2 tends to destabilize the Turing pattern and decrease its wavelength. We examine if the results deduced from a stability analysis can be used in a dynamical approach. The results of the numerical integration of Eqs. (4) and (5) for a homogeneous concentration R_2 and a piecewise linear profile are given in Fig. 8. The initial condition is a step function between the steady state $(A_\mathrm{T}, B_\mathrm{T})$ in the first 10 cells on the left and the steady state (A_0, B_0) in the remaining cells. The initial total number of cells is set at $n_0 = 610$. Introducing the cell label $i = x/\Delta x$, where Δx is the cell length, and the discrete time $s = t/\Delta t$, where Δt is the time step, we choose

$$A(i, s = 0) = A_\mathrm{T}\,, \qquad B(i, s = 0) = B_\mathrm{T}\,, \qquad \text{for} \qquad 1 \le i \le 10\,, \tag{14}$$

$$A(i, s = 0) = A_0\,, \qquad B(s, s = 0) = B_0\,, \qquad \text{for} \qquad 11 \le i \le n_0\,. \tag{15}$$

To account for the growth of the system and simultaneously avoid boundary effects that may alter the wavelength of the structure [16], we impose a fixed boundary on the left and a free growing end on the right [9, 23, 26]. For parameter values for which the steady state $(A_\mathrm{T}, B_\mathrm{T})$ is unstable with respect to inhomogeneous perturbations, a Turing pattern develops after the passage of a chemical wave front. More precisely, according to Eqs. (4) and (5) and

due to the no-flux boundary conditions applied on the left boundary, the concentrations in the first cell obey

$$\begin{aligned} A(1,s+1) &= A(1,s) - k_1\Delta t A(1,s) + k_2\Delta t A(1,s)^2 B(1,s) \\ &\quad + D_A \frac{\Delta t}{(\Delta x)^2}(A(2,s) - A(1,s))\,, \end{aligned} \tag{16}$$

$$\begin{aligned} B(1,s+1) &= B(1,s) + k_{-3}R_2\Delta t - k_3\Delta t B(1,s) - k_2\Delta t A(1,s)^2 B(1,s) \\ &\quad + D_B \frac{\Delta t}{(\Delta x)^2}(B(2,s) - B(1,s)) \end{aligned} \tag{17}$$

so that both $A(1,s)$ and $B(1,s)$ are extremum of the Turing pattern in the first spatial cell $i = 1$.

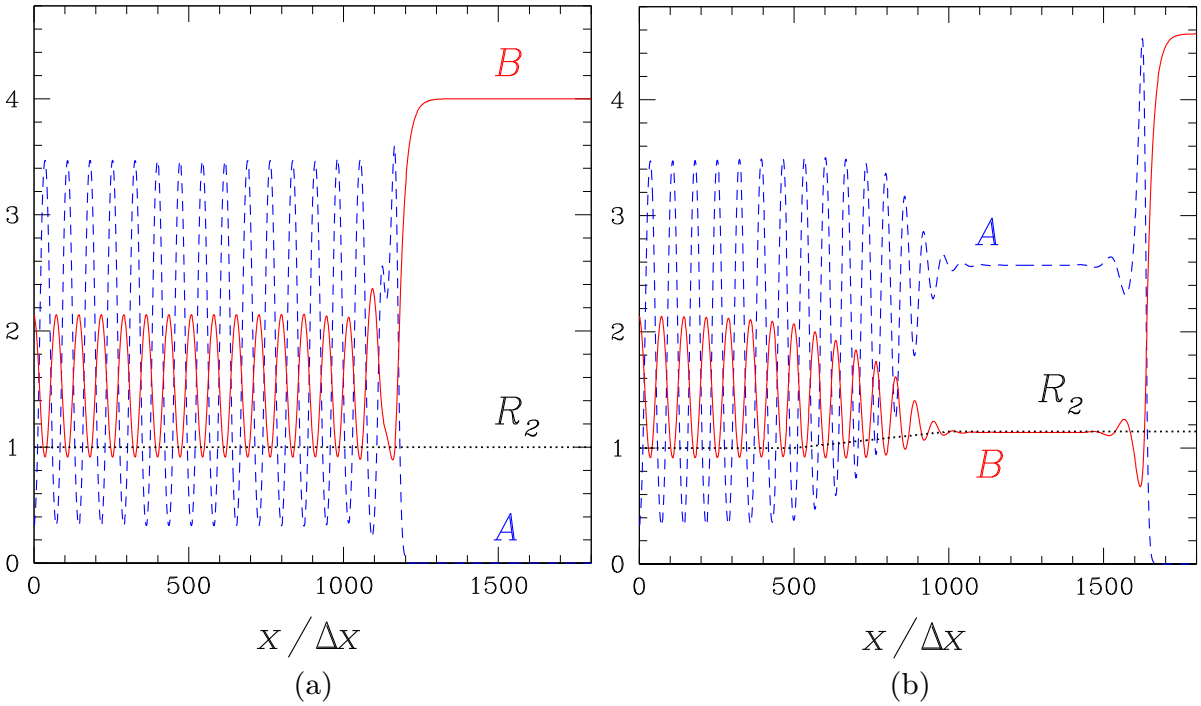

Fig. 8. Spatial profiles deduced from the numerical integration of Eqs. (4) and (5) for $k_1 = 2.92$, $k_2 = 1$, $k_3 = 2.19$, $k_{-3} = 8.76$, $D_A = 1$, $D_B = 10$, $\Delta t = 10^{-4}$, $t_{\text{end}}/\Delta t = 2000000$, $\Delta x = 0.1$. Black dotted line: Imposed concentration R_2 of the reservoir. (a) Homogeneous concentration $R_2 = 1$, (b) Piecewise linear R_2 profile. Gray/blue dashed line: Concentration of species A *versus* cell label $x/\Delta x$. Black/red solid line: Concentration of species B *versus* cell label $x/\Delta x$.

Spatial cells are added to the right end of the system at the front speed to counterbalance the progression of the wave front and mimic system growth: At all the discrete times s for which the concentration $B(n-600,s)$ of species B in the $n-600$ cell becomes smaller than $0.99B_0$, the total number n of cells is increased by 1. Provided that the front propagates at a speed smaller than $\Delta x/\Delta t$, this protocol ensures that a layer of about 600 cells

remains in the stationary state (A_0, B_0) on the right of the system, so that the propagation of the front is not significantly affected by the finite size of the system. To draw Fig. 8 (b), we have chosen the parameter values given in the caption of Fig. 1 and imposed $k_{-3} = 8.76$ for the following spatial profile for the concentration R_2 of the inhibitor reservoir:

$$R_2 = 1\,, \qquad \text{for} \quad 1 \leq i < 500\,, \tag{18}$$

$$R_2 = 2.83 \times 10^{-4} i + 0.858\,, \qquad \text{for} \quad 500 \leq i < 1000\,, \tag{19}$$

$$R_2 = 1.14\,, \qquad \text{for} \quad 1000 \leq i\,. \tag{20}$$

The simulation is stopped at time t_{end} for which the wave front has passed cell $i = 1000$. It is worth noting that the Turing pattern is unchanged for larger values of the final integration time. Then, only the position of the concentration gradients associated with the traveling wave evolve in time but the Turing structure has stopped growing and remains in a steady state with a fixed number of wavelengths. As desired, the increase of the concentration R_2 leads to the termination of the Turing structure.

As illustrated in Fig. 7, the Turing structure is expected to be stable in the range of $1 \leq i < 500$ for which $k_{-3}R_2 = 8.76$ and unstable in the range of $i \geq 1000$ for which $k_{-3}R_2 = 10$. More precisely, according to Eq. (13), the maximum of the eigenvalue $\mu_{\max}$ vanishes for $k_{-3}R_2 = 9.75$, *i.e.* $R_2 = 1.11$ for $k_{-3} = 8.76$, which occurs in spatial cell $i = 900$. Hence, the Turing pattern is predicted to be stable in the range of $0 \leq i < 900$ and unstable beyond this domain. The results shown in Fig. 8 (b) confirm the analytical predictions. The amplitude of the spatial oscillations decreases between $i \simeq 500$ and $i \simeq 1000$. The system is in a steady state in the range of $1000 \leq i < 1500$.

The increase of R_2 not only destabilizes the Turing structure but also modifies the steady state values and the propagation speed of the wave front. The comparison between Figs. 8 (a) and 8 (b) shows that, as R_2 increases, the wave front propagates faster, A_{T} increases, B_{T} decreases and B_0 increases. As a consequence of the variation of A_{T} and B_{T}, the oscillations of A and B concentrations are not symmetrical in the range of $500 \leq i < 900$. The decrease of the wavelength predicted in Fig. 7 is more difficult to check by a qualitative analysis. Using the numerical results illustrated in Fig. 8 (b), we evaluate the local wavelength by computing the number of cells between two minima of the A concentration profile. The results are given in Fig. 9 and compared to the analytical prediction deduced from Eqs. (11) and (12). The agreement between the numerical and analytical results is very satisfying in the range of $600 \leq i < 900$. Oscillations of very small amplitude are observed in Fig. 8 (b) in the range of $900 \leq i < 1000$, proving that a very damped Turing structure remains in a small area where instability was

predicted. The wavelength of the structure in the range of $1 \leq i < 500$ is slightly affected by the increase of R_2 from cell $i = 500$ but the deviation from the analytical prediction is only 2.5 percent. This small difference is related to the linear approximation used in wavelength evaluation that neglects non-linear terms that may be more important for large structures. Interestingly, the wavelength is sensitively decreased in the expected area in which the concentration of the reservoir R_2 increases: As shown in Fig. 9, the wavelength is reduced from 72 spatial cells to less than 61, before the structure disappears. We conclude that an increase in the concentration of the reservoir R_2 related to the inhibitor B is sufficient to account for the destabilization of the Turing pattern associated with a decrease of the wavelength. As anticipated by the results given in Fig. 7, according to which an increase of R_2 decreases the wavelength λ and leads to a negative eigenvalue $\mu_{\max}$ around (A_T, B_T), we suggest that an appropriate spatial variation of R_2 can be used in chemical engineering to stabilize the homogeneous steady state and induce a termination of the Turing pattern in a growing system.

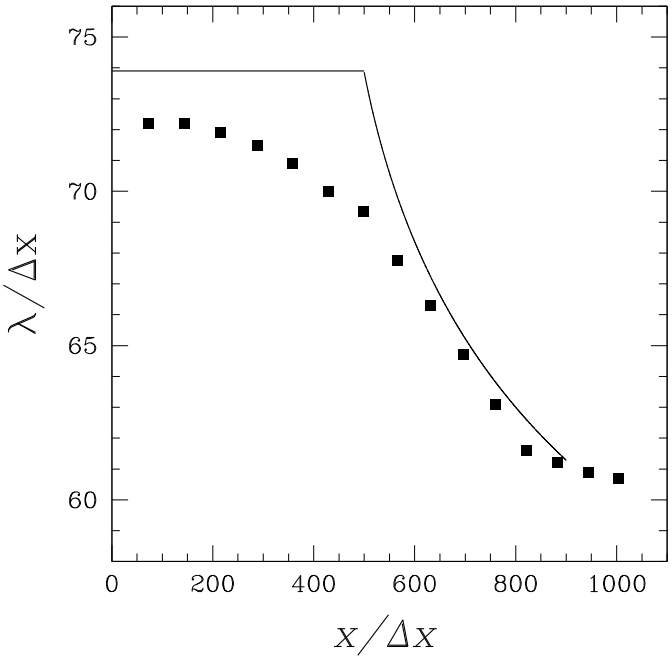

Fig. 9. Spatial variation of the scaled wavelength $\lambda/\Delta x$ of the Turing pattern *versus* cell label $x/\Delta x$ for the parameter values given in the caption of Fig. 8 (b). Symbols: Results deduced from the numerical integration of Eqs. (4) and (5). Solid line: Analytical prediction given in Eq. (12).

4. Conclusion

In a biomimetic approach, we have addressed the question of the termination of a Turing structure in a growing system. A free boundary is imposed at the growing part, which ensures that the wavelength of the pat-

tern is not perturbed by fixed boundary conditions. After deriving analytical expressions for the stability condition and the wavelength of the structure, we perform a systematic analysis of the effect of all dynamical parameters on the pattern. Apart from the variation of the diffusion coefficient of the activator, a well-chosen variation of the dynamical parameters leads to the desired behavior, *i.e.* the simultaneous loss of stability and the decrease of the wavelength. In particular, an increase of the effective rate constant $k_{-3}R_2$, where k_{-3} is the rate constant of the reaction injecting the inhibitor from the reservoir at the concentration R_2, is associated with a destabilization of the Turing pattern accompanied by a decrease of the wavelength.

Imposing a spatial variation of the concentration of the reservoir R_2 turns out to be an appropriate protocol for chemical engineering. However, the proposed procedure imposes the total length of the structure but not its number of wavelengths. In the framework of developmental biology, for example in the case of the growth of the digits or the spine of the vertebrates, the termination process has to respect the total number of segments for a possible variation in the length of the global structure. Therefore, it is necessary to imagine that the system itself is able to count the number of already formed segments and to trigger the variation of a parameter leading to smaller subsequently formed segments. If the concept of the Turing structure is kept in the formation of biological patterns, the presented results could be used to suggest such relevant parameters. The local increase of the rate constant k_{-3} that would be activated when a given number of segments has already been formed can be straightforwardly proposed. Similarly, the local increase of the rate constant k_2 controlling the autocatalytic production of the activator or the local decrease of the rate constant k_1 or k_3, associated with the absorption of the activator or the inhibitor by reservoirs, would lead to the desired phenomenon. The local decrease of the diffusion coefficient of the inhibitor offers an alternative. The nature of the mechanism that would trigger such a response of the system when a given number of segments has been created remains an open question.

This publication is part of a project that has received funding from the European Union's Horizon 2020 research and innovation programme under the Marie Skłodowska-Curie grant agreement No. 711859 and has benefited from financial resources for science awarded by the Polish Ministry of Science and Higher Education in the years 2017–2021 for the implementation of an international cofinanced project.

REFERENCES

[1] A.M. Turing, *Philos. Trans. R. Soc. London B* **237**, 37 (1952).
[2] B. Rudovics *et al.*, *J. Phys. Chem. A* **103**, 1790 (1999).
[3] F. Sagués, I.R. Epstein, *Dalton Trans.* **2003**, 1201 (2003).
[4] N. Tompkins *et al.*, *Proc. Natl. Acad. Sci. USA* **111**, 4397 (2014).
[5] J.D. Murray, *Mathematical Biology*, Springer, Berlin 1989.
[6] J. Raspopovic, L. Marcon, L. Russo, J. Sharpe, *Science* **345**, 566 (2014).
[7] P.K. Maini *et al.*, *Interface Focus* **2**, 487 (2012).
[8] L. Marcon, J. Sharpe, *Curr. Opin. Genet. Dev.* **22**, 578 (2012).
[9] P. Dziekan, L. Signon, B. Nowakowski, A. Lemarchand, *J. Chem. Phys.* **139**, 114107 (2013).
[10] A.D. Economou, J.B.A. Green, *Semin. Cell Dev. Biol.* **35**, 58 (2014).
[11] J.B.A. Green, J. Sharpe, *Development* **142**, 1203 (2015).
[12] L. Diambra, V. Raj Senthivel, D. Barcena Menendez, M. Isalan, *ACS Synth. Biol.* **4**, 177 (2015).
[13] L. Signon, B. Nowakowski, A. Lemarchand, *Phys. Rev. E* **93**, 042402 (2016).
[14] H. Meinhardt, A. Gierer, *Bioessays* **22**, 753 (2000).
[15] B.A. Grzybowski, *Chemistry in Motion: Reaction-diffusion Systems for Micro- and Nanotechnology*, Wiley, Chichester 2009.
[16] P. Dziekan, A. Lemarchand, B. Nowakowski, *J. Chem. Phys.* **137**, 074107 (2012).
[17] A.S. Mikhailov, G. Ertl, *Design and Control of Self-organizing Chemical Systems*, in: *Chemical Complexity*, Springer, Cham 2017.
[18] G. Ashkenasy, T.M. Hermans, S. Otto, A.F. Taylor, *Chem. Soc. Rev.* **46**, 2543 (2017).
[19] E. Nakouzi, O. Steinbock, *Sci. Adv.* **2**, e1601144 (2016).
[20] F.C. Simmel, R. Schulman, *MRS Bull.* **42**, 913 (2017).
[21] A. Zadorin *et al.*, *Nat. Chem.* **9**, 990 (2017).
[22] G. Morgado, B. Nowakowski, A. Lemarchand, *Phys. Rev. E* **98**, 032213 (2018).
[23] A. Lemarchand, B. Nowakowski, *Eur. Phys. Lett.* **94**, 48004 (2011).
[24] J. Schnakenberg, *J. Theor. Biol.* **81**, 389 (1979).
[25] P. Gray, S.K. Scott, *Chem. Eng. Sci.* **39**, 1087 (1984).
[26] P. Dziekan, L. Signon, B. Nowakowski, A. Lemarchand, *Commun. Theor. Phys.* **62**, 622 (2014).
[27] A.P. Minton, *J. Biol. Chem.* **276**, 10577 (2001).
[28] R.J. Ellis, A.P. Minton, *Nature* **425**, 27 (2003).
[29] J. Sun, H. Weinstein, *J. Chem. Phys.* **127**, 155105 (2007).
[30] Z.-R. Xie, J. Chen, Y. Wu, *J. Chem. Phys.* **140**, 054112 (2014).
[31] P.M. Kekenes-Huskey, C. Eun, J.A. McCammon, *J. Chem. Phys.* **143**, 094103 (2015).
[32] P. Nałęcz-Jawecki *et al.*, *J. Chem. Phys.* **143**, 215102 (2015).

III.3 Scaling of Turing patterns

III.3.1 Summary of the results

The lack of adaptability to the global size of the system is topical [82, 83, 84, 85, 86, 87, 88] and one of the main objections against Turing-based models in morphogenesis. Specifically, in somitogenesis, it is expected that vertebra size adapts to the size of the embryo. Just before my arrival in the group, B. Nowakowski and A. Lemarchand introduced a model, inspired by the Schnakenberg model [89] and the Gray-Scott model [73] capable of addressing this issue at the macroscopic scale [36]. They proposed to address the problem in the context of molecular crowding, known to lead to non-negligible effects on the chemical mechanism [90, 91, 92, 93, 94, 95]. They considered a concentrated system in which the variations of the concentration of the solvent cannot be neglected and admitted that the reaction scheme presented in Eqs. (III.1-III.3) is modified as follows

$$\mathrm{A} + \mathrm{S} \xrightarrow{k_1} \mathrm{R_A} \tag{III.21}$$

$$2\,\mathrm{A} + \mathrm{B} \xrightarrow{k_2} 3\,\mathrm{A} \tag{III.22}$$

$$\mathrm{B} + \mathrm{S} \underset{k_{-3}}{\overset{k_3}{\rightleftharpoons}} \mathrm{R_B} \tag{III.23}$$

They solved the partial differential equations governing the evolution of the concentrations and proved that the wavelength of the Turing pattern can be controlled by the deviation from the high-dilution limit, roughly defined as the ratio $(c_A + c_B)/c_S$ of the solute concentration and the solvent concentration.

The deviation from the high-dilution limit is more prevalent in smaller systems such as biological cells. The challenge I faced was to adapt the model to simulations of particle dynamics based on the direct simulation Monte Carlo method presented in Sec. I.4.2. Even if the number of particles in the system varies, one of the constraints of the simulations is to keep the total number of simulated particles constant, in order to check the absence of bias in the total momentum and kinetic energy. It may imply the creation of ghost particles that slow down the simulation. The scheme given in Eqs. (III.21-III.23) does not conserve the number of particles and involves reservoir particles that are also time consuming.

I proposed to solve the problem using the following scheme

$$\begin{aligned} \mathrm{A} + \mathrm{S} &\xrightarrow{k_1} 2\,\mathrm{S} \\ 2\,\mathrm{A} + \mathrm{B} &\xrightarrow{k_2} 3\,\mathrm{A} \\ \mathrm{B} + \mathrm{S} &\xrightarrow{k_3} 2\,\mathrm{S} \end{aligned} \tag{III.24}$$

$$\begin{cases} \mathrm{R_B} \xrightarrow{k_{-3}} \mathrm{B} \\ \mathrm{S} \longrightarrow \mathrm{R_S} \end{cases} \tag{III.25}$$

in which the solvent particles play the role of particles of the reservoirs $\mathrm{R_B}$ and $\mathrm{R_S}$. In other words, when the process given in Eq. (III.25) occurs in a given spatial box, the particle B is created with the velocity and the position of a randomly chosen particle S of the same box. At the same time, the particle S disappears exactly at the same constant rate k_{-3} as the particle B is created. The step cannot be written $\mathrm{S} \xrightarrow{k_{-3}} \mathrm{B}$, because it would introduce a term $k_{-3}S$ in the rate equation of B instead of the constant term k_{-3}. I performed DSMC simulations of a reactive ternary mixture of A, B, and S particles with different diameters in order to reproduce different diffusion coefficients as presented in Sec. I.4.2. My results show that the wavelength of Turing patterns can be tuned at the submicrometric scale by controlling the total concentration, i.e. the deviation from the high-dilution limit. More precisely, doubling the concentration of the solute decreases the wavelength of the structure by a factor of 2. The results can be considered as a possible interpretation for proportion preservation of embryos in morphogenesis. We suggest that they could be used to design biomimetic materials with controlled submicrometric properties in chemical engineering.

III.3.2 Publication

The results are published in the article “Scaling of submicrometric Turing patterns in concentrated growing systems”, G. Morgado, B. Nowakowski, and A. Lemarchand, Phys. Rev. E, **98**, 032213 (2018) [37].

Scaling of submicrometric Turing patterns in concentrated growing systems

Gabriel Morgado,[1,2] Bogdan Nowakowski,[1] and Annie Lemarchand[2,*]

[1]*Institute of Physical Chemistry, Polish Academy of Sciences, Kasprzaka 44/52, 01-224 Warsaw, Poland*

[2]*Sorbonne Université, Centre National de la Recherche Scientifique (CNRS), Laboratoire de Physique Théorique de la Matière Condensée (LPTMC), 4 place Jussieu, case courrier 121, 75252 Paris CEDEX 05, France*

(Received 4 July 2018; published 18 September 2018)

The wavelength of a periodic spatial structure of Turing type is an intrinsic property of the considered reaction-diffusion dynamics and we address the question of its control at the microscopic scale for given dynamical parameters. The direct simulation Monte Carlo method, initially introduced to simulate particle dynamics in rarefied gases, is adapted to the simulation of concentrated solutions. We perform simulations of a submicrometric Turing pattern with appropriate boundary conditions and show that taking into account the role of the solvent in the chemical mechanism allows us to control the wavelength of the structure. Typically, doubling the concentration of the solute leads to decreasing the wavelength by two. The results could be used to design materials with controlled submicrometric properties in chemical engineering. They could also be considered as a possible interpretation of proportion preservation of embryos in morphogenesis.

DOI: 10.1103/PhysRevE.98.032213

I. INTRODUCTION

The rational design of complex materials with predefined properties by controlling self-organization in far-from-equilibrium conditions is the promise of mesoscale chemical engineering [1–3]. Biological structures provide fascinating examples of organization, and the concepts introduced to model them offer a good guide in an engineering context [4]. In particular, the ability to control the association and denaturation kinetics of nucleic acids has been successfully harnessed to link biological organization and material design [5–8]. The model introduced by Turing [9] to account for periodic spatial structures in living organisms offers another example of mechanism inspired by biology that deserves to be reexamined with the goal of creating functional materials by biomimicry [10–12]. Turing proposed to model morphogenesis in the framework of far-from-equilibrium reaction-diffusion systems. Remarkably, Turing introduced a small number of processes based on a microscopic interpretation. A so-called activator is produced by an autocatalytic reaction while an inhibitor, associated with a larger diffusion coefficient, is consumed. An inhomogeneous perturbation is capable of destabilizing the homogeneous steady state in favor of a periodic spatial structure, whose wavelength is determined by the rate constants and the diffusion coefficients. There has been a recent revival of Turing's idea [2,4,10,13–16], and experimental evidence of Turing mechanism during embryogenesis has been provided [17–19]. However, the lack of scaling properties and versatility of Turing patterns is the main objection in biology as well as chemical engineering. For example, a model of somitogenesis should reflect the adaptation of vertebra size to embryo size, at constant number of vertebrae. More generally, in a homothetic structure, the wavelength of the pattern should adapt to the overall size of the embryo. Similarly, the chemical engineer expects to adjust the wavelength of the spatial structure by monitoring an easily controlled parameter while considering the same chemical species.

The problem of wavelength scaling in a Turing pattern has been addressed for many years [20–23] and remains topical [16,24–29]. Various scaling mechanisms have been proposed, mainly on a macroscopic scale. Partial differential equations with concentration-dependent diffusion terms [23,27,28] or involving an additional chemical species whose concentration is supposed to depend on system size [20,21,24–26,29,30] have been considered. Nevertheless, the control of a periodic spatial structure at a submicrometric scale in chemical engineering requires the design of a mechanism based on elementary processes, compatible with the simulation of particle dynamics. We recently proposed to place the problem of wavelength adaptation [31] in the context of molecular crowding [32–37]. Frequently, solvent involvement in the chemical mechanism cannot be ignored in a concentrated solution [38]. We proposed a mechanism relying on microscopic processes in which the solvent is considered as a reagent in itself. In particular, the model does not introduce any ad hoc spatially dependent variable. We studied the effect of the deviation from a dilute solution on the wavelength of a Turing pattern using partial differential equations. The perturbation of diffusion induced by crowding has been shown to have little effect on the wavelength of the structure [31].

In this paper, we address the question of wavelength adaptation in a submicroscopic Turing pattern in the framework of chemical engineering. It implies designing an algorithm of particle dynamics simulations in a concentrated system. Turing model requires that the activator and the inhibitor have sufficiently different diffusion coefficients. To this goal, we adapt the procedure developed in a dilute system with three species of different diameters [11]. The results obtained in

*anle@lptmc.jussieu.fr

the high dilution limit reveals that, in a small system, the wavelength may be influenced by the boundary conditions. In particular, particle dynamics simulations of a given system with zero-flux boundary conditions and a length slightly smaller than two wavelengths lead to the selection of either one-and-a-half-wavelength or two-wavelength Turing pattern [11]. To avoid this kind of boundary effect, we take advantage of the specific conditions chosen to model the formation of the spine in a vertebrate embryo in a macroscopic description [39–41]. To reproduce the growth and spatial organization of the embryo, we started from a step function between two steady states and generated a propagating wavefront in a growing system. Turing pattern was developing between a fixed boundary condition at the rostral end and a moving front, which does not impose constraints on the wavelength of the structure. Hence, modeling of somitogenesis suggested appropriate boundary conditions for a problem of chemical engineering.

The paper is organized as follows. In Sec. II, we present a reaction-diffusion model with an explicit effect of the solvent that fades in the high dilution limit. The particle dynamics simulation method is presented in Sec. III. The results are given in Sec. IV. Section V is devoted to conclusion.

II. MODEL

We consider a reaction scheme inspired by the Schnakenberg [42] and the Gray-Scott model [43]

$$A + S \xrightarrow{k_1^S} 2S, \tag{1}$$

$$2A + B \xrightarrow{k_2} 3A, \tag{2}$$

$$B + S \xrightarrow{k_3^S} 2S, \tag{3}$$

$$\begin{cases} R \xrightarrow{k_{-3}} B \\ S \to R, \end{cases} \tag{4}$$

in which the role of the solvent S has been made explicit in Eqs. (1) and (3) and where k_1^S, k_2, k_3^S, and k_{-3} are rate constants. The model involves two chemical species, the activator A and the inhibitor B, playing the role of two morphogens in somitogenesis. The reaction given in Eq. (2) consumes the inhibitor and autocatalytically produces the activator. The system is in contact with a reservoir R of species B, which maintains the system far from equilibrium. The reaction given in Eq. (4) consists of two steps, an injection of species B at constant rate k_{-3} and the simultaneous removal of the solvent S. The autocatalytic role played by the solvent in the two steps given in Eqs. (1) and (3) is not necessary to obtain the desired adaptability for the Turing pattern. In the framework of a macroscopic approach [31], we proved that these steps can be replaced by the simpler reactions $A + S \to R_1$ and $B + S \to R_2$, where R_1 and R_2 are reservoirs. This result gives some hints to find achievable experimental validation conditions. In the present simulation approach, autocatalysis for S is introduced for the sake of simplicity: In the simulations, the solvent S plays the double role of reagent and reservoir, which avoids introducing a fourth species. Moreover, all the reactions of the simulation model preserve the number of particles and simply consist of changes of chemical nature, which ensures total mass conservation for particles of same mass. The total concentration,

$$C = A(x,t) + B(x,t) + S(x,t), \tag{5}$$

where $A(x,t)$, $B(x,t)$, and $S(x,t)$ are the concentrations of species A, B, and S, respectively, is constant. In the following, the spatial and temporal dependence of the concentrations is implicit. In the framework of a macroscopic approach, the system obeys the following reaction-diffusion equations:

$$\frac{\partial A}{\partial t} = -k_1 A\left[1 - \frac{A+B}{C}\right] + k_2 A^2 B + D_A \frac{\partial^2 A}{\partial x^2}, \tag{6}$$

$$\frac{\partial B}{\partial t} = k_{-3} - k_3 B\left[1 - \frac{A+B}{C}\right] - k_2 A^2 B + D_B \frac{\partial^2 B}{\partial x^2}, \tag{7}$$

where Eq. (5) has been used to eliminate S and where the effective rate constants $k_1 = k_1^S C$ and $k_3 = k_3^S C$ have been introduced. The parameters D_A and D_B are the diffusion coefficients associated with species A and B, respectively. In the limit of a large amount of solvent S,

$$\frac{A+B}{C} \ll 1, \tag{8}$$

Eqs. (6) and (7) become

$$\frac{\partial A}{\partial t} = -k_1 A + k_2 A^2 B + D_A \frac{\partial^2 A}{\partial x^2}, \tag{9}$$

$$\frac{\partial B}{\partial t} = k_{-3} - k_3 B - k_2 A^2 B + D_B \frac{\partial^2 B}{\partial x^2}. \tag{10}$$

These reaction-diffusion equations can be associated with the chemical scheme that provides the benchmark in the high dilution limit:

$$A \xrightarrow{k_1} R_1, \tag{11}$$

$$2A + B \xrightarrow{k_2} 3A, \tag{12}$$

$$B \underset{k'_{-3}}{\overset{k_3}{\rightleftharpoons}} R_2, \tag{13}$$

where R_1 and R_2 are reservoirs and $k'_{-3} = \frac{k_{-3}}{R_2}$.

For appropriate parameter values, Eqs (6) and (7) admit a stable homogeneous steady state,

$$A^0 = 0, \tag{14}$$

$$B^0 = \frac{C}{2}\left(1 - \sqrt{1 - 4\frac{k_{-3}}{k_3 C}}\right), \tag{15}$$

and a steady state (A^T, B^T) given in the Appendix, evolving into a Turing pattern in the presence of inhomogeneous perturbations. The two steady states depend on the total concentration C and the rate constant ratios k_1/k_2, k_3/k_2, and k_{-3}/k_2.

Our aim is to characterize the impact of the deviation from the dilution limit,

$$\delta \equiv \frac{A^0 + B^0}{C} = \frac{1}{2}\left(1 - \sqrt{1 - 4\frac{k_{-3}}{k_3 C}}\right), \tag{16}$$

on the wavelength of the pattern. In a concentrated system, δ does not vanish and the system is described by the reactions given in Eqs. (1)–(4). In the high dilution limit, δ vanishes and the mechanism is given by Eqs. (11)–(13).

We perform a linear stability analysis of Eqs. (6) and (7) around the state (A^T, B^T). To this goal, the Fourier transforms $A_q(t) = \int_{-\infty}^{\infty} A(x,t)e^{-iqx}dx$ and $B_q(t) = \int_{-\infty}^{\infty} B(x,t)e^{-iqx}dx$ are introduced, where q is the Fourier mode. In the Fourier space, the linear stability operator M is given by

$$M = \begin{pmatrix} k_2\alpha - D_A q^2 & k_2 M_{12} \\ k_2 M_{21} & k_2\beta - d D_A q^2 \end{pmatrix}, \tag{17}$$

with

$$d = D_B/D_A, \tag{18}$$

$$\alpha = \frac{k_1}{k_2}\left(1 - \frac{B^T}{C}\right), \tag{19}$$

$$\beta = -\frac{k_{-3}}{k_2 B^T} + \frac{k_3 B^T}{k_2 C}, \tag{20}$$

$$M_{12} = \frac{k_1 A^T}{k_2 C} + A^{T2}, \tag{21}$$

$$M_{21} = \frac{k_3 B^T}{k_2 C} - 2\frac{k_1}{k_2}\left(1 - \frac{A^T + B^T}{C}\right), \tag{22}$$

where the steady states (A^0, B^0) and (A^T, B^T) are given in Eqs. (14) and (15) and Eqs. (A24) and (A25) of the Appendix, respectively. For appropriately chosen parameter values, the largest eigenvalue of the operator M,

$$\mu_+ = \tfrac{1}{2}\big(k_2(\alpha+\beta) - D_A(1+d)q^2 + \sqrt{[k_2(\alpha-\beta) - D_A(1-d)q^2]^2 + 4k_2^2 M_{12}M_{21}}\big), \tag{23}$$

is real and positive. Equation (16), relating δ and C, is used to introduce the dependence on the deviation from the dilution limit in the expression of the eigenvalue. The steady state (A^T, B^T) is then unstable with respect to inhomogeneous perturbations and the mode $q_{\max}$, which maximizes the eigenvalue μ_+, is the most unstable Fourier mode:

$$q_{\max} = \sqrt{\frac{k_2}{D_A}}\sqrt{\frac{\beta-\alpha}{d-1} + \frac{d+1}{d-1}\sqrt{\frac{-M_{12}M_{21}}{d}}}. \tag{24}$$

The wavelength of the periodic structure is then given by

$$\lambda = \frac{2\pi}{q_{\max}}. \tag{25}$$

In Eqs. (6) and (7), time can be scaled by $1/k_2$ and space by $\sqrt{D_A/k_2}$. Figure 1 shows the variation of the scaled eigenvalue μ_+/k_2 with respect to the square of the scaled Fourier mode $D_A q^2/k_2$ for two values of the deviation δ from the dilution limit. Interestingly, the most unstable mode $q_{\max}$ depends on δ. As the solution becomes more concentrated, $q_{\max}$ increases, i.e., the wavelength λ decreases. Moreover, the maximum eigenvalue $\mu_{\max} = \mu_+(q^2_{\max})$ decreases revealing that the deviation from the dilution limit tends to destabilize the Turing pattern.

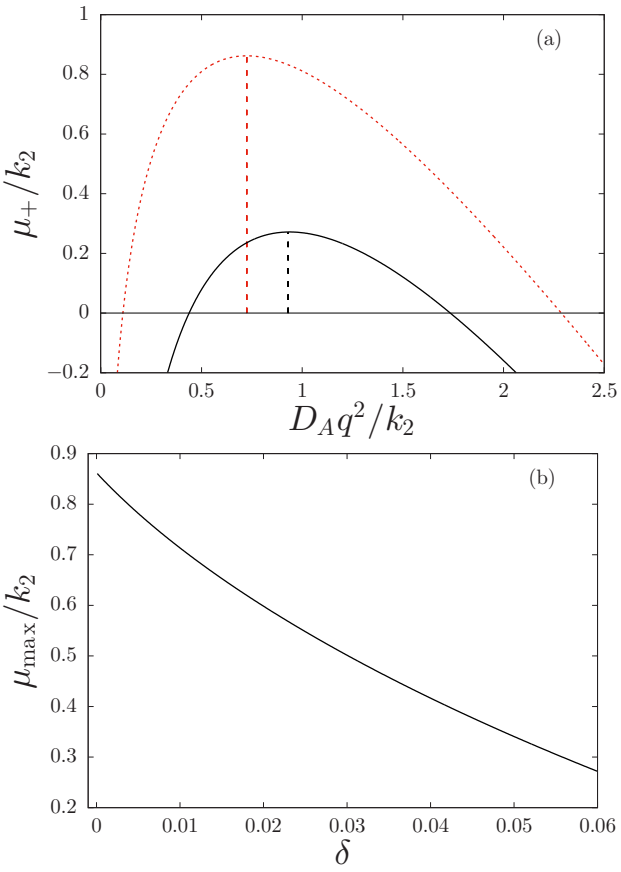

FIG. 1. (a) Scaled positive eigenvalue μ_+/k_2 of the linear stability operator given in Eq. (23) versus square of the scaled Fourier mode $D_A q^2/k_2$. Red dotted line: dispersion relation in the high dilution limit ($\delta = 0$). Black solid line: dispersion relation for $\delta = 0.05$. The square of the most unstable modes $q^2_{\max}$ are indicated by vertical dashed lines. (b) Maximum value of the scaled positive eigenvalue $\mu_{\max}/k_2$ versus the deviation δ from the dilution limit. The parameters take the following values: $\frac{k_1}{k_2} = 2.9 \times 10^4$, $\frac{k_3}{k_2} = 2.2 \times 10^4$, $\frac{k_{-3}}{k_2} = 8.8 \times 10^6$, $d = 10$.

The goal of the paper is to reexamine these properties at the microscopic scale using particle dynamics simulations. Following the results given in Fig. 1, the effect of the deviation from dilution limit on a Turing pattern will be explored in the range $0 \leqslant \delta \leqslant 0.05$.

III. PARTICLE DYNAMICS SIMULATIONS

We use the direct simulation Monte Carlo method (DSMC), introduced by Bird [44,45], to simulate the dynamics of a dilute gas. The method relies on a kinetic Monte Carlo algorithm and consists of a direct simulation of the Boltzmann equation including fluctuations. We already adapted the

method to the simulation of hard spheres with different diameters to reproduce sufficiently different diffusion coefficients for the activator and the inhibitor [11]. Obtaining different binary mutual diffusion coefficients requires a third type of encounter, whose role was played by the reservoir. Here, the reservoir plays also the role of the solvent involved in the chemical scheme.

Particles are hard spheres of mass $m = 1$ with continuous positions and velocities. The initial velocity of the particles is sampled from a Maxwellian distribution with $k_B T = 1$. During a time step, particle positions are updated according to their velocities. Updating of positions is performed along the x axis, whereas velocities are treated in a three-dimensional space. The treatment of the collisions requires space discretization. Only the particles belonging to the same spatial cell are susceptible to collide. Pairs of colliding particles are randomly chosen in a cell, according to the probability of collision. The latter is proportional to the relative velocity of the colliding pair, in agreement with the collision integral of the Boltzmann equation. Collisions are supposed to be elastic and the post-collision relative velocity is randomly chosen according to isotropic scattering.

We recall the procedure followed to obtain sufficiently different diffusion coefficients for species A and B in a ternary mixture of A, B, and S [11]. If the collisions A-B can be neglected with respect to the collisions A-S and B-S, i.e., if

$$S D_{AB} \gg A D_{BS} + B D_{AS}, \quad S \gg B, \quad S \gg A, \tag{26}$$

where D_{XY} is the mutual diffusion coefficient in a binary mixture of X and Y, then the diffusion coefficients in the ternary mixture at local equilibrium obey [11,46]

$$D_A \simeq D_{AS} = \frac{3}{8(A+S)(r_A + r_S)^2} \sqrt{\frac{k_B T}{\pi m}}, \tag{27}$$

$$D_B \simeq D_{BS} = \frac{3}{8(B+S)(r_B + r_S)^2} \sqrt{\frac{k_B T}{\pi m}}, \tag{28}$$

where m is particle mass and r_X is the radius of particles $X = A, B, S$. The choice

$$r_A = 2.2 r_S, \tag{29}$$

$$r_B = \frac{r_A + (1 - \sqrt{d'}) r_S}{\sqrt{d'}}, \tag{30}$$

where $d' = d \frac{C - A^T}{C - B^T}$, obeys the conditions given in Eq. (26) for a ratio $d = 10$ of the diffusion coefficients [11]. In the following, the radius of the solvent particles is set to $r_S = 0.5$. According to Eq. (30), the radius r_B slightly varies with the chosen total concentration C, i.e., with the deviation δ from the dilution limit.

During a collision, a chemical reaction may occur according to the mechanisms described in Eqs. (1)–(4) for $\delta \neq 0$ and Eqs. (11)–(13) for $\delta = 0$. A collision between appropriate species is reactive with a probability proportional to the corresponding rate constant imposed by a steric factor. To save computation time, we only perform the collisions between species susceptible to react: we omit A-A, B-B, and S-S collisions that would have no effect on the chemical evolution of the system. The two chemical steps given in Eqs. (1) and (3) are standard binary reactions. For example, a collision A-S leads to the change of chemical nature of the A particle into a S particle at a frequency proportional to k_1. The exchanges with the reservoir R given in Eq. (4) are treated as follows: in each cell, randomly chosen S particles are turned into B particles at the constant rate k_{-3}, which simulates both the creation of a particle B and the simultaneous removal of a particle S at constant rate. We follow a well-accepted procedure [47] to treat the ternary reaction given in Eq. (2). The reaction is divided into two steps, the rate-limiting binary step, $A + B \xrightarrow{k_2} AB$, and the instantaneous reaction of the complex AB, $AB + A \rightarrow 3A$. The formation of the complex AB is treated as a standard reactive binary collision with a condition on the relative velocity of the colliding pair. Considering that each cell is homogeneous, we evaluate the probability that the closest particle to the complex AB is of A type at A/C. Hence, the B particle is turned into an A particle with a probability equal to A/C. Consequently, the rate constant of the ternary reaction is given by

$$k_2 = \frac{4(r_A + r_B)^2}{C} \sqrt{\frac{\pi k_B T}{m}}. \tag{31}$$

It is worth noting that the total concentration C is related to the deviation δ from the dilution limit according to Eq. (16). Hence, the rate constant k_2 is affected by the dilution of the system. As already mentioned, the steady states (A^0, B^0) and (A^T, B^T) only depend on the ratios k_1/k_2, k_3/k_2, and k_{-3}/k_2. Consequently, we choose to assign constant values to these ratios, so that the steady states deduced from the simulations are expected to be identical to the steady states of the macroscopic description for all the studied values of δ. In all the simulations, the rate constant ratios and the diffusion coefficient ratio are set to

$$\frac{k_1}{k_2} = 2.9 \times 10^4, \quad \frac{k_3}{k_2} = 2.2 \times 10^4,$$
$$\frac{k_{-3}}{k_2} = 8.8 \times 10^6, \quad d = 10. \tag{32}$$

The different orders of magnitude of the rate constants reflect their different units. For example, k_1/k_2 scales as the square of a concentration. Hence, for $k_1/k_2 \simeq 10^4$, the terms $k_1 A$ and $k_2 A^2 B$ of the rate equation given in Eq. (9) have the same order of magnitude when the concentrations are in the order of 10^2. We have chosen units fulfilling this condition and such that the concentrations are simply given by the number of molecules in a spatial simulation cell of unit volume.

For a minimum chemical mechanism with only two chemical species, the emergence of a Turing pattern requires very different diffusion coefficients for the activator and the inhibitor [39]. However, the group of De Kepper demonstrated the possibility to experimentally stabilize Turing patterns using a complexing agent, typically long polymer chains, able to form a complex with the activator and sensitively decrease its diffusion coefficient [48]. Such a third heavy reagent, able to bind with the activator A, has been successfully introduced in molecular dynamics simulations of Turing patterns [12].

In the concentrated system of interest, the smallest mean free path,

$$\ell = \frac{1}{\sqrt{2}C\pi(r_A + r_S)^2}, \tag{33}$$

is associated with the collisions A-S. In dilute gases, cell length Δx is chosen smaller than the mean free path. Here, this condition would lead to prohibitive computation times. To reach a sufficient spatial resolution, we choose $\Delta x = \frac{\lambda}{50}$, where the wavelength λ of Turing pattern is evaluated according to Eq. (25). The variation of the concentration between two cells is sufficiently small to legitimate the choice of a cell length larger than the mean free path. Following the DSMC method [44,45], we impose the time step $\Delta t = \frac{\tau}{5}$ where $\tau = \frac{\ell}{\bar{v}}$ is the mean free time and $\bar{v} = 2\sqrt{\frac{2k_BT}{\pi m}}$ is the mean speed. The system size is set at $L = 10\lambda$. For a given value of the deviation δ from the dilution limit, the total concentration C is deduced from Eq. (16). The macroscopic initial condition is a step function between the steady state (A^T, B^T) in the first 50 cells on the left and the steady state (A^0, B^0) in the remaining cells. The concentration of the solvent S is deduced from the conservation relation given in Eq. (5). The initial numbers of particles A, B, and S in each simulation cell are the nearest integers to the corresponding real concentration values. Typically, for $\delta = 0.02$, we find the following initial numbers of particles in each cell prepared in the steady state (A^T, B^T):

$$N^0_{A^T} = 194, \quad N^0_{B^T} = 148, \quad N^0_{S^T} = 20\,058. \tag{34}$$

In these conditions, a Turing pattern develops behind a wave front propagating to the right. The propagation of the wave front is not disturbed by bulk nucleation. Indeed, the chemical mechanism given in Eqs. (1)–(4) involves a reservoir of species B but not of species A. Contrary to species B, species A is not injected into the system, which ensures the existence of a steady state with a vanishing number of particles A per cell. Hence, the system prepared in the steady state (A^0, B^0) cannot produce A particles, neither due to reaction nor injection, implying that the system remains in the state $(A^0 = 0, B^0)$ even in the presence of large fluctuations.

Cells that are more than $50\Delta x$ to the right of the wavefront are not updated to save computation time. Zero-flux boundary conditions are imposed which results in extremum concentrations for A and B species on the left boundary when a Turing pattern has developed. The simulation is stopped as the front traveled $0.75L$.

In the next section, we examine how the wavelength of the Turing pattern deduced from the simulations varies with the deviation δ from the dilution limit. The results will be compared to the macroscopic predictions.

IV. RESULTS

Instantaneous spatial profiles associated with species A and B are given in Fig. 2 in the case of a concentrated system for a deviation $\delta = 0.05$ from the dilution limit. The numerical solution of the reaction-diffusion equations given in Eqs. (6) and (7) and the simulation results for the chemical mechanism given in Eqs. (1)–(4) are compared for the same parameter values. As expected, a Turing pattern has developed behind a wave front and the wavelengths obtained for the macroscopic description and the simulations agree well. The position of the wave front deduced from DSMC differs from the position of the wave front solution of the deterministic equations. Fluctuations of the position of the wave front deduced from particle dynamics simulations are expected. However, for all the considered parameter values, the wave front deduced from the simulations is always located on the right of the wave front solution of Eqs. (6) and (7), with a greater or lesser advance. This result confirms that pushed fronts or trigger waves, associated with a cubic kinetics like in the Schlögl or Schnakenberg model, are accelerated in the presence of fluctuations [49]. We expect that the mean position difference between the wave fronts associated with the two approaches vanishes as the mean number of particles per cell increases in the simulations [49].

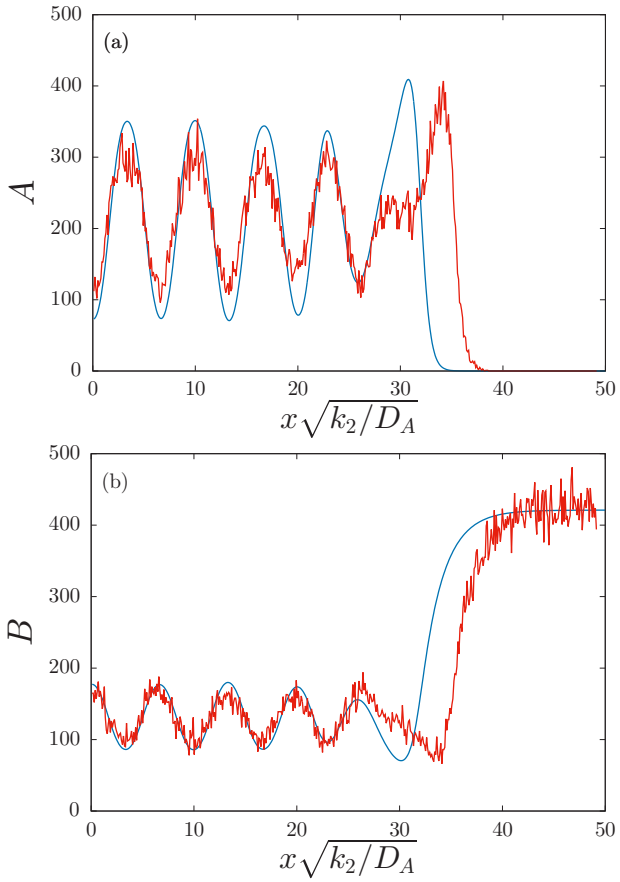

FIG. 2. Concentration profiles deduced from the numerical solution of Eqs. (6) and (7) (blue) and number of particles per cell in simulations (red) versus scaled spatial coordinate $x\sqrt{\frac{k_2}{D_A}}$ for Eqs. (1)–(4), for a given deviation $\delta = 0.05$ from the dilution limit, at scaled time $k_2t = 6986$. Snapshot of the profiles for species A (a) and B (b). The value of the other parameters is given in Sec. III.

The macroscopic predictions of the steady state (A^T, B^T) given in Eqs. (A24) and (A25) are compared to the spatially-averaged numbers $\langle N_{A^T}\rangle$ and $\langle N_{B^T}\rangle$ of particles A and B deduced from the simulations. The average is performed over four wavelengths. The results are displayed in Fig. 3 for

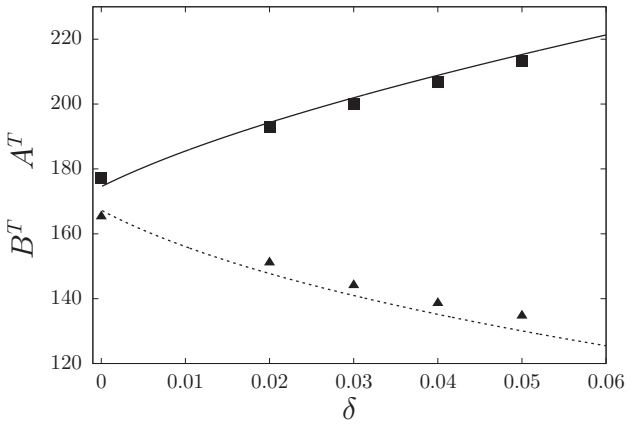

FIG. 3. Macroscopic prediction of the steady state concentrations A^T (solid line) given by Eq. (A24) and B^T (dotted line) deduced from Eq. (A25) versus the deviation δ from the dilution limit. Squares (triangles, respectively) give the mean number of A (B, respectively) particles per cell in the region of the simulated Turing pattern. For $\delta \neq 0$, the mechanism given in Eqs. (1)–(4) is used whereas the mechanism given in Eqs. (11)–(13) is used for $\delta = 0$. The value of the other parameters is given in Sec. III.

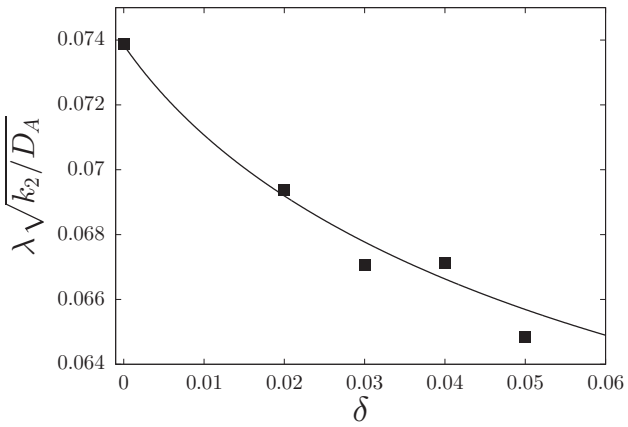

FIG. 4. Macroscopic prediction of the scaled wavelength of the Turing pattern given by Eqs. (24), (25), (27), and (31) (solid line) and scaled wavelength deduced from the simulations (squares) versus deviation δ from the dilution limit. For $\delta \neq 0$, the mechanism given in Eqs. (1)–(4) is used, whereas the mechanism given in Eqs. (11)–(13) is used for $\delta = 0$. The value of the other parameters is given in Sec. III.

different values of the deviation δ from the dilution limit. The simulation results are not displayed for $\delta = 0.01$ due to the prohibitive computation time necessary for the wave front to reach $7.5L$. The total number N_C of particles per cell to be considered dramatically increases as $\delta \to 0$. For example, N_C reaches 40 400 for $\delta = 0.01$.

The mechanism involving the solvent as a reactive species given in Eqs. (1)–(4) has been used to perform the reactive collisions for $\delta \neq 0$. The mechanism associated with the high dilution limit given in Eqs. (11)–(13) has been used to treat the reactive collisions in the case $\delta = 0$, for which the total concentration C can be arbitrary chosen since the solvent is chemically inert. We have checked that the mean numbers of particles $\langle N_{A^T} \rangle$ and $\langle N_{B^T} \rangle$ do not change in the explored range $7\,980 \leqslant N_C \leqslant 19\,950$ of total number N_C of particles values. As a result, increasing δ widens the gap between the stationary values A^T and B^T. The very good agreement between the macroscopic and simulation results can be considered as a test of the simulation procedure. However, the simulation results systematically slightly underestimate the gap between $\langle N_{A^T} \rangle$ and $\langle N_{B^T} \rangle$. The numerical cost prevents us from computing spatially averaged numbers of particles for a sufficient number of wavelengths far enough from the wave front. As shown in Fig. 1, the front associated with species A has a negative gradient. Thus, N_A decreases at the wave front whereas N_B increases. Consequently, the mean number $\langle N_{A^T} \rangle$ is slightly underestimated whereas $\langle N_{B^T} \rangle$ is slightly overestimated. The agreement between macroscopic and simulation results confirms that the simulation method correctly reproduces the ratios k_1/k_2, k_3/k_2, and k_{-3}/k_2 of the rate constants for all the considered values of the deviation δ from the dilution limit. This result *a posteriori* legitimates the choice of the cell length Δx for which the standard requirements of DSMC have not been strictly obeyed.

The simulation method being validated, we now report on the main issue of the paper: the ability of tuning the wavelength of a Turing pattern by controlling the dilution of the system. The simulation model leads to non trivial dependences of the dynamical parameters on the deviation δ from the dilution limit. As shown in Eqs. (27) and (31), the diffusion coefficient D_A and the rate constant k_2 depends on the total concentration C and, hence, on δ. Nevertheless, the ratios d, k_1/k_2, k_3/k_2, and k_{-3}/k_2 remain constant in the simulations, regardless of the deviation δ from the dilution limit. According to Eqs. (24) and (25), the dimensionless quantity $\lambda\sqrt{\frac{k_2}{D_A}}$ associated with the macroscopic description depends on the constant ratios and δ in the same way as the corresponding quantity deduced from the simulations. Figure 4 presents the scaled wavelength $\lambda\sqrt{\frac{k_2}{D_A}}$ of the Turing pattern versus the deviation δ from the dilution limit. The macroscopic results are deduced from Eqs. (24) and (25) for λ and Eqs. (27) and (31) for D_A and k_2. Whereas the macroscopic prediction of the wavelength λ computed according to Eqs. (24), (25), (27), and (31) diverges in the limit $\delta \to 0$, the scaled wavelength $\lambda\sqrt{\frac{k_2}{D_A}}$ tends to a finite value as shown in Fig. 4. The simulation results are obtained for the mechanism given in Eqs. (1)–(4) for a nonvanishing value of the deviation δ from the dilution limit and for the mechanism given in Eqs. (11)–(13) for $\delta = 0$. The same spatial averaging over four wavelengths has been applied to compute the scaled wavelength deduced from the simulations as for the determination of the steady states. The agreement between the macroscopic and simulation results about scaled wavelength versus δ is satisfactory. Nevertheless, the simulation results fluctuate more as δ increases. This result was expected due to the reduced stability of Turing structure observed in Fig. 1 when δ increases. Varying the dilution of the system enables adjusting the scaled wavelength of the Turing pattern. A 10% variation is reached when switching

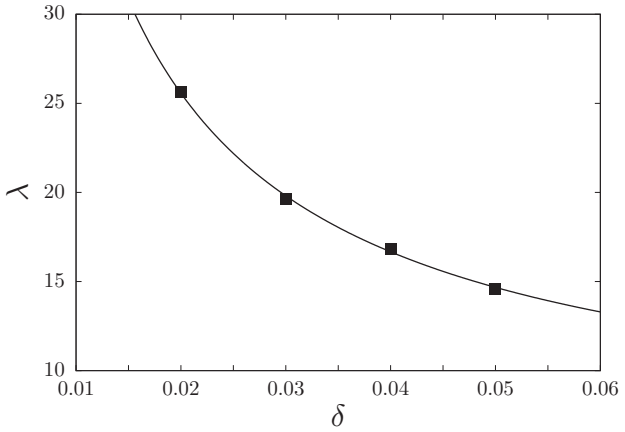

FIG. 5. Same as described in the caption of Fig. 4 but without scaling of the wavelength.

from $\delta = 0$ to $\delta = 0.05$, but only a 5% variation is obtained from $\delta = 0.02$ to $\delta = 0.05$.

However, the simulation results may be interpreted in a different way, in particular, in the perspective of chemical engineering. If we assume that it is possible to find an experimental chemical system obeying Eqs. (1)–(4) with the same dependencies of the dynamical parameters as in the chosen simulation model, then the wavelength of the observed Turing pattern will follow the non scaled dependence on the deviation δ from the dilution limit. The results shown in Fig. 5 mimic the results that could be deduced from such an experimental system. As already mentioned, the wavelength λ diverges as $\delta \to 0$. The variation between the wavelength values as δ increases from 0.02 to 0.05 reaches 67%. For such a large sensitivity of the wavelength to dilution, the fluctuations have a negligible effect and the simulation results perfectly agree with the macroscopic predictions. This excellent agreement between DSMC results and a macroscopic approach, which neglects the effect of the deviation from the dilution limit on diffusion, confirms that the main effect on the wavelength is induced by the perturbation of the reaction in a concentrated system. The simulation results have been given in arbitrary units. However, it is easy to evaluate the order of magnitude of the wavelength in nanometers. Typically, the simulations involve 350 particles A and B for 8500 particles in a cell in the case of a deviation $\delta = 0.05$ from the dilution limit. For small molecules A and B in water S, it amounts to total concentrations of the order of $C = 2.2\,\mathrm{mol/L}$, i.e., 1.4 particles per nm^3. The sum of the radii of the particles A and S is estimated at $r_A + r_S = 0.6\,\mathrm{nm}$. Using Eq. (33) for the mean free path ℓ and taking into account that we impose $\lambda \simeq 500\ell$, we find that the wavelength of the Turing pattern is in the order of 200 nm. The results of DSMC simulations including an explicit effect of the solvent in the chemical scheme show that varying dilution allows us to control the wavelength of a submicrometric spatial structure.

V. CONCLUSION

In this paper, we present a reaction-diffusion model based on elementary processes that enables the control of a spatially periodic pattern at the microscopic scale. The DSMC method has been extended to the simulation of concentrated solutions with the aim of generating Turing patterns with a tunable wavelength at a submicrometric scale. The wavelength of Turing pattern is imposed by dynamics and we show that the deviation from the dilution limit can be harnessed to adjust the wavelength to a selected value. Often, the role of the solvent as a reactive species cannot be ignored in concentrated solutions [38]. DSMC has been successfully used to show the possibility to monitor submicrometric Turing patterns by controlling the total concentration, provided that the chemical mechanism takes the solvent into account. In the high dilution limit, the considered reaction-diffusion equations converge to the equations associated with the chemical mechanism without explicit role of the solvent. We demonstrate that increasing the total concentration by a factor 2 is sufficient to obtain a wavelength reduction of the same factor.

The proposed scenario, involving a strengthening of molecular crowding in smaller embryos, could be considered to support the observed scaling of spatial structures in biology, for example, the adaptation of somite size to embryo size and, more generally, the preservation of proportions in morphogenesis [50]. The results give some hints to design a chemical scheme enabling the formation of a tailored Turing pattern in mesocale chemical engineering.

ACKNOWLEDGMENTS

This publication is part of a project that has received funding from the European Union's Horizon 2020 research and innovation programme under the Marie Skłodowska-Curie Grant Agreement No. 711859 and from the financial resources for science awarded for the implementation of an international cofinanced project.

APPENDIX

The Appendix is devoted to the derivation of the steady state (A^T, B^T):

$$0 = -\frac{k_1}{k_2}A^T\left[1 - \frac{A^T + B^T}{C}\right] + {A^T}^2 B^T, \tag{A1}$$

$$0 = \frac{k_{-3}}{k_2} - \frac{k_3}{k_2}B^T\left[1 - \frac{A^T + B^T}{C}\right] - {A^T}^2 B^T, \tag{A2}$$

associated with the mechanism given in Eqs. (1)–(4). It reads

$$B^T = \frac{(k_1/k_2)(C - A^T)}{(k_1/k_2) + A^T C}, \tag{A3}$$

$$a{A^T}^4 + b{A^T}^3 + c{A^T}^2 + dA^T + e = 0, \tag{A4}$$

where

$$a = -\frac{k_1}{k_2}C, \tag{A5}$$

$$b = \frac{k_1}{k_2}\left(\frac{k_3}{k_2} - \frac{k_1}{k_2} + C^2\right), \tag{A6}$$

$$c = -\frac{k_{-3}}{k_2}C^2 - \frac{k_1}{k_2}\left(2\frac{k_3}{k_2} - \frac{k_1}{k_2}C\right), \tag{A7}$$

$$d = \frac{k_1}{k_2}\left(\frac{k_3}{k_2}C^2 - 2\frac{k_{-3}}{k_2}C\right), \tag{A8}$$

$$e = -\frac{k_{-3}}{k_2}\frac{k_1}{k_2}\frac{k_1}{k_2}. \tag{A9}$$

Following the Ferrari method [51], we introduce

$$z = A^T + \frac{b}{4a}, \tag{A10}$$

$$p = \frac{-3b^2}{8a^2} + \frac{c}{a}, \tag{A11}$$

$$q = \frac{b^3}{8a^3} - \frac{bc}{2a^2} + \frac{d}{a}, \tag{A12}$$

$$r = -3\left(\frac{b}{4a}\right)^4 + \frac{b^2c}{16a^3} - \frac{bd}{4a^2} + \frac{e}{a}, \tag{A13}$$

and we write Eq. (A4) in the form

$$z^4 + pz^2 + qz + r = 0. \tag{A14}$$

It is sufficient to find a root of the third-order equation,

$$8y^3 - 4py^2 - 8ry + 4pr - q^2 = 0, \tag{A15}$$

to find the roots of Eq. (A14). Following the Cardan method [51], we introduce

$$a' = 8\,; \quad b' = -4p\,; \quad c' = -8r\,; \quad d' = 4rp - q^2,$$

$$p' = -\frac{b'^2}{3a'^2} + \frac{c'}{a'}\,; \quad q' = \frac{b'}{27a'}\left(\frac{2b'^2}{a'^2} - \frac{9c'}{a'}\right) + \frac{d'}{a'},$$

and the discriminant of Eq. (A15) reads

$$\Delta_3 = -(4p'^3 + 27q'^2). \tag{A16}$$

For the parameters given in Eq. (32), the discriminant Δ_3 is positive and Eq. (A15) has three real solutions, one of which obeys

$$y^0 = u + \bar{u} - \frac{b'}{3a'}, \tag{A17}$$

with $u = \left(\frac{-q' + i\sqrt{\frac{\Delta_3}{27}}}{2}\right)^{1/3}$. The quartic polynomial given in Eq. (A14) can be factorized in two quadratic polynomials associated with the following discriminants:

$$\Delta_4^{(1)} = -2y^0 - p + \frac{2q}{\sqrt{2y^0 - p}}, \tag{A18}$$

$$\Delta_4^{(2)} = -2y^0 - p - \frac{2q}{\sqrt{2y^0 - p}}. \tag{A19}$$

The four solutions of Eq. (A4) are given by

$$A^{T(1)} = \frac{1}{2}\left(-\sqrt{2y^0} + \sqrt{\Delta_4^{(1)}}\right) - \frac{b}{4a}, \tag{A20}$$

$$A^{T(2)} = \frac{1}{2}\left(-\sqrt{2y^0} - \sqrt{\Delta_4^{(1)}}\right) - \frac{b}{4a}, \tag{A21}$$

$$A^{T(3)} = \frac{1}{2}\left(\sqrt{2y^0} + \sqrt{\Delta_4^{(2)}}\right) - \frac{b}{4a}, \tag{A22}$$

$$A^{T(4)} = \frac{1}{2}\left(\sqrt{2y^0} - \sqrt{\Delta_4^{(2)}}\right) - \frac{b}{4a}. \tag{A23}$$

The solution sought must converge toward the known expression of the steady state [11] in the limit of a diluted system with $C \gg A + B$. Only $A^{T(4)}$ obeys the previous requirement. We find

$$A^T = \frac{1}{2}\left(\sqrt{2y^0} - \sqrt{\Delta_4^{(2)}}\right) - \frac{b}{4a}, \tag{A24}$$

$$B^T = \frac{(k_1/k_2)(C - A^T)}{(k_1/k_2) + A^T C}. \tag{A25}$$

Equations (A24) and (A25) are used to draw Fig. 3.

[1] B. A. Grzybowski, *Chemistry in Motion: Reaction-diffusion Systems for Micro- and Nanotechnology* (Wiley, Chichester, 2009).

[2] A. S. Mikhailov and G. Ertl, *Design and Control of Self-organizing Chemical Systems. In: Chemical Complexity* (Springer, Cham, 2017).

[3] G. Ashkenasy, T. M. Hermans, S. Otto, and A. F. Taylor, Chem. Soc. Rev. **46**, 2543 (2017).

[4] E. Nakouzi and O. Steinbock, Sci. Adv. **2**, e1601144 (2016).

[5] F. C. Simmel and R. Schulman, MRS Bull. **42**, 913 (2017).

[6] A. S. Zadorin, Y. Rondelez, J.-C. Galas, and A. Estevez-Torres, Phys. Rev. Lett. **114**, 068301 (2015).

[7] G. Gines, A. Zadorin, J.-C. Galas, A. Estevez-Torres, T. Fujii, and Y. Rondelez, Nat. Nanotechnol. **12**, 351 (2017).

[8] A. Zadorin, Y. Rondelez, G. Gines, V. Dilhas, G. Urtel, A. Zambrano, J.-C. Galas, and A. Estevez-Torres, Nat. Chem. **9**, 990 (2017).

[9] A. M. Turing, Philos. Trans. R. Soc. London, Ser. B **237**, 37 (1952).

[10] Z. Tan, S. Chen, X. Peng, L. Zhang, and C. Gao, Science **360**, 518 (2018).

[11] P. Dziekan, A. Lemarchand, and B. Nowakowski, J. Chem. Phys. **137**, 074107 (2012).

[12] P. Dziekan, J. S. Hansen, and B. Nowakowski, J. Chem. Phys. **141**, 124106 (2014).

[13] P. K. Maini, T. E. Woolley, R. E. Baker, E. A. Gaffney, and S. S. Lee, Interface Focus **2**, 487 (2012).

[14] L. Diambra, V. Raj Senthivel, D. Barcena Menendez, and M. Isalan, ACS Synth. Biol. **4**, 177 (2015).

[15] J. B. A. Green and J. Sharpe, Development **142**, 1203 (2015).

[16] M. i Rasolonjanahary and B. Vasiev, J. Theor. Biol. **404**, 109 (2016).

[17] L. Marcon and J. Sharpe, Curr. Opin. Genet. Dev. **22**, 578 (2012).

[18] A. D. Economou and J. B. Green, Semin. Cell Dev. Biol. **35**, 58 (2014).

[19] J. Raspopovic, L. Marcon, L. Russo, and J. Sharpe, Science **345**, 566 (2014).

[20] H. G. Othmer and E. Pate, Proc. Natl. Acad. Sci. USA **77**, 4180 (1980).

[21] A. Hunding and P. G. Sorensen, J. Math. Biol. **26**, 27 (1988).

[22] C. Varea, J. L. Aragon, and R. A. Barrio, Phys. Rev. E **56**, 1250 (1997).
[23] M. G. Clerc, E. Tirapegui, and M. Trejo, Phys. Rev. Lett. **97**, 176102 (2006).
[24] S. Ishihara and K. Kaneko, J. Theor. Biol. **238**, 683 (2006).
[25] D. Ben-Zvi and N. Barkai, Proc. Natl. Acad. Sci. USA **107**, 6924 (2010).
[26] D. M. Umulis and H. G. Othmer, Development **140**, 4830 (2013).
[27] W.-S. Li, W.-Y. Hu, Y.-C. Pang, T.-R. Liu, W.-R. Zhong, and Y.-Z. Shao, Phys. Rev. E **85**, 066132 (2012).
[28] E. P. Zemskov, K. Kassner, M. J. B. Hauser, and W. Horsthemke, Phys. Rev. E **87**, 032906 (2013).
[29] W.-C. Lo, S. Zhou, F. Y. M. Wan, A. D. Lander, and Q. Nie, J. R. Soc. Interface **12**, 20141041 (2015).
[30] S. Werner, T. Stückemann, M. Beiran Amigo, J. C. Rink, F. Jülicher, and B. M. Friedrich, Phys. Rev. Lett. **114**, 138101 (2015).
[31] L. Signon, B. Nowakowski, and A. Lemarchand, Phys. Rev. E **93**, 042402 (2016).
[32] A. P. Minton, J. Biol. Chem. **276**, 10577 (2001).
[33] R. J. Ellis and A. P. Minton, Nature **425**, 27 (2003).
[34] J. Sun and H. Weinstein, J. Chem. Phys. **127**, 155105 (2007).
[35] Z.-R. Xie, J. Chen, and Y. Wu, J. Chem. Phys. **140**, 054112 (2014).
[36] P. M. Kekenes-Huskey, C. Eun, and J. A. McCammon, J. Chem. Phys. **143**, 094103 (2015).
[37] P. Nalecz-Jawecki, P. Szymanska, M. Kochanczyk, J. Miekisz, and T. Lipniacki, J. Chem. Phys. **143**, 215102 (2015).
[38] P. Ball, Chem. Rev. **108**, 74 (2008).
[39] A. Lemarchand and B. Nowakowski, Europhys. Lett. **94**, 48004 (2011).
[40] P. Dziekan, L. Signon, B. Nowakowski, and A. Lemarchand, J. Chem. Phys. **139**, 114107 (2013).
[41] P. Dziekan, L. Signon, B. Nowakowski, and A. Lemarchand, Commun. Theor. Phys. **62**, 622 (2014).
[42] J. Schnakenberg, J. Theor. Biol. **81**, 389 (1979).
[43] P. Gray and S. K. Scott, Chem. Eng. Sci. **39**, 1087 (1984).
[44] G. A. Bird, *Molecular Gas Dynamics and the Direct Simulation of Gas Flows* (Clarendon, Oxford, 1994).
[45] F. J. Alexander and A. L. Garcia, Comput. Phys. **11**, 588 (1997).
[46] A. Lemarchand and B. Nawakowski, J. Chem. Phys. **109**, 7028 (1998).
[47] A. Lemarchand and B. Nowakowski, Physica A **271**, 87 (1999).
[48] B. Rudovics, E. Barillot, P. W. Davies, E. Dulos, J. Boissonade, and P. De Kepper, J. Phys. Chem. A **103**, 1790 (1999).
[49] M. A. Karzazi, A. Lemarchand, and M. Mareschal, Phys. Rev. E **54**, 4888 (1996).
[50] K. Ishimatsu, T. W. Hiscock, Z. M. Collins, D. W. K. Sari, K. Lischer, D. L. Richmond, Y. Bessho, T. Matsui, and S. G. Megason, Development **145**, 161257 (2018).
[51] M. R. Spiegel, *Mathematical Handbook of Formulas and Tables* (McGraw-Hill, New York, 1968).

Chapter IV

Fisher-Kolmogorov-Petrovsky-Piskunov front

For more than eighty years, the Fisher-Kolmogorov-Petrovsky-Piskunov (FKPP) wave front has been providing new puzzles to researchers in dynamical systems theory and statistical physics. Within the framework of a deterministic description, corrections to the asymptotic propagation speed have been determined depending on the steepness of the initial condition first by Bramson [96, 97], then by Ebert and Saarloos [98], and currently by Brunet and Derrida [99, 100]. The role of fluctuations on the propagation speed has been first numerically detected using Langevin equations [101, 102], a master equation, DSMC and molecular dynamics simulations [103] The analytical stochastic description of FKKP fronts continues to be developed [104]. My contribution to the subject differs by taking into account different diffusion coefficients for the two reacting species.

IV.1 State of the art for identical diffusion coefficients

The FKPP model generalizes the Verhulst model, presented in Eq. (I.39),

$$\mathrm{A} + \mathrm{B} \xrightarrow{k} 2\,\mathrm{A} \tag{IV.1}$$

to inhomogeneous systems. For species A and B with the same diffusion coefficient D, the rate equations are written

$$\partial_t c_A = k c_A c_B + D\partial_x^2 c_A \tag{IV.2}$$

$$\partial_t c_B = -k c_A c_B + D\partial_x^2 c_B \tag{IV.3}$$

According to Eq. (IV.1), the quantity $c^{\mathrm{tot}} = c_A + c_B$ is conserved, leading to the single

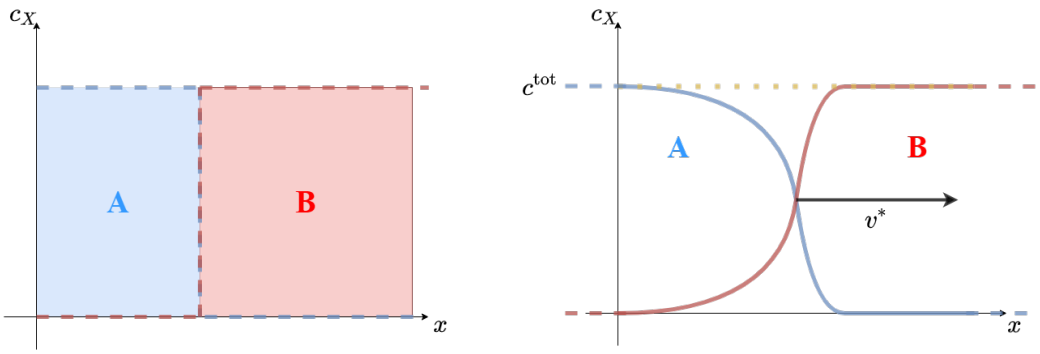

Fig. IV.1 *Left: Concentrations of A and B species vs. space coordinate x at time $t = 0$. Right: Concentrations of A and B species vs. space coordinate x when $t \to \infty$. The wave travels with a stationary velocity v^*.*

rate equation

$$\partial_t c_A = k c^{\text{tot}} c_A \left(1 - \frac{c_A}{c^{\text{tot}}}\right) + D\partial_x^2 c_A \tag{IV.4}$$

This equation exhibits traveling wave solutions, here between the unstable steady state $c_A = 0$ and the stable steady state $c_A = c^{\text{tot}}$.

IV.1.1 Minimum velocity v^*

The specific properties of an FKPP front can be qualitatively understood as follows. The unstability of the stationary state $c_A = 0$ makes the leading edge of the front sensitive to perturbations. From a theoretical point of view, the properties of the leading edge in which the concentration c_A is small can be studied within the framework of a linearized analysis. The front is "pulled" by the leading edge and the propagation speed does not depend on the nonlinearities of the dynamics.

The propagation speed v of the front is derived from the linearized version of Eqs. (IV.4) around the unstable state $(c_A = 0, c_B = c^{\text{tot}})$ in the moving frame $\zeta = x - vt$

$$-v\frac{\mathrm{d}c_A}{\mathrm{d}\zeta} = k c^{\text{tot}} c_A + D\frac{\mathrm{d}^2 c_A}{\mathrm{d}\zeta^2} \tag{IV.5}$$

Provided that the profile c_A follows an exponential form in the leading edge

$$c_A \simeq e^{-\gamma\zeta} \tag{IV.6}$$

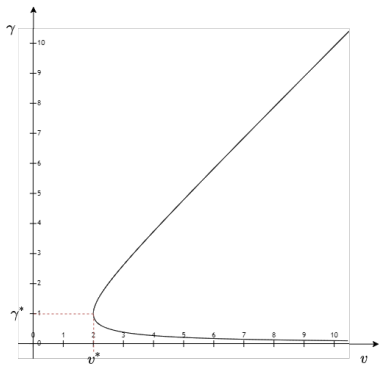

Fig. IV.2 *Diagram representing the two branches* $\gamma_+(v)$ *and* $\gamma_-(v)$ *for* $k = c^{tot} = D = 1$.

where γ depends on v, Eq. (IV.5) leads to a second-order polynomial

$$D\gamma^2 - v\gamma + kc^{\text{tot}} = 0 \tag{IV.7}$$

with real solutions

$$\gamma_\pm = \frac{v \pm \sqrt{v^2 - 4kc^{tot}D}}{2D} \tag{IV.8}$$

if $v^2 - 4kc^{tot}D \geq 0$.
For sufficiently steep initial conditions, in particular for the step function shown in Fig. IV.1, the wave front converges towards a stationary profile that travels at the minimum speed v^* [105]. According to Eq. (IV.8), the minimum speed v^* is given by

$$v^* = 2\sqrt{kc^{tot}D} \tag{IV.9}$$

Figure IV.2 shows the two branches $\gamma_+(v)$ and $\gamma_-(v)$. The minimum speed v^* corresponds to the meeting point $\gamma_+(v^*) = \gamma_-(v^*)$ of the two branches.

IV.1.2 Cutoff effect

In 1997, Brunet and Derrida showed that the introduction of a cutoff in the leading edge of the front significantly reduces the minimal velocity of the front. In this section, I recall the main lines of the demonstration [106]. If a cutoff ε is introduced in the reaction term of Eq. (IV.1), the rate equation for concentration c_A is

$$\partial_t c_A = kc^{\text{tot}} c_A \left(1 - \frac{c_A}{c^{\text{tot}}}\right) \Theta\left(\frac{c_A}{c^{\text{tot}}} - \varepsilon\right) + D\partial_x^2 c_A \tag{IV.10}$$

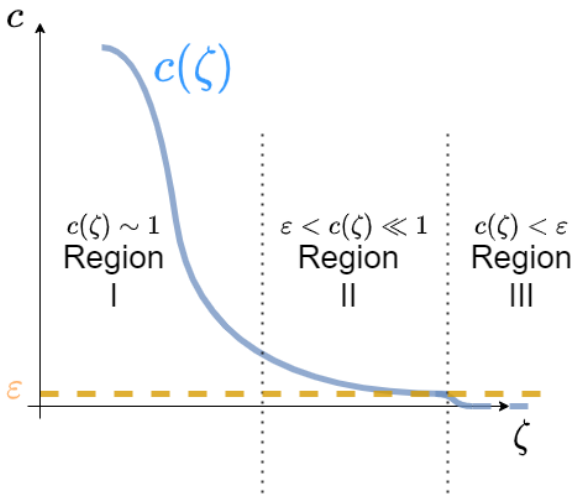

Fig. IV.3 *The three regions introduced by Brunet and Derrida [106] in the leading edge of an FKPP wave front with a cutoff ε.*

where $\Theta(x)$ is the Heaviside step function. Introducing the scale variables

$$c = \frac{c_A}{c^{\text{tot}}} \tag{IV.11}$$

$$x' = \sqrt{\frac{kc^{\text{tot}}}{D}}x \tag{IV.12}$$

$$t' = k(c^{\text{tot}})^2 t \tag{IV.13}$$

and the coordinate $\zeta = x' - vt'$ in the moving frame, and looking for stationary solutions $c(\zeta)$, we find

$$vc' + c'' + c(1-c)\Theta(c-\varepsilon) = 0 \tag{IV.14}$$

Denoting the velocity v_ε of the front with a cutoff, Brunet and Derrida introduce the shift Δ with respect to the minimum velocity

$$\Delta = v^* - v_\varepsilon \tag{IV.15}$$

As shown in Fig. IV.3, three different regions can be defined in the leading edge: In region I, c is of order 1, in region II $\varepsilon < c \ll 1$, and in region III $c < \varepsilon$. In region I, the front is not significantly affected by the cutoff and the differential equation is expected to be the same as Eq. (IV.5). In region II, the concentration c is negligible with respect to 1 and the nonlinear term c^2 can be neglected compared to the linear term. In region III, the reaction term vanishes due to the Heaviside funtion.

It reads

$$\begin{cases} \text{Region I} & v^* c' + c'' + c = 0 \\ \text{Region II} & v_\varepsilon c' + c'' + c = 0 \\ \text{Region III} & v_\varepsilon c' + c'' = 0 \end{cases} \tag{IV.16}$$

These three second-order linear differential equations can be solved. The main issue is to build a continuous, derivable solution at the boundaries of the different regions. Denoting γ^* and $\gamma_r \pm i\gamma_i$ the solutions of Eq. (IV.8) for v^* and v_ε respectively yields

$$\begin{cases} \text{Region I} & c_I(\zeta) \simeq C_I \zeta e^{-\gamma^* \zeta} \\ \text{Region II} & c_{II}(\zeta) \simeq C_{II} e^{-\gamma_r \zeta} \sin\left(\gamma_i \zeta + C'_{II}\right) \\ \text{Region III} & c_{III}(\zeta) \simeq \varepsilon e^{-v_\varepsilon (\zeta - \zeta_0)} \end{cases} \tag{IV.17}$$

where C_I, C_{II}, C'_{II}, and ζ_0 are constants that can be derived from the boundary conditions. Between the regions I and II, the boundary condition imposes

$$C_I \zeta e^{-(\gamma^* - \gamma_r)\zeta} = C_{II} \sin\left(\gamma_i \zeta + C'_{II}\right) \tag{IV.18}$$

On the one hand, it is expected that, according to Eq. (IV.15), the difference $\gamma^* - \gamma_r$ is of order Δ. On the other hand, Eq. (IV.8) shows that γ_i is of order $\Delta^{1/2}$. Therefore, imposing $C'_{II} = 0$ at the leading order in $\Delta^{1/2}$ yields

$$C_I = C_{II} \gamma_i \tag{IV.19}$$

Between regions II and III, the concentration is equal to the cutoff ε and $\zeta = \zeta_0$. The conditions of continuity and derivability of the function $c(\zeta)$ are given by

$$\begin{cases} C_I e^{-\gamma_r \zeta_0} \sin\left(\gamma_i \zeta_0\right) = \varepsilon \gamma_i \\ C_I e^{-\gamma_r \zeta_0} \left[-\gamma_r \sin\left(\gamma_i \zeta_0\right) + \gamma_i \cos\left(\gamma_i \zeta_0\right)\right] = -v_\varepsilon \varepsilon \gamma_i \end{cases} \tag{IV.20}$$

Combining these two equations gives

$$v_\varepsilon = \gamma_r - \frac{\gamma_i}{\tan(\gamma_i \zeta_0)} \tag{IV.21}$$

Intuitively, the difference Δ is expected to be small, i.e. $\gamma_r \simeq \gamma^* = 1$ and $v_\varepsilon \simeq v^* = 2$. Therefore, it is possible to write

$$\tan(\gamma_i \zeta_0) \simeq -\gamma_i \tag{IV.22}$$

which is ensured only if $\gamma_i \zeta_0 \simeq \pi + \gamma_i$. Introducing this last assumption in Eq. (IV.20) and assuming that $\zeta_0 \gg 1$ leads to

$$\zeta_0 \simeq -\frac{\ln \varepsilon}{\gamma^*} \tag{IV.23}$$

$$\gamma_i \simeq \frac{\pi}{\zeta_0 - 1} \simeq \frac{\pi}{\zeta_0} \simeq \frac{\pi \gamma^*}{|\ln \varepsilon|} \tag{IV.24}$$

Brunet and Derrida expand v_ε into power series of γ_i,

$$v_\varepsilon \simeq v(\gamma^* \pm i\gamma_i) \simeq v(\gamma^*) - \frac{1}{2} v''(\gamma^*) \gamma_i^2 \tag{IV.25}$$

and find that the shift in velocity due to the cutoff obeys

$$\Delta \simeq \frac{v''(\gamma^*) \pi^2 \gamma^{*2}}{2(\ln \varepsilon)^2} \tag{IV.26}$$

For the same parameter values as in Fig. IV.2, the shift is of order $\dfrac{\pi^2}{2(\ln \varepsilon)^2}$. The introduction of a cutoff in the deterministic equation has been shown to correctly reproduce the effect of fluctuations in different stochastic systems that can be associated with Eq. (IV.4) in the macroscopic limit. In particular, branching Brownian motion [107] and the reaction-diffusion master equation associated with the scheme $\mathrm{A} + \mathrm{B} \longrightarrow 2\,\mathrm{A}$ [103] both lead to corrections of the propagation speed obeying Eq. (IV.26). Qualitatively, the discrete nature of the random variables in the two considered stochastic approaches implies the existence of a rightmost particle, which plays the role of a cutoff in the leading edge of the front.

IV.2 Results for different diffusion coefficients

IV.2.1 Deterministic description

a) High-dilution limit

The result given in Eq. (IV.9) is obtained for $D_A = D_B$. I address the more general case $D_A \neq D_B$, which implies that the quantity $c_A + c_B$ is not constant. It is to be noted that the deterministic model with different diffusion coefficients cannot straightforwardly be associated with elementary diffusion processes at the particle scale. Indeed, in a binary mixture, the diffusion coefficients of the two species are identical as shown in Eq. (I.77). A ternary mixture involving a solvent S in addition to A and B species offers a possible microsocopic picture of a model with $D_A \neq D_B$., as shown in Sec. I.3.2. The excess of solvent with respect to the solute implies that the collisions between S and A particles,

on the one hand, and S and B particles, on the other hand, determine the diffusion coefficients of A and B, respectively. Therefore, we introduce a solvent S that allows the diffusion coefficients of A and B species to be different. The rate equations are

$$\partial_t c_A = k c_A c_B + D_A \partial_x^2 c_A \tag{IV.27}$$

$$\partial_t c_B = -k c_A c_B + D_B \partial_x^2 c_B \tag{IV.28}$$

Linearizing the equations in the moving frame $\zeta = x - vt$ around $(c_A = 0, c_B = c^0)$ leads to

$$-v\partial_\zeta c_A = k c^0 c_A + D_A \partial_\zeta^2 c_A \tag{IV.29}$$

$$-v\partial_\zeta c_B = -k c^0 c_A + D_B \partial_\zeta^2 c_B \tag{IV.30}$$

where c^0 is the boundary value of c_B on the right side of the system, According to Eq. (IV.29), c_A does not depend on c_B, which means that the same procedure as $D_A = D_B$ can be applied. We conclude that the minimum velocity of the front is given by

$$v^* = 2\sqrt{k c^0 D_A} \tag{IV.31}$$

for all D_B. Intuitively, the leading edge asymptotically tends to the state $(0, c^0)$, for any given value of D_B. The propagation speed of pulled fronts being imposed by the leading edge, it is not surprising that the velocity does not depend on D_B.

In the high-dilution limit, the challenge was to find properties of the front profile susceptible to be affected by the difference of diffusion coefficients between species A and B. The linearization of the Eqs. (IV.27) and (IV.28) does not help in achieving this objective. I worked to develop an analytical approach, important to test the quality of the numerical results for possibly small perturbations of front properties. I focused on an expansion method proposed by Murray to give an estimation of the profile width of an unperturbed FKPP front [2]. The idea implemented by Murray is to consider $1/v^2$ as a small parameter. Clearly, the quality of the expansion is not excellent, $v*$ being equal to 2 for the scaled variables given in Eqs. (IV.11-IV.13). As a consequence, the first-order expansion delivered results valid in a small interval of D_B close to the value set for D_A and I was obliged to determine the second-order corrections. According to the approach of Murray, it was legitimate to first consider whether the width of the front would be affected by different diffusion coefficients for A and B. Even if the width is perturbed, the effect remains small. By examining the results of the numerical integration of Eqs. (IV.27) and (IV.28), I then stated that the vertical shift between the profiles of A and B could be a good candidate. I proposed to use what I called the height h between the A and B profiles, defined as the difference $c_A(\zeta = 0) - c_B(\zeta = 0)$, where the origin $\zeta = 0$ of the

moving frame is set at $c_A(\zeta = 0) = c^{tot}/2$. The results are very satisfying. The height h changes sign for $D_A = D_B$ and reaches more than 5% of c^{tot} in the investigated range of D_B smaller than D_A and more than -25% of c^{tot} for values of D_B larger than D_A.

b) Concentrated system

The results I obtained in the dilute case were very encouraging regarding the initial goal of using the FKPP front as an indicator of diffusion perturbation in a concentrated system. I therefore considered the modified rate equations associated with the FKPP model

$$\partial_t c_A = k c_A c_B + D_A \partial_x \left[\left(1 - \frac{c_A}{c^{\text{tot}}} \right) \partial_x c_A \right] - D_B \partial_x \left(\frac{c_A}{c^{\text{tot}}} \partial_x c_B \right) \tag{IV.32}$$

$$\partial_t c_B = -k c_A c_B + D_B \partial_x \left[\left(1 - \frac{c_B}{c^{\text{tot}}} \right) \partial_x c_B \right] - D_A \partial_x \left(\frac{c_B}{c^{\text{tot}}} \partial_x c_A \right) \tag{IV.33}$$

obtained from Eqs. (IV.27) and (IV.28) by taking into account the modified Fick's law given in Eqs. (I.61) and (I.62). The same procedure than in Eqs.(IV.29) and (IV.30) is applied, but the minimal velocity of the front remains the same as in Eq. (IV.31). My initial motivation for studying the propagation of an FKPP front was to exploit its sensitivity to small perturbations in order to use the front as a sensor of the perturbation of diffusion induced by high concentrations. From this point of view, this result, which states that the propagation speed does not depend neither on the diffusion coefficient of species B nor the concentration of the system, is disappointing. However, the results that I obtained within the framework of a stochastic description based on a master equation, with the introduction of a cutoff, interestingly challenges the result given in Eq. (IV.31).

I used the same expansion technique as in the dilute case to determine analytical expressions of the width and the height in the concentrated case. The results were confirmed by the numerical solutions of Eqs (IV.32) and (IV.33). The height h proved to be a good criterion to reveal the perturbation of diffusion in a concentrated system. The high-concentration-induced correction to the height monotonically decreases as D_B increases and remains larger that 5% for $D_B = 20D_A$. Values of D_B smaller than D_A lead to high-concentration-induced corrections to the height of more than 25%. However, this good score is partly due to the intrinsically small values of h in the range $D_B \leq D_A$. In particular, it should not be forgotten that h vanishes for $D_B = D_A$ and cannot be used in this specific case.

To conclude, the experimental determination of the vertical shift h between the profiles of the two species at the origin of the moving frame and the comparison with the expected value in the high-dilution limit should provide a satisfying test of high-concentration-induced perturbation of diffusion, more accurate in the range $2D_A \leq D_B \leq 20D_A$.

c) Publication

The results about the deterministic approach to the perturbation of an FKPP front for different diffusion coefficients in the dilute and concentrated cases are published in "Fisher-Kolmogorov-Petroskii-Piskunov wave front as a sensor of perturbed diffusion in concentrated systems", G. Morgado, B. Nowakowski, and A. Lemarchand, Phys. Rev. E, **99**, 022205 (2019) [43]

Fisher-Kolmogorov-Petrovskii-Piskunov wave front as a sensor of perturbed diffusion in concentrated systems

Gabriel Morgado,[1,2] Bogdan Nowakowski,[1,3] and Annie Lemarchand[2,*]

[1]*Institute of Physical Chemistry, Polish Academy of Sciences, Kasprzaka 44/52, 01-224 Warsaw, Poland*

[2]*Laboratoire de Physique Théorique de la Matière Condensée, Sorbonne Université, CNRS UMR 7600, 4 place Jussieu, case courrier 121, 75252 Paris CEDEX 05, France*

[3]*SGGW, Warsaw University of Life Sciences, Nowoursynowska 159, 02-776 Warsaw, Poland*

(Received 13 November 2018; published 11 February 2019)

The sensitivity to perturbations of the Fisher and Kolmogorov, Petrovskii, Piskunov front is used to find a quantity revealing perturbations of diffusion in a concentrated solution of two chemical species with different diffusivities. The deterministic dynamics includes cross-diffusion terms due to the deviation from the dilution limit. The behaviors of the front speed, the shift between the concentration profiles of the two species, and the width of the reactive zone are investigated, both analytically and numerically. The shift between the two profiles turns out to be a well-adapted criterion presenting noticeable variations with the deviation from the dilution limit in a wide range of parameter values.

DOI: 10.1103/PhysRevE.99.022205

I. INTRODUCTION

The Fisher and Kolmogorov, Petrovskii, Piskunov (FKPP) wave front is the prototype of pulled fronts whose properties are strongly influenced by the leading edge of the profile [1,2]. From the perspective of applications, wave fronts of FKPP type are widely used in models of combustion [3] and biology [4–6], in particular to account for adaptation, mutation, and selection in evolutionary strategies. Sufficiently steep initial profiles converge to the front propagating at the minimum velocity deduced from a linear stability analysis [7,8]. The FKPP front is known to be highly sensitive to even small perturbations of many different origins. Brunet and Derrida proved that a small cutoff introduced in the leading edge of the front induces a negative correction to the front speed [9]. Fluctuations have also been shown to modify the propagation speed of pulled front [10]. The description of a reaction-diffusion system at a mesoscopic scale by a master equation [11,12] as well as particle dynamics simulations using the direct simulation Monte Carlo (DSMC) method [13] both revealed that the discrete nature of particle numbers induces analogous corrections to the front speed as a cutoff in the deterministic partial differential equations. Roughly speaking, the cutoff can be interpreted as the inverse of the particle number in the reactive zone [14]. It has then been shown in the framework of a Langevin approach that the effect of a multiplicative noise on the front speed can be studied under the scope of a modified cutoff theory [15,16]. The effect of a slightly exothermic reaction on the front speed has also been studied using DSMC. Below a critical heat release, the speed remains equal to the one in the isothermal case and is imposed by the Chapman-Jouguet criterion above it [17]. In addition, the DSMC method has been used to study the impact of the perturbation of local equilibrium by a fast reaction associated with a small activation energy: Reaction-induced non-Maxwellian particle velocity distributions result in positive corrections to the front speed [18]. Molecular dynamics simulations of dense fluids also lead to propagation speeds larger than the marginally stable one [14]. Recent articles focused on the effect of an advection term [19–21].

In this paper we study a reaction-diffusion wave front of FKPP type propagating in confined systems such as biological environments or more generally in concentrated chemical systems. We focus on the impact of molecular crowding on diffusion. Indeed, diffusion may be modified at high concentrations and the usual Fick's law relating the diffusion flux of a given species to the gradient of the concentration of that single species is not always valid. Linear nonequilibrium thermodynamics is used to extend Fick's law to concentrated systems, leading to diffusion flux depending on the concentration gradients of all the chemical components of the mixture [22–24]. In these conditions, the partial differential equations governing dynamics involve cross-diffusion terms. Experiments demonstrate that cross-diffusion coefficients can be quite significant in many kinds of chemical systems involving, for example, ions, micelles, surface, or polymer reactions [25–28]. *A priori*, cross-diffusion can lead to spatial and spatiotemporal pattern formation. Recently, hydrodynamic instabilities were observed in reaction-diffusion-convection patterns in microemulsions [29,30]. We checked that the wavelength of a Turing pattern is not affected and can therefore not characterize the perturbation of diffusion induced by high concentrations [24,31]. The goal of the paper is first to determine the impact of cross-diffusion on the properties of FKPP wave fronts involving two chemical species A and B of different diffusivities. Then we intend to harness the sensitivity of FKPP fronts to find a macroscopic quantity depending on the detail of the diffusion rates and thus sensitive to the deviation from the dilution limit. Literature mostly reports on corrections to the front speed [8,15,16,19–21,32,33]. We

*Corresponding author: anle@lptmc.jussieu.fr

will first examine the impact of diffusion perturbation on the front speed and then investigate the behavior of alternative quantities with the aim of defining a criterion that could be used in experiments to check if diffusion is perturbed in a concentrated system admitting a FKPP front.

The paper is organized as follows. We present the reaction-diffusion model in Sec. II. Analytical expressions of different quantities characterizing the wave front in dilute and concentrated systems are derived in Sec. III. Specifically, we look for effects of diffusion perturbation on the propagation speed, the shift between A and B profiles, and the width of the reactive zone. The analytical predictions are compared to numerical results in Sec. IV. Section V contains conclusions.

II. REACTION-DIFFUSION MODEL

The system is composed of three chemical species. Two of them, A and B, are reactive whereas the third species S is the solvent. The reaction scheme is given by

$$\mathrm{A} + \mathrm{B} \xrightarrow{k} 2\,\mathrm{A}, \tag{1}$$

where k is a rate constant. In a dilute system, the reaction-diffusion equations associated with the mechanism are

$$\partial_t A = kAB + D_A \partial_x^2 A, \tag{2}$$

$$\partial_t B = -kAB + D_B \partial_x^2 B, \tag{3}$$

where A and B are the concentrations of species A and B, and D_A and D_B are the diffusion coefficients of the A and B species, respectively. In a concentrated solution, the diffusion of A and B species may be perturbed. Nevertheless, we assume that the solution is ideal, in the sense that the activity remains equal to the concentration. In the framework of linear nonequilibrium thermodynamics, we derived linear relations between generalized diffusion fluxes and forces which couple the diffusion of a species with the gradients of each constituent of the mixture [22,24]. After the elimination of the solvent concentration S, we showed that the reaction-diffusion equations are given by

$$\partial_t A = kAB + D_A \partial_x \left[\left(1 - \frac{A}{C}\right) \partial_x A \right] - D_B \partial_x \left(\frac{A}{C} \partial_x B \right), \tag{4}$$

$$\partial_t B = -kAB + D_B \partial_x \left[\left(1 - \frac{B}{C}\right) \partial_x B \right] - D_A \partial_x \left(\frac{B}{C} \partial_x A \right), \tag{5}$$

where the total concentration $C = A + B + S$ is constant. Equations (4) and (5) converge to Eqs. (2) and (3) in the dilution limit $(A + B)/C \to 0$ and are valid for sufficiently small values of $(A + B)/C$.

We choose inhomogeneous initial conditions in the form of a step function for species A and B:

$$\begin{aligned} &x < 0, \quad A(x, t = 0) = V_0, \quad B(x, t = 0) = 0, \\ &x \geqslant 0, \quad A(x, t = 0) = 0, \quad B(x, t = 0) = V_0, \end{aligned} \tag{6}$$

where the constant V_0 characterizes the height of the step. The reaction-diffusion equations have wave front solutions which propagate at constant speed v_α where the index $\alpha = d$ for the dilute system and $\alpha = c$ for the concentrated system. These FKPP fronts are also called pulled fronts because the speed is determined by the leading edge of the profile which pulls the bulk to the right [7,9].

For identical diffusion coefficients $D_A = D_B$ and initially homogeneous conditions for S and $A + B = V_0$, the sum $A + B$ does not evolve. Then, introducing the conservation relation $A + B = V_0$ into Eqs. (4) and (5), we find that the concentrated solution obeys the same unperturbed equations given in Eqs. (2) and (3) as the diluted system. With the aim of specifying how the properties of a FKPP wave front are perturbed as the system becomes more concentrated, we consider different diffusion coefficients D_A and D_B in the following.

III. ANALYTICAL DERIVATION OF WAVE FRONT FEATURES IN DILUTE AND CONCENTRATED SYSTEMS

A. Propagation speed

To derive an approximate analytical expression of the propagation speed, we perform a linear stability analysis around the steady state $(A = 0, B = V_0)$ in the moving frame at speed v_α. Linearizing the reaction-diffusion equations is supposed to be valid in the leading edge of the front. We introduce the following transformation:

$$\xi = \frac{x}{v_\alpha} - t, \tag{7}$$

$$A(x, t) = f_\alpha(\xi), \tag{8}$$

$$B(x, t) = g_\alpha(\xi), \tag{9}$$

where $\alpha = d, c$.

We first address the case of a dilute system. Equations (2) and (3) can be rewritten as

$$0 = k f_d g_d + f_d' + \varepsilon_d D_A f_d'', \tag{10}$$

$$0 = -k f_d g_d + g_d' + \varepsilon_d D_B g_d'', \tag{11}$$

where $\varepsilon_d = 1/v_d^2$ and $'$ denotes the derivation with respect to ξ. The second-order differential equations are transformed into first-order equations in the four-dimension space (f_d, f_d', g_d, g_d'). We perform a linear stability analysis around the unstable steady state and obtain the following linearized uncoupled system for (f_d, f_d'):

$$\frac{df_d}{d\xi} = f_d', \tag{12}$$

$$\frac{df_d'}{d\xi} = -\frac{v_d^2}{D_A}(kV_0 f_d + f_d'), \tag{13}$$

which leads to the eigenvalues $\lambda_\pm$

$$\lambda_\pm = \frac{-v_d^2 \pm v_d \sqrt{v_d^2 - 4kV_0 D_A}}{2D_A}. \tag{14}$$

The existence of wave front solutions is ensured for real eigenvalues which imposes the minimum velocity

$$v_d^* = 2\sqrt{kV_0 D_A}. \tag{15}$$

In the concentrated case, Eqs. (4) and (5) read

$$0 = kf_c g_c + f_c' + \varepsilon_c\left(D_A\left[\left(1-\frac{f_c'}{C}\right)f_c'' - \frac{(f_c')^2}{C}\right] - D_B\left[\frac{f_c g_c''}{C} + \frac{f_c' g_c'}{C}\right]\right), \tag{16}$$

$$0 = -kf_c g_c + g_c' + \varepsilon_c\left(D_B\left[\left(1-\frac{g_c}{C}\right)g_c' - \frac{(g_c')^2}{C}\right] - D_A\left[\frac{g_c f_c''}{C} + \frac{f_c' g_c'}{C}\right]\right), \tag{17}$$

where $\varepsilon_c = 1/v_c^2$. Following the same procedure as in the dilute case, we find

$$v_c^* = 2\sqrt{kV_0 D_A}. \tag{18}$$

Hence, the front speeds in the dilute system and the concentrated system are identical in the framework of a linear stability analysis. Consequently, the following notations are introduced:

$$v_c^* = v_d^* = v, \tag{19}$$

$$\varepsilon_c = \varepsilon_d = \varepsilon. \tag{20}$$

We checked that for sufficiently steep initial conditions and after a transient regime, the wave front propagates at the minimum speed v, as in the case of identical diffusion coefficients [7,9]. Interestingly, in both the dilute and concentrated systems, the minimum propagation speed of the linearized system does not depend on the diffusion coefficient D_B of species B and only depend on the product kV_0D_A.

B. Front profile

A perturbation technique is used to determine analytical expressions of quantities characterizing the wave front profile. We look for solutions of the reaction-diffusion equations in the frame moving at front speed v as a Taylor expansion in the small parameter ε [4]. As ε tends to zero, Eqs. (10) and (11) and Eqs. (16) and (17) switch from second-order differential equations to first-order equations. The boundary conditions of the first-order equations must be compatible with the ones of the second-order equations. However, the reactive terms $\pm kf_\alpha g_\alpha$ and the first-order terms f_α' and g_α' equal zero at the boundaries $\xi = \pm\infty$ for all perturbation orders, which ensures the consistency of a regular perturbation procedure

$$f_\alpha = f_{\alpha,0} + \varepsilon f_{\alpha,1} + \varepsilon^2 f_{\alpha,2} + \cdots, \tag{21}$$

$$g_\alpha = g_{\alpha,0} + \varepsilon g_{\alpha,1} + \varepsilon^2 g_{\alpha,2} + \cdots, \tag{22}$$

where $f_{\alpha,i}$ and $g_{\alpha,i}$ are the ith order corrections with $i = 0, 1, 2, \ldots$ and $\alpha = d, c$. The boundary conditions obey

$$f_{\alpha,0}(-\infty) = V_0, \quad f_{\alpha,0} = (+\infty) = 0, \tag{23}$$

$$g_{\alpha,0}(-\infty) = 0, \quad g_{\alpha,0}(+\infty) = V_0, \tag{24}$$

$$f_{\alpha,i}(\pm\infty) = g_{\alpha,i}(\pm\infty) = 0, \quad \text{for} \quad i \geqslant 1. \tag{25}$$

The origin of the ξ axis is chosen such that

$$f_{\alpha,0}(0) = \frac{V_0}{2}, \tag{26}$$

$$f_{\alpha,i}(0) = 0, \quad \text{for} \quad i \geqslant 1. \tag{27}$$

The zeroth-order solutions are straightforwardly deduced from Eqs. (10) and (11) and Eqs. (16) and (17) without diffusion terms

$$f_{\alpha,0} = \frac{V_0}{1+e^{kV_0\xi}}, \tag{28}$$

$$g_{\alpha,0} = \frac{V_0}{1+e^{-kV_0\xi}}, \tag{29}$$

for $\alpha = d, c$.

Instead of determining the higher-order solutions, we focus on characteristic properties of the profiles. We define the height $h_\alpha = f_\alpha(0) - g_\alpha(0)$ as the difference of concentrations between species A and B in the moving frame at the origin $\xi = 0$. The height h_α evaluates the shift between the profiles of species A and B due to their different diffusivities. Using Eqs. (26) and (27), we obtain the evaluations of the height up to the first and second orders

$$h_{\alpha,1} = \varepsilon g_{\alpha,1}(0), \tag{30}$$

$$h_{\alpha,2} = \varepsilon g_{\alpha,1}(0) + \varepsilon^2 g_{\alpha,2}(0), \tag{31}$$

for $\alpha = d, c$. Using Eqs. (10) and (11), we obtain the first $h_{d,1}$ and second-order $h_{d,2}$ approximations of the height in the dilute case

$$h_{d,1} = \frac{V_0}{16}\left(1-\frac{D_B}{D_A}\right), \tag{32}$$

$$h_{d,2} = \frac{V_0}{16}\left(1-\frac{D_B}{D_A}\right)\left[1+\frac{1}{8}\left(1-\frac{D_B}{D_A}\right)\right]. \tag{33}$$

As a result, the height $h_{d,2}$ does not depend on the rate constant k and the scaled height $h_{d,2}/V_0$ only depends on the ratio D_B/D_A. Using Eqs. (16) and (17), we find in the concentrated case

$$h_{c,1} = \frac{V_0}{16}\left(1-\frac{D_B}{D_A}\right)\left(1-\frac{V_0}{C}\right), \tag{34}$$

$$h_{c,2} = \frac{V_0}{16}\left(1-\frac{D_B}{D_A}\right)\left(1-\frac{V_0}{C}\right) \times\left[1+\frac{1}{8}\left(1-\frac{D_B}{D_A}\right)\left(1-2\frac{V_0}{C}\right)\right]. \tag{35}$$

We check that, in the dilution limit $\frac{V_0}{C} \to 0$, the first- and second-order expressions of the height in the concentrated system given in Eqs. (34) and (35) converge to the first- and second-order expressions of the height in the dilute system given in Eqs. (32) and (33). Up to the second order, the scaled height h_c/V_0 only depends on the ratio of the diffusion coefficients D_B/D_A and the deviation V_0/C from the dilution limit. The parameter V_0/C varying in the range [0,1], the first-order evaluation $h_{c,1}$ in a concentrated system is always smaller than the corresponding quantity $h_{d,1}$ given in Eq. (32)

in the dilute system. High concentrations tend to reduce the shift between A and B profiles, at least at the first order.

The width W_α of the wave front is deduced from the inverse of the steepness of the A profile at $\xi = 0$

$$W_\alpha = -vV_0/f'_\alpha(0). \tag{36}$$

We consider the following evaluations of the width:

$$W_{\alpha,1} = \frac{-vV_0}{f'_{\alpha,0}(0) + \varepsilon f'_{\alpha,1}(0)}, \tag{37}$$

$$W_{\alpha,2} = \frac{-vV_0}{f'_{\alpha,0}(0) + \varepsilon f'_{\alpha,1}(0) + \varepsilon^2 f'_{\alpha,2}(0)}, \tag{38}$$

deduced from the first-order and the second-order expansions of f_α. For the sake of simplicity, $W_{\alpha,1}$ and $W_{\alpha,2}$ will be called first- and second-order evaluations of the width, respectively. In the dilute case, the first-order $W_{d,1}$ and the second-order $W_{d,2}$ expressions of the width are deduced from Eqs. (10) and (11)

$$W_{d,1} = 8\sqrt{\frac{D_A}{kV_0}}\left[1 + \frac{1}{8}\left(1 - \frac{D_B}{D_A}\right)\right]^{-1}, \tag{39}$$

$$W_{d,2} = 8\sqrt{\frac{D_A}{kV_0}}\left[1 + \frac{1}{8}\left(1 - \frac{D_B}{D_A}\right) - \frac{1}{64}\frac{D_B}{D_A}\left(3 - \frac{D_B}{D_A}\right)\right]^{-1}. \tag{40}$$

It is worth noting that $W_{d,0} = 8\sqrt{\frac{D_A}{kV_0}}$ is an approximation of the width in the case $D_A = D_B$ known to be valid up to the first order [4]. The second-order evaluation $W_{d,2}$ provides the corrected expression $8\sqrt{\frac{D_A}{kV_0}}(1-\frac{1}{32})$ of the width for $D_A = D_B$. Using Eqs. (16) and (17) in the concentrated case, we obtain after tedious calculations,

$$W_{c,1} = 8\sqrt{\frac{D_A}{kV_0}}\left[1 + \frac{1}{8}\left(1 - \frac{D_B}{D_A}\right)\left(1 - \frac{3V_0}{2C}\right)\right]^{-1}, \tag{41}$$

$$W_{c,2} = 8\sqrt{\frac{D_A}{kV_0}}\left[1 + \frac{1}{8}\left(1 - \frac{D_B}{D_A}\right)\left(1 - \frac{3V_0}{2C}\right) - \frac{1}{64}\left[\frac{D_B}{D_A}\left(3 - \frac{D_B}{D_A}\right) + \left(\frac{9}{2} - 8\frac{D_B}{D_A} + \frac{7}{2}\frac{D_B^2}{D_A^2}\right)\frac{V_0}{C} - \left(\frac{7}{2} - 7\frac{D_B}{D_A} + \frac{7}{2}\frac{D_B^2}{D_A^2}\right)\frac{V_0^2}{C^2}\right]\right]^{-1}. \tag{42}$$

We check that, in the dilution limit $\frac{V_0}{C} \to 0$, the first- and second-order expressions of the width in the concentrated system given in Eqs. (41) and (42) converge to the first and second-order expressions of the width in the dilute system given in Eqs. (39) and (40). In addition, the zeroth-order evaluations coincide, $W_{d,0} = W_{c,0} = 8\sqrt{\frac{D_A}{kV_0}}$. The scaled width $\sqrt{\frac{kV_0}{D_A}}W_c$ only depends on D_B/D_A and V_0/C as the height does. In the next section, the analytical predictions of the height and the width are compared to the corresponding numerical results deduced from Eqs. (2) and (3) in the dilute case and Eqs. (4) and (5) in the concentrated case.

IV. COMPARISON BETWEEN ANALYTICAL AND NUMERICAL RESULTS

Analytical results are derived from expansions with respect to $\varepsilon = \frac{1}{v^2}$. For the domain of validity of approximations to be the same for all the considered parameter values, we impose that the front speed remains constant, i.e., k, V_0, and D_A are constant. In addition, the values of k, V_0, and D_A are set such that ε is much smaller than 1:

$$k = 10, \quad V_0 = 10, \quad D_A = 1. \tag{43}$$

According to Brunet and Derrida [9], a small cutoff δ introduced in the nonlinear reactive term $\pm kAB$ induces a negative correction to the propagation speed

$$\frac{v - v_s}{v} = \frac{\pi^2}{2(\ln\delta)^2}, \tag{44}$$

where v_s is the velocity of the simulated front. More generally, FKPP wave fronts are known to be sensitive to small perturbations, including fluctuations [14] in stochastic descriptions, perturbation of velocity distribution function [18] in particle dynamics simulations. With the aim of unambiguously assigning the observed perturbations of a wave front to high concentrations, the effect of a cutoff on the numerical results has to be evaluated and disregarded. If sufficiently fine space and time discretizations are employed, the cutoff mainly originates from the precision of the computations involving real numbers. Choosing double precision leads to a cutoff $\delta \simeq 10^{-16}$. Using Eq. (44), the relative correction to the front speed is estimated at 0.4%. The effect of space discretization is similar on wave fronts with profile widths occupying the same number of spatial cells. According to Eqs. (39) and (41), at zeroth order, the width $W_{d,0} = W_{c,0} = 8\sqrt{\frac{D_A}{kV_0}}$ only depends on the rate constant k, the diffusion coefficient D_A of species A, and the boundary condition V_0. For the effect of the cutoff to be the same in all the numerical solutions for different parameters, we impose the cell length, $\Delta x = \frac{\pi W_{d,0}}{5000}$, the total number of cells, $n = 50\,000$, and the time step, $\Delta t = \frac{0.1\Delta x^2}{D_B^{\max}}$, where $D_B^{\max} = 16$ is the maximum diffusion coefficient considered. Hence, the width occupies about 1600 cells in all cases. For the initial condition defined in Eqs. (6), we numerically solve Eqs. (2) and (3) and Eqs. (4) and (5) using the Euler method for different values of the diffusion coefficient D_B in the interval $[\frac{1}{16}, 16]$ and the total concentration C in the interval $[25, 400]$.

To mimic an infinite system in the x direction, it is necessary to counterbalance the production of species A due to the propagation of the reactive front. At each time step where the sum of the concentrations of species A in each cell reaches the initial value $nV_0/2$, the first left cell is suppressed and a new cell is added to the right with no A species and a V_0 concentration for species B. This trick amounts to switching in the moving frame at the propagation speed of the wave front. The speed is numerically evaluated using the time difference between two creations of right cells after the stationary regime has been reached.

For these conditions, we find that the front speeds associated with the dilute and the concentrated cases are the same and about 0.5% smaller than the zeroth-order prediction

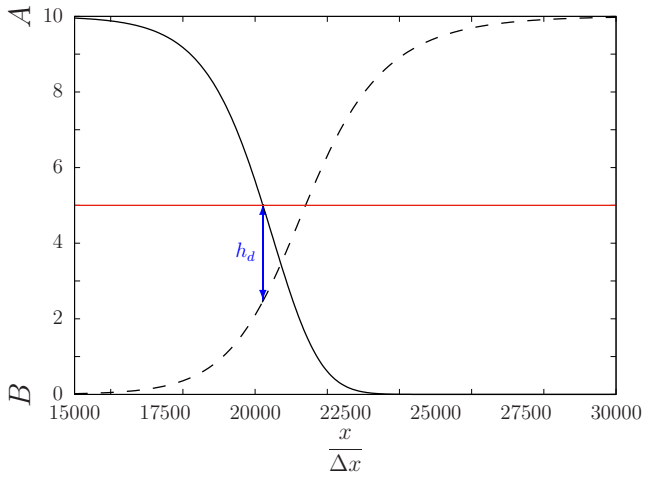

FIG. 1. Snapshot of the wave front profile deduced from Eqs. (2) and (3) with $D_B/D_A = 16$ at time $t = 400$. Concentration profiles of A (black solid line) and B (black dashed line) versus spatial coordinate $\frac{x}{\Delta x}$. The horizontal line represents $\frac{V_0}{2}$. The vertical segment represents the height h_d at $\xi = 0$.

v_d^*. This result is close to the estimation of the cutoff effect induced by double precision. The choice of the other parameters, such as cell length and time step, and the simulation procedure are therefore satisfying. In addition, the numerical results confirm that the propagation speed is not impacted by the perturbation of diffusion induced by high concentrations as predicted in Eq. (18).

Figure 1 shows the stationary concentration profiles of A and B species deduced from the numerical integration of Eqs. (2) and (3) in the dilute case. In agreement with Eq. (33), a large ratio D_B/D_A is chosen for the height h_d illustrating the shift between A and B profiles to be sufficiently large. Whereas the A concentration abruptly vanishes in the leading edge, the B concentration smoothly tends to V_0. A and B profiles are noticeably asymmetric with respect to the $A = \frac{V_0}{2}$ axis. This feature disappears for $D_A = D_B$.

Figure 2(a) shows the variation of the scaled height h_d/V_0 in the dilute case with respect to the ratio of the diffusion coefficients D_B/D_A in logarithmic scale. The first- and second-order analytical expressions $h_{d,1}$ and $h_{d,2}$ given in Eq. (32) and (33) are compared to the results deduced from the numerical integration of Eqs. (2) and (3). The uncertainty on the numerical results due to discretization is smaller than the symbols.

As expected, the height vanishes for $D_B = D_A$. For $D_B/D_A < 1$, the height h_d is positive, and the first-order expression already offers a satisfying approximation. Considering that D_A is set at 1 whereas D_B varies, and that the perturbative term in Eq. (11) is proportional to $\varepsilon_d D_B = \frac{1}{4kV_0}\frac{D_B}{D_A}$, the analytical result is correct provided that D_B is smaller or equal to 1, i.e., $D_B < D_A$. It is worth noting that, as $D_B \to 0$, the height h_d tends to a positive limit slightly larger than $V_0/16$ as predicted by Eq. (33): For fixed B particles, the concentration of species B in the moving frame reaches the value $h_d \simeq V_0/16$, independent of the diffusion coefficient D_A

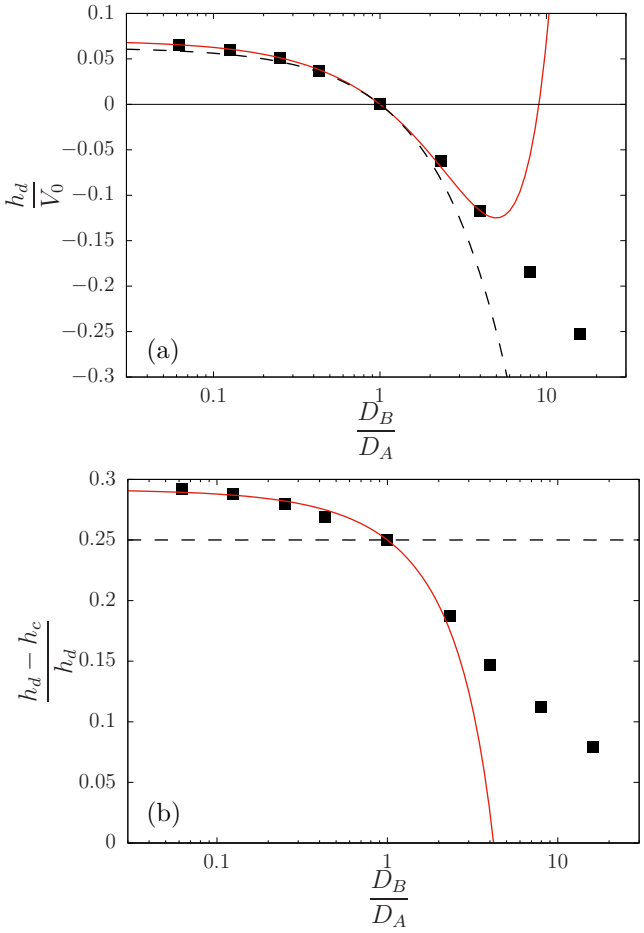

FIG. 2. (a) Scaled height h_d/V_0 in the dilution limit and (b) relative difference between the dilute case and the concentrated case for $V_0/C = 0.25$ versus diffusion coefficients ratio D_B/D_A. First-order approximation (black dashed line), second-order approximation (red solid line), and numerical results (black squares).

of species A at the abscissa $\xi = 0$ for which the concentration of species A equals $V_0/2$.

For $D_B/D_A > 1$, the height h_d is negative. The second-order approximation is valid until $D_B/D_A = 4$ and diverges for larger values of D_B/D_A. In the explored range of D_B/D_A, the height h_d significantly decreases. Still, the scaled height h_d/V_0 is bounded by -0.5 since concentrations cannot be negative.

The behavior of the height h_c associated with the concentrated system is similar to the one of h_d. Nevertheless, as shown in Fig. 2(b), the relative height difference $\frac{h_d - h_c}{h_d}$ is always positive in the entire range of D_B/D_A values. Hence, the shift between the concentration profiles of species A and B induced by the difference between the diffusion coefficients D_A and D_B is reduced in a concentrated system. Actually, according to Eqs. (4) and (5), the diffusion of a given species is affected by the diffusion coefficient of the other species which reduces the effect due to $D_A \neq D_B$. In the limit of large D_B, both h_d and h_c reach the extreme value -0.5 so that the difference $h_d - h_c$ tends to zero. As $D_B \to 0$, the relative height difference $\frac{h_d - h_c}{h_d}$ tends to a positive limit larger than the prediction V_0/C of the first-order approximation

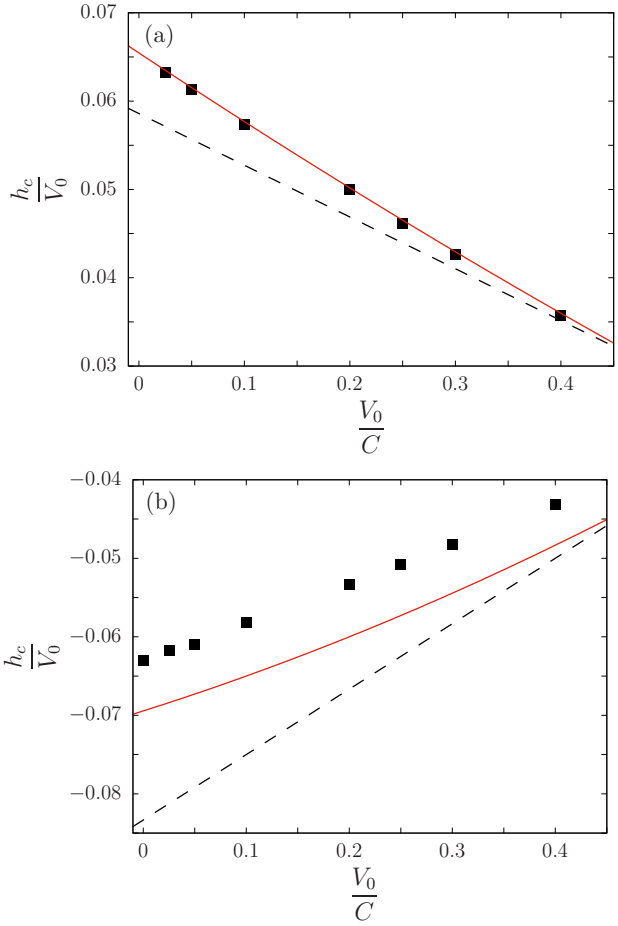

FIG. 3. Scaled height h_c/V_0 versus concentration ratio V_0/C. First-order approximation (black dashed line), second-order approximation (red solid line), and numerical results (black squares) are presented for (a) $D_B/D_A = 1/16$ and (b) $D_B/D_A = 7/3$.

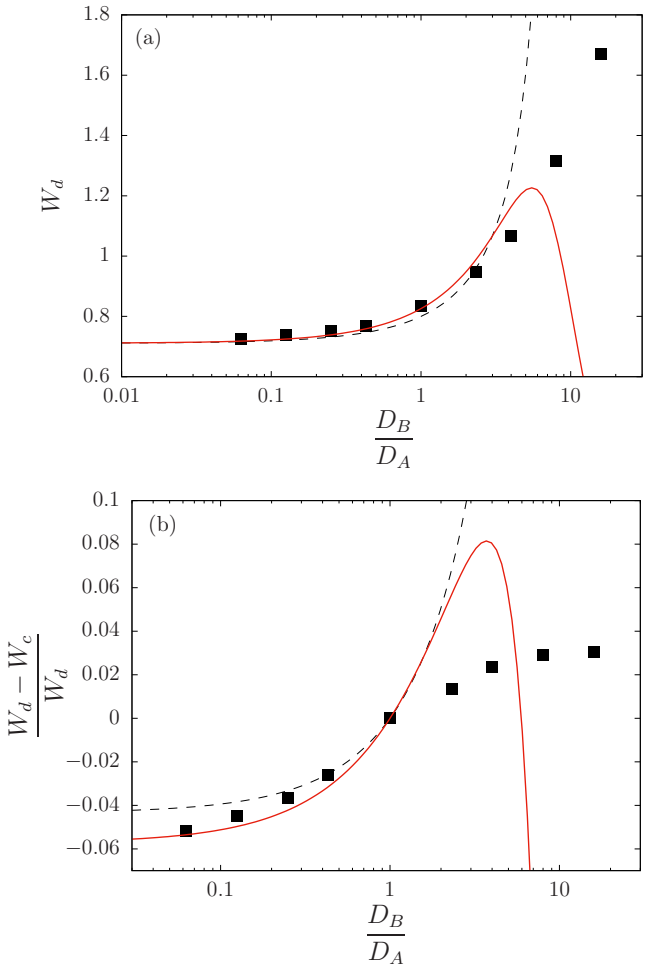

FIG. 4. (a) Width W_d in the dilution limit and (b) relative difference between the dilute case and the concentrated case for $V_0/C = 0.25$ versus the ratio D_B/D_A of diffusion coefficients. First-order approximation (black dashed line), second-order approximation (red solid line), and numerical results (black squares).

deduced from Eqs. (32) and (34). The first-order approximation does not account for the variation of the relative height difference $\frac{h_d - h_c}{h_d}$ with respect to D_B/D_A. The numerical results perfectly agree with the second-order prediction in the domain $D_B/D_A < 1$ for which perturbative analysis is valid. Interestingly, the relative difference of heights reaches 28% for small D_B/D_A values, making the shift between A and B profiles well adapted to the discrimination between the concentrated and the dilute system.

As mentioned in Sec. III, the height h_c only depends on D_B/D_A and V_0/C. The variations of the height h_c in the concentrated system with respect to V_0/C are given in Fig. 3 for two different values of D_B/D_A. The parameter V_0/C quantifies the deviation from the dilution limit obtained for $V_0/C \to 0$. We recall that a concentrated system does not refer to large values of C but to high concentrations $A + B$ of the solute. The results shown in Fig. 2(b) are given for $V_0/C = 0.25$ which is a good compromise between a too small value for which concentration effects would be negligible and a too large value for which the reaction-diffusion equations [Eqs. (4) and (5)] would not be valid. In Fig. 3(a), the results are given for $D_B/D_A = 1/16 < 1$, associated with a positive value of h_c in agreement with the results shown in Fig. 2. We find that the shift between the profiles of A and B species decreases as the system becomes more concentrated, i.e., as V_0/C increases. For the small value of D_B/D_A chosen, the expansion technique rapidly converges and the agreement between the numerical results and the second-order approximation is excellent. In Fig. 3(b), for $D_B/D_A = 7/3 > 1$, the height h_c is negative and decreases in absolute value as V_0/C increases. As already mentioned, the perturbation analysis is less relevant and the second-order prediction deviates from the numerical results. The concentrated system is closer to the standard FKPP front with $D_A = D_B$ than is the dilute system.

Figure 4(a) gives the variation of the front width W_d of species A with respect to the ratio of the diffusion coefficients D_B/D_A in logarithmic scale in the dilute case. The slope s_d of the A concentration profile at $\xi = 0$, deduced from the numerical integration of Eqs. (2) and (3), is evaluated according to

$$s_d = -\frac{0.2V_0}{\xi_2 - \xi_1}, \tag{45}$$

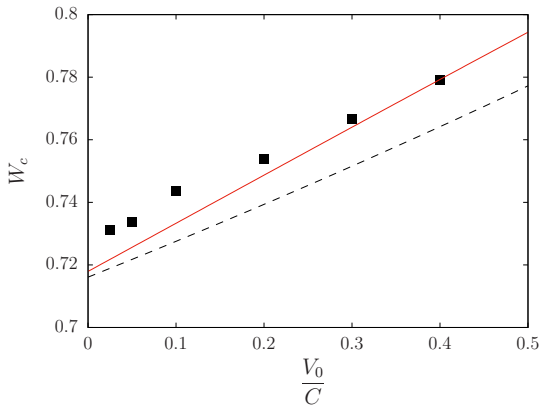

FIG. 5. Width W_c versus concentration ratio V_0/C. First-order approximation (black dashed line), second-order approximation (red solid line), and numerical results (black squares) are presented for $D_B/D_A = 1/16$.

where the abscissa ξ_1 and ξ_2 in the moving frame obey $f_d(\xi_1) = 0.6V_0$ and $f_d(\xi_2) = 0.4V_0$. Equation (36) is used to obtain an estimation of the width of the reactive front. Both the first- and second-order approximations given in Eqs. (39) and (40) satisfactorily agree with the numerical results for $D_B/D_A < 4$.

An analogous procedure is followed to determine an estimation of the width W_c in the concentrated system from the numerical integration of Eqs. (4) and (5). The relative difference $(W_d - W_c)/W_d$ between the widths in the dilute system and the concentrated system versus D_B/D_A is given in Fig. 4(b). It is worth noting that it has been necessary to decrease cell length Δx for $W_c\Delta x$ to reach about 1600 to obtain a sufficient precision in the numerical estimation of the relative correction. This constraint has motivated the choice of the cell length used in this study. For $D_B/D_A \leqslant 1$, a satisfying agreement is obtained between the numerical results and the first and second-order analytical predictions given in Eqs. (39) and (40) in the dilute case and Eqs. (41) and (42) in the concentrated case. Interestingly, the relative correction to the width induced by high concentrations changes sign as D_B/D_A varies but it does not exceed 6% in the best case as $D_B/D_A \to 0$. Hence, for small and medium D_B/D_A values, the width offers a worse criterion than the shift between A and B profiles to discriminate between the concentrated and the dilute systems. However, for significantly large D_B/D_A values, the relative difference of height vanishes whereas the relative difference of widths converges toward about 3%.

According to Eqs. (41) and (42), the front width W_c in a concentrated system depends on D_B/D_A and also the deviation from the dilution limit V_0/C. The variation of W_c with V_0/C is given in Fig. 5 for a sufficiently small ratio of diffusion coefficients $D_B/D_A = 1/16$ for the analytical prediction to be valid. As expected, the width W_c tends to the value $W_d = 0.719$ associated with $D_B/D_A = 1/16$ for $V_0/C \to 0$. The width W_c increases as V_0/C increases: As the system becomes more concentrated, W_c becomes closer to the zeroth-order prediction $W_{d,0} = W_{c,0} = 0.8$ obtained for $D_A = D_B$. Hence, the difference between the profile shape in a concentrated system with $D_B \neq D_A$ and the profile shape in a system with $D_A = D_B$ decreases as V_0/C increases. We already came to an analogous conclusion for the variation of the height h_c with V_0/C as shown in Fig. 3. In conclusion, high concentrations tend to reduce the asymmetry of the profiles induced by the difference of diffusivities D_A and D_B. This phenomenon is due to cross-diffusion in which the diffusion of both species influences the dynamics of each other.

V. CONCLUSION

In this work, we study the effects of concentration-induced perturbation of diffusion on FKPP wave fronts. The sensitivity of FKPP wave front to small perturbations makes it a good candidate for characterizing the effects of the deviation from the dilution limit on diffusion. We assume that high solute concentrations induce specific cross-diffusion terms in the reaction-diffusion equations in the framework of linear nonequilibrium thermodynamics. We consider two chemical species A and B engaged in the reaction $\mathrm{A} + \mathrm{B} \to 2\mathrm{A}$ and with different diffusion coefficients, knowing that the perturbation of diffusion vanishes in the limit of identical diffusion coefficients. The analytical results deduced from a linear stability analysis show that the propagation speed in a concentrated system is not appreciably affected by the perturbation of diffusion. The relative correction of the profile width with respect to the dilute case presents an interesting behavior: It changes sign as the ratio of diffusion coefficients varies. However, the relative correction is in the order of 6% for concentration values in the domain of validity of the reaction-diffusion equations. We introduce the height h as the difference of concentrations between A and B species in the moving frame at the origin to evaluate the shift between A and B profiles due to their different diffusion coefficients. Contrary to the width, the relative correction to the height h with respect to the dilute case reaches 28% for reasonable solute concentrations. The relative correction to the height is larger than 25% when the diffusion coefficient of species B is smaller than the one of species A. The diffusion coefficient of species B has to become at least 30 times larger than the diffusion coefficient of species A for the relative correction to the height to drop below 5%. In the limit of very large diffusion coefficients of species B, the width of the profile may be chosen as an alternative criterion to detect concentration-induced perturbations since the relative correction to the width converges to about 3% in this limit. We conclude that the FKPP wave front offers the opportunity to characterize concentration-induced perturbation of diffusion. Specifically, the shift of the concentration profiles of species associated with different diffusion coefficients is a well-adapted criterion showing significant variations with the deviation from the dilution limit in a wide range of diffusion coefficients.

ACKNOWLEDGMENTS

This publication is part of a project that has received funding from the European Union's Horizon 2020 (H2020-EU.1.3.4.) research and innovation program under the Marie Skłodowska-Curie Actions (MSCA-COFUND ID 711859) and from the Polish Ministry of Science and Higher Education for the implementation of an international cofinanced project.

[1] R. A. Fisher, Annals of Eugenics **7**, 355 (1937).
[2] A. N. Kolmogorov, I. G. Petrovsky, and N. S. Piskunov, Moscow Univ. Math. Bull. **1**, 1–25 (1937).
[3] J. Fort and T. Pujol, Rep. Prog. Phys. **71**, 086001 (2008).
[4] J. D. Murray, *Mathematical Biology* (Springer, Berlin, 1989).
[5] V. Mendez, S. Fedotov, and W. Horsthemke, *Reaction-Transport Systems: Mesoscopic Foundations, Fronts, and Spatial Instabilities* (Springer, Berlin, 2010).
[6] V. Mendez, D. Campos, and F. Bartumeus, *Stochastic Foundations in Movement Ecology: Anomalous Diffusion, Invasion Fronts and Random Searches* (Springer, Berlin, 2014).
[7] W. van Saarloos, Phys. Rep. **386**, 29 (2003).
[8] D. Panja and W. van Saarloos, Phys. Rev. E **65**, 057202 (2002).
[9] E. Brunet and B. Derrida, Phys. Rev. E **56**, 2597 (1997).
[10] D. Panja, Phys. Rep. **393**, 87 (2004).
[11] G. Nicolis and I. Prigogine, *Self-Organization in Nonequilibrium Systems* (Wiley, New York, 1977).
[12] C. W. Gardiner, *Handbook of Stochastic Methods for Physics, Chemistry and the Natural Sciences* (Springer, Berlin, 1985).
[13] G. A. Bird, *Molecular Gas Dynamics and the Direct Simulation of Glas Flows* (Clarendon, Oxford, 1994).
[14] J. S. Hansen, B. Nowakowski, and A. Lemarchand, J. Chem. Phys. **124**, 034503 (2006).
[15] J. G. Conlon and C. R. Doering, J. Stat. Phys. **120**, 421 (2005).
[16] E. Brunet, B. Derrida, A. H. Mueller, and S. Munier, Phys. Rev. E **73**, 056126 (2006).
[17] G. Dumazer, C. Antoine, A. Lemarchand, and B. Nowakowski, Phys. Rev. E **80**, 066309 (2009).
[18] A. Lemarchand and B. Nowakowski, J. Chem. Phys. **109**, 7028 (1998).
[19] V. Mendez, D. Campos, I. Pagonabarraga, and S. Fedotov, J. Theor. Biol. **309**, 113 (2012).
[20] A. Tzella and J. Vanneste, Siam J. Appl. Math. **75**, 1789 (2015).
[21] R. Kollar and S. Nowak, Bull. Math. Biol. **79**, 525 (2017).
[22] S. R. de Groot and P. Mazur, *Non-Equilibrium Thermodynamics* (North-Holland, Amsterdam, 1962).
[23] D. Bullara, Y. De Decker, and R. Lefever, Phys. Rev. E **87**, 062923 (2013).
[24] L. Signon, B. Nowakowski, and A. Lemarchand, Phys. Rev. E **93**, 042402 (2016).
[25] V. K. Vanag and I. R. Epstein, Phys. Chem. Chem. Phys. **11**, 897–912 (2009).
[26] D. G. Leaist, Phys. Chem. Chem. Phys. **4**, 4732 (2002).
[27] V. K. Vanag, F. Rossi, A. Cherkashin, and I. R. Epstein, J. Phys. Chem. B **112**, 9058 (2008).
[28] F. Rossi, V. K. Vanag, and I. R. Epstein, Chem. A Eur. J. **17**, 2138 (2011).
[29] M. A. Budroni, L. Lemaigre, A. De Wit, and F. Rossi, Phys. Chem. Chem. Phys. **17**, 1593 (2015).
[30] M. A. Budroni, J. Carballido-Landeira, A. Intiso, A. De Wit, and F. Rossi, Chaos **25**, 064502 (2015).
[31] G. Morgado, B. Nowakowski, and A. Lemarchand, Phys. Rev. E **98**, 032213 (2018).
[32] V. Mendez, J. Fort, H. G. Rotstein, and S. Fedotov, Phys. Rev. E **68**, 041105 (2003).
[33] J. Berestycki, E. Brunet, and B. Derrida, Europhys. Lett. **122**, 10001 (2018).

IV.2.2 Stochastic description

The results I obtained in Sec. IV.2.1 within the framework of a deterministic description show that introducing different diffusion coefficients $D_A \neq D_B$ does not modify the wave-front speed.

The contribution of a stochastic description involving discrete random variables, as is the case for a master equation, is specially valuable. Using Gillespie algorithm recalled in Sec.I.4.1, I performed simulations of the master equation associated with the reaction A+B $\longrightarrow$ 2 A and $D_A \neq D_B$. The results are qualitatively different from the results of the deterministic description. The master equation predicts that the propagation speed of the front is sensitively decreased if species B diffuses faster than species A. Typically, the front speed is reduced by 22% for $D_B = 16D_A$. This result can be qualitatively interpreted as follows. The fast diffusion of particles B quickly brings them to the vicinity of A particles where they are consumed by the autocatalytic reaction. Contrary to intuition, a large value of D_B leads to a smoother B profile. Hence, the rightmost particle A is surrounded by a smaller number of particles B than in the case $D_B \leq D_A$ and the front propagates more slowly.

From a theoretical point of view, this result is the most striking contribution of my PhD work. It is rewarding to bring out a new result on a problem that is more than 80 years old.

Using a deterministic analogy inspired from the cutoff approach of Brunet and Derrida, I consider Eqs. (IV.27) and (IV.28) in which a cutoff ϵ is introduced

$$\partial_t c_A = k c_A c_B \Theta(\frac{c_A}{c^{\text{tot}}} - \varepsilon) + D_A \partial_x^2 c_A \tag{IV.34}$$

$$\partial_t c_B = -k c_A c_B \Theta(\frac{c_A}{c^{\text{tot}}} - \varepsilon) + D_B \partial_x^2 c_B \tag{IV.35}$$

The linear analysis leads to a correction to front speed obeying Eq. (IV.26) which does not account for the behavior at large D_B. The problem is nonlinear and the linear cutoff approach presented in Sec. IV.1.2 fails. As suggested in Fig. IV.4, I conjecture that, for $D_B > D_A$, the leading edge of the A profile sees a smaller concentration of B than for $D_B \leq D_A$, leading to the empirical formula

$$v_\varepsilon = 2\sqrt{2 c_{B_\varepsilon} D_A}\left(1 - \frac{\pi^2}{2(\ln \varepsilon)^2}\right) \tag{IV.36}$$

where the B concentration c_{B_ϵ} at the abscissa x_ϵ for which $c_A(x_\epsilon)/c^{tot} = \epsilon$ is deduced from the numerical integration of the deterministic equations.

The results of the master equation satisfactorily agree with the empirical formula in which, according to reference [103], the cutoff ϵ is evaluated by the inverse of the

number of particles in the reactive interface. Despite intensive efforts and trials involving many methods, I could not derive an analytical prediction of the correction to the front speed for $D_B > D_A$. Using the perturbative approach in power of $1/v^2$ developed in the deterministic case as explained in Sec. IV.2.1 does not help as the nonlinear effect of D_B is lost when Eqs. (IV.34) and (IV.35) are linearized. Deducing the variance $\langle c_A c_B \rangle$ from a Langevin approach as in Sec. II is of no use because it involves continuous variables and even misses the linear cutoff effect. Applying the Hamilton-Jacobi technique to solve the master equation [108, 109] is also not successful. The effect of fast diffusion of the consumed species on the propagation speed that I numerically evidenced opens new perspectives in the fundamental description of Fisher - Kolmogorov, Petrovsky and Piskunov wave fronts.

a) Concentrated system

In a stochastic description using a master equation, diffusion is a jump process from one spatial cell to an adjacent cell. In a dilute system, the diffusion rate of a given species only depends on the number of particles of that species in the departure cell. The main difficulty in the master equation approach to a concentrated system is the definition of the transition rates including cross-diffusion.

I considered the master equation given in Eq. (I.30) and wrote the associated diffusion term as

$$\begin{aligned}\partial_t P(\{\Phi\},t)|_{\text{diffusion}} = \sum_i [&T^-_{N_A(i)+1} P(\{N_A(i-1)-1, N_A(i)+1\}) \\ &+ T^+_{N_A(i)+1} P(\{N_A(i)+1, N_A(i+1)-1\}) \\ &+ T^-_{N_B(i)+1} P(\{N_B(i-1)-1, N_B(i)+1\}) \\ &+ T^+_{N_B(i)+1} P(\{N_B(i)+1, N_B(i+1)-1\})] \end{aligned} \tag{IV.37}$$

where $T^{\pm}_{N_X(i)}$ are the transition rates associated with the jump of a particle X=A,B from cell i containing $N_X(i)$ particles to the left (-) or the right (+), respectively. The transition rates must be compatible with the macroscopic diffusion fluxes given in Eqs. (I.61) and (I.62). Consequently, $T^{\pm}_{N_X(i)}$ has a nontrivial dependence on the particle numbers of the two species in both the departure and arrival cells.

In order to propose an appropriate expression of $T^{\pm}_{N_X(i)}$, I introduced a discrete flux $j_X(i+1/2)$ at the interface between the cells i and $i+1$ and related it to the difference of transition rates to the left and to the right. Using Eqs. (I.61) and (I.62) and replacing $\partial_x c_X$ by $\dfrac{N_X(i+1)-N_X(i)}{\Omega \Delta x}$ where Ω stands for the volume of a single cell, I assigned

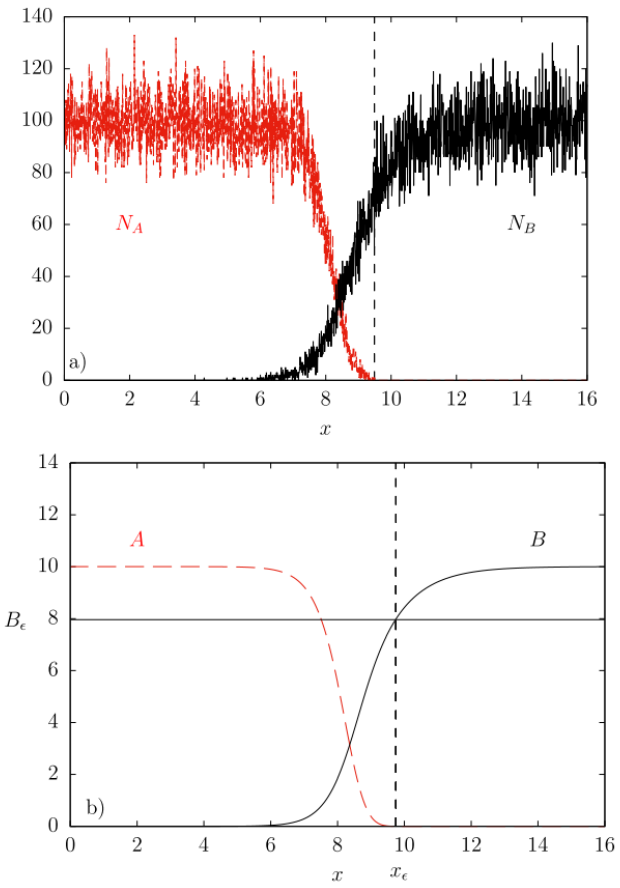

Fig. IV.4 *(a) Numbers N_A of particles A (red dashed line) and N_B of particles B (black solid line) versus spatial coordinate x deduced from simulation of the master equation for $D_A = 1$, $D_B = 16$ (other parameter values given in reference [44]). The vertical dashed line indicates the rightmost cell occupied by A particles. (b) Concentrations c_A of species A (red dashed line) and c_B of species B (black solid line) versus spatial coordinate x deduced from numerical integration of the deterministic equations in the presence of a cutoff ϵ. The vertical dashed line indicates the abscissa x_ϵ for which the scaled A concentration $c_A(x_\epsilon)/c^{tot}$ reaches the cutoff value ϵ. The horizontal line indicates the value c_{B_ϵ} of B concentration at the abscissa x_ϵ.*

well-chosen terms of the flux $j_X(i+1/2)$ to the transition rates to the left and to the right

$$T^{\pm}_{N_A(i)} = \frac{D_A}{\Delta x^2} N_A(i) - \frac{N_A(i \pm 1/2)}{\Omega c^{\text{tot}} \Delta x^2} [D_A N_A(i) - D_B N_B(i \pm 1)] \tag{IV.38}$$

$$T^{\pm}_{N_B(i)} = \frac{D_B}{\Delta x^2} N_B(i) - \frac{N_B(i \pm 1/2)}{\Omega c^{\text{tot}} \Delta x^2} [D_B N_B(i) - D_A N_A(i \pm 1)] \tag{IV.39}$$

in order to ensure that $T^{\pm}_{N_X(i)}$ is positive or equal to zero for any number of particles.

The expression of $T^{\pm}_{N_X(i)}$ depends on the number of particles $N_X(i+1/2)$ at the interface between two cells. Various definitions of this number of particles may be proposed. I checked that different definitions, all ensuring that the transition rate vanishes when the departure cell is empty, lead to similar results.
Simulations of the resulting master equation using Gillespie algorithm have been performed for different values of the diffusion coefficient D_B of species B. I found that the decrease of the propagation speed of the front observed as D_B increases is mitigated by cross-diffusion which reduces the impact of different diffusion coefficients.

b) Publication

In addition to evidencing fluctuation effects on front speed, which constitutes the major result, I characterized profile width W and height h in the stochastic approach, in both the dilute and concentrated cases. The results about W and h are closer to what could be expected after the deterministic study [43]. All my results about the stochastic approach to FKPP fronts are published in the article "Stochastic approach to Fisher and Kolmogorov, Petrovskii, and Piskunov wave fronts for species with different diffusivities in dilute and concentrated solutions", G. Morgado, B. Nowakowski, and A. Lemarchand, Physica A, **558**, 124954 (2020) [44].

Physica A 558 (2020) 124954

Contents lists available at ScienceDirect

Physica A

journal homepage: www.elsevier.com/locate/physa

Stochastic approach to Fisher and Kolmogorov, Petrovskii, and Piskunov wave fronts for species with different diffusivities in dilute and concentrated solutions

Gabriel Morgado [a,b], Bogdan Nowakowski [a], Annie Lemarchand [b,*]

[a] Institute of Physical Chemistry, Polish Academy of Sciences, Kasprzaka 44/52, 01-224 Warsaw, Poland
[b] Laboratoire de Physique Théorique de la Matière Condensée, Sorbonne Université, CNRS UMR 7600, 4 place Jussieu, case courrier 121, 75252 Paris CEDEX 05, France

ARTICLE INFO

Article history:
Received 6 November 2019
Received in revised form 6 July 2020
Available online 22 July 2020

Keywords:
Wave front
Stochastic description
Master equation
Cross-diffusion

ABSTRACT

A wave front of Fisher and Kolmogorov, Petrovskii, and Piskunov type involving two species A and B with different diffusion coefficients D_A and D_B is studied using a master equation approach in dilute and concentrated solutions. Species A and B are supposed to be engaged in the autocatalytic reaction A+B $\rightarrow$ 2A. Contrary to the results of a deterministic description, the front speed deduced from the master equation in the dilute case sensitively depends on the diffusion coefficient of species B. A linear analysis of the deterministic equations with a cutoff in the reactive term cannot explain the decrease of the front speed observed for $D_B > D_A$. In the case of a concentrated solution, the transition rates associated with cross-diffusion are derived from the corresponding diffusion fluxes. The properties of the wave front obtained in the dilute case remain valid but are mitigated by cross-diffusion which reduces the impact of different diffusion coefficients.

1. Introduction

Wave fronts propagating into an unstable state according to the model of Fisher and Kolmogorov, Petrovskii, and Piskunov (FKPP) [1,2] are encountered in many fields [3], in particular biology [4] and ecology [5]. Phenotype selection through the propagation of the fittest trait [6] and cultural transmission in neolithic transitions [7] are a few examples of applications of FKPP fronts. The model introduces a partial differential equation with a logistic growth term and a diffusion term.

The effect of non standard diffusion on the speed of FKPP front is currently investigated [8–11] and we recently considered the propagation of a wave front in a concentrated solution in which cross-diffusion cannot be neglected [12]. Experimental evidence of cross-diffusion has been given in systems involving ions, micelles, surface, or polymer reactions and its implication in hydrodynamic instabilities has been demonstrated [13–18]. In parallel, cross-diffusion is becoming an active field of research in applied mathematics [19–24].

The sensitivity of FKPP fronts to fluctuations has been first numerically observed [25,26]. An interpretation has been then proposed in the framework of a deterministic approach introducing a cutoff in the logistic term [27]. In mesoscopic or microscopic descriptions of the invasion front of A particles engaged in the reaction A + B $\rightarrow$ 2A, the discontinuity induced by the rightmost particle in the leading edge of species A profile amounts to a cutoff in the reactive term. The

* Corresponding author.
E-mail address: annie.lemarchand@sorbonne-universite.fr (A. Lemarchand).

https://doi.org/10.1016/j.physa.2020.124954
0378-4371/

inverse of the number of particles in the reactive interface gives an estimate of the cutoff [28]. The study of the effect of fluctuations on FKPP fronts remains topical [29,30]. In this paper we perform a stochastic analysis of a reaction–diffusion front of FKPP type in the case of two species A and B with different diffusion coefficients [31], giving rise to cross-diffusion phenomena in concentrated solutions.

The paper is organized as follows. Section 2 is devoted to a dilute system without cross-diffusion. The effects of the discrete number of particles on the front speed, the shift between the profiles of the two species and the width of species A profile are deduced from a master equation approach. In Section 3, we derive the expression of the master equation associated with a concentrated system inducing cross-diffusion and compare the properties of the FKPP wave front in the dilute and the concentrated cases. Conclusions are given in Section 4.

2. Dilute system

We consider two chemical species A and B engaged in the reaction

$$\mathrm{A} + \mathrm{B} \xrightarrow{k} 2\mathrm{A}, \tag{1}$$

where k is the rate constant. The diffusion coefficient, D_A, of species A may differ from the diffusion coefficient, D_B, of species B.

In a deterministic approach, the reaction–diffusion equations are

$$\partial_t A = D_A \partial_x^2 A + kAB \tag{2}$$

$$\partial_t B = D_B \partial_x^2 B - kAB \tag{3}$$

where the concentrations of species A and B are denoted by A and B. The system admits wave front solutions propagating without deformation at constant speed. For sufficiently steep initial conditions and in particular step functions ($A(x, t = 0) = C_0 H(-x)$ and $B(x, t = 0) = C_0 H(x)$), where C_0 is constant and $H(x)$ is the Heaviside function, the minimum velocity

$$v^* = 2\sqrt{kC_0 D_A} \tag{4}$$

is selected [3,4,27]. The parameter $C_0 = A(x, 0)+B(x, 0)$ is the sum of the initial concentrations of species A and B. Discrete variables of space, $i = x/\Delta x$, and time, $s = t/\Delta t$, where Δx is the cell length and Δt is the time step, are introduced in order to numerically solve Eqs. (2) and (3) in a wide range of diffusion coefficients D_B. We consider a system of $\ell = 2000$ spatial cells. The initial condition is a step function located in the cell $i_0 = \ell/2$

$$A(i, 0) = C_0 H(i_0 - i), \tag{5}$$

$$B(i, 0) = C_0 H(i - i_0), \tag{6}$$

where $H(i)$ is the Heaviside function. In order to simulate a moving frame and to counterbalance the autocatalytic production of species A in a finite system, the following procedure is applied. At the time steps s such that $\sum_{i=1}^{\ell} A(i, s) > \sum_{i=1}^{\ell} A(i, 0)$, the first cell is suppressed and a last cell with $A(\ell, s) = 0$ and $B(\ell, s) = C_0$ is created. Hence, the inflection point of the front profile remains close to the initial step of the Heaviside function.

In small systems with typically hundreds of particles per spatial cell, the deterministic description may fail and a stochastic approach is required. We consider the chemical master equation associated with Eq. (1) [32,33]. The master equation is divided into two parts

$$\left.\frac{\partial P(\phi)}{\partial t}\right| = \left.\frac{\partial P(\phi)}{\partial t}\right|_{\mathrm{reac}} + \left.\frac{\partial P(\phi)}{\partial t}\right|_{\mathrm{diff}} \tag{7}$$

where the first part corresponds to the reactive terms

$$\left.\frac{\partial P(\phi)}{\partial t}\right|_{\mathrm{reac}} = \sum_i \frac{k}{\Omega N_0}\Big[(N_A(i) - 1)(N_B(i) + 1)P(\{N_A(i) - 1, N_B(i) + 1\}) - N_A(i)N_B(i)P(\phi)\Big] \tag{8}$$

and the second part corresponds to the diffusion terms

$$\begin{aligned}\left.\frac{\partial P(\phi)}{\partial t}\right|_{\mathrm{diff}} = \sum_i \Bigg[& \frac{D_A}{\Delta x^2}(N_A(i) + 1)\Big[P(\{N_A(i-1) - 1, N_A(i) + 1\}) \\ & + P(\{N_A(i) + 1, N_A(i+1) - 1\})\Big] \\ & + \frac{D_B}{\Delta x^2}(N_B(i) + 1)\Big[P(\{N_B(i-1) - 1, N_B(i) + 1\}) \\ & + P(\{N_B(i) + 1, N_B(i+1) - 1\})\Big]\end{aligned}$$

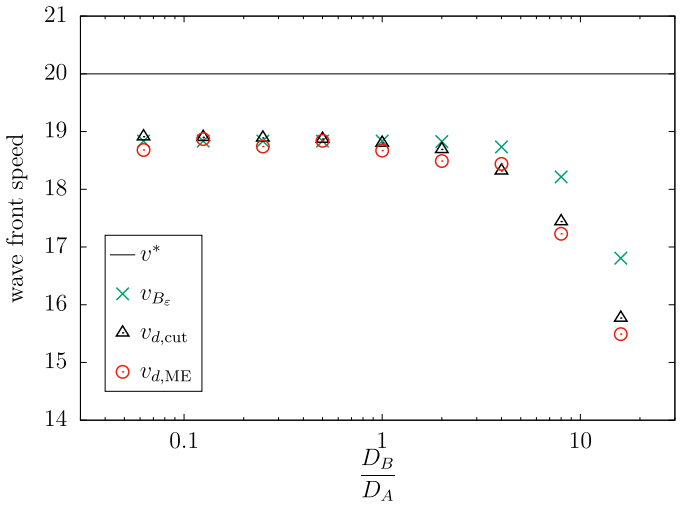

Fig. 1. Dilute system. Wave front speeds $v_{d,\mathrm{ME}}$, $v_{d,\mathrm{cut}}$, v_{B_ε}, and $v_d = v^*$ versus ratio of diffusion coefficients D_B/D_A in the dilute case. The values of $v_{d,\mathrm{ME}}$ (red circles) are deduced from the direct simulation of the master equation (Eqs. (7)–(9)) for $k = 10$, $\Omega = 10$, $N_0 = 100$, $D_A = 1$, $\ell = 2000$, and $\Delta x = 0.008$. The values of $v_{d,\mathrm{cut}}$ (black open triangles) are deduced from the numerical integration of the deterministic equations (Eqs. (14) and (15)) in the presence of a cutoff $\varepsilon = 10^{-4}$ for $k = 10$, $C_0 = 10$, $D_A = 1$, $\ell = 2000$, $\Delta x = 0.008$, and $\Delta t = 6.4 \times 10^{-6}$. The values of v_{B_ε} (green crosses) are deduced from Eq. (16) in which the value B_ε has been deduced from the numerical integration of Eqs. (14) and (15). The horizontal line gives the minimum velocity $v_d = v^*$ (Eq. (4)) of an FKPP front in the absence of a cutoff.

$$- \frac{2}{\Delta x^2}\big(D_A N_A(i) + D_B N_B(i)\big)P(\phi)\Big] \tag{9}$$

where $\phi = \{N_A(i), N_B(i)\}$ denotes the default state, Ω, the typical size of the system, $N_0 = \Omega C_0$, the initial total number of particles in a cell, and $N_A(i) = \Omega A(i)$ and $N_B(i) = \Omega B(i)$ are the numbers of particles A and B in cell i. We consider parameter values leading to the macroscopic values used in the deterministic approach. The initial condition is given by $(N_A(i) = N_0, N_B(i) = 0)$ for $1 \le i < \ell/2$ and $(N_A(i) = 0, N_B(i) = N_0)$ for $\ell/2 \le i \le \ell$ with $N_0 = 100$, $\Omega = 10$ ($C_0 = 10$).

The kinetic Monte Carlo algorithm developed by Gillespie is used to directly simulate the reaction and diffusion processes and numerically solve the master equation [34]. The procedure used in the deterministic approach to evaluate the front speed is straightforwardly extended to the fluctuating system.

2.1. Front speed

For sufficiently small spatial lengths Δx and time steps Δt, the numerical solution of the deterministic equations given in Eqs. (2) and (3) leads to the same propagation speed v_d, where the index d stands for dilute, in the entire range of D_B/D_A values [12]. The number of cells created during 10^7 time steps once a stationary propagation is reached is used to evaluate the front speed. For the chosen parameter values, we find a propagation speed obeying $v_d = v^* = 20$ with an accuracy of 0.4%: No appreciable deviation from the unperturbed deterministic prediction given in Eq. (4) is observed. In particular, the front speed v_d does not depend on the diffusion coefficient D_B. The front speed deduced from the direct simulation of Eqs. (7)–(9) is denoted $v_{d,\mathrm{ME}}$ where the index d stands for dilute and the index ME for master equation. As shown in Fig. 1, the velocity $v_{d,\mathrm{ME}}$ is smaller than the deterministic prediction v^* given in Eq. (4).

As long as D_B remains smaller than or equal to D_A, the velocity $v_{d,\mathrm{ME}}$ is constant. The main result of the master equation approach is that the front speed drops as D_B increases above D_A. Typically, for $D_B/D_A = 16$, the velocity $v_{d,\mathrm{ME}}$ is reduced by 22% with respect to $v_d = v^*$. Due to computational costs, larger D_B/D_A values were not investigated.

In the case of identical diffusion coefficients for the two species, the decrease of the front speed observed in a stochastic description is interpreted in the framework of the cutoff approach introduced by Brunet and Derrida [27]. For $D_A = D_B$, the dynamics of the system is described by a single equation. When a cutoff ε is introduced in the reactive term according to

$$\partial_t A = \partial_x^2 A + kA(C_0 - A)H(A - \varepsilon), \tag{10}$$

the velocity is given by

$$v_\varepsilon = v^*\left(1 - \frac{\pi^2}{2(\ln \varepsilon)^2}\right) \tag{11}$$

In a particle description, the cutoff is interpreted as the inverse of the total number of particles in the reactive interface [28]:

$$\varepsilon = \frac{\Delta x}{N_0 W^*} \tag{12}$$

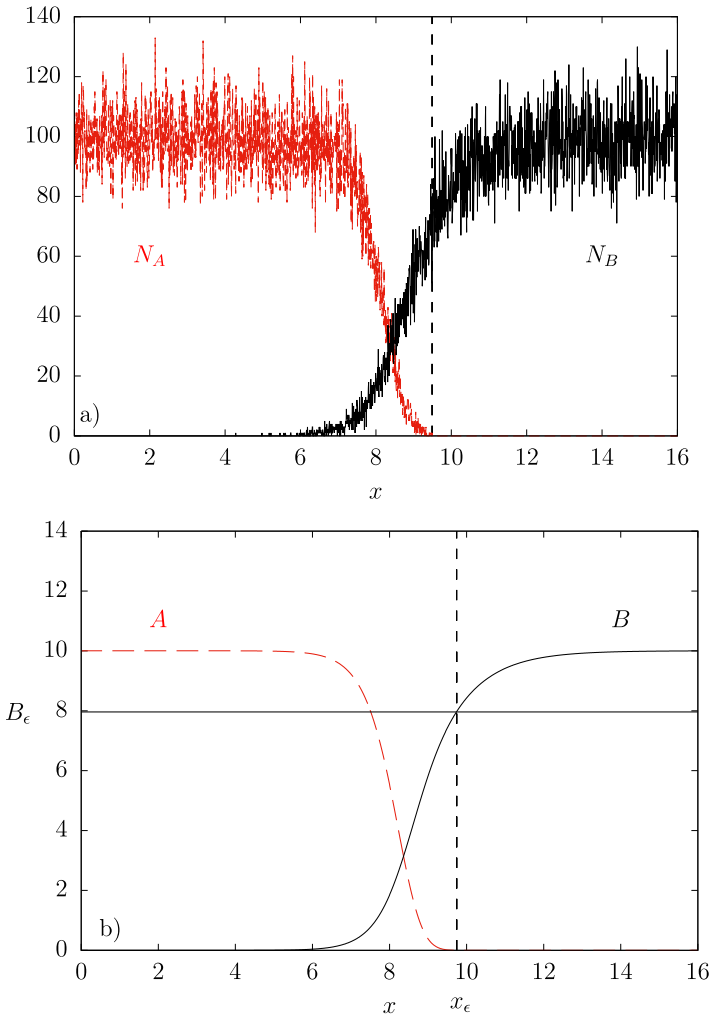

Fig. 2. Dilute system. (a) Numbers N_A of particles A (red dashed line) and N_B of particles B (black solid line) versus spatial coordinate x deduced from direct simulation of the master equation (Eqs. (7)–(9)) using Gillespie method. The snapshot is given at time $t = 9$ for $k = 10$, $\Omega = 10$, $N_0 = 100$, $D_A = 1$, $D_B = 16$, $\ell = 2000$, and $\Delta x = 0.008$. The vertical dashed line indicates the rightmost cell occupied by A particles. (b) Concentrations A of species A (red dashed line) and B of species B (black solid line) versus spatial coordinate x deduced from numerical integration of the deterministic equations (Eqs. (14) and (15)) in the presence of a cutoff $\varepsilon = 10^{-4}$. The snapshot is given at time $t = 640$ for the same other parameters as in the master equation approach. The vertical dashed line indicates the abscissa x_ε for which the scaled A concentration $A(x_\varepsilon)/C_0$ reaches the cutoff value. The horizontal line indicates the value B_ε of B concentration at the abscissa x_ε.

where the width of the interface is roughly evaluated at [4,12]

$$W^* = 8\sqrt{\frac{D_A}{kC_0}} \tag{13}$$

For the chosen parameter values, the cutoff equals $\varepsilon = 10^{-4}$ leading to the corrected speed $v_\varepsilon = 18.84$. According to Fig. 1, the velocity $v_{d,\mathrm{ME}}$ deduced from the master equation for $D_A = D_B$ agree with the velocity v_ε deduced from the cutoff approach. The results are unchanged for $D_B < D_A$ and Eq. (11) correctly predicts the velocity in a fluctuating system. For $D_B > D_A$, Eq. (11) is not valid. Nevertheless, the relevance of the cutoff approach can be checked by numerically integrating the two following equations

$$\partial_t A = D_A \partial_x^2 A + kABH(A - \varepsilon) \tag{14}$$

$$\partial_t B = D_B \partial_x^2 B - kABH(A - \varepsilon) \tag{15}$$

The values of the front speed $v_{d,\mathrm{cut}}$ deduced from the numerical integration of Eqs. (14) and (15) are given in Fig. 1 and satisfactorily agree with the results $v_{d,\mathrm{ME}}$ of the master equation, including for large D_B/D_A values.

According to Fig. 2a, the A profile is steeper than the B profile for $D_B > D_A$. The mean number of B particles in the leading edge smoothly converges to N_0. In average, the rightmost A particle sees a number of B particles smaller than N_0. The significant decrease of the front velocity $v_{d,\mathrm{cut}}$ for $D_B > D_A$ is qualitatively interpreted by the apparent number N_ε of B particles seen by the rightmost A particle in the leading edge. The linear analysis of Eqs. (14) and (15) according to the

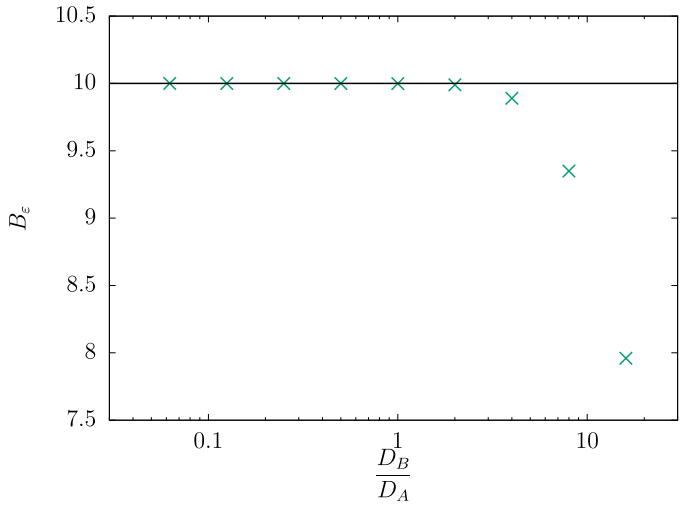

Fig. 3. Dilute system. The green crosses give the value B_ε deduced from the numerical integration of the deterministic equations (Eqs. (14) and (15)) with a cutoff $\varepsilon = 10^{-4}$ versus the ratio of the diffusion coefficients D_B/D_A. The horizontal line indicates the concentration C_0. The parameters are given in the caption of Fig. 1.

cutoff approach [27] leads to Eq. (11) which does not account for the behavior at large D_B. A nonlinear analysis would be necessary. Using the perturbative approach that we developed in the case of the deterministic description [4,12], applying the Hamilton–Jacobi technique [35,36], or deducing the variance $\langle AB\rangle$ from a Langevin approach [37], we unsuccessfully tried to find an analytical estimation of the front speed. Instead, we suggest the following empirical expression of the velocity of an FKPP front for two species with different diffusion coefficients

$$v_{B_\varepsilon} = 2\sqrt{kB_\varepsilon D_A}\left(1 - \frac{\pi^2}{2(\ln\varepsilon)^2}\right) \tag{16}$$

where B_ε denotes the concentration of B species at the abscissa x_ε at which the scaled concentration $A(x_\varepsilon)/C_0$ is equal to the cutoff ε (see Fig. 2b). The variation of B_ε versus D_B/D_A is numerically evaluated using Eqs. (14) and (15). The result is given in Fig. 3.

As shown in Fig. 1, the variation of the front speed v_{B_ε} with D_B/D_A deduced from Eq. (16) slightly underestimates the results $v_{d,\mathrm{cut}}$ deduced from the numerical integration of the deterministic equations (Eqs. (14) and (15)) with a cutoff.

2.2. Profile properties

We focus on two steady properties of the wave front, the shift between the profiles of species A and B and the width of species A profile [12].

For a wave front propagating at speed v and using the coordinate $z = x - vt$ in the moving frame, the shift between the profiles of the two species is defined as the difference $A(z=0) - B(z=0)$ of concentrations between species A and B at the origin $z = 0$ chosen such that $A(z=0) = C_0/2$. The shift is denoted by h_d, where the index d stands for dilute, when the concentrations are solutions of the deterministic equations without cutoff given in Eqs. (2) and (3). As shown in Fig. 4, the shift h_d significantly varies with the ratio D_B/D_A, in particular when D_B is larger than D_A [12]. The shift vanishes for $D_A = D_B$, is positive for $D_B < D_A$ and negative for $D_B > D_A$.

The direct simulation of the master equation leads to highly fluctuating profiles. We use the following strategy to compute the shift $h_{d,\mathrm{ME}}$. First, starting from the leftmost cell, we scan to the right to determine the label i_l of the first cell in which the number of A particles drops under $N_0/2$ and store $N_B(i_l, s)$ for a large discrete time s at which the profile has reached a steady shape. Then, starting from the rightmost cell labeled ℓ, we follow a similar procedure and determine the label i_r of the first cell in which the number of A particles overcomes $N_0/2$ and store $N_B(i_r, s)$ for the same discrete time s. The instantaneous value of the shift deduced from the master equation at discrete time s is then given by $(N_0 - N_B(i_l, s) - N_B(i_r, s))/2\Omega$. The values of the shift $h_{d,\mathrm{ME}}$ used to draw Fig. 4 are obtained after a time average between the times $t = 1$ and $t = 10$ in arbitrary units, i.e. between $s = 1.5 \times 10^5$ and $s = 1.5 \times 10^6$ in number of time steps.

The shift $h_{d,\mathrm{ME}}$ between the profiles of A and B is sensitive to the fluctuations of the number of particles described by the master equation. Introducing an appropriate cutoff satisfying Eq. (12) in the reactive term of the deterministic equations given in Eqs. (14) and (15) leads to values of the shift $h_{d,\mathrm{cut}}$ in very good agreement with the results $h_{d,\mathrm{ME}}$ of the master equation.

Considering the deterministic equations, we deduce the width of A profile from the steepness $A'(0)$ in the moving frame at the origin $z = 0$ and find

$$W_d = C_0/|A'(0)| \tag{17}$$

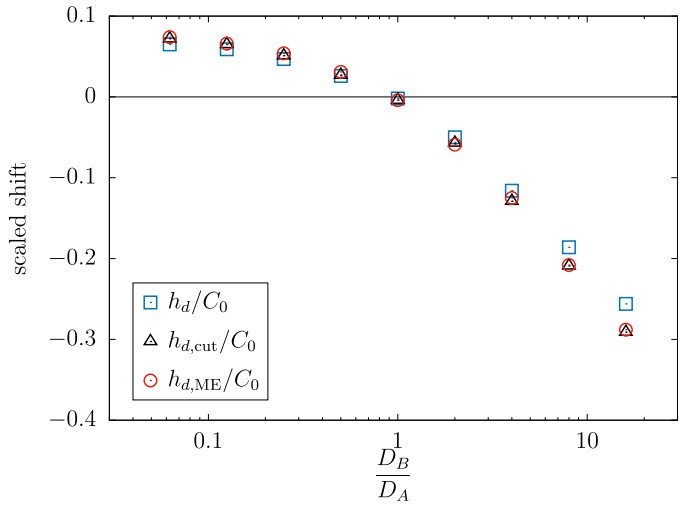

Fig. 4. Dilute system. Scaled shifts $h_{d,\mathrm{ME}}/C_0$, $h_{d,\mathrm{cut}}/C_0$, and h_d/C_0 between the profiles of species A and B versus ratio of diffusion coefficients D_B/D_A. The values of $h_{d,\mathrm{ME}}/C_0$ (red circles) are deduced from the master equation (Eqs. (7)–(9)). The values of $h_{d,\mathrm{cut}}/C_0$ (black open triangles) are deduced from the deterministic equations (Eqs. (14) and (15)) with a cutoff $\varepsilon = 10^{-4}$. The values of h_d/C_0 (blue open squares) are deduced from the deterministic equations (Eqs. (2) and (3)) without cutoff. The line gives the results for $D_A = D_B$. The parameters are given in the caption of Fig. 1.

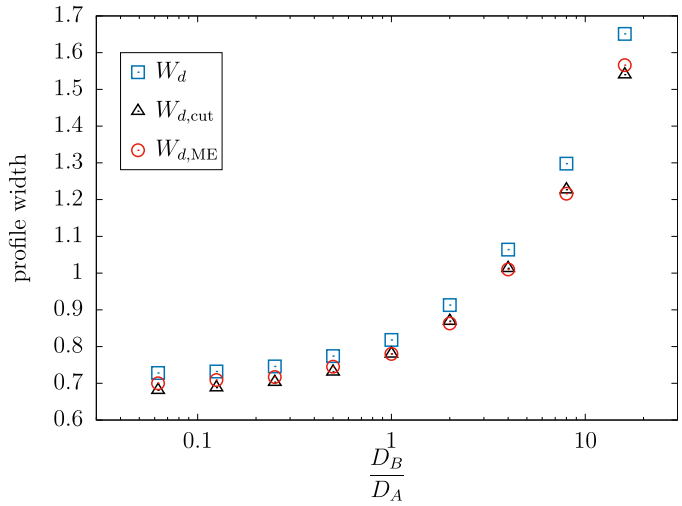

Fig. 5. Dilute system. Profile widths deduced from different approaches versus ratio of diffusion coefficients D_B/D_A. The values of $W_{d,\mathrm{ME}}$ (red circles) are deduced from the master equation (Eqs. (7)–(9)). The values of $W_{d,\mathrm{cut}}$ (black open triangles) are deduced from the numerical integration of the deterministic equations (Eqs. (14) and (15)) with a cutoff $\varepsilon = 10^{-4}$. The values of W_d (blue open squares) are deduced from the numerical integration of the deterministic equations (Eqs. (2) and (3)) without cutoff. The parameters are given in the caption of Fig. 1.

where A is solution of Eqs. (2) and (3) without cutoff. The same definition is applied to Eqs. (14) and (15) to obtain the width $W_{d,\mathrm{cut}}$ in the presence of a cutoff. The definition has to be adapted to take into account the fluctuations of the profile deduced from the master equation. Using the cell labels i_l and i_r determined for the shift between the fluctuating A and B profiles solutions of Eqs. (7)–(9), we define the mean cell label i_m as the nearest integer to the average $(i_l + i_r)/2$. We use Eq. (17) with $|A'(0)| \simeq (N_A(i_m - 40) - N_A(i_m + 40))/(81\Delta x\Omega)$ to compute the instantaneous width. As in the case of the shift $h_{d,\mathrm{ME}}$ between the fluctuating profiles of A and B, the values $W_{d,\mathrm{ME}}$ of the width used to draw Fig. 5 are obtained after a time average between the times $t = 1$ and $t = 10$.

As shown in Fig. 5, the width W_d deduced from the deterministic equations without cutoff is smaller (resp. larger) for $D_B < D_A$ (resp. $D_B > D_A$) than the width evaluated at W^* in the case of identical diffusion coefficients $D_B = D_A$ [12]. The width $W_{d,\mathrm{ME}}$ deduced from the master equation (Eqs. (7)–(9)) and the width $W_{d,\mathrm{cut}}$ deduced from the deterministic equations (Eqs. (14) and (15)) with a cutoff obeying Eq. (12) agree and are both smaller than the width W_d of the wave front, solution of the deterministic equations without cutoff.

According to the good agreement between the results of the master equation and the deterministic equations with a cutoff, it is more relevant to describe the effect of the fluctuations on the wave front as the effect of the discretization of the variables than a pure noise effect.

Fig. 6 summarizes the effect of the fluctuations on the three quantities q for $q = v, h, W$ in the whole range of considered values of the ratio D_B/D_A for the dilute system. The relative differences $(q_{d,\mathrm{ME}} - q_d)/q_d$ between the results

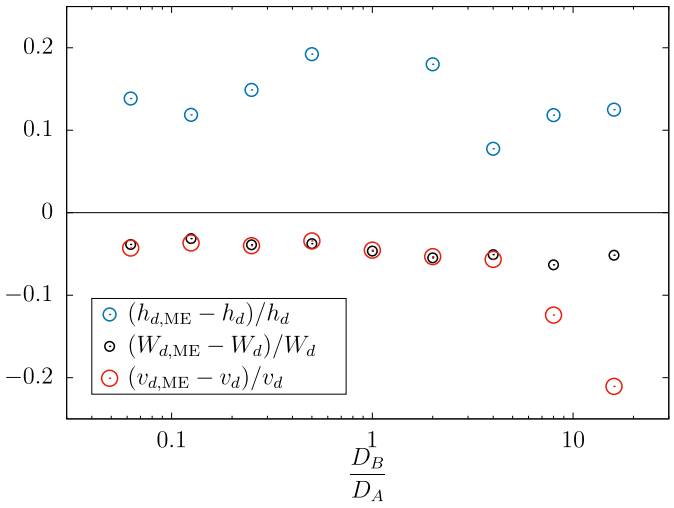

Fig. 6. Dilute system. Relative differences between the front properties deduced from the master equation (Eqs. (7)–(9)) and the analogous properties deduced from the deterministic equations without cutoff (Eqs. (2) and (3)) versus D_B/D_A. The large red circles give the relative difference $(v_{d,\mathrm{ME}} - v_d)/v_d$ for the front speed, the blue circles of intermediate size give the relative difference $(h_{d,\mathrm{ME}} - h_d)/h_d$ for the shift between A and B profiles, and the small black circles give the relative difference $(W_{d,\mathrm{ME}} - W_d)/W_d$ for the width of A profile. The parameters are given in the caption of Fig. 1.

deduced from the master equation and the deterministic equations without cutoff are given in Fig. 6 for the velocity, the shift, and the width. In the whole range of D_B/D_A, the discrete nature of the number of particles in the master equation induces a small decrease of 5% of the profile width with respect to the deterministic description without cutoff. A significant increase of 14% of the shift between the A and B profiles is observed in the presence of fluctuations in the entire interval of ratios of diffusion coefficients. As for the width, the relative difference of velocity $(v_{d,\mathrm{ME}} - v_d)/v_d$, with $v_d = v^*$, is negative and takes the same value of -5% for $D_B/D_A \leq 1$. However, the relative difference of velocity is not constant for $D_B/D_A > 1$ and reaches -22% for $D_B/D_A = 16$. Hence, a significant speed decrease is observed whereas the shift and the width, far behind the leading edge of the front, are not affected by large diffusion coefficients of species B with respect to the diffusion coefficient of species A.

3. Concentrated system

In a dilute system, the solvent S is in great excess with respect to the reactive species A and B. The concentration of the solvent is then supposed to remain homogeneous regardless of the variation of concentrations A and B. In a concentrated solution, the variation of the concentration of the solvent cannot be ignored. In the linear domain of irreversible thermodynamics, the diffusion fluxes are linear combinations of the concentration gradients of the different species. The flux j_X of species X=A, B, S depends on the concentration gradients and the diffusion coefficients of all species A, B, and S [38,39]. Using the conservation relations $C_{tot} = A + B + S$, where C_{tot} is a constant, we eliminate the explicit dependence of the fluxes on the concentration S of the solvent and find

$$j_A = -\left(1 - \frac{A}{C_{tot}}\right) D_A \partial_x A + \frac{A}{C_{tot}} D_B \partial_x B \tag{18}$$

$$j_B = \frac{B}{C_{tot}} D_A \partial_x A - \left(1 - \frac{B}{C_{tot}}\right) D_B \partial_x B \tag{19}$$

According to the expression of the diffusion fluxes in a concentrated system, the reaction–diffusion equations associated with the chemical mechanism given in Eq. (1) read [39]

$$\partial_t A = D_A \partial_x \left[\left(1 - \frac{A}{C_{tot}}\right) \partial_x A\right] - D_B \partial_x \left(\frac{A}{C_{tot}} \partial_x B\right) + kAB \tag{20}$$

$$\partial_t B = D_B \partial_x \left[\left(1 - \frac{B}{C_{tot}}\right) \partial_x B\right] - D_A \partial_x \left(\frac{B}{C_{tot}} \partial_x A\right) - kAB \tag{21}$$

The discrete expression of the flux at the interface between cells i and $i+1$ is related to the difference of the transition rates in the master equation according to

$$j_X(i + 1/2) = -\frac{1}{\Delta x}\left(T^-_{N_X(i+1)} - T^+_{N_X(i)}\right) \tag{22}$$

where $X = A, B$, the transition rate $T^-_{N_X(i+1)}$ is associated with the jump of a particle X to the left from cell $i+1$ to cell i, and $T^+_{N_X(i)}$ is associated with the jump of a particle X to the right from cell i to cell $i+1$. Using Eqs. (18) and (19) and

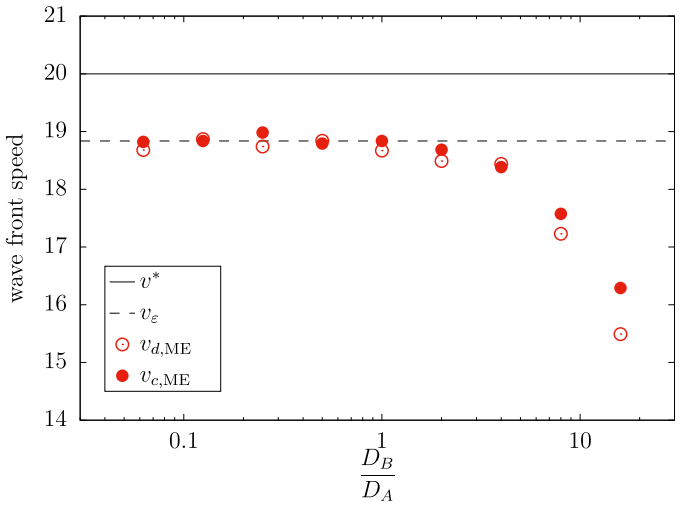

Fig. 7. Concentrated system. Wave front speed $v_{c,\mathrm{ME}}$ deduced from the master equation (Eqs. (7), (8), and (26)) in a concentrated system (red solid disks) for $C_{tot} = 50$ and speed $v_{d,\mathrm{ME}}$ deduced from the direct simulation of the master equation (Eqs. (7)–(9)) associated with the dilute system (red circles) versus ratio of diffusion coefficients D_B/D_A. The horizontal solid line gives the minimum velocity v^* (Eq. (4)) of an FKPP front in the absence of a cutoff. The horizontal dashed line gives the velocity $v_\varepsilon = 18.84$ given in Eq. (11) for a cutoff $\varepsilon = 10^{-4}$ and $D_A = D_B$. The parameters are given in the caption of Fig. 1.

replacing $\partial_x X$ by $(N_X(i+1) - N_X(i))/\Omega\Delta x$ for $X = A, B$, we assign well-chosen terms of the flux $j_X(i+1/2)$ to the transition rates to the left and to the right

$$T^{\pm}_{N_A(i)} = \frac{D_A}{\Delta x^2} N_A(i) - \frac{N_A\,(i \pm 1/2)}{\Omega C_{tot}\Delta x^2}\left[D_A N_A(i) - D_B N_B(i \pm 1)\right] \tag{23}$$

$$T^{\pm}_{N_B(i)} = \frac{D_B}{\Delta x^2} N_B(i) - \frac{N_B\,(i \pm 1/2)}{\Omega C_{tot}\Delta x^2}\left[D_B N_B(i) - D_A N_A(i \pm 1)\right] \tag{24}$$

to ensure that they are positive or equal to zero for any number of particles. A standard arithmetic mean for the number $N_X\,(i \pm 1/2)$ of particles $X = A, B$ in the virtual cell $i \pm 1/2$ cannot be used since it may lead to a non-zero transition rate when the departure cell is empty. Instead, we choose the harmonic mean between the number of particles in cells i and $i \pm 1$:

$$N_X\,(i \pm 1/2) = \frac{N_X(i) N_X(i \pm 1)}{N_X(i) + N_X(i \pm 1)} \tag{25}$$

which ensures that no jump of X from cell i to cell $i \pm 1$ occurs when the number of particles N_X vanishes in cell i. We checked different definitions of the mean obeying the latter condition and found that the results are not significantly affected when choosing for $N_X\,(i \pm 1/2)$ a modified arithmetic mean which vanishes if $N_X(i) = 0$ and equals $(N_X(i) + N_X(i \pm 1))/2$ otherwise, or a geometric mean $\sqrt{N_X(i) N_X(i \pm 1)}$.

It is worth noting that, contrary to the dilute case for which the transition rate associated with the diffusion of particles X only depends on the number of particles X in the departure cell, the transition rate in the concentrated case also depends on the number of particles A and B in the arrival cell. In the case of a concentrated system, the diffusion term reads

$$\begin{aligned}\left.\frac{\partial P(\phi)}{\partial t}\right|_{\mathrm{diff}} = \sum_i \Big[& T^-_{N_A(i)+1} P(\{N_A(i-1)-1, N_A(i)+1\}) \\ & + T^+_{N_A(i)+1} P(\{N_A(i)+1, N_A(i+1)-1\}) \\ & + T^-_{N_B(i)+1} P(\{N_B(i-1)-1, N_B(i)+1\}) \\ & + T^+_{N_B(i)+1} P(\{N_B(i)+1, N_B(i+1)-1\}) \\ & - \left(T^-_{N_A(i)} + T^+_{N_A(i)} + T^-_{N_B(i)} + T^+_{N_B(i)}\right) P(\phi) \Big]\end{aligned} \tag{26}$$

The reaction term $\left.\frac{\partial P(\phi)}{\partial t}\right|_{\mathrm{reac}}$ of the master equation given in Eq. (8) for the dilute system is unchanged in the case of a concentrated system. The kinetic Monte Carlo algorithm and the initial and boundary conditions used for the dilute system are straightforwardly extended to the concentrated system.

The front speeds $v_{c,\mathrm{ME}}$ and $v_{d,\mathrm{ME}}$ deduced from the master equation in concentrated and dilute cases, respectively, are compared in Fig. 7. The correction to the wave front speed induced by an increase of the ratio of diffusion coefficients

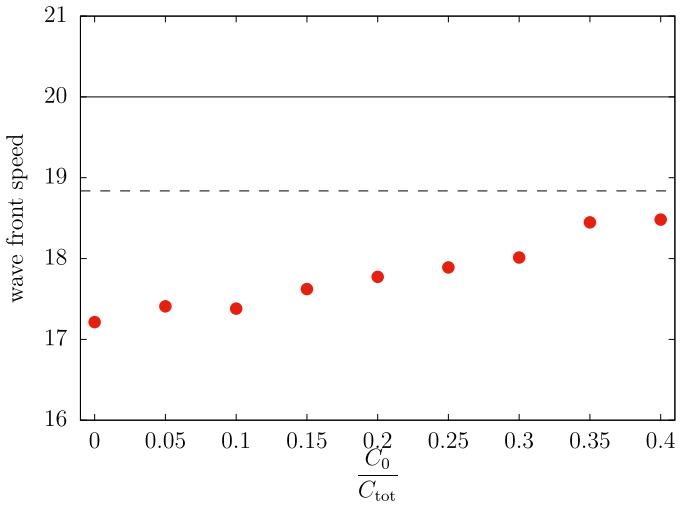

Fig. 8. Concentrated system. Wave front speeds versus the deviation from the dilution limit C_0/C_{tot}. The values of $v_{c,\rm ME}$ (red disks) are deduced from the direct simulation of the master equation (Eqs. (7), (8), and (26)) for $k = 10$, $\Omega = 10$, $N_0 = 100$, $D_A = 1$, $D_B = 8$, $\ell = 2000$, and $\Delta x = 0.008$ ($C_0 = N_0/\Omega$). The horizontal solid line gives the minimum velocity $v^* = 20$ (Eq. (4)) of an FKPP front, solution of the deterministic equations (Eqs. (2) and (3)) without cutoff. The horizontal dashed line gives the velocity $v_\varepsilon = 18.84$ given in Eq. (11) for a cutoff $\varepsilon = 10^{-4}$ and $D_A = D_B$.

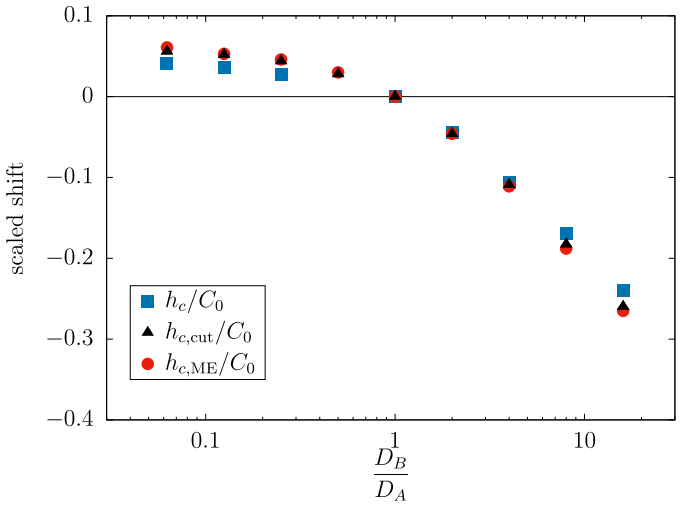

Fig. 9. Concentrated system. Scaled shifts $h_{c,\rm ME}/C_0$, $h_{c,\rm cut}/C_0$, and h_c/C_0 between the profiles of species A and B versus ratio of diffusion coefficients D_B/D_A. The values of $h_{c,\rm ME}/C_0$ (red disks) are deduced from the master equation (Eqs. (7), (8), and (26)). The values of $h_{c,\rm cut}/C_0$ (black solid triangles) are deduced from the deterministic equations (Eqs. (20) and (21)) with a reactive term multiplied by the cutoff $H(A-\varepsilon)$ for $\varepsilon = 10^{-4}$. The values of h_c/C_0 (blue solid squares) are deduced from the deterministic equations (Eqs. (20) and (21)) without cutoff. The other parameters are given in the caption of Fig. 7. The line gives the results for $D_A = D_B$.

D_B/D_A is smaller for a concentrated system than for a dilute system. Indeed, in the concentrated case, the diffusion of a species depends on the diffusion coefficients of both species. Hence, increasing D_B at constant D_A has a smaller impact on the velocity since the contribution depending on D_B is partly compensated by the unchanged terms depending on D_A.

The effect of the departure from the dilution limit on the wave front speed $v_{c,\rm ME}$ deduced from the master equation given in Eqs. (7), (8), and (26) is shown in Fig. 8. The dilution limit $v_{d,\rm ME}(D_B/D_A = 8) = 17.20$ is recovered for $C_0/C_{tot} \to 0$. As C_0/C_{tot} increases, the solution is more concentrated and the cross-diffusion terms become more important, so that the system is less sensitive to the difference between the diffusion coefficients D_A and D_B: The wave front speed $v_{c,\rm ME}$ increases and tends to the value $v_\varepsilon = 18.84$ predicted by Eq. (11) for the cutoff $\varepsilon = 10^{-4}$ and $D_A = D_B$.

The variation of the shifts $h_{c,\rm ME}$, $h_{c,\rm cut}$, and h_c between the two profiles with respect to the ratio of the diffusion coefficients D_B/D_A is shown in Fig. 9 in a concentrated system for the three approaches, the master equation and the deterministic descriptions with and without cutoff. As revealed when comparing the results given in Figs. 4 and 9, the effect of the departure from the dilution limit on the shift is too small for us to evaluate the difference $(h_{c,\rm ME} - h_{d,\rm ME})/h_{d,\rm ME}$ with a sufficient precision for the fluctuating results deduced from the master equations.

The effects of the departure from the dilution limit on the widths $W_{c,\rm ME}$, $W_{c,\rm cut}$, and W_c of the profile are given in Fig. 10 for the three approaches. The agreement between the results $W_{c,\rm ME}$ and $W_{c,\rm cut}$ deduced from the master equation (Eqs. (7), (8), and (26)) and the deterministic equations (Eqs. (14) and (15)) with a cutoff, respectively, is satisfying considering

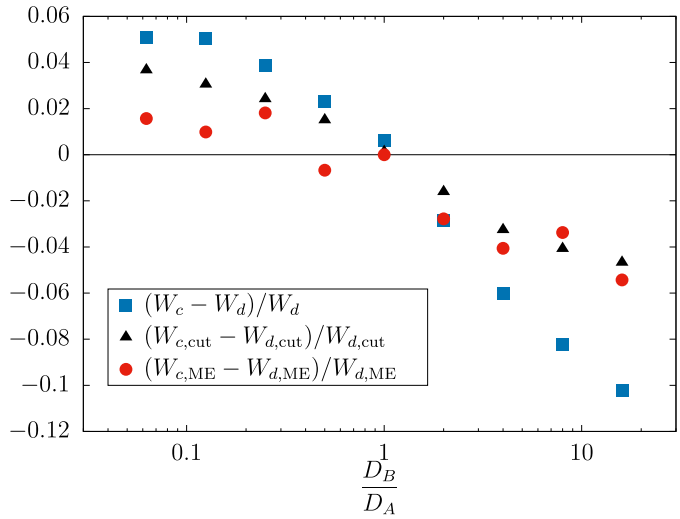

Fig. 10. Relative differences $(W_{c,\mathrm{ME}} - W_{d,\mathrm{ME}})/W_{d,\mathrm{ME}}$, $(W_{c,\mathrm{cut}} - W_{d,\mathrm{cut}})/W_{d,\mathrm{cut}}$, and $(W_c - W_d)/W_d$ between the widths in a concentrated system and a dilute system for different approaches versus D_B/D_A. The values of $W_{c,\mathrm{ME}}$ and $W_{d,\mathrm{ME}}$ (red disks) are deduced from the master equation (Eqs. (7), (8), and (26) and Eqs. (7)–(9), respectively). The values of $W_{c,\mathrm{cut}}$ and $W_{d,\mathrm{cut}}$ (black solid triangles) are deduced from the deterministic equations (Eqs. (20) and (21) and Eqs. (14) and (15), respectively) with a reactive term multiplied by the cutoff $H(A - \varepsilon)$ for $\varepsilon = 10^{-4}$. The values of W_c and W_d (blue solid squares) are deduced from the deterministic equations (Eqs. (20) and (21) and Eqs. (2) and (3), respectively) without cutoff.

the high level of noise on the evaluation of the width $W_{c,\mathrm{ME}}$. According to Fig. 5, the width in a dilute system is smaller than the width obtained for identical diffusion coefficients if $D_B < D_A$ and larger if $D_B > D_A$. The results displayed in Fig. 10 prove that, for each description method, the width in a concentrated system is larger than the width in a dilute system if $D_B < D_A$ and smaller if $D_B > D_A$. Hence, in the entire range of ratios of diffusion coefficients and for deterministic as well as stochastic methods, the width in a concentrated system is closer to the width obtained for identical diffusion coefficients. As for the front speed, the departure from the dilution limit reduces the effects induced by the difference between the diffusion coefficients.

4. Conclusion

We have performed kinetic Monte Carlo simulations of the master equation associated with a chemical system involving two species A and B. The two species have two different diffusion coefficients, D_A and D_B, and are engaged in the autocatalytic reaction $\mathrm{A} + \mathrm{B} \rightarrow 2\mathrm{A}$. The effects of fluctuations on the FKPP wave front have been studied in the cases of a dilute solution and a concentrated solution in which cross-diffusion cannot be neglected.

In the case of a dilute system, the linearization of the deterministic equations with a cutoff in the leading edge of the front leads to a speed shift independent of the diffusion coefficient D_B of the consumed species. The speed shift obtained for two different diffusion coefficients is the same as in the case $D_A = D_B$. The main result deduced from the master equation is that the front speed sensitively depends on the diffusion coefficient D_B. For D_B larger than D_A, the front speed decreases as D_B increases and is significantly smaller than the prediction of the linear cutoff theory. The speed decrease obtained for large values of D_B/D_A is related to the number N_{B_ε} of B particles at the position of the most advanced A particle in the leading edge of the front. When species B diffuses faster that species A, N_{B_ε} is significantly smaller than the steady-state value N_0.

We carefully derived the nontrivial expression of the master equation in a concentrated system with cross-diffusion. The transition rates are deduced from the diffusion fluxes in the linear domain of irreversible thermodynamics. The transition rates associated with diffusion depend on the number of particles not only in the departure cell but also in the arrival cell. Qualitatively, the conclusions drawn for a dilute solution and $D_A \neq D_B$ remain valid, but the front properties deduced from the master equation with cross-diffusion depart less from those obtained for $D_A = D_B$. The dependence of the front properties on D_B/D_A in a concentrated system are softened with respect to the dilute case. Cross-diffusion mitigates the impact of the difference between the diffusion coefficients.

CRediT authorship contribution statement

Gabriel Morgado: Methodology, Software, Investigation, Writing - original draft, Visualization. **Bogdan Nowakowski:** Conceptualization, Validation, Writing - review & editing, Supervision. **Annie Lemarchand:** Definition, Conceptualization, Validation, Resources, Writing - original draft, Review & editing, Supervision.

Declaration of competing interest

The authors declare that they have no known competing financial interests or personal relationships that could have appeared to influence the work reported in this paper.

Acknowledgments

This publication is part of a project that has received funding from the European Union's Horizon 2020 (H2020-EU.1.3.4.) research and innovation program under the Marie Sklodowska-Curie Actions (MSCA-COFUND ID 711859) and from the Ministry of Science and Higher Education, Poland, for the implementation of an international cofinanced project.

References

[1] R.A. Fisher, Ann. Eugen. 7 (1937) 355.
[2] A.N. Kolmogorov, I.G. Petrovsky, N.S. Piskunov, Bull. Moscow State Univ. Ser. A: Math. Mech. 1 (1937) 1–25.
[3] W. van Saarloos, Phys. Rep. 386 (2003) 29–222.
[4] J.D. Murray, Mathematical Biology, Springer, Berlin, 1989.
[5] V. Mendez, D. Campos, F. Bartumeus, Stochastic Foundations in Movement Ecology: Anomalous Diffusion, Invasion Fronts and RandOm Searches, Springer, Berlin, 2014.
[6] E. Bouin, V. Calvez, N. Meunier, S. Mirrahimi, B. Perthame, G. Raoul, R. Voituriez, C. R. Acad. Sci., Paris I 350 (2012) 761.
[7] J. Fort, N. Isern, A. Jerardino, B. Rondelli, in: J.A. Baracelo, F. Del Castillo (Eds.), Simulating Prehistoric and Ancient Worlds, Springer, Cham, 2016, pp. 189–197.
[8] R. Mancinelli, D. Vergni, A. Vulpiani, Physica D 185 (2003) 175.
[9] D. Froemberg, H. Schmidt-Martens, I.M. Sokolov, F. Sagues, Phys. Rev. E 78 (2008) 011128.
[10] X. Cabré, J.-M. Roquejoffre, C. R. Acad. Sci., Paris I 347 (2009) 1361.
[11] F. El Adnani, H. Talibi Alaoui, Topol. Methods Nonlinear Anal. 35 (2010) 43.
[12] G. Morgado, B. Nowakowski, A. Lemarchand, Phys. Rev. E 99 (2019) 022205.
[13] V.K. Vanag, I.R. Epstein, Phys. Chem. Chem. Phys. 11 (2009) 897–912.
[14] D.G. Leaist, Phys. Chem. Chem. Phys. 4 (2002) 4732–4739.
[15] V.K. Vanag, F. Rossi, A. Cherkashin, I.R. Epstein, J. Phys. Chem. B 112 (2008) 9058–9070.
[16] F. Rossi, V.K. Vanag, I.R. Epstein, Chem. A Eur. J. 17 (2011) 2138–2145.
[17] M.A. Budroni, L. Lemaigre, A. De Wit, F. Rossi, Phys. Chem. Chem. Phys. 17 (2015) 1593.
[18] M.A. Budroni, J. Carballido-Landeira, A. Intiso, A. De Wit, F. Rossi, Chaos 25 (2015) 064502.
[19] L. Desvillettes, Th. Lepoutre, A. Moussa, SIAM J. Math. Anal. 46 (2014) 820.
[20] L. Desvillettes, A. Trescases, J. Math. Anal. Appl. 430 (2015) 32.
[21] L. Desvillettes, T. Lepoutre, A. Moussa, A. Trescases, Comm. Partial Differential Equations 40 (2015) 1705.
[22] A. Jüngel, L. Chen, L. Desvillettes (Eds.), Advances in reaction-cross-diffusion systems, Nonlinear Anal. 159 (2017) 1–492.
[23] E. Daus, L. Desvillettes, H. Dietert, J. Differ. Equ. 266 (2019) 3861.
[24] A. Moussa, B. Perthame, D. Salort, J. Nonlinear Sci. 29 (2019) 139.
[25] H.P. Breuer, W. Huber, F. Petruccione, Physica D 73 (1994) 259.
[26] A. Lemarchand, A. Lesne, M. Mareschal, Phys. Rev. E 51 (1995) 4457.
[27] E. Brunet, B. Derrida, Phys. Rev. E 56 (1997) 2597.
[28] J.S. Hansen, B. Nowakowski, A. Lemarchand, J. Chem. Phys. 124 (2006) 034503.
[29] D. Panja, Phys. Rep. 393 (2004) 87–174.
[30] J.G. Conlon, C.R. Doering, J. Stat. Phys. 120 (2005) 421.
[31] J. Mai, I.M. Sokolov, V.N. Kuzovkov, A. Blumen, Phys. Rev. E 56 (1997) 4130.
[32] G. Nicolis, I. Prigogine, Self-Organization in Nonequilibrium Systems, Wiley, New York, 1977.
[33] C.W. Gardiner, Handbook of Stochastic Methods for Physics, Chemistry and the Natural Sciences, Springer, Berlin, 1985.
[34] D.T. Gillespie, J. Chem. Phys. 81 (1977) 2340.
[35] S. Fedotov, Wave front for a reaction–diffusion system and relativistic Hamilton–Jacobi dynamics, Phys. Rev. E 59 (1999) 5040.
[36] S. Mirrahimi, G. Barles, B. Perthame, P.E. Souganidis, SIAM J. Math. Anal. 44 (2012) 4297.
[37] C. Bianca, A. Lemarchand, Physica A 438 (2015) 1.
[38] S.R. de Groot, P. Mazur, Non-Equilibrium Thermodynamics, North-Holland, Amsterdam, 1962.
[39] L. Signon, B. Nowakowski, A. Lemarchand, Phys. Rev. E 93 (2016) 042402.

Conclusion

In this work, I have been concerned with the formation of structures in living organisms. I chose to describe biological systems at an intermediate, mesocopic scale, using methods of statistical physics, such as kinetic theory and stochastic methods. My contribution to the stochastic elimination of fast variables in the framework of chemical kinetics [29] has illustrated the complex interplay between nonlinear deterministic dynamics and fluctuations. Specifically, I have shown that the linearized Langevin equations used to analytically compute the correlations of concentration fluctuations around steady values do not correctly capture the behavior of the system, in particular close to bifurcations. As a perspective, with the aim of developing an improved analytical approach, I suggest to consider the procedure proposed by Roberts and collaborators [110, 111, 112, 113] to derive stochastic normal forms valid in the vicinity of the center manifold. Roberts *et al.* assign orders of magnitude to the different terms of the evolution equations, in particular the Langevin forces. They derive approximate equations for the slow variables, describing the dynamics on the center manifold up to the desired order. The technique generalizes the ideas developed by Arnold to derive deterministic normal forms [114]. The treatment of the vicinity of a bifurcation is naturally included in the method and simply consists in including small terms related to the bifurcation parameter in the expansion procedure. It is to be noted that the expansion leads to non trivial noise terms involving convolution integrals of exponential terms and Langevin forces, which introduce memory noise terms in the reduced stochastic dynamics. Higher order terms of the expansion even yield nonlinear noise combinations between a Langevin force and a convolution integral of an exponential function and a Langevin force, which shows how complex the stochastic elimination of fast variables is [110]. The quality of the approach, i.e. the order at which the expansion can be troncated, could be checked by numerical integration of the Langevin equations, using the Euler-Maruyama method with Itô interpretation of the multiplicative noise [115]. The great advantage of the numerical integration of the Langevin equations would be to facilitate the comparison with the simulation of the master equation. As proved in the study of time asymmetry of correlation functions in far-from-equilibrium conditions in a bistable system [63], in oscillating systems close to a Hopf bifurcation [63, 62] and a saddle-node

infinite period bifurcation [63], it is however probable that the Langevin approach, although including multiplicative noise terms and all the nonlinearities of the dynamics, will not be sufficient to capture the subtleties of the interaction between fluctuations and deterministic nonlinearities. In general, the non Gaussian character of chemical noise intrinsically invalidates the Langevin approach. It is especially true in the intricate case of the stochastic elimination of fast variables. The correct description of concentration fluctuations is essential to predict the behavior of many systems that are sensitive to perturbations, in particular due to explosive behavior, the vicinity of a bifurcation, the existence of many simultaneously stable states or simply because they are small [116]. Hence, combustion hazards, pattern formation in developmental biology including Turing structures and Fisher - Kolmogorov, Petrovsky, Piskunov (FKPP) wave fronts require stochastic analyses.
The simulations of a submicrometric Turing pattern in a concentrated system I performed refute certain objections to Turing's model regarding the preservation of proportions in embryos. Assuming an appropriate role of the solvent in the chemical mechanism is sufficient to control the wavelength of the structure by monitoring the concentration of the solution. A significant decrease of the wavelength is obtained in a more concentrated solution for the considered chemical scheme. The adaptation of the size of the structure to the size of the embryo then follows from the hypothesis that a smaller embryo has greater concentrations of morphogens, imposed by the mother and not by the size of the embryo. In this respect, small embryos lead to a crowded environment [117, 118, 119]. The results can be exploited to design materials with controlled submicrometric properties in chemical engineering [120, 121, 122, 123]. Following a biomimetic approach, I proposed experimental conditions, compatible with the requirements of chemical engineering, to observe the termination of a Turing structure in a growing system. Among the different parameters playing on the stability of the pattern and the value of the wavelength, I selected the concentration of the reservoir which sets the injection rate of the inhibitor into the system for its easy control in the region where the experimentalist wishes the structure to stop.

I also characterized the effect of concentrated solutions on another spatio-temporal structure, often encountered in biology, a Fisher - Kolmogorov, Petrovsky, Piskunov (FKPP) wave front, used to model the propagation of a virus or a favorable genetic trait in a population. I focused on the modification of diffusion due to high concentrations. Beyond the description of concentrated solutions, I was led to consider reactive species with different diffusion coefficients. Performing simulations of the master equation, I obtained a nice result stating that an FKPP front is slowed down when the consumed species diffuses faster than the autocatalytically produced species. The analytical description of this phenomenon, using a nonlinear cutoff approach, is certainly a reasonable perspec-

tive. The consequences of high concentrations on biological structures deserves further attention. The results show that, using particle dynamics simulations, it is possible to check the validity of macroscopic models at the submicrometric scale. The new directions explored in the field of chemical engineering, as part of a biomimetic approach, could encourage experimentalists to design model systems for testing the main influence of high concentrations on organized behaviors.

The results obtained during my PhD led me to formulate some general ideas about the modeling of structures in biology and prompted me to revisit how the vision of biological patterns had evolved over the last century and the beginning of 21st century. Morphogenesis is an important part of developmental biology. Axial segmentation and the formation of periodic patterns are observed in invertebrates such as insects and crustaceans as well as in vertebrate embryos. The striking analogies between biological structures and the patterns that spontaneously emerge in far-from-equilibrium chemical systems logically incited theoreticians to use models of chemical kinetics to study biological phenomena. Experimental evidence of periodic spatial structures in a reaction-diffusion system, without the contribution of physical phenomena such as gravity and mechanical instabilities, was given in 1990 [72], long after the corresponding model was proposed by Turing in 1952. Previously, it had taken even more time to apply the concepts of dynamical systems, developed by mathematicians such as Henri Poincaré around 1900, to the description of far-from-equilibrium nonlinear phenomena in uniform systems. The temporal organization in homogeneous chemical systems, from periodic oscillations to chaos, has been interpreted in the context of dynamical systems theory in the 70s, first from a theoretical point of view, in particular in the group of the Nobel prize Ilya Prigogine in Brussels. Then, in the 80s, the Belousov–Zhabotinsky (BZ) reaction has been extensively studied. With the development and mastery of continuously stirred tank reactors (CSTRs) ensuring far-from-equilibrium conditions, the BZ reaction proved to provide an ideal experimental example of dynamical systems exhibiting all the different types of bifurcations and scenarios to chaos [124, 125, 126, 127, 128]. Application to biology arrived later and, at the very beginning of the 2000s, the concept of systems biology was introduced. It is indeed tempting to apply the notions of the theory of dynamical systems to model certain biological phenomena. Living systems are typically maintained far from equilibrium by exchanges of energy and matter with the environment and spontaneously evolve into organized structures.

Two antagonistic views, known as holism and reductionism, are usually adopted to study chemical systems and provide disjointed information. On the one hand, holism proposes a global approach to a system and neglects the discrete nature of matter. After a modeling effort to identify essential mechanisms and extract a small number of dynamical variables, the system is described at the macroscopic scale. It is then possible to

write differential equations governing the evolution of a homogeneous system and partial differential equations in the case of an inhomogeneous system. The nonlinearities of the equations determine the behavior of the system, depending on the parameter values and the involved bifurcations. A global, general classification of some biological phenomena can be obtained within the framework of such a deterministic, macroscopic analysis. Such a description ignores the fluctuations of the macroscopic variables that are induced by the microscopic dynamics of a huge number of elementary constituents. This global approach can be misleading in systems of small size like the systems typically studied in developmental biology. The role of fluctuations on the macroscopic behavior of a system is also significant, even in a large system, close to bifurcations [29] or for marginally stable solutions such as FKPP fronts [44].

On the other hand, reductionism focuses on the atomistic or molecular scale. However, the huge number of particles prompts the use of numerical simulations. The evolution of wave functions or particle positions and velocities, dictated by fundamental interactions according to quantum or classical mechanics, can then be followed. Even with the latest generation of computers, it is still extremely long to reach the space and time scales necessary to observe the formation of macroscopic patterns using ab-initio simulations, density functional theory, and even molecular dynamics. Moreover, the connection between changing a parameter characterizing atomistic interactions and changing a macroscopic property of a structure is not firmly established. The numerical simulations at the microscopic scale may provide empirical knowledge but it remains difficult to build qualitative relationships between the molecular structure and the macroscopic properties of the system. Reductionism gives access to the specific properties of a given system but the prediction of the behavior of a system showing a small difference in the microscopic characteristics often fails. Generalization within a reductionist approach is delicate.

In order to bridge the gap between the two remote microscopic and macroscopic scales, I chose to develop a description at the mesoscopic scale, which presents the advantage of accounting for the fluctuations as well as providing a general framework to develop analytical approaches. The strength of statistical physics is to propose a probabilistic description of a system composed of a large number of components. Microscopic features of molecules such as their atomic components, their chemical functions, and their structure are not explicitly taken into account by the stochastic description, which retains some consequences of these microscopic properties at the mesoscopic scale and take them into account in a coarse-grained manner. In particular, the notion of stochastic trajectory includes dissipation and irreversibility but with a more refined approach than the macroscopic description. Specifically, microscopic reversibility with respect to time reversal is lost in a master equation approach [61, 62, 63] but the production of entropy may decrease along a stochastic trajectory. The fluctuation theorem demonstrated by Galavotti

and Cohen makes precise the probability that such an event occurs [129, 130, 131, 132]. Writing a master equation associated with a given system, for example to account for cross-diffusion in a concentrated system [44], already represents an effort of modeling, i.e. an effort to extract ingredients from the microscopic scale that are essential to describe the phenomenon of interest at the mesoscopic scale. Approximating a master equation by Langevin equations makes it possible to derive analytical expressions that better point out the discontinuities in the properties induced by bifurcations [29]. From a general point of view, the analytical approaches made available by statistical physics offer the possibility to better « understand » complex phenomena. They at least guide the intuition and make it possible to guess the behavior of an unknown system having some points in common with the one previously studied.

The categorization of a given description into a holistic approach or a reductionist approach is not always clear. Specifically, the stochastic description using Langevin equations is obtained by adding a noise term to the deterministic equations, which includes a part of the microscopic complexity into the equations. In this respect, the description by Langevin equations lies between the two approaches.

Kinetic theory offers another interesting view by considering both deterministic macroscopic behavior and intrinsic probabilistic behavior of matter: It looks at the evolution of the distributions of the position and velocity of the particles. In particular, collision integrals govern the evolution of particle velocities. I have illustrated how kinetic theory is able to make the link between the elastic and reactive collisions between hard spheres and macroscopic parameters such as diffusion coefficients and rate constants [37]. The need for considering a mixture of at least three different species to obtain different diffusion coefficients for two reactants becomes obvious in kinetic theory whereas it is hidden in the two partial differential equations governing the macroscopic evolution of the concentrations of the two reactants [37]. As a conclusion, I would like to point out the value of describing a biological system on a mesoscopic scale in order to extract minimal ingredients, decipher mechanisms, and obtain some analytical results guiding intuition and understanding [133, 134, 135, 136]. However, the master equation and the kinetic equations are not usually solvable without strong approximations. It is of primer importance to check the validity of the analytical results. In this respect, both approaches benefit from the possibility to perform direct simulations of the equations using kinetic Monte Carlo simulations. Gillespie algorithm simulates stochastic trajectories obeying the master equation and the direct simulation Monte Carlo method (DSMC) introduced by Bird is a direct simulation of the kinetic equations including fluctuations. In a DSMC simulation, a particle represents thousands of true molecules [18], is assimilated to a hard sphere, and its collisions are randomly treated in an approximate way. Under these assumptions, particle dynamics is simulated up to thousand times faster than using molecular dynamics,

which allows us to simulate Turing patterns in a reasonable computation time, even in a concentrated system [37]. Finally, it is worthwhile to notice that the efficient simulation tools provided by kinetic Monte Carlo algorithms, that I first applied to materials science, specifically to the submicrometric simulation of gypsum crystallization [137, 138], are particularly well adapted to the simulations of biological submicrometric systems, which gives an idea of the potential of such methods.

Bibliography

[1] G. Nicolis & I. Prigogine; *Self-organization in nonequilibrium systems : from dissipative structures to order through fluctuations* (Wiley, New York) (1977); ISBN 978-0471024019. ix, x, 5, 8, 9

[2] J. D. Murray; *Mathematical biology* (Springer-Verlag, Berlin New York) (1993); ISBN 978-3-662-08542-4. ix, 4, 79

[3] A. Gadomski, M. Bier & J. Siódmiak; «Spatiotemporal models in biology and the health sciences»; Biosystems **179**, p. 15–16 (2019). https://doi.org/10.1016/j.biosystems.2019.02.006. ix

[4] S. Białecki, P. Nałęcz-Jawecki, B. Kaźmierczak & T. Lipniacki; «Traveling and standing fronts on curved surfaces»; Physica D: Nonlinear Phenomena **401**, p. 132 215 (2020). https://doi.org/10.1016/j.physd.2019.132215. ix

[5] A. M. Turing; «The Chemical Basis of Morphogenesis»; Philosophical Transactions of the Royal Society of London. Series B, Biological Sciences **237**, p. 37–72 (1952). https://doi.org/10.1098/rstb.1952.0012. ix, 41

[6] H. G. E. Hentschel, T. Glimm, J. A. Glazier & S. A. Newman; «Dynamical mechanisms for skeletal pattern formation in the vertebrate limb»; Proceedings of the Royal Society of London. Series B: Biological Sciences **271**, p. 1713–1722 (2004). https://doi.org/10.1098/rspb.2004.2772. ix

[7] I. Salazar-Ciudad & J. Jernvall; «A computational model of teeth and the developmental origins of morphological variation»; Nature **464**, p. 583–586 (2010). https://doi.org/10.1038/nature08838. ix

[8] R. Baker, S. Schnell & P. Maini; «A clock and wavefront mechanism for somite formation»; Developmental Biology **293**, p. 116–126 (2006). https://doi.org/10.1016/j.ydbio.2006.01.018. ix

[9] A. Goldbeter & O. Pourquié; «Modeling the segmentation clock as a network of coupled oscillations in the Notch, Wnt and FGF signaling pathways»; Journal of Theoretical Biology **252**, p. 574–585 (2008). https://doi.org/10.1016/j.jtbi.2008.01.006. ix

[10] C. Gomez, E. M. Özbudak, J. Wunderlich, D. Baumann, J. Lewis & O. Pourquié; «Control of segment number in vertebrate embryos»; Nature **454**, p. 335–339 (2008). https://doi.org/10.1038/nature07020. ix

[11] G. Falasco, R. Rao & M. Esposito; «Information Thermodynamics of Turing Patterns»; Physical Review Letters **121** (2018). https://doi.org/10.1103/physrevlett.121.108301. ix

[12] F. Avanzini, G. Falasco & M. Esposito; «Thermodynamics of chemical waves»; The Journal of Chemical Physics **151**, p. 234 103 (2019). https://doi.org/10.1063/1.5126528. ix

[13] N. G. Van Kampen; *Stochastic processes in physics and chemistry* (Elsevier, Amsterdam Boston London) (2007); ISBN 978-0444529657. ix, 5

[14] C. W. Gardiner; *Handbook of stochastic methods for physics, chemistry, and the natural sciences* (Springer-Verlag, Berlin New York) (1983); ISBN 978-3540113577. ix, 5, 8, 9, 10

[15] T. Lipniacki; «Chemically driven traveling waves in DNA»; Physical Review E **60**, p. 7253–7261 (1999). https://doi.org/10.1103/physreve.60.7253. ix

[16] P. J. Zuk, M. Kochańczyk, J. Jaruszewicz, W. Bednorz & T. Lipniacki; «Dynamics of a stochastic spatially extended system predicted by comparing deterministic and stochastic attractors of the corresponding birth–death process»; Physical Biology **9**, p. 055 002 (2012). https://doi.org/10.1088/1478-3975/9/5/055002. ix, 5

[17] G. A. Bird; *Molecular gas dynamics and the direct simulation of gas flows* (Clarendon Press Oxford University Press, Oxford New York) (1994); ISBN 978-0198561958. x, 17

[18] G. A. Bird; *The DSMC method* (CreateSpace, U.S.) (2013); ISBN 978-1492112907. x, 17, 109

[19] A. Donev, A. L. Garcia & B. J. Alder; «An Event-Driven Hybrid Molecular Dynamics and Direct Simulation Monte Carlo Algorithm»; Journal of Computational Physics **227**, p. 2644–2665 (2008)https://digital.library.unt.edu/ark:/67531/metadc899250/. x

[20] M. S. Ivanov & S. V. Rogasinsky; «Analysis of numerical techniques of the direct simulation Monte Carlo method in the rarefied gas dynamics»; Soviet Journal of Numerical Analysis and Mathematical Modelling **3** (1988). https://doi.org/10.1515/rnam.1988.3.6.453. x

[21] R. Wilmoth, A. Carlson & G. LeBeau; «DSMC grid methodologies for computing low-density, hypersonic flows about reusable launch vehicles»; dans «31st Thermophysics Conference», (American Institute of Aeronautics and Astronautics) (1996). https://doi.org/10.2514/6.1996-1812. x

[22] S. F. Gimelshein, M. S. Ivanov, G. N. Markelov & Y. E. Gorbachev; «Statistical Simulation of Nonequilibrium Rarefied Flows with Quasiclassical Vibrational Energy Transfer Models»; Journal of Thermophysics and Heat Transfer **12**, p. 489–495 (1998). https://doi.org/10.2514/2.6394. x

[23] W. Wagner; «A convergence proof for Bird's direct simulation Monte Carlo method for the Boltzmann equation»; Journal of Statistical Physics **66**, p. 1011–1044 (1992). https://doi.org/10.1007/bf01055714. x

[24] D. McQuarrie; *Statistical mechanics* (Harper & Row, New York) (1975); ISBN 9780060443665. x, 17

[25] T. Abe; «Generalized scheme of the no-time-counter scheme for the DSMC in rarefied gas flow analysis»; Computers & Fluids **22**, p. 253–257 (1993). https://doi.org/10.1016/0045-7930(93)90057-g. x

[26] S. R. De Groot & P. Mazur; *Non-equilibrium thermodynamics* (Dover Publications, New York) (1984); ISBN 978-0486647418. x, 12

[27] H. Qian & E. L. Elson; «Fluorescence correlation spectroscopy with high-order and dual-color correlation to probe nonequilibrium steady states»; Proceedings of the National Academy of Sciences **101**, p. 2828–2833 (2004). https://doi.org/10.1073/pnas.0305962101. xi

[28] S. Charier, A. Meglio, D. Alcor, E. Cogné-Laage, J.-F. Allemand, L. Jullien & A. Lemarchand; «Reactant Concentrations from Fluorescence Correlation Spectroscopy with Tailored Fluorescent Probes. An Example of Local Calibration-Free pH Measurement»; Journal of the American Chemical Society **127**, p. 15 491–15 505 (2005). https://doi.org/10.1021/ja053909w. xi

[29] G. Morgado, B. Nowakowski & A. Lemarchand; «Elimination of fast variables in stochastic nonlinear kinetics»; Physical Chemistry Chemical Physics **22**, p.

20 801–20 814 (2020). https://doi.org/10.1039/d0cp02785e. xi, 7, 10, 17, 25, 105, 108, 109

[30] A. Blokhuis, D. Lacoste & P. Nghe; «Universal motifs and the diversity of autocatalytic systems»; Proceedings of the National Academy of Sciences **117**, p. 25 230–25 236 (2020). https://doi.org/10.1073/pnas.2013527117. xi

[31] H. Meinhardt & A. Gierer; «Pattern formation by local self-activation and lateral inhibition»; BioEssays **22**, p. 753–760 (2000). https://doi.org/10.1002/1521-1878(200008)22:8<753::aid-bies9>3.0.co;2-z. xi

[32] T. Gregor, W. Bialek, R. R. d. R. van Steveninck, D. W. Tank & E. F. Wieschaus; «Diffusion and scaling during early embryonic pattern formation»; Proceedings of the National Academy of Sciences **102**, p. 18 403–18 407 (2005). https://doi.org/10.1073/pnas.0509483102. xi

[33] D. Ben-Zvi, B.-Z. Shilo, A. Fainsod & N. Barkai; «Scaling of the BMP activation gradient in Xenopus embryos»; Nature **453**, p. 1205–1211 (2008). https://doi.org/10.1038/nature07059. xi

[34] S. Restrepo & K. Basler; «Morphogen Gradients: Expand and Repress»; Current Biology **21**, p. R815–R817 (2011). https://doi.org/10.1016/j.cub.2011.08.041. xi

[35] D. Cheung, C. Miles, M. Kreitman & J. Ma; «Adaptation of the length scale and amplitude of the Bicoid gradient profile to achieve robust patterning in abnormally large Drosophila melanogaster embryos»; Development **141**, p. 124–135 (2013). https://doi.org/10.1242/dev.098640. xi

[36] L. Signon, B. Nowakowski & A. Lemarchand; «Modeling somite scaling in small embryos in the framework of Turing patterns»; Physical Review E **93** (2016). https://doi.org/10.1103/physreve.93.042402. xi, xii, 12, 44, 61

[37] G. Morgado, B. Nowakowski & A. Lemarchand; «Scaling of submicrometric Turing patterns in concentrated growing systems»; Physical Review E **98** (2018). https://doi.org/10.1103/physreve.98.032213. xii, 19, 62, 109, 110

[38] G. Morgado, B. Nowakowski & A. Lemarchand; «DSMC simulations of Turing patterns in concentrated growing systems»; dans «31ST INTERNATIONAL SYMPOSIUM ON RAREFIED GAS DYNAMICS: RGD31», (AIP Publishing) (2019). https://doi.org/10.1063/1.5119562. xii

[39] G. Morgado, L. Signon, B. Nowakowski & A. Lemarchand; «Termination Mechanisms of Turing Patterns in Growing Systems»; Acta Physica Polonica B **50**, p. 1369 (2019). https://doi.org/10.5506/aphyspolb.50.1369. xiii, 5, 45

[40] D. Panja; «Effects of fluctuations on propagating fronts»; Physics Reports **393**, p. 87–174 (2004). https://doi.org/10.1016/j.physrep.2003.12.001. xiii

[41] A. Lemarchand & B. Nowakowski; «Different description levels of chemical wave front and propagation speed selection»; The Journal of Chemical Physics **111**, p. 6190–6196 (1999). https://doi.org/10.1063/1.479923. xiii

[42] A. Lemarchand & B. Nawakowski; «Perturbation of local equilibrium by a chemical wave front»; The Journal of Chemical Physics **109**, p. 7028–7037 (1998). https://doi.org/10.1063/1.477685. xiii

[43] G. Morgado, B. Nowakowski & A. Lemarchand; «Fisher-Kolmogorov-Petrovskii-Piskunov wave front as a sensor of perturbed diffusion in concentrated systems»; Physical Review E **99** (2019). https://doi.org/10.1103/physreve.99.022205. xiii, 81, 93

[44] G. Morgado, B. Nowakowski & A. Lemarchand; «Stochastic approach to Fisher and Kolmogorov, Petrovskii, and Piskunov wave fronts for species with different diffusivities in dilute and concentrated solutions»; Physica A: Statistical Mechanics and its Applications **558**, p. 124 954 (2020). https://doi.org/10.1016/j.physa.2020.124954. xiii, 10, 17, 92, 93, 108, 109

[45] W. Ebeling, E. Gudowska-Nowak & I. M. Sokolov; «On Stochastic Dynamics in Physics — Remarks on History and Terminology»; Acta Physica Polonica B **39**, p. 1003 (2008). 5

[46] D. T. Gillespie; «The chemical Langevin equation»; The Journal of Chemical Physics **113**, p. 297–306 (2000). https://doi.org/10.1063/1.481811. 5

[47] J. Łuczka, P. Hänggi & A. Gadomski; «Non-Markovian process driven by quadratic noise: Kramers-Moyal expansion and Fokker-Planck modeling»; Physical Review E **51**, p. 2933–2938 (1995). https://doi.org/10.1103/physreve.51.2933. 8

[48] P.-F. Verhulst; *Correspondance mathématique et physique, Volume 10*; p. 113–121 (Impr. d'H. Vandekerckhove) (1838). 11

[49] D. T. Gillespie; «Exact stochastic simulation of coupled chemical reactions»; The Journal of Physical Chemistry **81**, p. 2340–2361 (1977). https://doi.org/10.1021/j100540a008. 15

[50] E. Roohi & S. Stefanov; «Collision partner selection schemes in DSMC: From micro/nano flows to hypersonic flows»; Physics Reports **656**, p. 1–38 (2016). https://doi.org/10.1016/j.physrep.2016.08.002. 17

[51] M. Mareschal & A. D. Wit; «Microscopic simulation of a chemical instability»; The Journal of Chemical Physics **96**, p. 2000–2004 (1992). https://doi.org/10.1063/1.462102. 19

[52] A. Lemarchand & B. Nowakowski; «Perturbation of particle velocity distribution in a bistable chemical system»; Physica A: Statistical Mechanics and its Applications **271**, p. 87–101 (1999). https://doi.org/10.1016/s0378-4371(99)00202-2. 19

[53] P. Dziekan, A. Lemarchand & B. Nowakowski; «Particle dynamics simulations of Turing patterns»; The Journal of Chemical Physics **137**, p. 074 107 (2012). https://doi.org/10.1063/1.4743983. 19, 21

[54] J. Hirschfelder; *Molecular theory of gases and liquids* (Wiley, New York) (1954); ISBN 978-0-471-40065-3. 20

[55] M. Frankowicz, M. Moreau, P. P. Szczesny, J. Toth & L. Vicente; «Fast variables elimination in stochastic kinetics»; The Journal of Physical Chemistry **97**, p. 1891–1895 (1993). https://doi.org/10.1021/j100111a029. 23

[56] Y. Lan, T. C. Elston & G. A. Papoian; «Elimination of fast variables in chemical Langevin equations»; The Journal of Chemical Physics **129**, p. 214 115 (2008). https://doi.org/10.1063/1.3027499. 23

[57] N. A. Sinitsyn, N. Hengartner & I. Nemenman; «Adiabatic coarse-graining and simulations of stochastic biochemical networks»; Proceedings of the National Academy of Sciences **106**, p. 10 546–10 551 (2009). https://doi.org/10.1073/pnas.0809340106. 23

[58] P. Thomas, R. Grima & A. V. Straube; «Rigorous elimination of fast stochastic variables from the linear noise approximation using projection operators»; Physical Review E **86** (2012). https://doi.org/10.1103/physreve.86.041110. 23, 24

[59] G. W. A. Constable, A. J. McKane & T. Rogers; «Stochastic dynamics on slow manifolds»; Journal of Physics A: Mathematical and Theoretical **46**, p. 295 002 (2013). https://doi.org/10.1088/1751-8113/46/29/295002. 23

[60] G. W. A. Constable & A. J. McKane; «Fast-mode elimination in stochastic metapopulation models»; Physical Review E **89** (2014). https://doi.org/10.1103/physreve.89.032141. 23

[61] C. Bianca & A. Lemarchand; «Temporal cross-correlation asymmetry and departure from equilibrium in a bistable chemical system»; The Journal of Chemical Physics **140**, p. 224 105 (2014). https://doi.org/10.1063/1.4882070. 24, 25, 108

[62] C. Bianca & A. Lemarchand; «Determination of reaction flux from concentration fluctuations near a Hopf bifurcation»; The Journal of Chemical Physics **141**, p. 144 102 (2014). https://doi.org/10.1063/1.4897325. 24, 25, 105, 108

[63] C. Bianca & A. Lemarchand; «Evaluation of reaction fluxes in stationary and oscillating far-from-equilibrium biological systems»; Physica A: Statistical Mechanics and its Applications **438**, p. 1–16 (2015). https://doi.org/10.1016/j.physa.2015.06.012. 24, 25, 105, 106, 108

[64] P. Thomas, A. V. Straube & R. Grima; «The slow-scale linear noise approximation: an accurate, reduced stochastic description of biochemical networks under timescale separation conditions»; BMC Systems Biology **6**, p. 39 (2012). https://doi.org/10.1186/1752-0509-6-39. 24

[65] S. Smith, C. Cianci & R. Grima; «Model reduction for stochastic chemical systems with abundant species»; The Journal of Chemical Physics **143**, p. 214 105 (2015). https://doi.org/10.1063/1.4936394. 24, 25

[66] D. Magde, E. Elson & W. W. Webb; «Thermodynamic Fluctuations in a Reacting System—Measurement by Fluorescence Correlation Spectroscopy»; Physical Review Letters **29**, p. 705–708 (1972). https://doi.org/10.1103/physrevlett.29.705. 24

[67] A. Wachtel, R. Rao & M. Esposito; «Thermodynamically consistent coarse graining of biocatalysts beyond Michaelis–Menten»; New Journal of Physics **20**, p. 042 002 (2018). https://doi.org/10.1088/1367-2630/aab5c9. 25

[68] R. Grima, P. Thomas & A. V. Straube; «How accurate are the nonlinear chemical Fokker-Planck and chemical Langevin equations?»; The Journal of Chemical Physics **135**, p. 084 103 (2011). https://doi.org/10.1063/1.3625958. 25

[69] R. Grima; «Noise-Induced Breakdown of the Michaelis-Menten Equation in Steady-State Conditions»; Physical Review Letters **102** (2009). https://doi.org/10.1103/physrevlett.102.218103. 25

[70] B. P. Belousov; «Периодически действующая реакция и ее механизм [Periodically acting reaction and its mechanism]»; Сборник рефератов по радиационной медицине **147**, p. 145 (1959). 41

[71] A. M. Zhabotinsky; «Периодический процесс окисления малоновой кислоты растворе [Periodical process of oxidation of malonic acid solution]»; Биофизика **9**, p. 306–311 (1964). 41

[72] V. Castets, E. Dulos, J. Boissonade & P. D. Kepper; «Experimental evidence of a sustained standing Turing-type nonequilibrium chemical pattern»; Physical Review Letters **64**, p. 2953–2956 (1990). https://doi.org/10.1103/physrevlett.64.2953. 41, 107

[73] P. Gray & S. Scott; «Autocatalytic reactions in the isothermal, continuous stirred tank reactor»; Chemical Engineering Science **39**, p. 1087–1097 (1984). https://doi.org/10.1016/0009-2509(84)87017-7. 41, 61

[74] A. Lemarchand & B. Nowakowski; «Do the internal fluctuations blur or enhance axial segmentation?»; EPL (Europhysics Letters) **94**, p. 48 004 (2011). https://doi.org/10.1209/0295-5075/94/48004. 44

[75] P. Dziekan, L. Signon, B. Nowakowski & A. Lemarchand; «Reaction-diffusion approach to prevertebrae formation: Effect of a local source of morphogen»; The Journal of Chemical Physics **139**, p. 114 107 (2013). https://doi.org/10.1063/1.4820952. 44

[76] P. Dziekan, L. Signon, B. Nowakowski & A. Lemarchand; «Effect of a Local Source or Sink of Inhibitor on Turing Patterns»; Communications in Theoretical Physics **62**, p. 622–630 (2014). https://doi.org/10.1088/0253-6102/62/4/20. 44

[77] H. G. Othmer & E. Pate; «Scale-invariance in reaction-diffusion models of spatial pattern formation.»; Proceedings of the National Academy of Sciences **77**, p. 4180–4184 (1980). https://doi.org/10.1073/pnas.77.7.4180. 44

[78] A. Hunding & P. G. Sørensen; «Size adaptation of Turing prepatterns»; Journal of Mathematical Biology **26**, p. 27–39 (1988). https://doi.org/10.1007/bf00280170. 44

[79] M. G. Clerc, E. Tirapegui & M. Trejo; «Pattern Formation and Localized Structures in Reaction-Diffusion Systems with Non-Fickian Transport»; Physical Review Letters **97** (2006). https://doi.org/10.1103/physrevlett.97.176102. 44

[80] P. J. Scherz; «The Limb Bud Shh-Fgf Feedback Loop Is Terminated by Expansion of Former ZPA Cells»; Science **305**, p. 396–399 (2004). https://doi.org/10.1126/science.1096966. 44

[81] J. M. Verheyden & X. Sun; «An Fgf/Gremlin inhibitory feedback loop triggers termination of limb bud outgrowth»; Nature **454**, p. 638–641 (2008). https://doi.org/10.1038/nature07085. 44

[82] M. Rasolonjanahary & B. Vasiev; «Scaling of morphogenetic patterns in reaction-diffusion systems»; Journal of Theoretical Biology **404**, p. 109–119 (2016). https://doi.org/10.1016/j.jtbi.2016.05.035. 61

[83] S. Ishihara & K. Kaneko; «Turing pattern with proportion preservation»; Journal of Theoretical Biology **238**, p. 683–693 (2006). https://doi.org/10.1016/j.jtbi.2005.06.016. 61

[84] D. Ben-Zvi & N. Barkai; «Scaling of morphogen gradients by an expansion-repression integral feedback control»; Proceedings of the National Academy of Sciences **107**, p. 6924–6929 (2010). https://doi.org/10.1073/pnas.0912734107. 61

[85] W.-S. Li, W.-Y. Hu, Y.-C. Pang, T.-R. Liu, W.-R. Zhong & Y.-Z. Shao; «Regulation of Turing patterns in a spatially extended chlorine–iodine–malonic-acid system with a local concentration-dependent diffusivity»; Physical Review E **85** (2012). https://doi.org/10.1103/physreve.85.066132. 61

[86] E. P. Zemskov, K. Kassner, M. J. B. Hauser & W. Horsthemke; «Turing space in reaction-diffusion systems with density-dependent cross diffusion»; Physical Review E **87** (2013). https://doi.org/10.1103/physreve.87.032906. 61

[87] D. M. Umulis & H. G. Othmer; «Mechanisms of scaling in pattern formation»; Development **140**, p. 4830–4843 (2013). https://doi.org/10.1242/dev.100511. 61

[88] W.-C. Lo, S. Zhou, F. Y.-M. Wan, A. D. Lander & Q. Nie; «Robust and precise morphogen-mediated patterning: trade-offs, constraints and mechanisms»; Journal of The Royal Society Interface **12**, p. 20141 041 (2015). https://doi.org/10.1098/rsif.2014.1041. 61

[89] J. Schnakenberg; «Simple chemical reaction systems with limit cycle behaviour»; Journal of Theoretical Biology **81**, p. 389–400 (1979). https://doi.org/10.1016/0022-5193(79)90042-0. 61

[90] A. P. Minton; «The Influence of Macromolecular Crowding and Macromolecular Confinement on Biochemical Reactions in Physiological Media»; Journal of Biological Chemistry **276**, p. 10 577–10 580 (2001). https://doi.org/10.1074/jbc.r100005200. 61

[91] R. J. Ellis & A. P. Minton; «Join the crowd»; Nature **425**, p. 27–28 (2003). https://doi.org/10.1038/425027a. 61

[92] J. Sun & H. Weinstein; «Toward realistic modeling of dynamic processes in cell signaling: Quantification of macromolecular crowding effects»; The Journal of Chemical Physics **127**, p. 155 105 (2007). https://doi.org/10.1063/1.2789434. 61

[93] Z.-R. Xie, J. Chen & Y. Wu; «A coarse-grained model for the simulations of biomolecular interactions in cellular environments»; The Journal of Chemical Physics **140**, p. 054 112 (2014). https://doi.org/10.1063/1.4863992. 61

[94] P. M. Kekenes-Huskey, C. Eun & J. A. McCammon; «Enzyme localization, crowding, and buffers collectively modulate diffusion-influenced signal transduction: Insights from continuum diffusion modeling»; The Journal of Chemical Physics **143**, p. 094 103 (2015). https://doi.org/10.1063/1.4929528. 61

[95] P. Nałęcz-Jawecki, P. Szymańska, M. Kochańczyk, J. Miękisz & T. Lipniacki; «Effective reaction rates for diffusion-limited reaction cycles»; The Journal of Chemical Physics **143**, p. 215 102 (2015). https://doi.org/10.1063/1.4936131. 61

[96] M. D. Bramson; «Maximal displacement of branching brownian motion»; Communications on Pure and Applied Mathematics **31**, p. 531–581 (1978). https://doi.org/10.1002/cpa.3160310502. 73

[97] M. Bramson; *Convergence of solutions of the Kolmogorov equation to travelling waves* (American Mathematical Society, Providence, R.I) (1983); ISBN 978-0-8218-2285-2. 73

[98] U. Ebert & W. van Saarloos; «Front propagation into unstable states: universal algebraic convergence towards uniformly translating pulled fronts»; Physica D: Nonlinear Phenomena **146**, p. 1–99 (2000). https://doi.org/10.1016/s0167-2789(00)00068-3. 73

[99] É. Brunet & B. Derrida; «An Exactly Solvable Travelling Wave Equation in the Fisher–KPP Class»; Journal of Statistical Physics **161**, p. 801–820 (2015). https://doi.org/10.1007/s10955-015-1350-6. 73

[100] J. Berestycki, É. Brunet, S. C. Harris & M. Roberts; «Vanishing Corrections for the Position in a Linear Model of FKPP Fronts»; Communications in Mathematical Physics **349**, p. 857–893 (2016). https://doi.org/10.1007/s00220-016-2790-9. 73

[101] A. Lemarchand, A. Lesne & M. Mareschal; «Langevin approach to a chemical wave front: Selection of the propagation velocity in the presence of internal noise»; Physical Review E **51**, p. 4457–4465 (1995). https://doi.org/10.1103/physreve.51.4457. 73

[102] M. A. Karzazi, A. Lemarchand & M. Mareschal; «Fluctuation effects on chemical wave fronts»; Physical Review E **54**, p. 4888–4895 (1996). https://doi.org/10.1103/physreve.54.4888. 73

[103] J. S. Hansen, B. Nowakowski & A. Lemarchand; «Microscopic simulations of an exothermic chemical wave front: Departure from the continuity equations»; The Journal of Chemical Physics **125**, p. 044 313 (2006). https://doi.org/10.1063/1.2217441. 73, 78, 90

[104] E. Brunet, B. Derrida, A. H. Mueller & S. Munier; «Phenomenological theory giving the full statistics of the position of fluctuating pulled fronts»; Physical Review E **73** (2006). https://doi.org/10.1103/physreve.73.056126. 73

[105] W. van Saarloos; «Front propagation into unstable states»; Physics Reports **386**, p. 29–222 (2003). https://doi.org/10.1016/j.physrep.2003.08.001. 75

[106] E. Brunet & B. Derrida; «Shift in the velocity of a front due to a cutoff»; Physical Review E **56**, p. 2597–2604 (1997). https://doi.org/10.1103/physreve.56.2597. 75, 76

[107] É. Brunet; *Some aspects of the Fisher-KPP equation and the branching Brownian motion*; Habilitation à diriger des recherches; UPMC (2016). https://tel.archives-ouvertes.fr/tel-01417420. 78

[108] S. Fedotov; «Wave front for a reaction-diffusion system and relativistic Hamilton-Jacobi dynamics»; Physical Review E **59**, p. 5040–5044 (1999). https://doi.org/10.1103/physreve.59.5040. 91

[109] S. Mirrahimi, G. Barles, B. Perthame & P. E. Souganidis; «A Singular Hamilton–Jacobi Equation Modeling the Tail Problem»; SIAM Journal on Mathematical Analysis **44**, p. 4297–4319 (2012). https://doi.org/10.1137/100819527. 91

[110] C. Xu & A. J. Roberts; «On the low-dimensional modelling of Stratonovich stochastic differential equations»; Physica A: Statistical Mechanics and its Applications **225**, p. 62–80 (1996). https://doi.org/10.1016/0378-4371(95)00387-8. 105

[111] A. J. Roberts; «Normal form transforms separate slow and fast modes in stochastic dynamical systems»; Physica A: Statistical Mechanics and its Applications **387**, p. 12–38 (2008). https://doi.org/10.1016/j.physa.2007.08.023. 105

[112] A. J. Roberts; *Model emergent dynamics in complex systems* (Society for Industrial and Applied Mathematics, Philadelphia) (2015); ISBN 978-1611973556. 105

[113] E. Forgoston, L. Billings & I. B. Schwartz; «Model Reduction in Stochastic Environments»; dans «Stochastic PDEs and Modelling of Multiscale Complex System», p. 37–61 (WORLD SCIENTIFIC) (2019). https://doi.org/10.1142/9789811200359_0003. 105

[114] V. I. Arnold; *Chapitres supplémentaires de la théorie des équations différentielles ordinaires* (Editions Mir Librairie du globe, Moscou Paris) (1996); ISBN 978-2855360454. 105

[115] S. Cohen; *Stochastic calculus and applications* (Birkhäuser, New York, NY) (2015); ISBN 978-1493928668. 105

[116] R. Grima; «An effective rate equation approach to reaction kinetics in small volumes: Theory and application to biochemical reactions in nonequilibrium steady-state conditions»; The Journal of Chemical Physics **133**, p. 035 101 (2010). https://doi.org/10.1063/1.3454685. 106

[117] R. Grima; «Intrinsic biochemical noise in crowded intracellular conditions»; The Journal of Chemical Physics **132**, p. 185 102 (2010). https://doi.org/10.1063/1.3427244. 106

[118] S. Smith, C. Cianci & R. Grima; «Macromolecular crowding directs the motion of small molecules inside cells»; Journal of The Royal Society Interface **14**, p. 20170 047 (2017). https://doi.org/10.1098/rsif.2017.0047. 106

[119] S. Smith & R. Grima; «Fast simulation of Brownian dynamics in a crowded environment»; The Journal of Chemical Physics **146**, p. 024 105 (2017). https://doi.org/10.1063/1.4973606. 106

[120] A. S. Zadorin, Y. Rondelez, G. Gines, V. Dilhas, G. Urtel, A. Zambrano, J.-C. Galas & A. Estevez-Torres; «Synthesis and materialization of a reaction–diffusion French flag pattern»; Nature Chemistry **9**, p. 990–996 (2017). https://doi.org/10.1038/nchem.2770. 106

[121] G. Urtel, A. Estevez-Torres & J.-C. Galas; «DNA-based long-lived reaction–diffusion patterning in a host hydrogel»; Soft Matter **15**, p. 9343–9351 (2019). https://doi.org/10.1039/c9sm01786k. 106

[122] A. Senoussi, S. Kashida, R. Voituriez, J.-C. Galas, A. Maitra & A. Estevez-Torres; «Tunable corrugated patterns in an active nematic sheet»; Proceedings of the National Academy of Sciences **116**, p. 22 464–22 470 (2019). https://doi.org/10.1073/pnas.1912223116. 106

[123] M. V. D. Hofstadt, J.-C. Galas & A. Estevez-Torres; «Spatiotemporal Patterning of Living Cells with Extracellular DNA Programs»; ACS Nano (2020). https://doi.org/10.1021/acsnano.0c09422. 106

[124] R. J. Field, E. Koros & R. M. Noyes; «Oscillations in chemical systems. II. Thorough analysis of temporal oscillation in the bromate-cerium-malonic acid system»; Journal of the American Chemical Society **94**, p. 8649–8664 (1972). https://doi.org/10.1021/ja00780a001. 107

[125] R. A. Schmitz, K. R. Graziani & J. L. Hudson; «Experimental evidence of chaotic states in the Belousov–Zhabotinskii reaction»; The Journal of Chemical Physics **67**, p. 3040–3044 (1977). https://doi.org/10.1063/1.435267. 107

[126] F. Argoul, A. Arneodo, P. Richetti & J. C. Roux; «From quasiperiodicity to chaos in the Belousov–Zhabotinskii reaction. I. Experiment»; The Journal of Chemical Physics **86**, p. 3325–3338 (1987). https://doi.org/10.1063/1.452751. 107

[127] I. R. Epstein & K. Showalter; «Nonlinear Chemical Dynamics: Oscillations, Patterns, and Chaos»; The Journal of Physical Chemistry **100**, p. 13 132–13 147 (1996). https://doi.org/10.1021/jp953547m. 107

[128] A. S. Mikhailov & K. Showalter; «Control of waves, patterns and turbulence in chemical systems»; Physics Reports **425**, p. 79–194 (2006). https://doi.org/10.1016/j.physrep.2005.11.003. 107

[129] D. J. Evans, E. G. D. Cohen & G. P. Morriss; «Probability of second law violations in shearing steady states»; Physical Review Letters **71**, p. 2401–2404 (1993). https://doi.org/10.1103/physrevlett.71.2401. 109

[130] G. Gallavotti & E. G. D. Cohen; «Dynamical Ensembles in Nonequilibrium Statistical Mechanics»; Physical Review Letters **74**, p. 2694–2697 (1995). https://doi.org/10.1103/physrevlett.74.2694. 109

[131] G. Gallavotti & E. G. D. Cohen; «Dynamical ensembles in stationary states»; Journal of Statistical Physics **80**, p. 931–970 (1995). https://doi.org/10.1007/bf02179860. 109

[132] R. Rao & M. Esposito; «Detailed Fluctuation Theorems: A Unifying Perspective»; Entropy **20**, p. 635 (2018). https://doi.org/10.3390/e20090635. 109

[133] S. Schnell, R. Grima & P. Maini; «Multiscale Modeling in Biology»; American Scientist **95**, p. 134 (2007). https://doi.org/10.1511/2007.64.134. 109

[134] R. Grima; «Multiscale Modeling of Biological Pattern Formation»; dans «Current Topics in Developmental Biology», p. 435–460 (Elsevier) (2008). https://doi.org/10.1016/s0070-2153(07)81015-5. 109

[135] M. Voliotis, P. Thomas, R. Grima & C. G. Bowsher; «Stochastic Simulation of Biomolecular Networks in Dynamic Environments»; PLOS Computational Biology **12**, p. e1004 923 (2016). https://doi.org/10.1371/journal.pcbi.1004923. 109

[136] D. Schnoerr, G. Sanguinetti & R. Grima; «Approximation and inference methods for stochastic biochemical kinetics—a tutorial review»; Journal of Physics A: Mathematical and Theoretical **50**, p. 093 001 (2017). https://doi.org/10.1088/1751-8121/aa54d9. 109

[137] G. Morgado, M. Collet, R. Lespiat, H. Rétot & A. Lemarchand; «Submicrometric Picture of Plaster Hydration: Optimization of the Addition of Gypsum Needles»; The Journal of Physical Chemistry C **121**, p. 5657–5666 (2017). https://doi.org/10.1021/acs.jpcc.7b00482. 110

[138] G. Morgado, L. Masurel, Z. Rhodes, R. Lespiat, H. Rétot & A. Lemarchand; «Kinetics of plaster hydration and structure of gypsum: Experiments and kinetic Monte Carlo simulations with added gypsum seeds»; Journal of Crystal Growth **507**, p. 124–133 (2019). https://doi.org/10.1016/j.jcrysgro.2018.11.006. 110